



Tathiana Caram Souza de Paula Figueiredo

**On the Mechanical Behavior of Strain
Hardening Cementitious Composites
(SHCC) under Combined and Impact
Loading**

Tese de Doutorado

Thesis presented to the Programa de Pós-Graduação
em Engenharia Civil of PUC-Rio in partial fulfillment
of the requirements for the degree of Doutor em
Ciências – Engenharia Civil.

Advisor: Prof. Flávio de Andrade Silva

Rio de Janeiro
September 2021



Tathiana Caram Souza de Paula Figueiredo

**On the Mechanical Behavior of Strain
Hardening Cementitious Composites
(SHCC) under Combined and Impact
Loading**

Thesis presented to the Programa de Pós-Graduação
em Engenharia Civil of PUC-Rio in partial fulfillment
of the requirements for the degree of Doutor em
Engenharia Civil. Approved by the Examination
Committee:

Prof. Flávio de Andrade Silva

Advisor

Departamento de Engenharia Civil e Ambiental – PUC-Rio

Prof. Daniel Carlos Taissum Cardoso

Departamento de Engenharia Civil e Ambiental – PUC-Rio

Prof. Luiz Carlos Wrobel

Departamento de Engenharia Civil e Ambiental – PUC-Rio

Prof. Antonio Domingues de Figueiredo

USP

Prof. Joaquim António Oliveira de Barros

UMINHO

Rio de Janeiro, 29th September, 2021.

All rights reserved.

Tathiana Caram Souza de Paula Figueiredo

Construction technical degree at CEFET-RJ in 2007, undergrad in Civil Engineering at PUC-Rio in 2010, M.Sc. Degree in Civil Engineering also at PUC-Rio in 2014. Areas of interest: cementitious composites, building pathologies, structural rehabilitation, retrofitting, structural modeling.

Bibliographic data

Figueiredo, Tathiana Caram Souza de Paula

On the Mechanical Behavior of Strain Hardening Cementitious Composites (SHCC) under Combined and Impact Loading / Tathiana Caram Souza de Paula Figueiredo ; advisor: Flávio de Andrade Silva. – 2021.

216 f. : il. color. ; 30 cm

Tese (doutorado) – Pontifícia Universidade Católica do Rio de Janeiro, Departamento de Engenharia Civil e Ambiental, 2021.

Inclui referências bibliográficas.

1. Engenharia Civil e Ambiental - Teses. 2. Concreto armado. 3. SHCC. 4. Impacto. 5. Carregamento combinado. 6. Torção. I. Silva, Flávio de Andrade. II. Pontifícia Universidade Católica do Rio de Janeiro. Departamento de Engenharia Civil e Ambiental. III. Título.

CDD: 624

I dedicate this thesis to my
beloved grandparents
Marilda and Augusto Caram,
who first taught me how to
be captivated by knowledge.

Acknowledgments

When finishing such an expensive and time-consuming experimental program, one has many things to be thankful for.

First, I would like to express my kindest and sincerest gratitude to my advisor, Prof. Flávio de Andrade Silva, first for his trust in a student who spent so much time in the industry, and then for his continuous supervision and motivation, which were essential not only for the development of the present research but for my academic development.

This work was only possible due to the invaluable financial support of three agencies. First, of the National Council for Scientific and Technological Development (CNPq, from the name in Portuguese), which granted my scholarships during my time in Brazil (GM/GD 141936/2017-7, 141075/2018-0, 141201/2019-3, and 140106/2020-0). Then of the Coordination for the Improvement of High Education (CAPES, from the name in Portuguese), which financed part of the used supplies, and granted my financial support during my sandwich time in Germany through the PROBRAL program (no. 12/2017), accorded with the German Academic Exchange Service (DAAD, from the name in German) under the project number 8887.144079/2017-00. Last, to the German Research Foundation (DFG, from the name in German) in the framework of the Research Group GRK 2250/1: “Mineral-bonded composites for enhanced structural impact safety” (project number 287321140), which financed my research activities developed in Germany.

I am honored to be part of PUC’s family for so long. For me, this institution was always a synonym of scientific exponent, and as such, house great minds, with whom I had the opportunity to learn. I’m grateful to all my professors. Once again I’m thankful to Prof. Marta Velasco, my Master’s advisor, for her participation in so many important moments during my academic career, being the most recent, the

introduction to Prof. Silva and his work, on my return to academia. A special thanks must be given to Prof. Daniel Cardoso, who besides being an example of professionalism in the lab and at academic venues, gave me prompt support during the definition of parameters of my structural program, for which I would be ever grateful. To Dr. Cassio Gaspar, my deepest appreciation for all his patient guidance and contributions through the modal assessment of the structural tests. A kind thanks must also be given to Mrs. Luana Martins and Mrs. Rita de Cassia Leite for their ever care and readiness to help, which were so many times indispensable during my research.

I would also like to express my kindest gratitude to the staff of the Laboratory of Structures and Materials (LEM-DEC, from the name in Portuguese) of PUC-Rio: Euclides Domingues, Bruno Viana, José Marques, José Nilson, Rogério Rossi, Jhansen Salles, and Anderson Viana. These guys spent much time helping, sharing knowledge, and encouraging me. From PUC-Rio's Mechanical Engineering Department, I must also express my sincere gratitude to Dr. Giancarlo Gonzáles who embraced the combined loading analysis with me, enabling the acquisition of state-of-the-art results, and to M.Sc. Adrian Giassone, technical manager from the department's technical institute (ITUC, from the name in Portuguese), who kindly opened his lab for me, helped me with the development of our combined loading tests and assisted through all the experimental program.

I know I will be ever thankful to all the LEM-DEC's team, especially the mates that shared their time with me at the lab, and outside of it. Kind gratefulness must be given to Kíssila Goliath, Fernanda Salgado, Felipe Pinheiro, Rafael Manfredi and Victor Nogueira for all the sharing of ideas, concerns, and above all, laughs during the breaks. I'm most grateful for my time spent with the researcher Renata Lorenzoni in Dresden, which besides allowing the expansion of my admiration for her work, enabled the establishment of a new fellowship and productive partnership. Lastly, this doctorate brought me the friendship of an incredible group, with whom I started to share achievements, anxieties, and support. My greatest estimation and

admiration are given to Ana Carolina Trindade, Daiana Eringer, Letícia Oliveira, Raylane Castoldi, and Rebecca Mansur, who will always have a special place with me.

During my sandwich period, I had the opportunity to work in two forefront institutes regarding SHCC and extreme scenarios: the Institute of Construction Materials (iFB, from the name in German) and the Institute of Solid Structures (iFM), both from the Technical University of Dresden (TUD). I would like to express my sincere gratitude to Prof. Victor Mechtcherine for hosting me with his group (iFB), enabling the development of my experimental program. I am grateful for all the technical and scientific support given by researchers and laboratory staff from both institutes. I express my acknowledgments in particular to Dr. Ali Heravi, M.Sc. Ameer H. Ahmed, Mr. Fabian Israel, M.Sc. Franz Bracklow, Mr. Kai-Uwe Mehlisch, and Mr. Tilo Günzel for their help during the preparation and execution of the experiments. Special gratitude must be also given to Dr. Iurie Curuso for his constant support and encouragement of ideas, which were invaluable during this time. Moreover, a special thanks must be given to Dr. Marcus Hering for his help conducting the structural tests but especially enabling my activities at the iFM. This experience also brought me a lifetime friendship with the researcher Irina Ivanova, who incite my great esteem, both professionally, and as a human being.

For the Professors who compose this thesis committee, I express my sincere gratefulness for their availability, careful reading, and considerations.

My kindest appreciation will always be given to my family, especially my mother and sister, Cristina and Sylvia Caram, for their continued faithfulness and love. And finally, but most importantly, for his permanent support, encouragement, and unwavering confidence, I give my ultimate gratitude to my husband Jefferson Figueiredo, my home wherever our geographic distance.

This study was financed in part by the Coordenação de Aperfeiçoamento de Pessoal de Nível Superior – Brasil (CAPES) – Finance Code 001.

Abstract

Figueiredo, Tathiana Caram Souza de Paula; Silva, Flávio de Andrade (Advisor). **On the Mechanical Behavior of Strain Hardening Cementitious Composites (SHCC) under Combined and Impact Loading.** Rio de Janeiro, 2021. 216 p. Tese de Doutorado – Departamento de Engenharia Civil e Ambiental, Pontifícia Universidade Católica do Rio de Janeiro.

Reinforced concrete (RC) has been widely used in civil constructions for almost two centuries due to its versatility and relatively low cost-effectiveness ratio when compared with other structural systems. It is notably the preferred material for the construction of strategic infrastructures. However, RC constructions are in constant deterioration. Special attention had been given in the last decades to the influence of dynamic scenarios on RC structures due to concrete's inherent low tensile strength and brittle nature, which promotes intense cracking during these events. The present research focused on the assessment of two variations of strain-hardening cementitious composites (SHCC) as strengthening material to improve the impact resistance of existing buildings, moreover structural members with critical shear failure. SHCC is a somewhat new class of fiber-reinforced composite reinforced with synthetic microfibers with an average content of 2 % in volume. Previous research studies already demonstrated that this composite is able to yield substantial deformations under tension (up to 6 % depending on the dosage) during its multiple-cracking phase, while enduring a crack-width limit of 100 μm . SHCC seems especially appropriate to withstand high-velocity impacts due to the relevant number of surfaces that are formed during its deformation phase since it represents a high perspective of energy dissipation without reducing load-bearing capacity. Two types of normal-strength SHCC were chosen to be assessed in this research. The composites differed mainly in the type of reinforcing fiber: PVA, and UHMWPE. As structural members embodied in structures are often subjected to multiaxial stress states, to evaluate SHCC's potential as a strengthening material, combined torsion and tension tests were developed. These tests deepen the understanding of SHCC's mechanical performance under shear, while also enabled

the combination with normal stresses. Then, SHCC's actual potential to improve the impact resistance and afterlife of existing structural members was investigated during an extensive experimental program that counted with 24 real-scale beams. The varied parameters were: (i) the type of SHCC; (ii) the internal reinforcement configuration (specimens with, and without stirrups); (iii) the impact energy (which was varied between 2.1 kJ and 6.4 kJ, corresponding to approximated velocities of 17 m/s to 30 m/s, respectively). The results were assessed in terms of their mechanical response, cracking patterns, and modal analysis. It was demonstrated that both types of composites improved the impact resistance of the strengthened RC members, outstandingly improving the impact safety with regards to residual dynamic response and stability while presenting a substantial reduction of spalling and scabbing material. The SHCC produced with UHMWPE fibers appeared to be less sensitive to the presence or absence of stirrups, posing as more suitable alternative for shear strengthening applications within dynamic scenarios where there is a deficient, or even uncertainty, about the internal transversal reinforcement of the existing members.

Keywords

Reinforced concrete; SHCC; Impact; Combined loading; Torsion.

Resumo

Figueiredo, Tathiana Caram Souza de Paula; Silva, Flávio de Andrade (Advisor). **Desempenho Mecânico de Compósitos Cimentícios de Comportamento Strain-Hardening Submetidos a Carregamentos Combinados e de Impacto.** Rio de Janeiro, 2021. 216 p. Tese de Doutorado – Departamento de Engenharia Civil e Ambiental, Pontifícia Universidade Católica do Rio de Janeiro.

O concreto armado (CA) tem sido amplamente utilizado em construções civis durante quase dois séculos devido a sua versatilidade e relativamente baixo custo-benefício quando comparado com outros sistemas estruturais. É, notoriamente, o sistema mais adotado na construção de obras estratégicas e de infraestrutura. No entanto, as construções de CA estão em constante deterioração. Sobretudo nas últimas décadas, atenção especial vem sendo dada à influência de cenários dinâmicos nesse tipo de sistema estrutural devido à intrínseca baixa resistência à tração e fragilidade do concreto, que promovem extensos horizontes de fissuração na ocorrência desses eventos. A presente investigação dedicou-se à avaliação de duas variações de compósitos cimentícios de comportamento *strain-hardening* (SHCC) como material de reforço para melhorar a resistência ao impacto de edifícios existentes, em especial membros estruturais com falhas críticas por cisalhamento. SHCC é uma classe relativamente nova de compósito cimentício reforçado com fibras, em geral microfibras sintéticas com fração volumétrica média de 2 %. Estudos recentes já demonstraram que este compósito é capaz de deformar-se substancialmente quando submetido à tração direta (até 6% dependendo da dosagem) durante o estágio de múltipla-fissuração, enquanto sustenta uma abertura de fissura de até 100 μm . O SHCC parece especialmente adequado para resistir a impactos de alta velocidade devido ao número relevante de superfícies que se formam durante a sua fase de deformação, uma vez que a grande quantidade de superfícies que são formadas durante o processo de múltipla-fissuração representa uma perspectiva elevada de dissipação de energia sem reduzir a capacidade de carregamento. Dois tipos de SHCC de resistência normal foram escolhidos para serem avaliados nesta investigação. Os compósitos diferenciavam-se

principalmente no tipo de fibra de reforço: PVA e UHMWPE. Como os elementos estruturais incorporados em estruturas estão frequentemente sujeitos a estados multiaxiais de tensão, para avaliar o potencial de SHCC como material de reforço, ensaios combinados de torção e tensão foram desenvolvidos. Tais resultados permitiram o aprofundamento da compreensão do desempenho mecânico dos SHCC em análise sob cisalhamento, ao mesmo tempo que permitem a combinação desses esforços com tensões normais de tração. Em seguida, o potencial efetivo do SHCC no melhoramento da resistência e resiliência de elementos estruturais existentes a cargas de impacto foi investigado por um extenso programa experimental que contou com 24 vigas de escala real. Os parâmetros variados foram: (i) o tipo de SHCC; (ii) a configuração de reforço interno (espécimes com e sem estribos); (iii) a energia de impacto (que variou entre 2,1 kJ e 6,4 kJ, correspondendo a velocidades aproximadas de 17 m/s a 30 m/s, respectivamente). Os resultados foram avaliados em termos da resposta mecânica, padrões de fissuração, e análise modal. Foi demonstrado que ambos os tipos de SHCC contribuíram para a melhora da resistência ao impacto das vigas de CA reforçadas, melhorando expressivamente a resposta dinâmica residual e de estabilidade, enquanto contribuíram efetivamente para segurança de usuários ao propiciar uma redução substancial de detritos desprendidos durante os testes. O SHCC reforçado com fibras de UHMWPE mostrou-se menos sensível à presença ou ausência de estribos, sugerindo que esse compósito seja o mais adequado para aplicações de reforço de cisalhamento em cenários dinâmicos onde existe uma deficiência, ou incerteza, sobre o reforço transversal interno dos membros existentes.

Palavras-chave

Concreto armado; SHCC; Impacto; Carregamento combinado; Torção.

Summary

Abstract	8
Resumo	10
Summary	12
List of figures	15
List of tables	21
1 Introduction	23
1.1. Motivation	23
1.2. Goals	25
1.3. Thesis organization	25
1.4. General remarks	26
2 State of the art review	28
2.1. Understanding SHCC	28
2.1.1. Performance under direct tensile loading	28
2.1.2. SHCC tailoring	32
2.1.3. Extreme scenarios	36
2.1.4. Shear behavior	41
2.1.5. Structural applications	43
2.2. Torsion	47
2.2.1. Torsional behavior of FRC	48
2.3. Impact loading scenarios	49
2.3.1. Reinforced concrete subjected to impact	49
2.3.2. FRC subjected to impact	54

3 Mechanical behavior of strain-hardening cement-based composites (SHCC) subjected to torsional loading and to combined torsional and axial loading	56
3.1. Introduction	56
3.2. Materials and methods	58
3.2.1. SHCC compositions	58
3.2.2. Specimen preparation	60
3.3. Experimental program	61
3.3.1. Testing setup and load cases	61
3.3.2. 3D optical measurements and DIC	62
3.4. Results and discussion	65
3.4.1. Uniaxial tension experiments (LC1)	65
3.4.2. Torsion experiments with blocked axial deformation (LC2)	69
3.4.3. Torsion experiments with free axial deformation (LC3)	72
3.4.4. Combined torsion and axial tension (LC4)	75
3.4.5. Concluding comparisons of all load cases	77
3.5. Conclusions	79
3.6. Overview	81
4 Effect of shear reinforcement and external strengthening with strain-hardening cement-based composites (SHCC) on the impact resistance of reinforced concrete beams	82
4.1. Introduction	82
4.2. Experimental program	84
4.2.1. Materials	84
4.2.2. RC beams production and strengthening	86
4.2.3. Specimens' details and setup	88
4.2.4. Methodology for indirect parameters estimation	92
4.3. Results and discussion	93
4.3.1. Non-strengthened beams	94
4.3.2. Beams strengthened with SHCC	100
4.4. Conclusions	110

5 Experimental modal analysis of RC beams strengthened with SHCC subjected to shear under impact strain rates	112
5.1. Introduction	112
5.2. Materials and methods	114
5.2.1. Materials	114
5.2.2. Test specimens and setup	116
5.3. Analysis methodology	118
5.4. Results and discussion	121
5.4.1. RC-beams	121
5.4.2. RC-beams strengthened with SHCC	125
5.5. Conclusions	132
6 Conclusions and outlook	133
6.1. Conclusions	133
6.2. Suggestions for future works	136
References	137
Appendix 1 – Cracking patterns of the structural tests	160
Appendix 2 – Datasheets of the structural tests	164

List of figures

Fig. 1.1 – Examples of structures with complex stress trajectories and deleterious effects: (a) spillways subjected to erosion, abrasion, and cavitation due to the water action; (b) dams subjected to the impact of wood logs; (c) offshore wind power towers; (d) viaducts and bridges subjected to traffic and environmental effects.....	24
Fig. 2.1 – Mechanical behavior of SHCC [19]: (a) Typical stress-strain curve; (b) SHCC additional energy absorption potential due multiple cracking process.....	30
Fig. 2.2 – SHCC link slab reinforced with FRP [30].	30
Fig. 2.3 – Typical strain hardening behavior of SHCC reinforced with PVA fibers during a direct tensile test [34].	31
Fig. 2.4 – Graphical comparison of PVA-SHCC dosages in terms of the main inputs. Values in kg/m^3	34
Fig. 2.5 – Typical stress-displacement curve of SHCC [10,46,51,52].	35
Fig. 2.6 – Types of crack derived from cross-sectional tension stress [56]: (a) Griffith-type, with values of CMOD (δm) exceeding the critical size (δp); (b) Flat, or steady-state type, with CMOD (δss) smaller than the critical value on the whole length of the crack.....	36
Fig. 2.7 – Failure mechanisms of SHCC at low and high strain rates: (a) fracture surface of a specimen tested at 10^{-3} s^{-1} (b) fracture surface of a specimen tested at 25 s^{-1} [23].	37
Fig. 2.8 – Stress-strain curves of normal-strength (M1) SHCC reinforced with PVA and PE fibers [63]. Curves (a) and (b) refers to quasi-static tension tests ($5 \cdot 10^{-4} \text{ s}^{-1}$); curves (c) and (d) to high-speed tension tests (120 s^{-1}). Note the different axes' limits.....	38
Fig. 2.9 – ESEM images of normal strength SHCC with PVA fibers [10]. Fractured surfaces of samples tested in different strain-rate regimes: (a) quasi-static; (b) dynamic.....	39

Fig. 2.10 – ESEM images of normal strength SHCC with PE fibers [10]. Fractured surfaces of samples tested in different strain-rate regimes: (a) quasi-static; (b) dynamic.	39
Fig. 2.11 – Pullout force <i>versus</i> displacement slip from pullout tests made with PVA fibers in normal-strength matrix with an embedded length of 2 mm under different displacement rates: (a) $5 \cdot 10^{-3} \text{ mm.s}^{-1}$; (b) 5.10 mm.s^{-1}	40
Fig. 2.12 – Pullout force <i>versus</i> displacement slip from pullout tests made with PE fibers in normal-strength matrix with an embedded length of 2 mm under different displacement rates: (a) $5 \cdot 10^{-3} \text{ mm.s}^{-1}$; (b) 5.10 mm.s^{-1}	40
Fig. 2.13 – Effect of temperature in the tensile strength, strain capacity and work-to-fracture of PVA-SHCC tested at a quasi-static strain rate ($3 \cdot 10^{-4} \text{ s}^{-1}$) [26].	41
Fig. 2.14 – Effect of temperature exposure on PVA-fibers' strength [65].	41
Fig. 2.15 – Test methods for shear transfer in concrete and FRC [68–70]: (a) Ohno shear beam; (b) Iosipescu beam; (c) single-plane, push-off specimen; (d) double-plane shear test regulated by the Japan Society of Civil Engineers (JSCE); (e) single-plane shear test regulated by the <i>fib</i>	42
Fig. 2.16 – Illustration of an RC concrete element exposed to chloride ions [88].	44
Fig. 2.17 – Possible combinations of SHCC and regular RC for steel-reinforcement protection: (a) regular matrix replacement; (b) patch-material / cover-layer [88].	44
Fig. 2.18 – Bonding influence in the crack patterns of SHCC patches: (a) Good bond relates to multiple-cracking formation; (b) Bad bond relates to the patch spalling [25].	46
Fig. 2.19 – Crack patterns and failure modes of the beams strengthened with SHCC [17].	47
Fig. 2.20 – Summary of different types of damage on RC structures coming from impact scenarios [119,133].	51
Fig. 2.21 – Summary of typical strain-rate ranges of RC structures matched with available strain-rate ranges of tests available in the literature [11].	52
Fig. 2.22 – Impact behavior of RC members strengthened with FRC [adapted from 118]: (a) without strengthening; (b) with strengthening on the front-surface (impacted plane); (c) with strengthening on the rear-surface (opposite to the	

impacted plane); (d) with strengthening on the surfaces parallel to the impactor's trajectory (side surfaces).....	55
Fig. 3.1 – Specimen fixation, geometry and dimensions in mm.	62
Fig. 3.2 – (a) Dumbbell-shaped specimen with dimensions in mm indicating the positions of the global (GCS) and the local coordinate systems (LCS) as well as the virtual calipers. The grey portions at the specimens' ends represent the regions embedded in the glue and encased by the metal rings. (b) Schematic representation of the assessed CFD in the DIC analysis.....	64
Fig. 3.3 – Schematic, exaggerated representation of the influence of cross-sectional shape in mm and location of the DIC caliper on the measured CFD II and CFD III.	65
Fig. 3.4 – Uniaxial tensile behavior of PVA-SHCC and PE-SHCC: (a) load-deformation curves and (b) stress-strain curves.	66
Fig. 3.5 – CFD analysis under LC1: (a) PVA-SHCC and (b) PE-SHCC. Note different x-axes (diagrams on the left) and different color scales (pictures on the right).	68
Fig. 3.6 – (a) Torque-rotation angle curves and (b) compression force-rotation angle curves of PVA-SHCC and PE-SHCC obtained in LC2.	69
Fig. 3.7 – CFD analysis LC2: (a) PVA-SHCC and (b) PE-SHCC. Note the difference in the horizontal axes (diagrams on the left).	71
Fig. 3.8 – Mechanical behavior of PVA-SHCC and PE-SHCC under LC3: (a) torque-rotation angle curves; (b) torque-axial expansion curves.	72
Fig. 3.9 – CFD analysis under LC3: (a) PVA-SHCC; (b) PE-SHCC. Note difference in the horizontal axes (diagrams on the left) and color scales (pictures on the right).	74
Fig. 3.10 – Behavior of PVA-SHCC and PE-SHCC under LC4: (a) axial load-deformation; (b) torque-rotation curves.	75
Fig. 3.11 – CFD-analysis of the specimens tested under LC4: (a) PVA-SHCC and (b) PE-SHCC. Note different axes (diagrams on the left) and different color scales (pictures on the right).	76
Fig. 3.12 – Envelopes of the axial load-deformation curves under LC1 (uniaxial tension) and LC4 (combined tension and torsion): (a) PVA-SHCC and (b) PE-SHCC.....	77

Fig. 3.13 – Influence of load case on the torsional response of (a) PVA-SHCC and (b) PE-SHCC.....	78
Fig. 3.14 – Multiple cracking patterns of representative specimens in each load case.	79
Fig. 4.1 – Representative tensile stress-strain curves of the studied SHCC tested under monotonic strain rates at 28 days.	86
Fig. 4.2 – Casting procedures of the strengthening with SHCC: (a) Substrate preparation by washing the superficial cement-paste layer; (b) Fixation of the wood templates; (c) Molding process; (d) Surface correction.	87
Fig. 4.3 – Geometry of the RC beams, layout of the steel reinforcement and location of the embodied instrumentation: (a) Beams without stirrups (Se); (b) Beams with stirrups (Ce). Dimensions in mm.	88
Fig. 4.4 – Testing setup's boundary conditions.....	90
Fig. 4.5 – Configurations of the specimens, charging gas pressures and number of impacts.....	90
Fig. 4.6 – Accelerated configuration of the impact system [115]: (a) Schematic sketch of the testing facility; (b) Detailed image of the projectile including the retraction device.	91
Fig. 4.7 – Assumed shape of the loading pulse.	93
Fig. 4.8 – Impactor velocity and calculated impact load obtained for each loading pressure.....	94
Fig. 4.9 – Time histories of the summed reaction forces measured by the load cells and the displacements obtained through the LDV during the experiments of the non-strengthened beams.	95
Fig. 4.10 – Time histories of the LDV displacements during the experiment for the specimen Ce-PVA-0.8.	97
Fig. 4.11 – Load-deflection curves of the RC-beams during the experiments.....	98
Fig. 4.12 – Acceleration histories of the specimens with and without stirrups during the experiment.	99
Fig. 4.13 – Damage extent in the RC beams after the impact tests with different charges.	100
Fig. 4.14 – Time histories of the summed reaction forces measured by the load cells and the displacements obtained through the LDV during the experiments of the strengthened beams.....	102

Fig. 4.15 – Maximum reaction loads: (a) reference beams; (b) beams strengthened with PVA-SHCC; (c) beams strengthened with PE-SHCC.	102
Fig. 4.16 – Time histories of the bearing loads of the specimens subjected to repeated impact loads.	103
Fig. 4.17 – Load-deflection curves of impacted beams strengthened with SHCC.	104
Fig. 4.18 – Acceleration histories of the specimens reinforced with SHCC with and without stirrups during the experiment.....	107
Fig. 4.19 – Peak values of strain on the: (a) longitudinal rebars, in the specimens without stirrups; (b) longitudinal rebars, in the specimens with stirrups; (c) stirrups.	108
Fig. 4.20 – Comparative damage assessment of the specimens tested under 29.9 m/s: influence of the stirrups and the SHCC reinforcement: (a) Cracking pattern of the reference specimen without stirrups; (b) Highlighted cracking pattern and middle cross-section of the specimen without stirrups and strengthened with PVA-SHCC; (c) Highlighted cracking pattern and middle cross-section of the specimen without stirrups and reinforced with PE-SHCC; (d) Cracking pattern of the reference specimen with stirrups; (e) Highlighted cracking pattern and middle cross-section of the specimen with stirrups and reinforced with PVA-SHCC; (f) Highlighted cracking pattern and middle cross-section of the specimen with stirrups and strengthened with PE-SHCC.	109
Fig. 4.21 – Lateral and upper view of the specimens impacted more than one time. Photo report of the cracking patterns after the first and the last impact: (a) Se-PVA; (b) Ce-PVA; (c) Se-PE; (d) Ce-PE.	110
Fig. 5.1 – Direct tensile behavior of the studied SHCC at 28 days: (a) PE-SHCC; (b) PVA-SHCC. Note different scale of the x-axes.	115
Fig. 5.2 – Test configuration: (a) View of the test set-up; (b) Illustration of the boundary conditions and positioning of the transducers (dimensions in mm); (c) Schematic representation of the measuring steps considered on the experimental modal analysis.	117
Fig. 5.3 – Summary of the specimen characteristics and loading conditions.....	118
Fig. 5.4 – Three first theoretical vibrational modes with indication of the transducers' positioning (e.g. WOS-Ref): (a) mode shapes and corresponding	

- natural frequencies obtained through numerical modeling; (b) correlation example of the NMC with the analytical formulations. 119
- Fig. 5.5 – Typical vibration spectrums for an intact specimen (e.g. WOS-Ref): (a) acceleration-time response considering the four accelerometers; (b) acceleration-frequency response coming from the FFT; (c) ANPSD-frequency response; (d) ANPSD-frequency response on decibel scale. 120
- Fig. 5.6 – Typical vibration spectra for the RC specimens and natural frequencies associated with the three first vibrational modes (e.g. WOS-Ref): (a) FFT before the impact; (b) FFT after the impact; (a) ANPSD before the impact; (b) ANPSD after the impact. 122
- Fig. 5.7 – Typical vibration spectra for the strengthened specimens and natural frequencies associated with the three first vibrational modes (e.g. WOS-PVA): (a) FFT before the impact; (b) FFT after the impact; (a) ANPSD before the impact; (b) ANPSD after the impact. 125
- Fig. 5.8 – Average values (A.V.) and standard-deviation (S.D.) of the natural frequencies obtained through TD and FD on the intact specimens classified by type: (a) Mode 1; (b) Mode 2; (c) Mode 3. Note different y-axes. 126
- Fig. 5.9 – Average values of the natural frequencies obtained through TD and FD in function of the impactor speed regarding the SHCC damaged specimens classified by type: (a) Mode 1; (b) Mode 2; (c) Mode 3. Note different y-axes. Values on the x-axis are out of phase to improve the visualization. The reference values (Ref. Value) corresponds to the average value obtained on the damaged RC beams with stirrups (see also Table 5.5). 128
- Fig. 5.10 – Average values of the natural frequencies of the SHCC specimens subjected to more than one impact at the speed of 26.1 m/s: (a) Mode 1; (b) Mode 2; (c) Mode 3. Note different y-axes. Values on the x-axis are out of phase to improve the visualization. 129
- Fig. 5.11 – Average values of damping on the specimens subjected to more than one impact at the speed of 26.1 m/s: (a) Mode 1; (b) Mode 2; (c) Mode 3. Note different y-axes. Values on the x-axis are out of phase to improve the visualization. 130

List of tables

Table 2.1 – Mechanical properties of normal-strength SHCC [40].	32
Table 2.2 – Mechanical properties of high-strength SHCC (HS-SHCC) [39,41].	32
Table 2.3 – Geometrical properties of fibers commonly applied in SHCC manufacturing [37,39,40,42].	33
Table 2.4 – Strain rates associated with dynamic loading scenarios [23].	37
Table 2.5 – Summary of previous studies with regards to the shear behavior of SHCC.	43
Table 2.6 – Summary of previous studies with regards to SHCC on the structural scale.	45
Table 2.7 – Summary of previous studies regarding torsion of FRC beams.....	48
Table 2.8 – Summary of previous studies regarding impact loading on RC beams.	53
Table 3.1 – Geometric and mechanical properties of PVA and PE fibers according to producers.	59
Table 3.2 – Mixture compositions of the medium-strength SHCC under investigation.	60
Table 3.3 – Schematic representation and description of the load cases under investigation.	63
Table 3.4 – Mechanical parameters of PVA-SHCC and PE-SHCC under LC1. Standard deviations are given in parentheses.	66
Table 3.5 – Mechanical parameters of PVA-SHCC and PE-SHCC under LC2. Standard deviations are given in parentheses.	70
Table 3.6 – Mechanical parameters of PVA-SHCC and PE-SHCC under LC3. Standard deviations are given in parentheses.	73
Table 3.7 – Mechanical parameters of PVA-SHCC and PE-SHCC under LC4. Standard deviations are given parentheses.	75
Table 4.1 – Mixture design of the ordinary concrete.	84
Table 4.2 – Mixture compositions of the SHCC under investigation.	85

Table 4.3 – Geometric and mechanical properties of PVA and PE fibers according to producers [187,206].....	85
Table 4.4 – Static design values.	89
Table 4.5 – Resume of the results regarding loads and detached mass for the specimens subjected to a singular impact event.	105
Table 5.1 – Concrete composition (kg/m ³).....	115
Table 5.2 – Geometric and mechanical properties of PVA and PE fibers according to producers [187,206].....	116
Table 5.3 – Compositions of the SHCC under investigation.	116
Table 5.4 – Natural frequencies and damping values of the undamaged RC beams obtained through TD and FD for the first three theoretical modes regarding the specimens without transversal reinforcement (WOS) and specimens with transversal reinforcement (WS). Standard-deviation in parenthesis.	123
Table 5.5 – Natural frequencies and damping values of the damaged RC beams with stirrups obtained through TD and FD for the first three theoretical modes.	124
Table 5.6 – Natural frequencies and damping values of the intact strengthened beams obtained through TD and FD for the first three theoretical modes. .	126
Table 5.7 – Natural frequencies of the damaged strengthened beams for the first three theoretical modes.....	127
Table 5.8 – Damping values of the damaged strengthened beams for the first three theoretical modes.....	129
Table 5.9 – Stiffness degradation (DI_f) and damping degradation (DI_ζ) indices. ..	131

1 Introduction

1.1. Motivation

Structural members are commonly subjected to the combined action of multiaxial stress states and a variety of deleterious effects, which can affect the serviceability of structures; see Fig. 1.1. Civil engineers are more and more having to account for a variety of dynamic hazards such as seismic loads, blasts, wind gusts, the impact of moving objects, and vibrations. Impact loads in special are historically most commonly considered in bridges, dams, tunnels, military structures, airport pavements, and industrial floors overlay [1–3], but can affect all types of civil buildings. Depending on the type of loading, position, and direction of the element, different axial-shear stress combinations will occur under these scenarios. Moreover, violent dynamic loadings can generate high levels of triaxial stresses [4], which deeply affects the response of viscous solids such as concrete.

In addition, the development of new material and computational technologies has been globally improving the structural design for decades, and now the design codes are adjusted to include the conception of slimmer/thinner elements [5,6]. These slender structures are much more susceptible to cracking than their old sturdy versions. Cracking is an intrinsic characteristic of materials, being extremely pronounced in cementitious matrices (CM) such as concrete due to its relatively low tensile strength (when in comparison with its compression strength) in association with its brittle failure characteristic of ceramic materials [7–9]. Therefore, reinforced concrete (RC) structures generally suffer pronounced damage at high rates, usually presenting matrix spalling, which leads to effective cross-sections reduction and loss of structural integrity [10].

For this reason, CM are traditionally reinforced with some type of second phase [10], which can present itself as a continuity reinforcement, such as metallic reinforcements and textiles, or in a discrete way as aggregates and fibers. These cementitious composites excel in a variety of properties, influencing positively from the fabrication costs to improved mechanical, rheological, and durability

properties. In the last five decades, special attention has been given to Fiber-Reinforced Composites (FRC). The past years brought many research studies about these materials, mainly in initiatives aiming to develop more sustainable and efficient substrates, focusing on the new design challenges of the present and future eras [11,12].

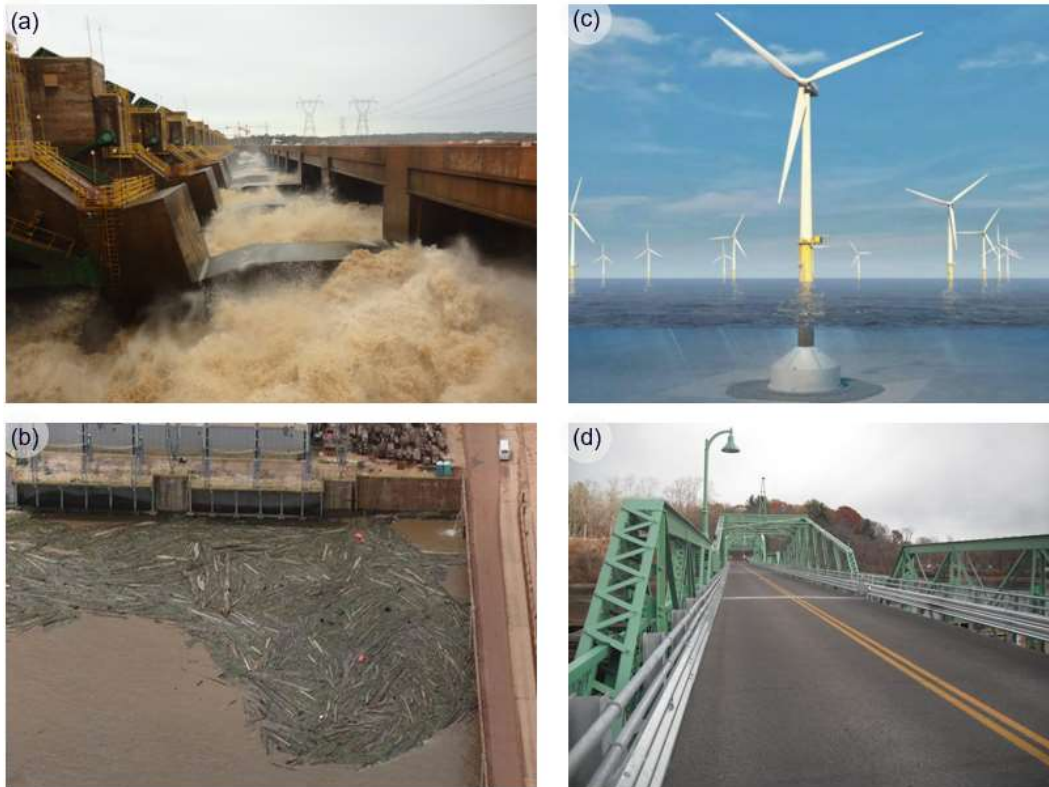


Fig. 1.1 – Examples of structures with complex stress trajectories and deleterious effects: (a) spillways subjected to erosion, abrasion, and cavitation due to the water action; (b) dams subjected to the impact of wood logs; (c) offshore wind power towers; (d) viaducts and bridges subjected to traffic and environmental effects.

The present research focused on a special type of FRC called Strain-Hardening Cementitious Composites (SHCC), often also referred to as Engineered Cementitious Composites (ECC). SHCC is produced by the association of a very fine cementitious matrix, and randomly distributed micro-fibers in contents of up to 2 % in volume. This material exhibits a pronounced pseudo ductility prior to failure localization [13,14], enabled by the formation of multiple cracks during its strain-hardening phase, with crack widths below 100 μm . Additionally, the constitutive nature and fresh-state properties of SHCC enable its application by

spraying or lamination techniques, which is an important prerequisite for structural strengthening [15]. These features raise the hypothesis that SHCC could be suitable both as the main material for structural elements subject to extreme loading scenarios such as impact, as well as supplementary applied retrofit and strengthening layers of existing structural members for enhancing their structural durability and resilience under unfavorable exposure and loading conditions [16,17].

Based on the concept of sustainability, more specifically the legitimacy of rehabilitation of existing structures, the aim of this research was to fill some knowledge gaps regarding SHCC potential under multiaxial stress states and under very high strain rates such as impact. In addition, SHCC potential contributions as a strengthening layer to improve the resilience of RC elements under impact was assessed, aiming the validation of its bond with the existing substrate, and the influence analysis of its addition on the dynamic response of the original members.

1.2. Goals

The present research aimed to assess the structural contribution of two types of normal-strength SHCC as strengthening layers to improve the afterlife of structural members under impact scenarios. The composites differed mainly on the type of reinforcing fiber. Synthetic short fibers polyvinyl-alcohol (PVA) and ultra-high molecular weight polyethylene (UHMWPE) fibers were chosen for being widely assessed in previous material-level studies regarding SHCC. The composites were mechanically characterized under distinct regimes (static and dynamic) and loading cases (direct tensile, torsion, combined torsion, and tension). The structural tests used to evaluate SHCC feasibility as strengthening layers of real-scale RC beams initially subjected to shear due to impact were assessed in terms of their mechanical response, cracking patterns, and modal analysis.

1.3. Thesis organization

The present thesis was structured in six chapters, plus references and appendixes. The first chapter is composed by the present introduction. It is followed

by a literature review, where the main features of SHCC are detailed, as previous experimental studies addressing torsion and impact loading. Next, three chapters structured as individual, independent full manuscripts are presented, including one already published paper, followed by two others under review. Each manuscript deals with an important evaluation towards the understanding of the SHCC under assessment, presenting the applied methodologies and obtained results in each experimental study. They were arranged as:

- Chapter 3: Mechanical behavior of strain-hardening cement-based composites (SHCC) subjected to torsional loading and to combined torsional and axial loading [18];
- Chapter 4: Effect of shear reinforcement and external strengthening with strain-hardening cement-based composites (SHCC) on the impact resistance of reinforced concrete beams;
- Chapter 5: Experimental modal analysis of RC beams strengthened with SHCC subjected to shear under impact strain rates.

In the following, the global conclusions of the present research are presented, relating the most relevant results of the previous chapters, and indicating suggestions for future research studies on this field.

1.4. General remarks

As will be addressed in Chapter 2, SHCC carries a very distinct composition that requires proper balancing to ensure a multiple-cracking performance. Although the design of a new dosage was not the purpose of the present research, an exploratory program was first developed in the Structures and Materials Laboratory from PUC-Rio to achieve the desirable rheological and mechanical characteristics for the appliance of SHCC as strengthening layers. Several established mixing proportions were evaluated during this phase, e.g. [10,43,44]. In parallel, adjustments were being made on the material suppliers available, both of the raw materials and chemical additives, as well as of some of the testing apparatus (such as the glue used on the direct tensile and torsion tests).

While these changes do not embody new contributions for the global scientific community, they were of invaluable worth for the development of the experimental program reported on the following. In the end, all the results reported in this thesis

were based on specimens manufactured in the Institute of Construction Materials of the Technische Universität Dresden, in Germany. Thus, this exploratory program developed at PUC-Rio is not being reported at this instance. However, it represents meaningful contributions for the research group, that since 2018 initiated new research studies on SHCC.

2 State of the art review

2.1. Understanding SHCC

The development of composite materials made by the addition of discontinuous reinforcement in cement-based matrices dates back to the mid-nineteenth century [19]. Research studies of cement-based composites that display strain-hardening behavior with high strain-rate levels were started in the '60s with Prof. Antoine Naaman and Prof. Victor Li initiatives. Since the early '90s, the number of research papers under this topic has been increasing [14,20].

Nowadays this class of materials holds a deep interest of the scientific community, being the essence of the international conference named SHCC, which occurs approximately every three years (South Africa, 2005; Brazil, 2011; The Netherlands, 2014; Germany, 2017) organized by the International Union of Laboratories and Experts in Construction Materials, Systems and Structures (RILEM, from the name in French), in association with the International Federation for Structural Concrete (*fib*, also from the name in French). SHCC was the main subject of the Technical Committee 240-FDS from RILEM, named “A framework for durability design of SHCC”, led by Prof. Gideon Van Zijl and Prof. Flávio de Andrade Silva between the years of 2010 and 2016. The material is also being investigated by the Research Training Group GRK 2250, titled “Mineral-bonded composites for enhanced structural impact safety”, sponsored by the German Research Society (DFG, from the name in German) since 2017.

This section brings an overview of SHCC's design and mechanical properties. An extensive literature review regarding the behavior of the composite in the micro, meso, and macro scale is presented.

2.1.1. Performance under direct tensile loading

Strain-hardening cement-based composites (SHCC), often referred to as Engineered Cement-based Composites (ECC), exhibit improved load-bearing capacity after the first crack formation and pseudo-ductility under uniaxial tensile

loads at quasi-static strain rates [1,21,22]. Their pronounced strain capacity is due to the formation of multiple-cracks with exceptional Crack-Mouth Opening Displacement (CMOD) control, with values ranging from 20–100 μm width [23–25]. This multiple-cracking process grants the specimen a stable cracking propagation at the macroscopic level, which reflects in a pseudo-ductile post-cracking behavior. The establishment of this process is enabled by the optimized crack-bridging action of short, thin, and randomly distributed fibers [21]. As shown in the stress-strain curve in Fig. 2.1a, a typical stress-strain curve of this composite presents three stages:

- (1) First, a clear linear/elastic stretch can be noticed, mainly influenced by the mechanical properties of the cement-based matrix. During this phase, the composite is undamaged, and no cracks had occurred.
- (2) Next, the second branch corresponds to the multiple-cracking stage, which is the most relevant phase of this type of composite. A sort of plateau is observed, starting with the first crack of the matrix, which substantially reduces the composite's rigidity, and finishing with the moment when the composite starts to significantly lose its load-bearing capacity. Despite the reduction of the Young's Modulus, due to the exceptional crack-bridging performance, the composite's load-bearing capacity is at times sustained, or more commonly, expanded during the multiple-cracking process.
- (3) At last, the third segment corresponds to the critical-crack localization, commonly referred to as the "softening phase". This stage is defined by the local failure of the crack-bridging process. At this stage, the composite rapidly loses its load-bearing capacity, presenting or not any additional strain capacity. For all purposes, the strain capacity value of an SHCC is assumed as the boundary value between the second and third segments.

Fig. 2.1b highlights the additional energy absorption capacity of SHCC when compared to regular cement-based matrices, which present brittle behavior, and, the strain-softening performance of FRC. SHCC presents a distinct matrix dosage, constituted only by fine-grained inputs which directly affect its fracture energy and the adherence with the fibers [10,26,27]. These characteristics allow this material to obtain much higher levels of strain than other fiber-reinforced cementitious composites.

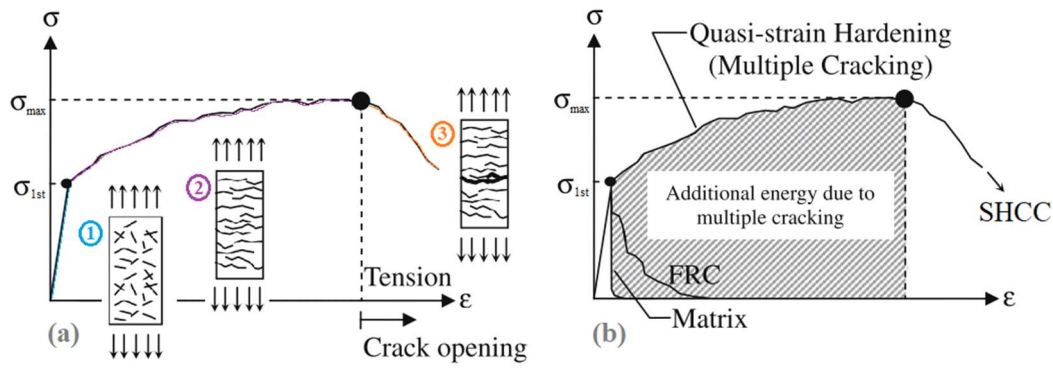


Fig. 2.1 – Mechanical behavior of SHCC [19]: (a) Typical stress-strain curve; (b) SHCC additional energy absorption potential due multiple cracking process.

The creation of a large number of surfaces during the multiple-cracking process indicates a significant energy absorption potential for SHCC [10,28]. Due to the association of this tenacity performance and the distinctive crack width control, this composite entails high suitability for applications where high ductility and high non-elastic deformability with stable cracking is needed [27]. Some examples are plastic hinges [29,30] (Fig. 2.2), dynamic loading in general [2,31], and patch/repair materials [32,33]. Moreover, the exquisite crack width control [34] (Fig. 2.3) poses as an additional capacity of preventing rebars' corrosion on reinforced concrete (RC) [35–38].

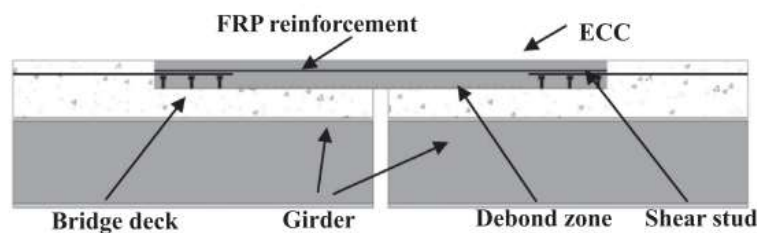


Fig. 2.2 – SHCC link slab reinforced with FRP [30].

SHCCs are traditionally reinforced with short (12 mm max. length) synthetic fibers [21]. The first dosages were developed with PolyVinil Alcohol fibers (PVA) associated with normal-strength cementitious matrices ($f_{ck} \approx 20 - 45$ MPa). Thus, the number of research studies regarding PVA-SHCC is significantly higher than other types of SHCC. PVA fibers are intrinsically hydrophilic, even when produced with an oiling coating agent [34,39]. Thus, they present an outrageous high chemical bond with the cementitious matrix, which reflects a tendency of fiber

rupture rather than fiber pullout. This characteristic must be taken into account so the multi-cracking behavior is not jeopardized.

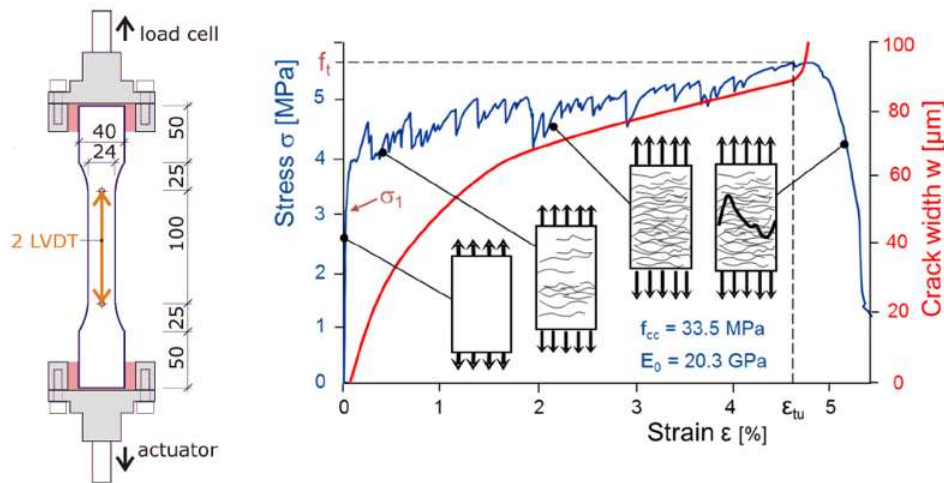


Fig. 2.3 – Typical strain hardening behavior of SHCC reinforced with PVA fibers during a direct tensile test [34].

More recent studies, both in normal and high-strength matrices, have been carried out to assess Ultra High Molecular Weight Polyethelene (UHMWPE) as the reinforcing type of fiber. UHMWPE, as will hereupon shortly be referred to as PE, are in contrast to PVA, hydrophobic [40]. This property disbenefit the occurrence of the hydration products in the ITZ [34], resulting in a poor chemical bond. Thus, PE fibers tend to present a pullout behavior governed by friction, the reason why they are frequently considered better suited for high-strength matrices ($f_{ck} \approx 45 - 160$ MPa). The lower water-binder ratio and higher packing density contribute to the fiber anchorage, enhancing the stress necessary to pull out the fibers [19,31].

In general, the SHCC produced with PVA and PE fibers are considered much common, having transhipped the academy border, and presenting some industry suppliers and applications. The mechanical behavior of the final composites is strongly dependent on the dosage and quality of the inputs, a topic which will be further addressed in the next section. Thus, sizeable discrepancies can be observed in the mechanical parameters of these composites from different research studies; see Table 2.1 and

Table 2.2. Other initiatives can be found with respect to additional fibers, such as aramid and p-phenylene-2,6-benzobisoxazole (PBO) in the variations *as-spun* (PBO-AS) and *high-modulus* (PBO-HM) [41], with the purpose to find better

solutions for the variety of potential applications of SHCC. Geographic and economical constraints are also motivations behind the search for new fibers. The effective fiber content, i.e., the real amount of fibers bridging each crack, is deeply affected by the geometrical properties of the fibers, some of which are related in Table 2.3.

Table 2.1 – Mechanical properties of normal-strength SHCC [40].

See complementary footnotes.

Content		M1 + PVA	M1 + PVA	M1 + HDPE
Compressive strength ¹	[MPa]	44.8 ²	44.8 ³	44.8 ³
First-crack stress	[MPa]	3.5	3.1	2.4
Tensile strength	[MPa]	5.3	3.8	3.6
Gauge-length	[mm]	25	50	50
Ultimate strain	[%]	3.6	1.5	1.7
Work-to-fracture	[kJ/m ³]	157.8	52.7	53.5
Average crack spacing	[mm]	7.0	15.3	9.3

Table 2.2 – Mechanical properties of high-strength SHCC (HS-SHCC) [39,41].

See complementary footnotes.

Content		M2 + PE	M2 + PE	M2 + PE	M2 + ARA	M2 + PBO AS	M2 + PBO HM
Compressive strength ²	[MPa]	141.8 ³	141.8 ³	133.5	144.8	140.3	142.9
First-crack stress	[MPa]	3.8	3.0	3.8	6.3	5.5	4.2
Tensile strength	[MPa]	8.5	6.5	7.6	9.4	9.8	8.4
Gauge-length	[mm]	25	50	100	100	100	100
Ultimate strain	[%]	6.1	3.6	3.9	1.4	1.4	1.6
Work-to-fracture	[kJ/m ³]	438.8	206.5	227.0	118.0	113.0	109.0
Average crack spacing	[mm]	2.0	2.6	2.3	1.3	1.7	2.4

2.1.2. SHCC tailoring

Typical dosages of SHCC count with the suppression of coarse aggregates, resulting in composites with two distinct phases in the meso-scale: (i) the cement-

¹ Cube, 28d.

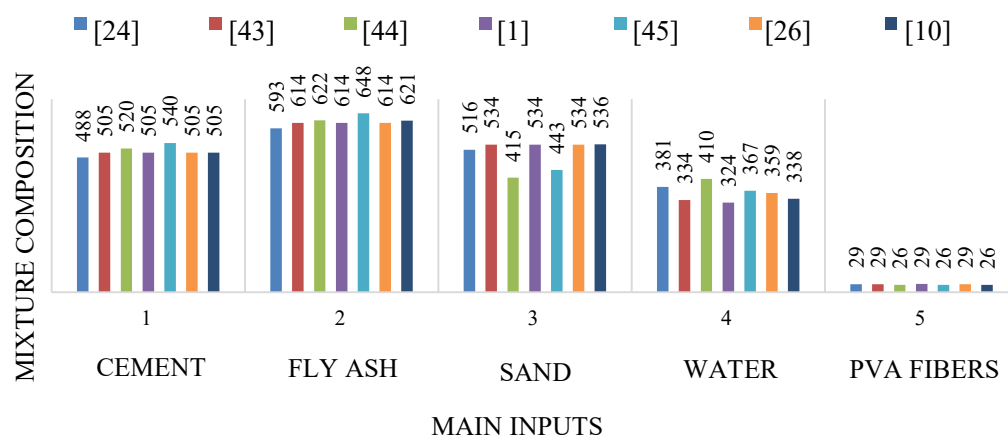
² Matrix only.

based matrix, which includes the embodied fine aggregates, (ii) and the fibers [19]. The normal strength SHCC mortar generally is formed by the hydration of two binders, these being Portland cement Type 1 and fly ash. A very fine quartz-sand ($\varnothing \leq 200 \mu\text{m}$) is used as second-phase particle reinforcement. Chemical additives such as superplasticizers and viscosity modifiers are commonly added to achieve the desired rheology and pumpability.

Table 2.3 – Geometrical properties of fibers commonly applied in SHCC manufacturing [37,39,40,42].

Fiber	Brand	Product	\varnothing_f [μm]	L_f [mm]	γ_f [g/cm ³]	σ_f [MPa]	ϵ_f [%]	E_f [GPa]
HDPE	DSM TM	Dynceema®	20	12 ³	0.97	2580	3.5	88
PVA	Kuraray TM	Kuralon®	40	12	1.30	1600	6.0	40
Aramid	Teijin TM	Technora®	12	6	1.39	3400	4.5	74
PBO-AS	Toyobo TM	Zylon®	13	6	1.54	5800	3.5	180
PBO-HM	Toyobo TM	Zylon®	13	6	1.56	5800	2.5	270

The matrix dosage directly affects its rheology, long-term behavior, fracture energy, and the bond with the fibers, being the main variable in the SHCC design [10,27]. Fig. 2.4 points to variations of dry materials content in different research studies for the same type of reinforcing fiber (PVA). Different locations often require adjustments on the dosage due to variations in the geometrical and reactivity properties of the dry components locally available. These adjustments are necessary to ensure the proper cracking energy, which is deeply related to the multiple-cracking behavior. This subject will be further addressed ahead.



³ Also presented with 6 mm length.

Fig. 2.4 – Graphical comparison of PVA-SHCC dosages in terms of the main inputs. Values in kg/m³.

On SHCC, the fibers are usually short (máx. length 12 mm), with large aspect ratios ($\approx 300^4 - 1000^5$). Analogous to other FRC, the reinforcing fibers also influence the performance of SHCC. The type of fiber affects the morphology of the Interfacial Transition Zone (ITZ), and thus, the adhesion between fibers and cementitious matrix, often requiring some dosage and/or mixing adjustments. Usually a pullout mechanism tending to the fibers being pulled out of the matrix is considered more stable, which favours the crack opening control. This property depends on the fiber hydrophilicity; e.g. PVA fibers, which are highly hydrophilic present a predominance of the chemical bond even when coated, tending to fiber rupture [34,40,46]. PE, aramid, and PBO fibers are hydrophobic, and therefore, present a more expressive frictional bond. In general, the predominance of frictional bond favors the fibers being pulled out of the matrix. The association of the (i) fibers being pulled out, and (ii) enhancement of the load necessary to continue the slip during the pullout phase, is a good sign that the composite will display strain-hardening macroscopic behavior [39].

Being such a sensitive topic, there are several research studies specifically regarding the SHCC tailoring [46–48]. Steady-state cracking is the first step to obtain strain-hardening behavior [49,50]. Two criteria –strength and energy – can be used to guide the achievement of this behavior; see Fig. 2.5:

i. **Strength criteria** [49,50]

The composite's ultimate tensile strength (σ_{peak}) must be greater than the matrix tensile strength (σ_m), which corresponds to the composite's first crack stress:

$$\sigma_{peak} \leq \sigma_m \quad \text{Eq. 1}$$

ii. **Energy criteria** [49,50]

The composite's complementary energy (J'_b) must be greater than the composite crack tip toughness (J_{tip}):

⁴ PVA Kuraray™ Kuralon® $l = 12 \text{ mm}$; $\varnothing = 40 \text{ }\mu\text{m}$.

⁵ PE DSM™ Dyneema® $l = 12 \text{ mm}$; $\varnothing = 12 \text{ }\mu\text{m}$.

$$J'_b \leq J_{tip}$$

Eq. 2

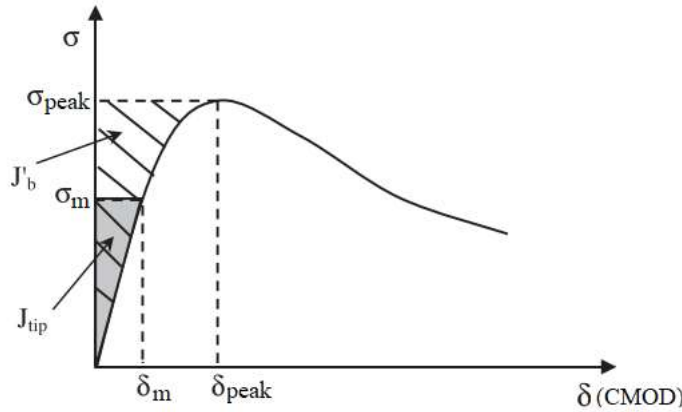


Fig. 2.5 – Typical stress-displacement curve of SHCC [10,46,51,52].

The strength criteria is more tangible and directly evaluated from three-point bending tests. The energy criteria requires some fracture mechanics knowledge and the addition of results from pullout tests to obtain the necessary micromechanics parameters [10].

Based on the J-integral interpretation [53], the crack tip stress concentration is independent of the crack length, depending only on the matrix characteristics is:

$$J_{tip} = \frac{(K_m)^2}{E_m} \quad \text{Eq. 3}$$

where K_m corresponds to the matrix fracture-toughness and E_m is the matrix Young's Modulus.

The complementary energy considers the whole composite, therefore depends on the properties of the fiber-matrix interface characteristics:

$$J'_b = V_f \frac{L_f}{d_f} \left(\frac{\tau_f^2 L_f^2}{6 d_f E_f} - 2 \tau_c \right) \quad \text{Eq. 4}$$

being the fibers content (V_f), length (L_f), diameter (d_f) and Young's Modulus (E_f); and the frictional (τ_f) and chemical bond (τ_c) between the fibers and the matrix.

Two additional performance indices can be used to guide the practical design for pseudo-strain-hardening (PSH) behavior regarding the previously presented criteria [47]:

$$PSH_{Strength} = \frac{\sigma_{peak}}{\sigma_m} > 1,3 \quad \text{Eq. 5}$$

$$PSH_{Energy} = \frac{J'_b}{J_{tip}} > 2,7 \quad \text{Eq. 6}$$

Usually, the matrix is tailored so the composite presents failure through the fibers pullout, not fiber rupture [47]. And as aforementioned, slip-hardening response during fiber pullout is desirable [46]. **Eq. 4** shows a clear dependency on the chemical bond. An increase in its value diminishes the complementary energy. This subject is especially approached during PVA-SHCC design [51,54,55]. The PVA fibers intrinsically present an outrageous high chemical bond with cementitious matrices due to their hydrophilic properties. Thus, additional agents such as oiling coatings are commonly adopted [23].

High complementary energy values result in flat-type cracks (not Griffith-type), which enable regular stress states (without concentration) through the fractured surface [14,49]; see Fig. 2.6. The crack-width control due to the bridging of the fibers enables the formation of new cracks, which results in a macroscopic steady-state non-elastic deformation.

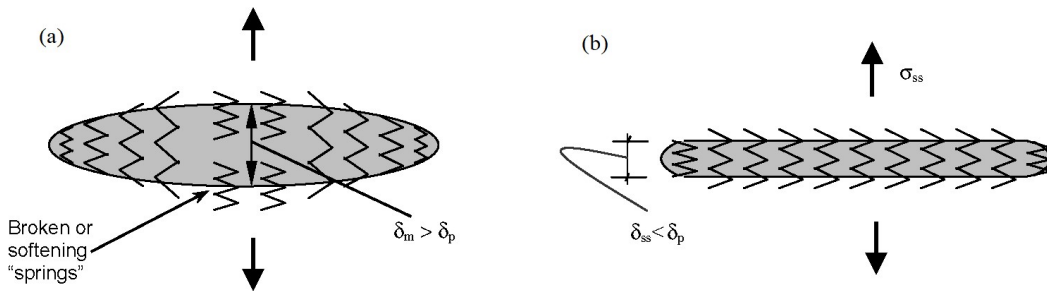


Fig. 2.6 – Types of crack derived from cross-sectional tension stress [56]: (a) Griffith-type, with values of CMOD (δ_m) exceeding the critical size (δ_p); (b) Flat, or steady-state type, with CMOD (δ_{ss}) smaller than the critical value on the whole length of the crack.

2.1.3. Extreme scenarios

Extreme loading scenarios can result in internal damage, often hard to detect by visual inspection [57]. Despite the SHCC previous pointed potential of energy dissipation, it exhibits a strain-rate sensitivity [26,41,58,59] that requires proper assessment to enable its use for high-strain rates and impact applications. Table 2.4 brings strain-rates values for typical dynamic loading scenarios for civil engineering structures.

Table 2.4 – Strain rates associated with dynamic loading scenarios [23].

Dynamic loading origin	Strain-rate [s ⁻¹]
Fast moving traffic	$1.10^{-6} - 5.10^{-4}$
Gas explosions	$5.10^{-5} - 5.10^{-4}$
Earthquakes	$5.10^{-3} - 5.10^{-1}$
Pile driving	$1.10^{-2} - 1.10^0$
Aircraft landing	$5.10^{-2} - 2.10^0$

Generally, SHCC behavior implies an increase in strength and decrease in strain capacity for strain-rates' enhancements of 10^{-5} s^{-1} to 10^{-2} s^{-1} [26,60–62]. Mechtcherine *et al.* [23] observed that the failure mechanism of PVA-SHCC tends to change from fiber-pullout to fiber-rupture (see Fig. 2.7), which reduces the general number of cracks due to rapid failure localization [22,23]. At very-high strain-rates (from 10 s^{-1} to 50 s^{-1}) the material showed an increase in both tensile strength and strain capacity. Almost no multiple-cracking behavior was observed, and the strain capacity enhancement being due to an increase in the fiber pullout length to 2.5 mm^6 . This suggests a failure mechanism related to the plastic deformation of the fibers.

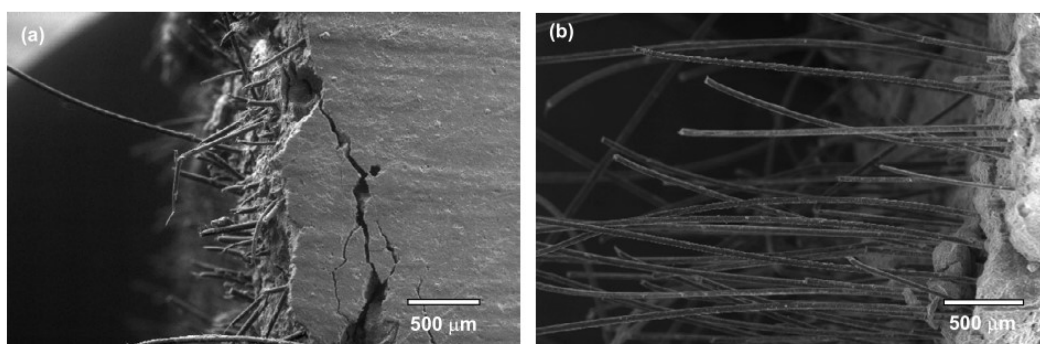


Fig. 2.7 – Failure mechanisms of SHCC at low and high strain rates: (a) fracture surface of a specimen tested at 10^{-3} s^{-1} (b) fracture surface of a specimen tested at 25 s^{-1} [23].

The study [63] showed that the strain-rate sensitivity of SHCC is strongly influenced by the fiber type and matrix composition (see Fig. 2.8). Indeed, as

⁶ Usually considerably lower, being $0.3 - 0.5 \text{ mm}$ for strain-rates about of 10^{-3} [23].

different fibers present different bond-mechanisms with the cement-based matrix, this conclusion was expected. When comparing two normal-strength dosages with reinforced with PVA and PE fibers, the one made with PE presents relative higher tensile strength, strain capacity and fracture energy [10,58,63].

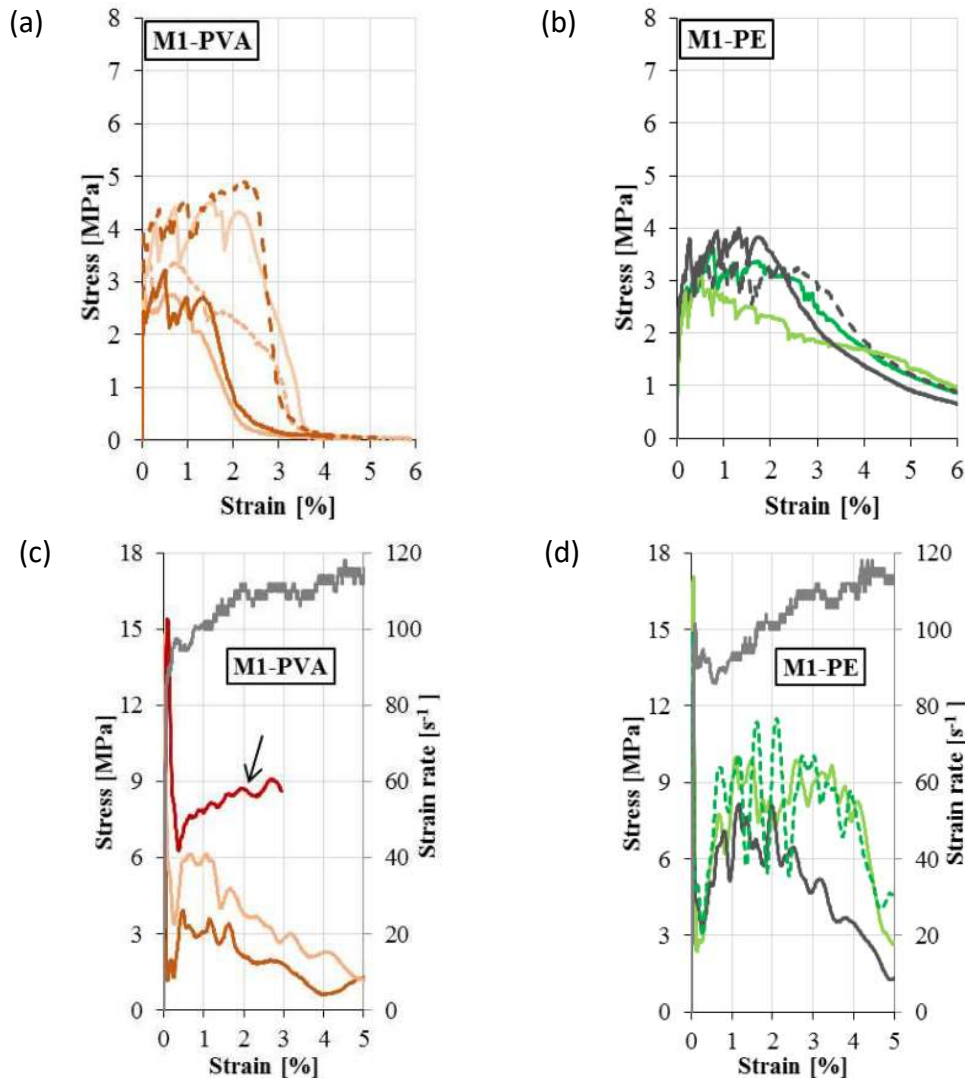


Fig. 2.8 – Stress-strain curves of normal-strength (M1) SHCC reinforced with PVA and PE fibers [63]. Curves (a) and (b) refers to quasi-static tension tests (5.10^{-4} s^{-1}); curves (c) and (d) to high-speed tension tests (120 s^{-1}). Note the different axes' limits.

The bond differences that lead to distinct failure modes can be better understood through microscopy observations. Environmental Scanning Electron Microscopy (ESEM) images of PVA-SHCC samples from [10] show damage on the fiber surface in the form of pilling and scratching for quasi-static strain-rates (Fig. 2.9a). For dynamic regimes, the fiber surface is smooth, with no pronounced

damage, which indicates a total slip of the fiber (Fig. 2.9b). Normal strength SHCC made with PE fibers show some level of scratching and matrix damaging for quasi-static rates (Fig. 2.10a). On dynamic regimes, an even higher concentration of matrix fragments can be detected attached to the debonded PE fibers, which suggests an increase in the interfacial shear resistance with increasing loading rate for these fibers (Fig. 2.10b) [10]. These assumptions are in accordance with the findings of [64]; see Fig. 2.11 and Fig. 2.12.

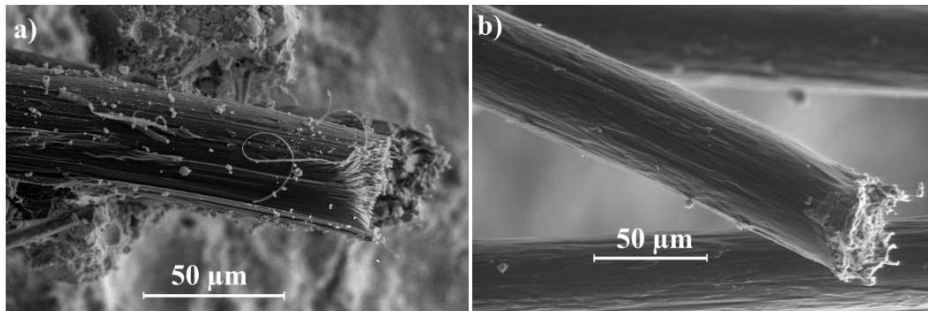


Fig. 2.9 – ESEM images of normal strength SHCC with PVA fibers [10]. Fractured surfaces of samples tested in different strain-rate regimes: (a) quasi-static; (b) dynamic.

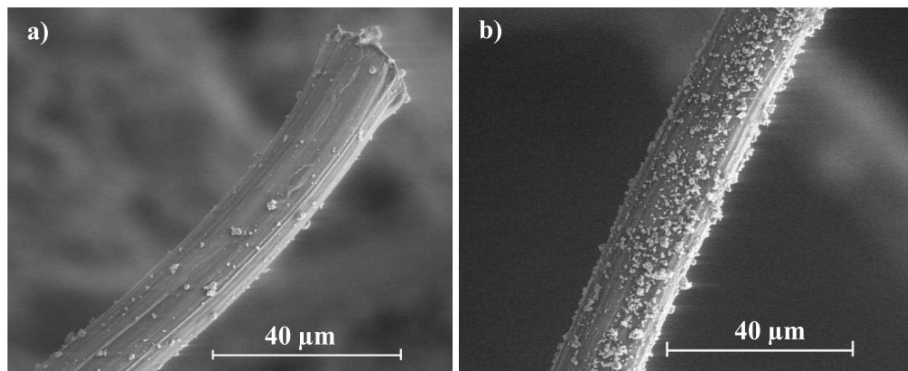


Fig. 2.10 – ESEM images of normal strength SHCC with PE fibers [10]. Fractured surfaces of samples tested in different strain-rate regimes: (a) quasi-static; (b) dynamic.

Due to the polymeric nature of most of the reinforcing fibers used in SHCC, these composites also present a sensitivity to temperature gradients. Studies regarding the influence of high-temperatures in the mechanical behavior of normal-strength PVA-SHCC show that the ultimate tensile strength tends to decrease with the enhancement of temperature (Fig. 2.13) [21,26]. This behavior can be explained by the low melting point of PVA fibers (90 °C – 95 °C) and the oiling agent used as

a coating (55 °C – 60 °C). Due to their polymeric base, a similar performance can be extrapolated to other polymeric fibers, although with different thresholds. However, studies demonstrated that the strain-capacity tends to grow until the level of 100 °C (Fig. 2.13b), and starts to drop after this value. This performance can be explained by the fiber degradation and shrinkage that starts to happen in the range of 90 °C – 95 °C (Fig. 2.14) [21,65,66]. At even higher temperatures, the composite shows no pseudo-ductility, losing completely its multiple-crack capacity due to an expressive decrease in the strength of the fibers, which negatively impairs the CMOD control, and thus the fracturing-energy [26].

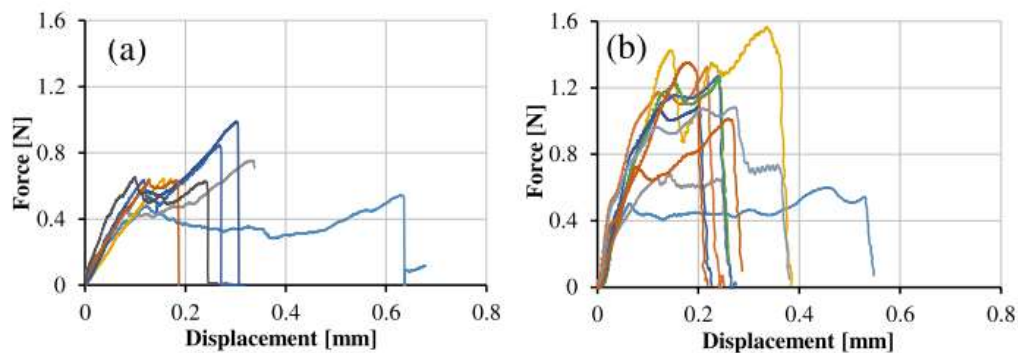


Fig. 2.11 – Pullout force *versus* displacement slip from pullout tests made with PVA fibers in normal-strength matrix with an embedded length of 2 mm under different displacement rates: (a) $5.10^{-3} \text{ mm.s}^{-1}$; (b) 5.10 mm.s^{-1} .

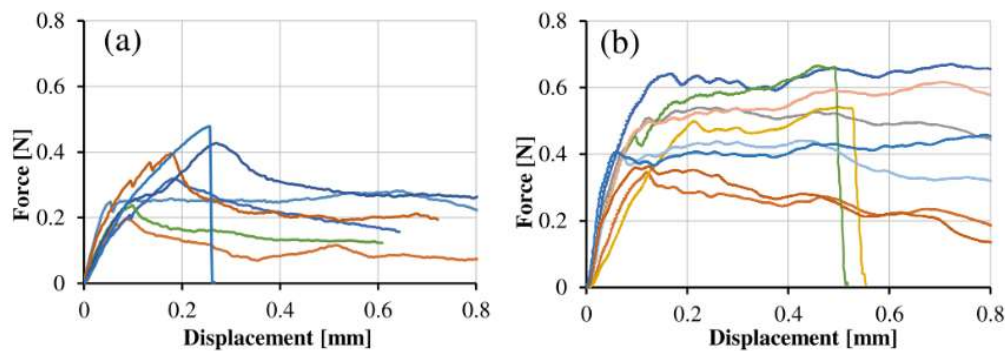


Fig. 2.12 – Pullout force *versus* displacement slip from pullout tests made with PE fibers in normal-strength matrix with an embedded length of 2 mm under different displacement rates: (a) $5.10^{-3} \text{ mm.s}^{-1}$; (b) 5.10 mm.s^{-1} .

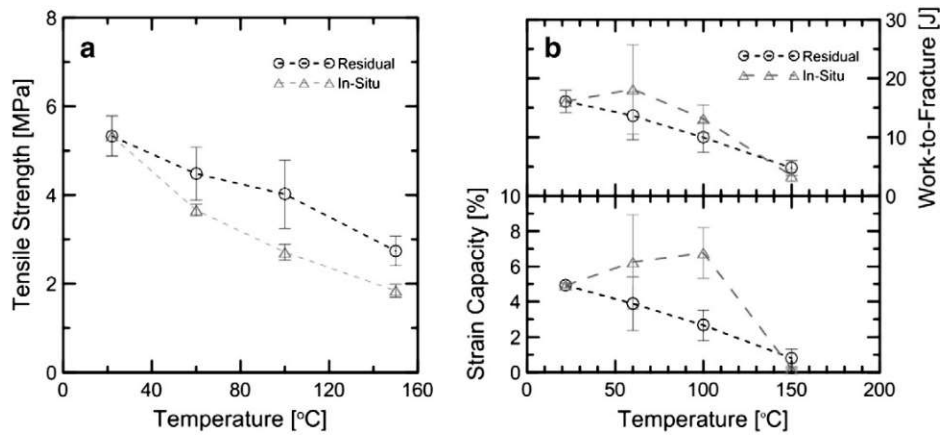


Fig. 2.13 – Effect of temperature in the tensile strength, strain capacity and work-to-fracture of PVA-SHCC tested at a quasi-static strain rate ($3 \cdot 10^{-4} \text{ s}^{-1}$) [26].

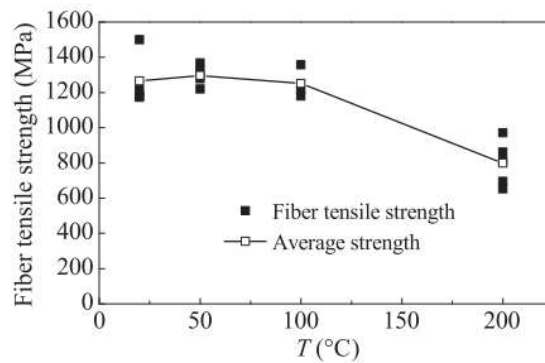


Fig. 2.14 – Effect of temperature exposure on PVA-fibers' strength [65].

2.1.4. Shear behavior

There is a wide range of testing setups reported in the literature for the shear behavior assessment of cement-based materials. These can be sorted as single, and double plane shear tests depending on the number of critical surfaces. Fig. 2.15 displays five variations of testing setups most commonly found in the literature. One of the main variables that guide the selection of one of these setups is the coarse aggregate size. Thus, cement-based composites such as SHCC, that count with the suppression of the coarse aggregate phase, associated to short fibers, can afford smaller specimens than the ones required for concrete, and other FRC reinforced with longer fibers (e.g. steel and polypropylene). In general for RC and FRC reinforced with steel fibers, the aggregates dimensions (increases with the size) and

shape (reduces with the roundness) improve the shear strength through interlocking [67,68].

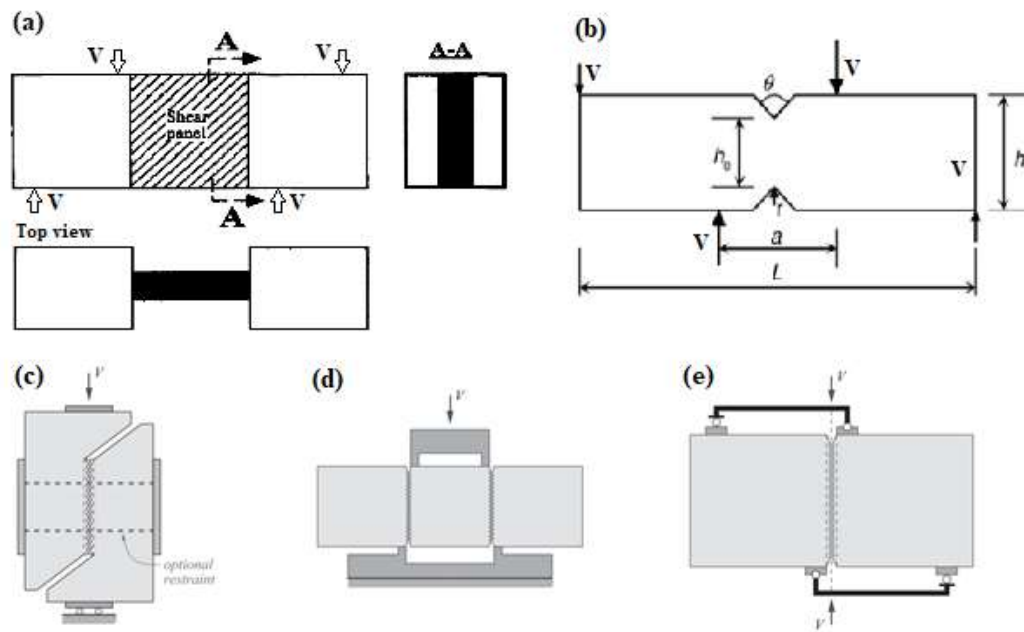


Fig. 2.15 – Test methods for shear transfer in concrete and FRC [68–70]: (a) Ohno shear beam; (b) Iosipescu beam; (c) single-plane, push-off specimen; (d) double-plane shear test regulated by the Japan Society of Civil Engineers (JSCE); (e) single-plane shear test regulated by the *fib*.

The behavior of SHCC under shear have been addressed by some research studies up to the moment. In addition to some structural investigations on the performance of SHCC as main material [71–75] and for strengthening layers subject to shear [17,76–82] the number of reports on its material-level characterization [69,70,83,84] is still quite limited, especially regarding the influence of the type of fiber. Moreover, quantitative comparisons between different endeavors represent a challenge due to the variety of testing methods and geometries (see Table 2.5). However, it has become clear that the remarkable crack control in SHCC, which leads to multiple cracking under tensile and compressive forces, is also responsible for an advantageous performance under shear of these composites [69].

Table 2.5 – Summary of previous studies with regards to the shear behavior of SHCC.

Study	Type of fiber and fiber content in volume	Test specimen geometry	Tensile strength [MPa]	Shear strength [MPa]
Li et al 1994 [69]	Brass-coated steel 6mm, 7 % PE 12.7 mm, 2 %	Ohno shear beams	4.7/6.2	Not quantified
Van Zijl 2007 [70]	Fiber not informed, 0.0/1.0/2.0/2.5 %	Modified Iosipescu beam	2.7/2.9	0.0/0.0/4.0/4.1
Kanakubo et al 2010 [84]	PVA, 1.5/2.0 %	Single-plane under crossed tension	2.4/4.8	1.19-1.78/ 1.13-2.62
Baghi e Barros 2016 [85]	PVA, 2.0 %	Modified Iosipescu beam	3.4	3.9
Heravi et al 2020 [86]	PE 6 mm, 2.0 %	Adapted double-plane shear beam	–	12.5

2.1.5. Structural applications

SHCC has been assessed both as the main material as much as strengthening layers in structural level research studies. Its application as a strategic reinforcement material comes as an advantage within the sustainability concept, more specifically the rehabilitation of existing structures. However, a disadvantage is the SHCC relatively higher cost when compared with normal concrete (2-3 times higher), which is mainly ruled by the cost of the fibers [87]. Nevertheless, SHCC costs are usually still quite far below the price of the most commonly marketed repair materials [87], arising as a more affordable alternative in structural recovery scenarios.

According to [88], so far most of the applications with SHCC are non-structural. Indeed, many research papers refer to SHCC's durability potential towards minimizing deleterious incursions due to its high cracking-width control [89–92]. As most common forms of degradation in regular RC structures starts in the elements external surfaces due to concrete brittleness (Fig. 2.16), SHCC is most

commonly used as a patch material or cover for the steel-reinforcement protection from corrosion (Fig. 2.17) [93–98].

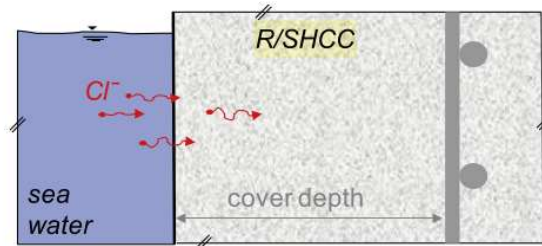


Fig. 2.16 – Illustration of an RC concrete element exposed to chloride ions [88].

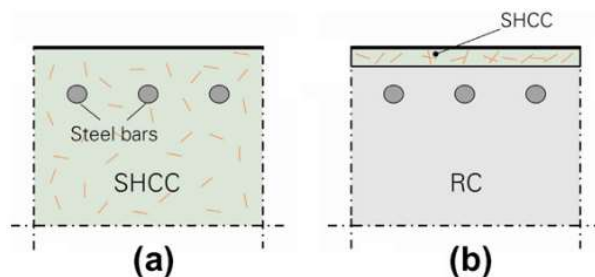


Fig. 2.17 – Possible combinations of SHCC and regular RC for steel-reinforcement protection: (a) regular matrix replacement; (b) patch-material / cover-layer [88].

With respect to any structural application of SHCC, analogous to conventional concrete, the bond with the steel rebars plays a decisive role in the final performance of the structural member [99]. This parameter was assessed by [100] using pullout tests of ribbed-rebars embedded in an SHCC with 2.2% in volume of PE fibers ($\sigma_{1st} \approx 6$ MPa, $\sigma_{max} \approx 10$ MPa, and $\varepsilon_{max} \geq 3.5$ %). They found that SHCC presents a greater bond with the steel rebars than regular concrete due to the improved control of the splitting cracks that tend to form when the rebar is being tensioned and the ribs are activated. Other important variables of interest are: (i) the diameter of the rebar, which interferes with the ribs geometry and spacing (the larger is the diameter, smaller is the bond, thus a larger embedded length is required), and (ii) the thickness of the SHCC cover, which in turn affects the lateral confinement (the larger is the cover, greater is the confinement, which favors the bond).

Table 2.6 – Summary of previous studies with regards to SHCC on the structural scale.

Year	Authorship	SHCC application	SHCC fiber	Element	Type of test	Strain rate
2004	Shimizu et al. [75]	Substrate	PVA	Beams	Ohno test	Quasi-static
2011	Zhang et al. [71]	Substrate	PE	Beams	Three-point bending	Quasi-static
2012	Xu et al. [72]	Substrate	PVA	Beams	Three-point bending	Quasi-static
2012	Xu et al. [65]	Substrate	PVA	Beams	Three-point bending	Quasi-static
2013	Hou et al. [66]	Substrate	PVA	Beams	Three-point bending	Quasi-static
2013	Yun [98]	Strengthening layer 30-50 mm thk ⁷	Hybrid: PVA and PE	Plain concrete beam	Four-point bending	Quasi-static
2017	Khalil et al. [69]	Strengthening layer 40 mm thk	PE	Beams	Four-point bending	Quasi-static Cyclic
2017	Choi et al. [100]	Substrate	PE, Steel	Steel reinforced bars	Direct tension Tension stiffening	Quasi-static Cyclic
2018	Adhikary et al. [101]	Strengthening layer 10-40 mm thk	PE	Panels	Blast explosions	Impact
2018	Chen et al. [16]	Substrate	PE	Beams	Four-point bending	Quasi-static
2018	Georgiou e Pantazopoulou [102]	Substrate	PVA	Beams	Four-point bending	Quasi-static
2018	Zhang et al. [78]	Strengthening layer 10 mm thk	PE	Beams	Three-point bending	Quasi-static
2019	Wei et al. [80]	Strengthening layer 10 mm thk	PE	Beams	Four-point bending	Quasi-static
2019	Wang et al. [79]	Strengthening layer 20-40 mm thk	PVA	Beams	Four-point bending	Quasi-static
2020	Hassan et al. [103]	Strengthening layer 10 mm thk	PP ⁸	Beams	Four-point bending	Quasi-static
2020	Wei [104]	Strengthening layer 15-25 mm thk	PE	Beams	Four-point bending	Quasi-static

As can be seen in Table 2.6, many research studies assess the structural performance of SHCC at quasi-static strain rates. As aforementioned, due to its

⁷ thickness

⁸ Polypropylene

strain-rate sensitivity, there are still uncertainties regarding the full potential of these composites for dynamic applications, from cyclic loading, which would relate to its fatigue response, to its behavior under high-speed and impact rates. In addition, the number of studies that specifically assess the influence of the reinforcing fiber is quite limited. As the composite energy, and thus its energy absorption capacity, are intimately dependent on the type of fiber, additional studies comparing different fibers would be deeply relevant.

Apart from the type of the critical stress acting on the structural element, special precautions must be taken to apply additional SHCC layers, like with all repair materials. It is imperative to prepare the surface for the strengthening layer, increasing roughness and adequately cleaning it [105]. There is the possibility of spalling of the SHCC patch layers due to inadequate bond with the substrate [25]; see **Fig. 2.18**. As it is often indicated for repairs and constructions joints, [25] suggests the use of polymer-modified epoxy to improve the bonding.



Fig. 2.18 – Bonding influence in the crack patterns of SHCC patches: (a) Good bond relates to multiple-cracking formation; (b) Bad bond relates to the patch spalling [25].

Four variations of SHCC strengthening layers were tested by [17] under monotonic and cyclic loading: plain, with no steel bars (BS0), then three levels of linear steel content (BS1, BS2, BS3); see Fig. 2.19. No delamination could be detected between the concrete substrate and the SHCC layers. However, great damage was observed in the unreinforced patches (without the steel rebars). These results suggest that a small amount of continuous reinforcement embedded in the SHCC layer can reduce the stiffness degradation, especially for dynamic loading.

A total of 9 simply supported beams of SHCC made with PVA fibers at 2.0 % in volume were subjected to a concentrated load at the mid-span to evaluate the

influence of the shear-span ratio (2, 3, and 4), and longitudinal reinforcement ratio (2.28 %, 3.25 %, 4.25 %) [72]. None of the beams had any type of transversal reinforcement. It was found that the shear effective span-depth ratio (SESDR) is determinant to the shear strength of the specimens (\downarrow ratio, \uparrow shear strength), and has little influence on the extension of the cracking pattern. The SHCC beams presented diagonal multiple cracks regardless of the SESDR, indicating a prominent crack dispersion capacity. The maximum crack width was 300 μm at the ultimate load, and 100 μm at the limit service state, satisfying the crack width demand for harsh environments of most design codes.



Fig. 2.19 – Crack patterns and failure modes of the beams strengthened with SHCC [17].

2.2.Torsion

Torsion effects are often dominant in RC bridges elements, peripheral beams in multi-story buildings, ring beams of circular tanks, edge beams in foundation slabs, and helicoidal staircases beams [105,106]. From the fundamentals of the Strength of Materials, torsional moments lead to shear stresses [107], which are highly dependent on the position of an assessed element and its geometry [105]. For instance, consider a constant torsional moment applied to a simple shaft: the shear stresses will exhibit null values on the shaft's longitudinal axis, enhancing their values while approaching the cross-section edges. In the case of a rectangular shaft, higher stress values will be obtained on the edges nearest to the shaft's longitudinal axis (larger sides) [105,108]. In the case of material yielding, it will start on the cross-section edges, and progress inwards toward the torsional axis.

Under a pure torsion state (without normal constraints), Mohr's Circle shows that a pure shear stress configuration is equivalent to a biaxial state of balanced tensile and compressive stresses oriented at 45° to the torsional shaft axis [105]. Being the tensile strength of cement-based matrices substantially lower than their compressive strength, torsion effects can produce dramatic structural damage in RC members by the formation of spiralled cracks through the length of the torsional shaft axis, usually of large width, resulting in a skewed fracture plane [107].

2.2.1. Torsional behavior of FRC

While the subject torsion can not be considered ever-popular, especially with regards to FRC, it has been steadily assessed since the 1980s, as shown in Table 2.7. It was found that the addition of discrete fibers (in particular steel) contributes to enhancing the torsional strength by up to 27 %, and twist angle by up to 100% when compared to plain concrete [107,109]. Moreover, the addition of fibers substantially improved the ductility of the specimens, as well as the torsional toughness (given by the area under the torque-twist curve) [110]. It contributed to a reserve of strength after the first crack, while the brittleness of the reference RC specimens took them to sudden collapses at this stage [107]. As evidenced by the values of maximum torque (T_{max}) and rotation angle ($\theta_{T,max}$) presented in the Table 2.7, the geometry of the specimen carries great influence on the torsional performance both for RC and FRC. The type of fiber and its content comes as additional variables.

Table 2.7 – Summary of previous studies regarding torsion of FRC beams.

Research	Cross-section [mm × mm]	Length [mm]	T_{max} [N.m]	$\theta_{T,max}$ [°]
1982 Mansur and Paramaslvam [109]	102 × 102	760	850 – 1000	0,3 – 2,6
1983 Narayanan e Kareem-Palanjian [107]	85 × (85-178)	2200	748 – 2243	0,1 – 0,2
2003 Rao e Seshu [111]	100 × 200	2000	1,7 – 3,0	0,3 – 0,5
2015 Ju et al. [112]	150 × 250	1200	8000 – 17500	4,1 – 8,3
2016 Patil e Sangle [110]	140 × 140	1420	2500 – 3000	0,7 – 0,9

In general, one should expect higher rotation angles to longer effective lengths, but as it happens to other stress states, this outcome depends on the properties of the fibers, matrix, and the ITZ, which are influencing factors to the pullout behavior and bridging capacity, thus ruling the cracking process [113]. For instance, it was found that the higher the fiber content and aspect ratio of the fibers, the greater is the improvement of all mechanical properties [109]. However, usually adequate rheology and casting become a challenge with large values of these parameters, which need to be taken into account during the design and dosage tailoring phases to avoid construction gaps.

It is also important to notice that often research studies results are based on settings quite difficult to achieve on the construction sites, especially with regards to structural level tests. E.g., the very favorable conclusions of [109] were based on fiber lengths varying between 15 mm and 44 mm with under contents of up to 3 %, which is a significant high value for long fibers such as these. Moreover, while the fibers could contribute to the metallic reinforcement reduction, usually members under torsion involve a high concentration of rebars, which is an additional challenge for casting by itself. New studies are yet to be developed to assess the influence of other types of fibers, with different compositions and geometries.

2.3. Impact loading scenarios

2.3.1. Reinforced concrete subjected to impact

RC has been widely used in civil constructions for almost two centuries due to its versatility and relatively low cost-effectiveness ratio when compared with other structural systems [114]. It is notably the preferred material for the construction of strategic infrastructures such as power plants, bridges, and nuclear power stations [115]. However, RC structures are in constant deterioration due to moisture, pollution, chemical attack, and, as it has become even more important in the last decades, dynamic effects [116,117]. RC structures exhibit inherent low resistance to various types of dynamic loadings, such as earthquake, blast, and impact due to concrete's low tensile strength and pronounced brittleness, which promotes intense cracking during these scenarios [118]. Lately, the impact of moving objects, extreme earthquakes and tsunami has been gaining public attention due to terrorist attacks such as on the World Trade Center (USA) on September 11,

2001, and the devastating accident in the nuclear power plant of Fukushima (Japan) in the spring of 2011 [115], taking public authorities worldwide to sponsor new academic studies in this field.

The term *impact* itself is generally related to a variety of loading scenarios, such as the impact of vehicles and rockfalls to structures, armor-piercing bullets, shaped and explosive charges, or even the impact of aircrafts [11,115,118,119]. Focusing on the construction design (both in the structural systems and materials fields), many questions arise regarding the possibility, and not less important, feasibility, to protect civil structures of these extreme events, or at least secure enough structural stability to enable the safe evacuation of users. Moreover, even though these scenarios are often referred to as *impact*, they will produce very distinct patterns of pressure waves on structures, impairing that they are similarly accounted for, which explains the variety of research studies about this topic. The present review will overlook to describe shaped and explosive charges studies, focusing on hard and soft impact works, as they afford a better basis of the civil engineering field without military interest [115].

RC is highly sensitive to the loading rate, exhibiting very distinct behavior under impact when compared to static conditions. The Model Code 2010 [120,121] states an enhancement of material strength for both concrete and steel, both under compression and tension, with the change from quasi-static to dynamic strain rates. However, experimental studies already reported that quasi-brittle materials such as concrete also display a tendency of a switch from failure mode I to mixed mode on the material scale with the increase of loading rate [122–124], which undoubtedly affects the tension stiffening performance of RC members [125,126]. Moreover, normal-strength concretes were reported as being more rate-sensitive than high-strength ones [127–130]. This variation alone is likely to influence the global change on the critical mode of failure from flexural to shear, noticed in some research studies [131,132]. This is considered undesirable since is related to a more relatively unstable failure of the affected structural member. Additionally, local damaging processes such as scabbing and spalling can occur during impact events, which can also significantly affect the safety of users; see Fig. 2.20 [119,133].

The available literature carries a variety of impact test methods. They can be subdivided into four classes [11,134]: (i) tests based on potential energy, such as drop-weight, Charpy, and Izod (ASTM) methods; (ii) tests based on kinetic energy,

in which the mass/projectile strikes the specimen with an accelerated velocity; (iii) tests in which hydraulic machines connected to closed-loops systems deform the specimens at medium-high loading rates; and (iv) tests where the stress wave is generated and propagated through an auxiliary element, which is in contact with the specimens, such as the split Hopkinson pressure bar (SHPB), and the split Hopkinson tension bar (SHTB). The type of impact scenario (that will determine the strain rate), and the type of loading (compression, tension, flexure, etc), will constrain the testing method that should be performed; see Fig. 2.21. From the mentioned classes, two will be further discussed, as they will be addressed in the present research.

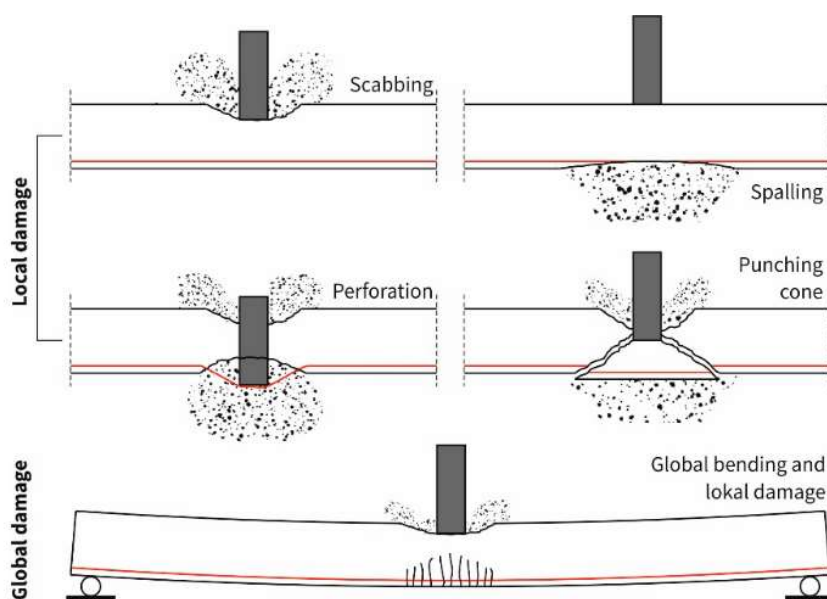


Fig. 2.20 – Summary of different types of damage on RC structures coming from impact scenarios [119,133].

Testing methods based on kinetic energy entail the acceleration of the projectile, usually through air pressure [11,115]. As high velocities are feasible, local damages as perforation and punching cones (Fig. 2.20) are possible. Besides the acceleration pressure, geometric and material characteristics of the projectile such as mass, length, nose shapes (conical, ogive, flat) enable several testing variations [135]. Depending on the projectile's path (vertical, or horizontal), gravity effects should be distinctly taken into consideration. In particular, in the case of vertical accelerated systems [115], assuming that there is no friction between the projectile and the railing tube, the impact energy can be simply assumed as $E_c = 0.5 m v^2$, where m and v are the projectile's mass and velocity respectively, as it

happens for gravity drop-weight systems [11,115,135]. As the measurement of the impact load from a load cell anyhow attached to the projectile (on the top, or bottom) would include the inertial loads, which in turn would impair the interpretation of results, two methods for measuring the impact loads are reported [115,135,136]: (i) measuring the reaction loads on the supports; and (ii) measuring the impact load from a load cell attached to the projectile, and deducting the inertial loads based on the accelerometers signals, taking into consideration that the inertial loads assume some type of continuous distribution (linear, quadratic, etc), which should be confirmed through the amplitude's values.

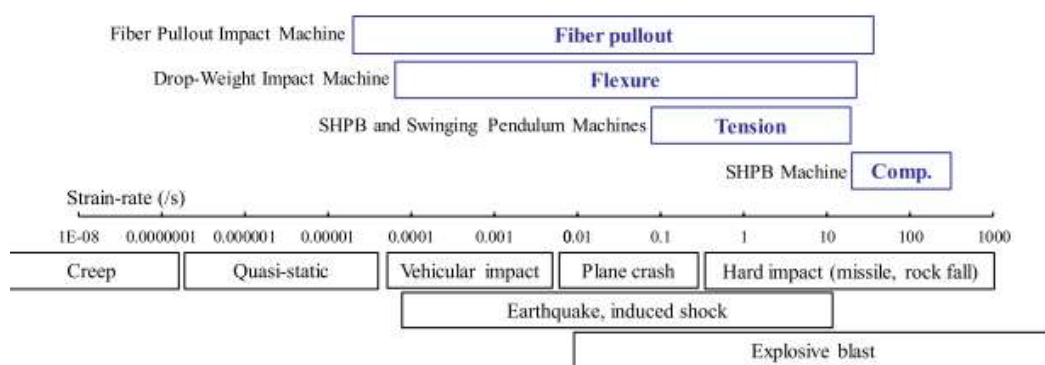


Fig. 2.21 – Summary of typical strain-rate ranges of RC structures matched with available strain-rate ranges of tests available in the literature [11].

Table 2.8 summarizes some previous works that addressed the impact performance of RC beams. It can be noticed a fair correlation between the geometrical characteristics of the specimens. The high variation of equivalent kinetic energy is due to the high variance of weight between the masses used to perform the impact. Thus, most of the mechanical studies on the structural scale are primarily based on the response of signals in time, eventually counting with additional analysis, such as the numerical modelling of the experimental program, usually using the software LS-DYNA.

Tests based on wave propagation are frequently adopted to assess the fracturing behavior of materials under dynamic loading (material scale) [137–139]. These tests are usually based on two basic assumptions: (i) that the stress pulse assumes a one-dimensional propagation; and (ii) that the stress distribution along the specimen cross-section is uniform. The literature reports a number of different bars configurations (considering their material, diameter, and length), since each type of material under testing, which may display distinct fracturing processes,

requires adjustments to enable a reliable interpretation of results [140]. Brittle materials such as concrete are commonly assessed in compression systems, while the ultimate performance of FRC requires their evaluation under tension (SHTB).

Table 2.8 – Summary of previous studies regarding impact loading on RC beams.

Study	Cross-section [mm × mm]	Efec. length [mm]	Velocity of the impactor [m/s]	Equivalent Energy [kJ]	Analyzed parameters
Bentur et al. 1986 [136]	100 × 125	1400	3.0	1.5	→ Support loads and acceleration in time → Load-displacement response
Kishi et al. 2002 [141]	150 × 250	1000 – 2000	1.0 – 5.0	0.2 – 3.8	→ Cracking patterns → Load in time (both from the load cells on the supports, as of the one fixed on the drop hammer) → Mid-displacement deflections in time → Load-displacement response
Adhikary et al. 2012 [142]	150 × 250	1400	0.4	N/A	→ Load in time from a load cell fixed on the drop hammer → Strain-gages installed at the mid-span of selected internal reinforcements → Accelerometers positioned on the top-surface of the specimens; used to check inertia effects
Soleimani and Bantia 2014 [143]	150 × 150	800	7.0	14.5	→ Load in time (both from the load cells on the supports, as of the one fixed on the drop hammer)
Pham et al. 2018 [144]	150 × 250	1900	6.3	4.0	→ Load in time (both from the load cells on the supports, as of the one fixed on the drop hammer) → Mid-displacement deflections in time

With the advent of structural health monitoring (SHM) techniques for civil engineering, a number of new studies have been focused on the evaluation of the vibrational response of structural members to detect damage, being the mode shapes, natural frequencies, and damping ratios, the parameters typically monitored [117,133,145–150]. Although it is an intrinsically non-destructive technique, it can also be used to assess the residual response of damaged systems when considering an intact referential [146,151]. While the mode shapes and natural frequencies are deeply connected to geometrical and stiffness properties of the analysed members, damping coefficients are more related to the type and state of the material that embodies an element, enabling some quantitative correlation between different studies. For instance, it was already reported that undamaged reinforced concrete members display damping values of $\sim 0.85\%$, while cracked ones can provide larger coefficients, with values varying between $0.5 - 4.0\%$ [152–154].

2.3.2. FRC subjected to impact

The addition of discrete fibers on RC members subjected to impact has been extensively assessed, with emphasis on the ones produced with steel fibers. In comparison to plain RC, FRC exhibits improved impact resistance and energy absorption capacity [155–159]. When shifting from quasi-static loading ($\dot{\epsilon} \approx 10^{-6}$) to impact loading ($\dot{\epsilon} \approx 10^0$; impactor velocity of 1.4 m/s), FRC beams yielded a decrease in the nonlinearity of the load-deflection curves [129,159]. FRC specimens were also reported to bear higher deflections than plain concrete before failure [3,124,127–130,132,159–162]. These traits relate to the finding that the fibers are able to limit the crack growth (width and length) even at large openings [127,163,164], with their contribution being narrowed by its type, geometry, and content [124,165–168]. Boundary conditions were also reported to interfere with the performance of FRC subjected to impact, let alone on their cracking patterns [168]. The amount of dissipated energy (through cracking) tends to grow with the confinement level, improving the overall impact resistance, load-bearing capacity, and in some cases, preventing the failure.

The use of short fibers, as substrate or strengthening layers, has been more scarcely addressed up to now [169], being limited on their contribution on the front and rear sides, on specimens under critical bending as slabs [135]; see Fig. 2.22. It was found that slabs strengthened with SHCC on the rear side endure several more

impact blows than the non-strengthened ones (impactor weight of 13 kg at velocities varying between 4.4 m/s and 6.3 m/s) [169]. The surface preparation process was also found to affect the impact resistance. E.g., a combination of substrate gridding and a bed of epoxy adhesive before the casting of SHCCs turned out to be the most efficient strengthening method for these composites [170]. As it will be addressed in chapters 4 and 5, the present research will focus on the strengthening of the sides parallel to the trajectory of the impactor on specimens under critical shear when subjected to impact (Fig. 2.22d).

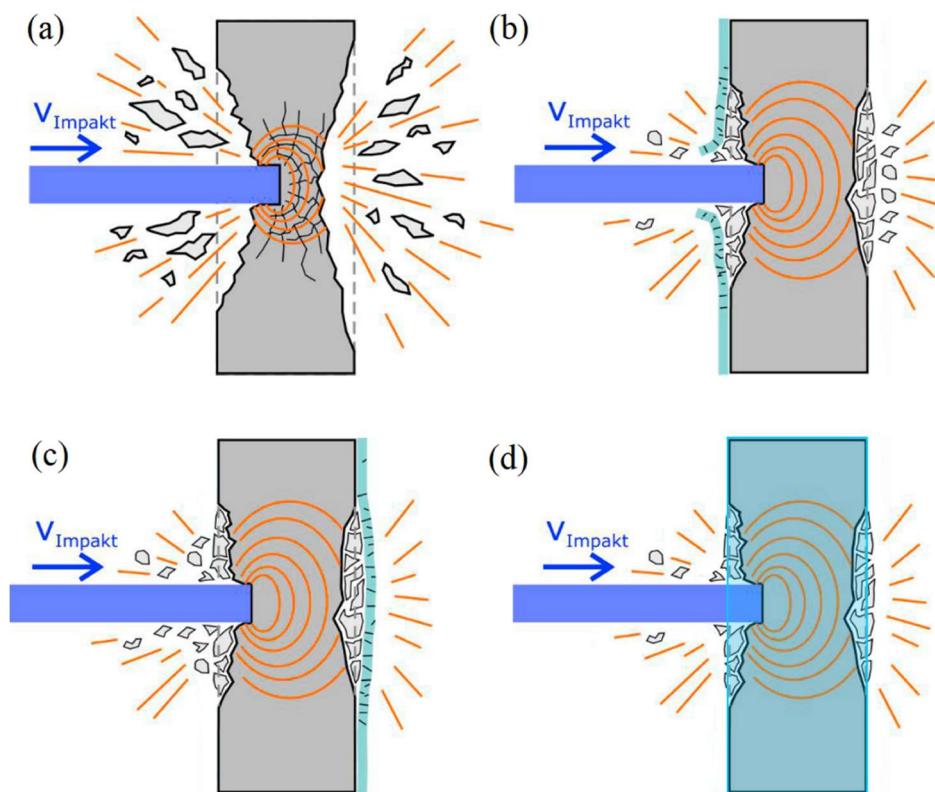


Fig. 2.22 – Impact behavior of RC members strengthened with FRC [adapted from 118]: (a) without strengthening; (b) with strengthening on the front-surface (impacted plane); (c) with strengthening on the rear-surface (opposite to the impacted plane); (d) with strengthening on the side surfaces parallel to the impactor's trajectory (side surfaces).

3 Mechanical behavior of strain-hardening cement-based composites (SHCC) subjected to torsional loading and to combined torsional and axial loading

3.1. Introduction

Reinforced concrete (RC) structures are generally possessed of limited damage tolerance and energy dissipation capacity, traceable back to the low tensile strength and pronounced brittleness of concrete. These drawbacks can become critical under shear and torsional loading, especially when caused by intense dynamic actions [171–173]. The main risk related to such load scenarios is the sudden reduction of load-bearing capacity due to the concrete's pronounced cracking and spalling, both of which can render the steel reinforcement ineffective; see, for example, [11,116,174]. Furthermore, highly dynamic loading scenarios can cause failure modes different from the quasi-static ones, thereby increasing the risk of shear failure [131]. Thus, to increase the impact resilience of existing critical infrastructure there is the need for appropriate strengthening solutions [175].

The application of additional layers of RC for structural strengthening has obvious disadvantages related to significant increases in the cross-sectional dimensions and in the dead weight of the structure's elements. Carbon fiber-reinforced polymers (CFRP) have been widely investigated and implemented as strengthening covers in the form of sheets [12,176–178] or grid-like fabrics [179–183]. Such strengthening layers are of small thickness and can considerably increase the load-bearing capacity of RC structural members. In the case of sheets, disadvantages include the requirement of polymeric-based adhesives, precluded observability of crack formation in the substrate, and low fire resistance. In the case of grid-reinforced strengthening layers, cracks will still start in the base element, but will propagate into the strengthening layer, usually displaying smaller widths and finer distribution. However, grid or textile reinforcements based on continuous fibers exhibit brittle behavior, which impair their resistance to shear or torsional loading. Moreover, their strengthening performance is intimately dependent on the bond with the substrate.

Strain-Hardening Cement-based Composites (SHCC), also Engineered Cementitious Composites (ECC), represent a special type of fiber-reinforced concrete with short and randomly distributed micro-fibers in volume fractions of up to 2 %. SHCC exhibit pronounced ductility prior to failure localization [14,84], while multiple cracks formed in the strain-hardening phase yield crack widths in a favorable sense less than 100 μm . These features make SHCC suitable both as main material for structural elements subject to extreme loading scenarios as well as supplementary applied retrofit and strengthening layers for enhanced structural durability and resilience under unfavorable exposure and loading conditions [16,17]. It is worthy of note that the constitutive nature and fresh-state properties of SHCC enable their application by spraying or lamination, which is an important prerequisite for structural strengthening through thin covers [15].

The remarkable crack control in SHCC leading to multiple cracking under tensile and compressive forces is responsible for the advantageous shear behavior of these composites [69]. In addition to some structural investigations on the performance of SHCC as main material [74] and for strengthening layers subject to shear [79,80], to date only a few investigations have been reported on the material characterization of SHCC under shear loading. Li *et al.* [69] investigated the shear behavior of SHCC using Ohno shear beams. Although SHCC demonstrated strain-hardening and extensive deformations after the formation of the first crack, the non-uniform shear stress distribution in the middle of the beams complicated the proper characterization of shear strength. Van Zijl [70] optimized the Iosipescu beam geometry and calibrated a material constitutive law employing a numerical parametric study. He found that the shear strength of SHCC exceeded its direct tensile strength by up to 50 %. However, due to the purposefully designed shape and size of the specimen, the cracked region was restricted to the notch area, impairing the load-bearing capacity and thus, obstructing the direct detection of strain-hardening behavior. Kanakubo *et al.* [84] extended the Iosipescu beam configuration by applying additional axial tensile loading. This method facilitated the analysis of the shear transfer mechanisms depending on the degree of tensile deformation.

The wide range of reported testing methods and specimen geometries arises out of the difficulties in assuring a pure shear state in the specimen and makes comparison of different investigations unduly complex. Moreover, the

experimental derivation of constitutive material laws is not trivial, requiring additional numerical simulations. Except for analytical studies in [184], no attempts have been made so far in characterizing the shear transfer mechanisms at the single-crack level in dependence on the crack opening. Furthermore, the influence of matrix composition and fiber type has not been assessed either.

In the work reported herewith, torsion and combined torsion-tension experiments were used to characterize the multi-axial and shear behavior of two types of medium-strength SHCC, which were adopted from previous studies by the authors, see e.g. [40,58,185,186], with no further adjustments. The comparative study involved SHCC made with polyvinyl-alcohol (PVA) and ultra-high molecular weight polyethylene (UHMWPE) fibers, which allowed for a clear demonstration of the influence of the fiber type. The experiments were performed under controlled loading and boundary conditions and involved four different load cases: (1) uniaxial tension; (2) torsion with blocked axial deformation; (3) torsion with free axial deformation and (4) combined torsion-tension. Optical crack monitoring of the loaded specimens with a stereo-camera system and the subsequent analysis using Digital Image Correlation (DIC) allowed a detailed characterization of the crack opening modes depending on the load case and state-of-stress in the sample. Besides offering a detailed material characterization, the experimental results in this work represent a comprehensive basis for the derivation of numerical constitutive models for SHCC subject to multi-axial loading in general and shear or torsion in particular.

3.2. Materials and methods

3.2.1. SHCC compositions

In this study, two types of SHCC were investigated. Their mixture compositions were already addressed by Curosu and Mechtcherine in previous works [40,58,185,186]. Both held the same normal-strength matrix, differing only in the type of dispersed fiber. One SHCC was made with polyvinyl alcohol (PVA) fibers produced under the brand name Kuralon REC15 (by Kuraray, Japan) [187]. The other SHCC was reinforced with UHMWPE fibers produced under the brand name Dyneema SK62 (by DSM, the Netherlands) [188]. The UHMWPE fibers will be more compactly referred to as PE in this chapter, and the composites will be

named according to the reinforcing fibers, i.e., PVA-SHCC and PE-SHCC, respectively. In both SHCC compositions the fiber volume fraction was 2 %, which is a typical content for this kind of composites. The PVA and PE fibers presented in the chapter at hand are most commonly used in SHCC compositions. The discrepant aspect ratios of these fibers (see Table 3.1) in conjunction with their specific bond properties with the investigated normal-strength matrix result in distinct crack-bridging performances.

Despite their oil coating, the PVA fibers remain predominantly hydrophilic and form a considerable chemical bond with the cementitious matrix [189–191]. Furthermore, they exhibit relatively low abrasion resistance and pronounced slip-hardening pullout behavior, with a likely occurrence of fiber rupture at larger crack openings [192]. For this reason, the normal-strength cementitious matrix under investigation was developed specifically with respect to PVA fibers and had to ensure a limited fiber-matrix bond strength to mitigate excessive and premature fiber rupture [186]. This explains the high content of fly ash compared with the contents of cement and quartz sand; see Table 3.2.

Table 3.1 – Geometric and mechanical properties of PVA and PE fibers according to producers.

Fiber		PVA	UHMWPE
Diameter	[μm]	40	20
Length	[mm]	12	12
Density	[g/cm ³]	1.26	0.97
Tensile strength	[MPa]	1600	2500
Young's modulus	[GPa]	40	80
Elongation at break	[%]	6.0	3.5

In contrast, the PE fibers are hydrophobic and hence only frictionally/mechanically anchored in the matrix [193]. Furthermore, they exhibit superior tensile strength, Young's modulus, and abrasion resistance, making them especially suitable for use in high-strength cementitious matrices [194]. The crack-bridging behavior of these fibers in the normal-strength matrix was addressed in previous investigations by the authors Curosu and Mechtcherine [40,58,185]. Despite the relatively low bond strength in comparison to the PVA fibers, the smaller diameter of the PE fibers ensures sufficient collective crack-bridging capacity for tensile strain-hardening and multiple cracking. Furthermore, PE-SHCC

is more suitable for applications involving highly dynamic loading [40,58] and when proper crack control at larger crack openings is required [185].

Table 3.2 – Mixture compositions of the medium-strength SHCC under investigation.

Components and content in [kg/m ³]	PVA-SHCC	PE-SHCC
Portland cement CEM I 42.5 R-HS (Schwenk, Germany)	505	505
Fly ash Steament H4 (Steag Power Minerals, Germany)	621	621
Quartz sand 60 – 200 µm (Strobel Quarzsand, Germany)	536	536
Water	338	333
Superplasticizer Glenium ACE 30 (BASF, Germany)	10	25
Viscosity modifying agent (SIKA, Switzerland)	4.8	4.8
PVA fiber 2 % by volume (Kuraray, Japan)	26	–
UHMWPE fiber 2 % by volume (DSM, the Netherlands)	–	20

Note that the cementitious matrices in both SHCCs are practically identical. The minor differences as shown in Table 3.2 are related to the slightly higher content of superplasticizer in PE-SHCC. This was required by the smaller fiber diameter of PE and the need to compensate for some decrease in workability when PE fiber is used instead of PVA fiber. Moreover, the relatively large size of the fly ash and quartz sand particles in comparison to the diameter of the PE fibers represented a drawback in terms of fiber dispersion [186]. This additionally demanded an adjustment to the mixing process, involving higher mixing energy and duration [186].

3.2.2. Specimen preparation

Dumbbell-shaped specimens were used in this investigation. The cross-section of the specimens in the 100 mm-long gauge portion had dimensions of 24 mm × 40 mm, the total specimen length was 250 mm, and the end sections had cross-sections of 40 mm × 40 mm; see Fig. 3.1. This specimen geometry is not typical of torsion experiments. Previous tests showed that in the case of cylindrical specimens it is difficult to realize the tapered geometry required to confine the damage to the middle section out of the need to avoid failure initiation at the fixities. At the same time, besides the challenges related to specimen production, pronouncedly curved surfaces of cylindrical specimens would be disadvantageous as regards the optical monitoring of deformations and crack analysis by means of

Digital Image Correlation (DIC) with the technical equipment available. Finally, the geometry chosen is common in uniaxial tension experiments for SHCC characterization [193], enabling a closer link between this program and other studies. The torsion experiments presented in this article represent the first study of this type, and they are intended to form a basis for adjustments and optimization in future works.

Batches of 3 liters were produced in each casting series of six specimens. Due to the high cohesiveness of the fresh SHCC, the specimens were not provided with a smooth top surface during production. Instead they were cast manually with a superfluous top layer, which was subsequently removed by cutting the hardened SHCC prior to testing. To avoid failure localization at the fixities due to stress concentrations, the specimens were additionally strengthened at their ends by embedding 50 mm-long metallic screws of 5 mm diameter during casting.

The samples were demolded 24 hours after casting, sealed in plastic sheets and stored in a curing chamber with controlled temperature of 20 °C and relative humidity of 65 %. After 14 days of curing, the specimens were prepared for testing by cutting the superfluous layers and roughening the lateral surfaces of the end (anchorage) portions. Because of logistical considerations, testing was performed at an average age of 65 days. At this age the hardening process is practically complete [195].

3.3. Experimental program

3.3.1. Testing setup and load cases

The dimensions of the dumbbell-shaped specimens with view on their tapered side are given in Fig. 3.1. In the third direction the specimens had a constant width of 40 mm, as presented in Fig. 3.2. The mechanical testing was performed using an Instron™ 8874 testing machine with ± 25 kN axial load capacity and ± 100 Nm torque capacity. The specimens were first glued at one end into a steel ring in a special frame outside the testing machine, aiming at accurate specimen alignment and centered position in the ring. After the hardening of the glue, the specimen with the ring was bolted at the top to the loading assembly. By tightening four bolts in each pair of pressure rings, the assembly was pre-stressed, in this way hindering the relative sliding of the steel elements during the torsion tests. Subsequently, the

sample was driven downwards into the bottom ring filled with glue; see Fig. 3.1. A bi-component X60 glue (HBM, Germany) was used, which enabled testing after only 15 min of hardening.

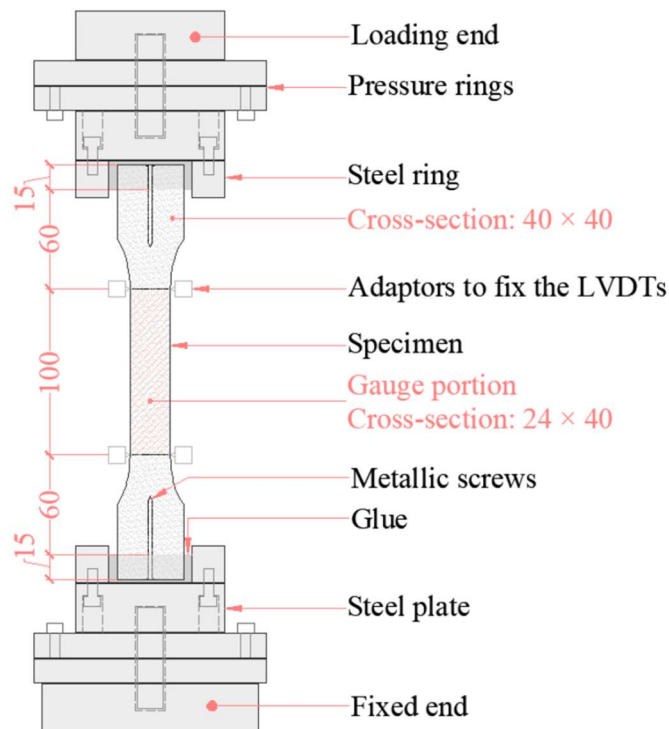


Fig. 3.1 – Specimen fixation, geometry and dimensions in mm.

In the case of the uniaxial tension experiments, the deformation of the 100 mm long gauge portion in the middle of the specimens was measured by two Linear Displacement Transducers referred as LDT (by Gefran, Italy). The LDTs had a maximum stroke of 10 mm and were attached to the specimens through a specially fabricated aluminum frame. The data acquisition system consisted of a QuantumX model MX1615B unit and a Catman DAQ software V5 (both from HBM, Germany). Four different load cases were investigated in the presented study, as summarized in Table 3.3.

3.3.2.3D optical measurements and DIC

A stereo system consisting of two CMOS cameras with 2.3 megapixels (Basler acA1920-155um) coupled to adjustable focal length lenses (Tamron A031 AF28-200mm F / 3.8-5.6) was used to capture images of the loaded specimens. This enabled a detailed analysis of the crack opening modes depending on loading case. The softwares VIC-Snap and VIC-3D (Correlated Solutions, USA) were used for

image acquisition and analysis, respectively. The images were processed using a normalized-sum-of-squared differences (NSSD) with a subset of 21 pixels, a step of 7 pixels, and a strain window of 15 displacement points. With these parameters, the analysis provided displacement measurements with an uncertainty of approximately 0.005 %.

Table 3.3 – Schematic representation and description of the load cases under investigation.

	<p>Load case 1 (LC1): Uniaxial tension with non-rotatable boundary conditions. Displacement-controlled mode with a displacement rate 0.05 mm/s.</p>
	<p>Load case 2 (LC2): Torsion with blocked axial deformation. Angle-controlled mode with an angular rate of 0.1 °/s. The axial compression force resulting from the hindered specimen expansion due to cracking while twisting was measured during the test.</p>
	<p>Load case 3 (LC3): Torsion with free axial deformation. Angle controlled mode with an angular rate of 0.1 °/s. The axial displacement was force controlled under an imposed axial force of 0 N to enable free expansion of the specimens.</p>
	<p>Load case 4 (LC4): Combined torsion and tension. Controlled axial displacement of 0.05 mm/s combined with an angle-controlled torsional loading at an angular rate of 0.1 °/s.</p>

A speckle pattern was applied onto one of the 40 mm-wide lateral surfaces of the samples. This allowed resolving the strains and cracks in the gauge portion of the samples as illustrated in Fig. 3.2. The global coordinate system (GCS) in the DIC analysis was positioned in the left bottom corner of the surface observed. The

crack angle relative to the horizontal x-axis was derived in AutoCad (Autodesk, USA) by approximating the cracks to inclined lines.

To monitor the crack-flank displacements (CFD), virtual calipers were placed on the crack flanks, and local coordinate systems (LCS) were defined according to the crack inclination angle; see Fig. 3.2. The calipers were placed parallel to the y-axis of the LCS, i.e. orthogonal to the crack. To be noted here is that the resolution of the DIC system was not sufficient to distinguish single cracks in dense crack clusters. Because of this, the distance between the digital markers u_i and v_i was 8 mm in order to include the entire width of the resolved strain bands. After the experiments, the paint was removed from the observed regions and the correct number of cracks was determined using a digital microscope VHX-6000 (Keyence, USA) with a CMOS sensor camera with 18 megapixels, providing the means accurately to interpret the crack opening values yielded by DIC. The CFD histories were evaluated in three directions as shown in Fig. 3.2: I – normal opening, II – in-plane sliding, III – out-of-plane sliding.

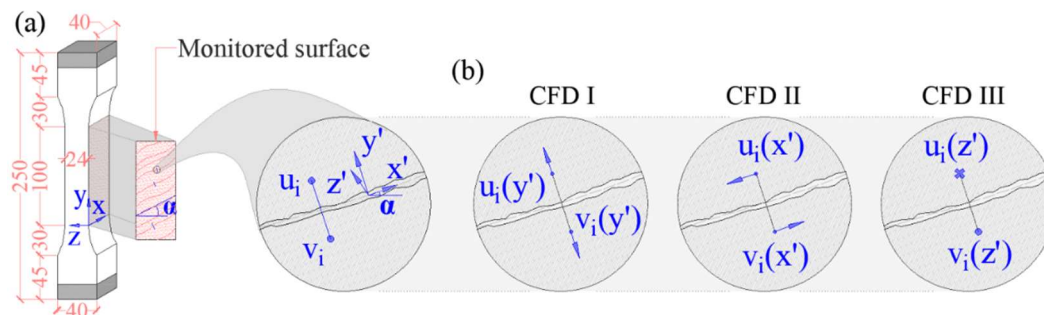


Fig. 3.2 – (a) Dumbbell-shaped specimen with dimensions in mm indicating the positions of the global (GCS) and the local coordinate systems (LCS) as well as the virtual calipers. The grey portions at the specimens' ends represent the regions embedded in the glue and encased by the metal rings. (b) Schematic representation of the assessed CFD in the DIC analysis.

The CFD analysis as presented in Fig. 3.2 was not meant for the monitoring of the cracking process in the entire specimen, but to observe the relative displacement of the crack flanks of formed steady-state cracks. In the case of torsional loading, the crack-flank kinematics are determined by three components, which vary in magnitude according to the distance from the cross-sectional centroid; see Fig. 3.3. With the given shape of the cross-section in the gauge portion,

the relative magnitudes of CFD II and CFD III also depend on the position of the virtual calipers. Coming closer to the margin of the observation field CFD III should yield higher magnitudes than CFD II, while in the vicinity of the longitudinal axes of the specimen the values are negligible (Fig. 3.3). Thus, the virtual calipers only offer a local description of the crack flanks' displacements. To ensure consistency of the quantitative data, the virtual calipers were positioned in the quarter-span of the transverse section. Their longitudinal position was defined to avoid regions of failure localization.

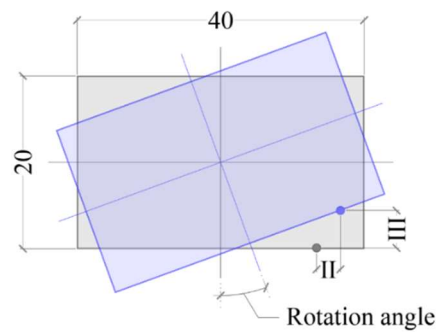


Fig. 3.3 – Schematic, exaggerated representation of the influence of cross-sectional shape in mm and location of the DIC caliper on the measured CFD II and CFD III.

3.4. Results and discussion

Given the multi-axial state of stress in the specimens subjected to torsion, the comparative assessment of the specimens' responses in this chapter is done based on load or torque to axial deformation or rotational relationships. Note that four to five specimens were tested for each parameter combination, but only the curves corresponding to successful tests yielding accurate material responses are presented. The discarded tests were those yielding failure at the fixities.

3.4.1. Uniaxial tension experiments (LC1)

Fig. 3.4a shows the axial load-deformation curves of the SHCC under investigation, with the axial deformation (recorded as the cross-head displacement of machine) related to the total free length of the specimen, while Fig. 3.4b shows the corresponding stress-strain curves, in which the strain applies to the 100 mm-long gauge portion. The force-displacement curves allow a direct comparison with the torsional load cases while the stress-strain curves enable the derivation of the

tensile material parameters and the comparison with previous studies by the authors on identical SHCC. The tensile material parameters are summarized in Table 3.4.

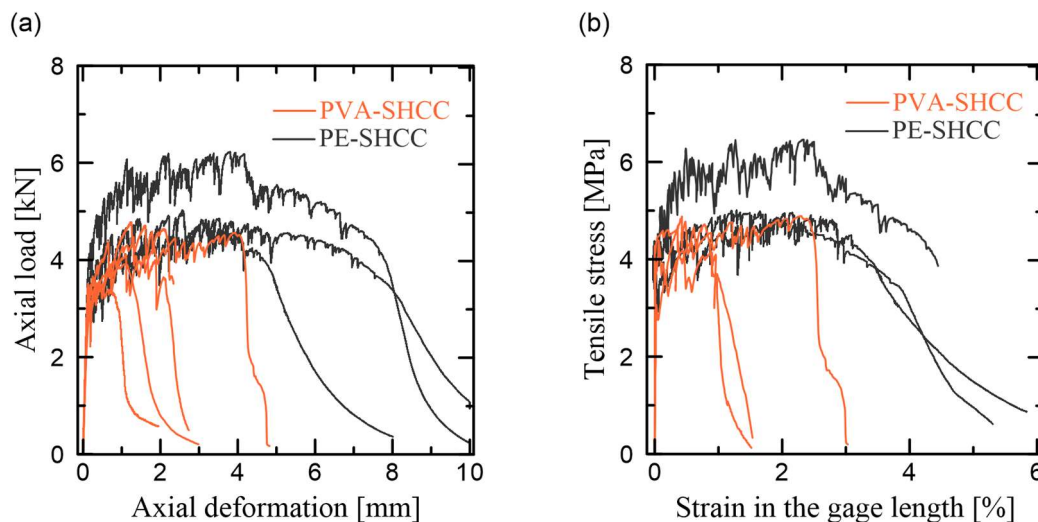


Fig. 3.4 – Uniaxial tensile behavior of PVA-SHCC and PE-SHCC: (a) load-deformation curves and (b) stress-strain curves.

The average first crack stress (σ_{1st}) of PVA-SHCC was 3.7 MPa, while in the case of PE-SHCC it was 4.1 MPa. Also, the tensile strength (σ_{max}) of PE-SHCC was higher than that of PVA-SHCC: 5.2 MPa vs. 4.3 MPa, respectively. Furthermore, the strain capacity (ϵ_{max}) up to failure localization showed considerably higher values for PE-SHCC compared to PVA-SHCC: 2.5 % vs. 1.0 %. In combination with the lower tensile strength, PVA-SHCC also yielded significantly lower work-to-fracture (G_{MC}) of 37.6 kJ/m³, which is the area under the stress-strain curves up to failure localization. PE-SHCC yielded an average work-to-fracture of 127.1 kJ/m³. These results do not completely agree with the findings of the previous studies by Curosu and Mechtcherine [40,185,196], in which PVA-SHCC yielded superior mechanical properties despite their lower aspect ratio, e.g. the strain capacity of 1.5% [185].

Table 3.4 – Mechanical parameters of PVA-SHCC and PE-SHCC under LC1.

Standard deviations are given in parentheses.

	σ_{1st} [MPa]	σ_{max} [MPa]	ϵ_{max} [%]	G_{MC} [kJ/m ³]
PVA-SHCC	3.7 (0.5)	4.3 (0.5)	1.0 (0.9)	37.6 (41.1)
PE-SHCC	4.1 (0.3)	5.2 (0.7)	2.5 (0.4)	127.1 (24.6)

The reason for this is likely to be the age at testing [195]. In the current work, the average age at testing was 65 days, while in the previous studies it was 14 days only. The ongoing hydration of the cementitious matrix enhanced the fiber-matrix bond strength. This had a positive effect in the case of PE-SHCC and allowed for more efficient exploitation of the high tensile strength of the PE fibers. In contrast, in the case of PVA-SHCC, the excessive bond strength enhancement had a negative effect on the micromechanical balance leading to a pronounced fiber rupture at crack formation [49]. Detailed data on the pullout behavior of these fibers out of the normal-strength cementitious matrix can be found in [58].

The different crack-bridging behavior of the fibers is also mirrored in the softening patterns of the corresponding SHCC. The steeply descending (softening) branch of the stress-strain curves for PVA-SHCC indicates fiber rupture after only limited fiber pullout, while the shallow softening of PE-SHCC suggests a lengthier fiber pullout phase. The involvement of these mechanisms was also confirmed by the visual inspection of the fracture surfaces. In the case of PVA-SHCC the protruding fibers' ends were short, at approximately 2 mm, while in the case of PE-SHCC the protruding fiber ends were longer.

The DIC evaluation was performed on several cracks for representative specimens; it indicated a significant scattering of the extent and mode of crack opening. The crack analysis presented is only valid for the representative cracks, which were neither first cracks nor localization cracks. Fig. 3.5 presents the axial load-deformation curves along with the CFD histories of selected cracks in representative PVA-SHCC and PE-SHCC specimens. The CFDs were evaluated at three different load stages, as marked on the axial load-deformation curves and in the DIC images.

Whereas for PVA-SHCC the CFD I, i.e., normal crack opening, history shows values of about 100 μm shortly before the beginning of the softening phase, the apparent crack opening in the case of PE-SHCC reached values of 275 μm . However, the microscopic analysis of the specimen surface after the mechanical testing indicated that the PVA-SHCC specimen indeed had a single crack at the location of the virtual caliper, while in the case of PE-SHCC the strain band actually contained seven micro-cracks. The stepwise increase in CFD I in Fig. 3.5b can be thus attributed to the successive formation of seven micro-cracks in a dense cluster.

By dividing the peak CFD I value to seven cracks, the resulting average crack width is approximately 41 μm .

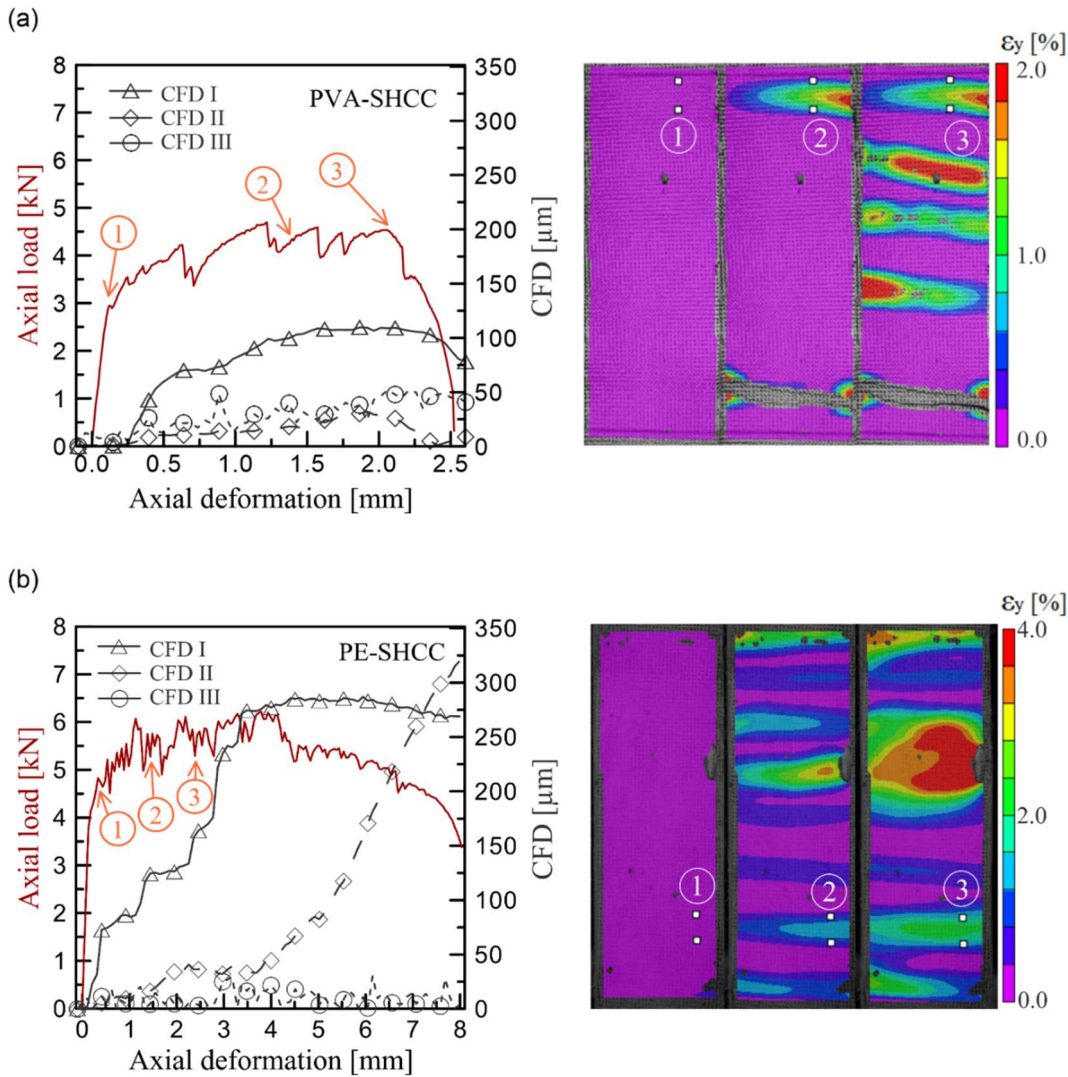


Fig. 3.5 – CFD analysis under LC1: (a) PVA-SHCC and (b) PE-SHCC. Note different x-axes (diagrams on the left) and different color scales (pictures on the right).

The average inclination angles of the cracks were 4.1° for PVA-SHCC and 5.9° for PE-SHCC. Although the CFD I histories had dominant magnitudes in both specimens, the DIC evaluation yielded significant crack-flank sliding, CFD II, defined as in-plane sliding, and III, out-of-plane sliding, in the strain-hardening phase. PE-SHCC showed a marked increase in CFD II after failure localization, despite the monitored cracks' distance from the localization crack. The crack-flank sliding can be partly traced back to the small crack inclination caused by possible specimen misalignment and the intrinsic variations of the material properties, i.e.,

flaws, non-uniform fiber distribution, etc. Another reason is the cracked samples' reduced stiffness, which allows specimen readjustment (rotation) and stress redistribution under increasing deformation.

It is shown in the next sections that the superior crack control and multiple cracking of PE-SHCC together with the effective crack-bridging at larger crack openings play a decisive role in the behavior of these composites under torsional loading.

3.4.2. Torsion experiments with blocked axial deformation (LC2)

Among the loading cases studied, LC2 simulates confined shear loading. The response of the specimens tested in LC2 is presented in Fig. 3.6. To repeat, five samples were tested per SHCC composition. The torque-rotation angle curves show the torsional resistance and the deformation capacity of the specimens depending on the type of fiber, while the compression force-rotation angle curves give a measure of the degree of axial expansion caused by matrix cracking. The experimental results of LC2 are summarized in Table 3.5.

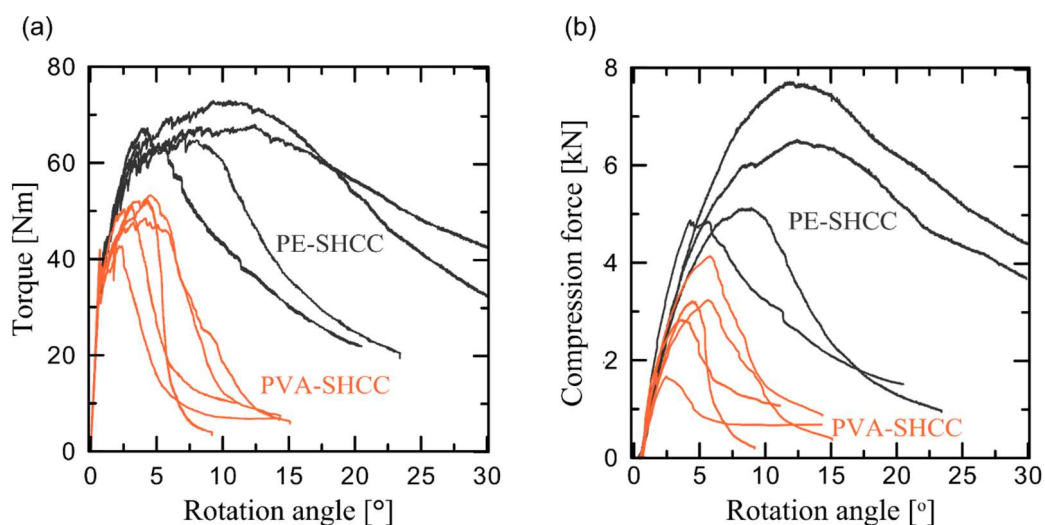


Fig. 3.6 – (a) Torque-rotation angle curves and (b) compression force-rotation angle curves of PVA-SHCC and PE-SHCC obtained in LC2.

Although the first crack torques (T_{1st}) of the analyzed SHCC are similar, PE-SHCC yielded 39 % higher maximum torque (T_{max}) and 112 % higher rotational deformation at peak torque ($\theta_{T,max}$) than PVA-SHCC; see Table 3.5 . Moreover, PE-SHCC yielded significantly higher angles of twist at peak torque as well as higher torsional deformations in the softening phase. The average rotation angle at peak torque was 4.2° for PVA-SHCC and 8.8° for PE-SHCC. PE-SHCC exhibited a

considerably denser crack pattern with smaller crack widths, while PVA-SHCC formed few cracks with visibly larger widths.

Table 3.5 – Mechanical parameters of PVA-SHCC and PE-SHCC under LC2.

Standard deviations are given in parentheses.

	T_{1st} [Nm]	θ_{1st} [°]	T_{max} [Nm]	$\theta_{T,max}$ [°]	F_{max} [kN]	$\theta_{F,max}$ [°]
PVA-SHCC	34.7 (4.0)	0.7 (0.1)	48.5 (4.2)	4.2 (1.0)	3.2 (0.9)	5.7 (1.4)
PE-SHCC	34.4 (2.8)	0.7 (0.0)	67.6 (3.3)	8.8 (3.6)	5.8 (1.3)	10.4 (3.7)

Due to the more pronounced multiple cracking, PE-SHCC yielded more pronounced expansion and an average peak compression force of 5.8 kN, which is 81 % higher than the average value of 3.2 kN for PVA-SHCC. Note that the magnitudes of the compressive forces depend mainly on the extent of multiple cracking, which is clearly indicated by the PE-SHCC curves. At its turn, the extent of multiple cracking exhibits a statistical character and depends on fiber distribution as well as on the content and size of inherent flaws. The pronounced scattering in this respect is typical for SHCC and should be taken into account while formulating design concepts for large-scale implementation.

The compressive force in PVA-SHCC decreased rapidly in the softening phase, while in the case of PE-SHCC, it lessened slowly and even at large rotation angles showed higher values. Note that the rotation angles at maximum torque ($\theta_{T,max}$) were lower than the angles at maximum compression force ($\theta_{F,max}$). In the case of PVA-SHCC, the difference between the rotation angles at maximum torque and at peak axial compression force was 27 %, while in the case of PE-SHCC the difference was only 7 %.

Fig. 3.7 shows the crack analysis for representative PVA-SHCC and PE-SHCC specimens. The average crack angle in the case of PVA-SHCC was 43° and in the PE-SHCC sample it was 44°. It seems that the axial compressive forces were not high enough to keep the crack inclination considerably below that of the purely torsional case, i.e. 45°. The DIC images indicate clearly the different extents of multiple cracking depending on the type of fiber. In the case of PVA-SHCC, the monitored crack showed predominantly CFD I up to peak load, with a gradual decrease in the softening phase. At the same time, CFD II and III continued increasing after failure localization. The monitored strain band actually contained two micro-cracks. By considering the CFDs at peak torque, dividing them by two

cracks and summing them up, the resultant crack opening is approximately $127\ \mu\text{m}$, which is comparable to the resultant CFD in LC1.

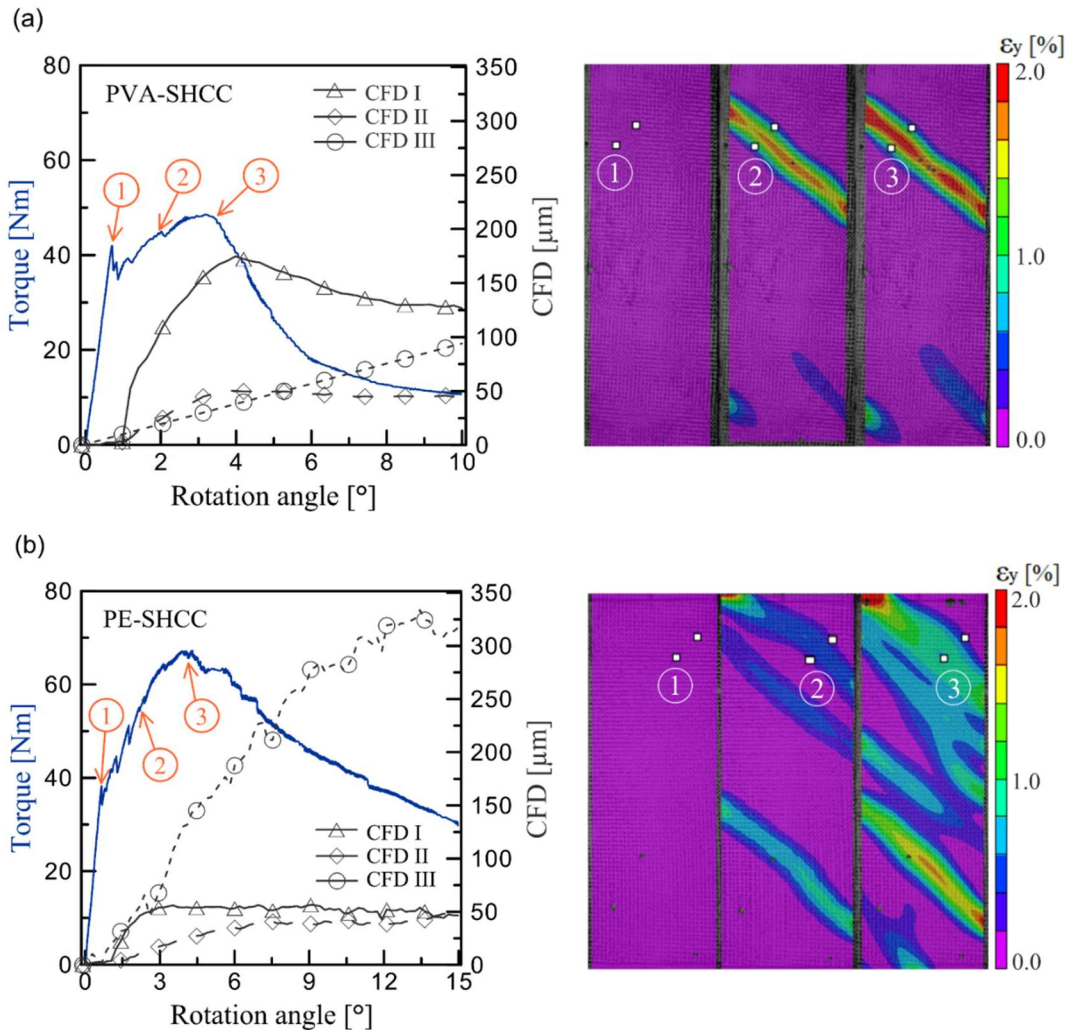


Fig. 3.7 – CFD analysis LC2: (a) PVA-SHCC and (b) PE-SHCC. Note the difference in the horizontal axes (diagrams on the left).

It can be asserted that torsional loading represents an unfavorable case with regard to steady-state cracking, since the diagonal cracks propagate through a longer and more complex path compared to that in uniaxial tension experiments. Moreover, the crack openings are not uniform, and the crack-bridging capacity of the fibers is exhausted stepwise beginning at the corners. PVA-SHCC exhibits a significant drawback in this respect, because its crack-bridging action vanishes completely at relatively small crack openings, see previous works by the authors [40,58,185].

PE-SHCC yielded predominantly CFD III prior to and after peak torque, with CFD I and CFD II showing lower but similar magnitudes along the entire deformation history. The increasing width of the strain band in the DIC images

clearly indicates the subsequent formation of additional micro-cracks. CFD I reaches a plateau at 50 μm prior to peak load, with no reduction during the softening phase. The magnitude of CFD I is comparable to that measured under LC1. Interestingly, the out-of-plane sliding (CFD III) continues increasing, even in the softening phase. Similar phenomena were observed under LC3 and LC4, as presented in the next sections. Moreover, the higher rotations displayed by the specimens of PE-SHCC when compared with PVA-SHCC can be attributed to the more uniform distribution of cracks, and thus, deformation along the gauge portion.

3.4.3. Torsion experiments with free axial deformation (LC3)

LC3 simulates an unconfined shear action. The free axial deformation of the specimens was ensured through a force controlled axial loading under imposed zero force. The behavior of the specimens subjected to LC3 is presented in Fig. 3.8 and the experimental results are summarized in Table 3.6.

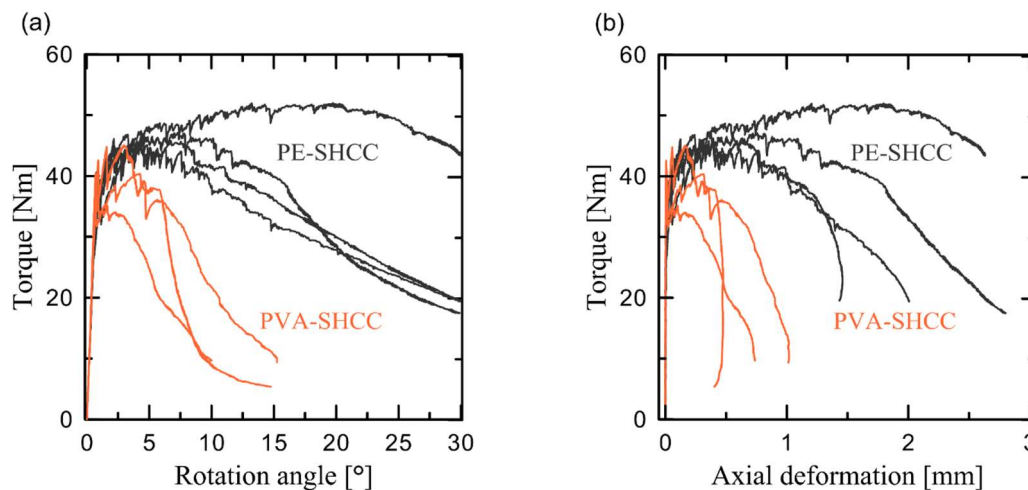


Fig. 3.8 – Mechanical behavior of PVA-SHCC and PE-SHCC under LC3: (a) torque-rotation angle curves; (b) torque-axial expansion curves.

Except for the lower peak torque and less pronounced strain-hardening, the pattern of the torque-rotation angle curves is similar to that observed under LC2. The average values for the torque at first crack formation (T_{1st}) are also very close to those measured under LC2; see Tables 3.5 and 3.6. In the case of PVA-SHCC the maximum torque dropped just slightly from 48.5 Nm under LC2 to 45.0 Nm under LC3. For PE-SHCC the reduction in peak torque was considerably higher: 67.6 Nm for LC2 compared to 47.2 Nm under LC3. The difference can be attributed

to the higher axial confinement of PE-SHCC under LC2 compared to PVA-SHCC. The rotation angles at peak torque showed a considerable drop for both SHCC from 4.2° (LC2) to 0.9° (LC3) in the case of PVA-SHCC and from 8.8° (LC2) to 5.8° (LC3) in the case of PE-SHCC.

Table 3.6 – Mechanical parameters of PVA-SHCC and PE-SHCC under LC3.

Standard deviations are given in parentheses.

	T_{1st} [Nm]	θ_{1st} [°]	T_{max} [Nm]	$\theta_{T,max}$ [°]
PVA-SHCC	40.2 (1.1)	0.7 (0.1)	45.0 (2.9)	0.9 (1.3)
PE-SHCC	36.3 (5.3)	0.7 (0.2)	47.2 (2.6)	5.8 (7.9)

Fig. 3.8b presents the axial expansion of the specimens under LC3. The latter is in good agreement with the derived axial compression forces under LC2 and depends on the degree of multiple-cracking. Furthermore, similar to the axial compressive forces under LC2, the axial expansion in the case of LC3 yields a considerable scattering. Whereas the average axial deformation of PVA-SHCC prior to softening was approximately 0.1 mm, PE-SHCC showed an average deformation at peak torque higher than 0.6 mm. Considering that the multiple cracking was mostly confined in the gauge portion, this elongation is equivalent to approximately 0.6 % strain. The formation of cracks in SHCC is associated both with elastic and plastic deformations in the cracks' domains. The plastic deformations originate from the permanent delamination and partial pullout of the crack-bridging fibers and by the plastic deformation of the fibers themselves, as demonstrated in cyclic tension experiments [197]. Besides the permanent nature of these deformations, the Mode II and III crack openings might have an additional contribution to the resulting axial expansion through the interlock caused by the uneven crack flanks and by the fibers.

Under LC3 the average inclination of the cracks was 44° in the case of PVA-SHCC and 46° in the case of PE-SHCC. Seen in this way, these values are very close to the theoretical inclination of the principal stresses under pure torsion. The DIC evaluations as shown in Fig. 3.9 indicate a dominating CFD III in the case of PVA-SHCC throughout the entire deformation history, with the magnitudes of CFD I and CFD II in the pre-peak phase being considerably smaller. The dominance of CFD III is partly related to the location of the virtual calipers, as discussed above in section 3.3.2. In the same fashion as under LC2, after failure

localization, i.e., in the softening regime, the CFD I decreased while CFD II and III increased. It can be also seen that the crack bands formed at the ends of the gauge portion, this being caused by the stress concentrations in the transition regions of gradual cross-section reduction.

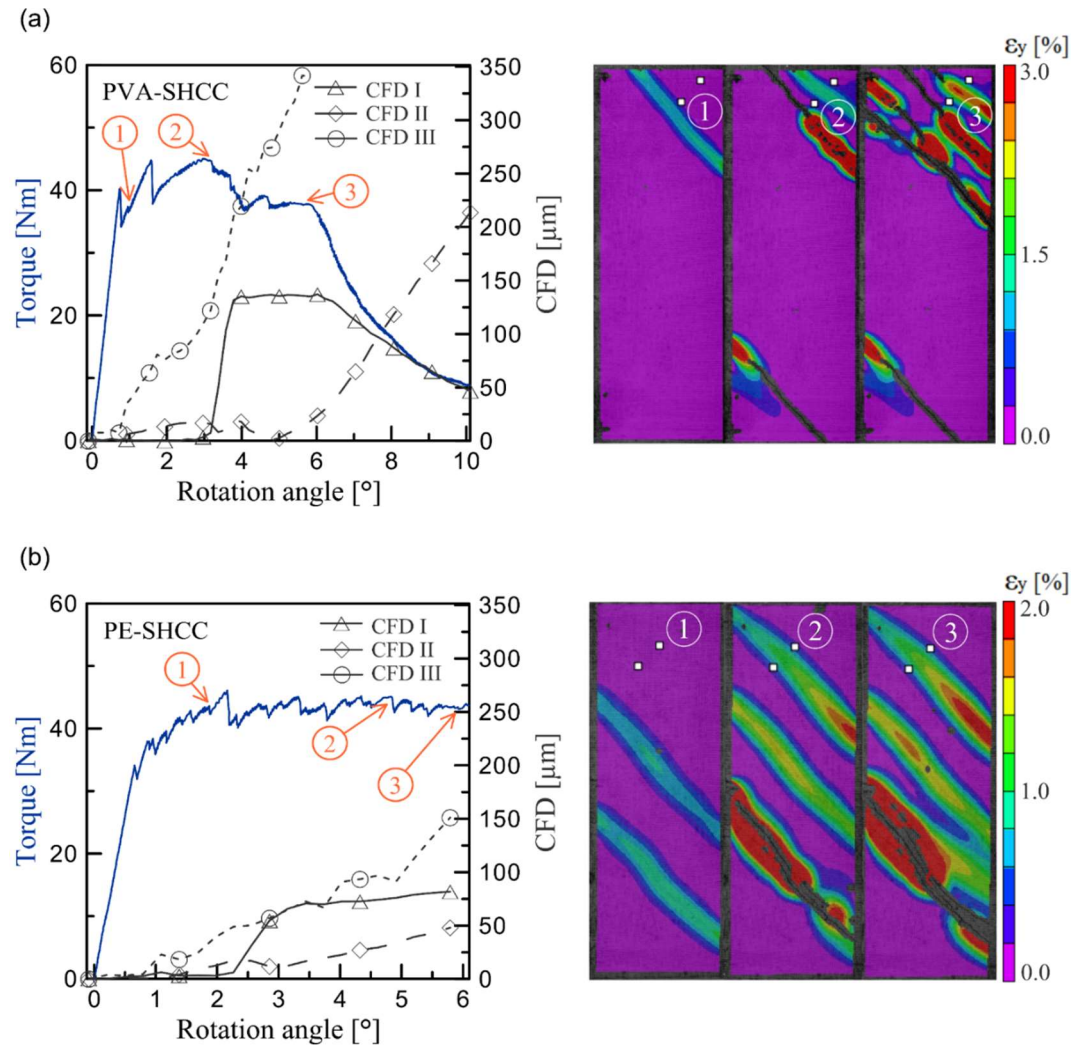


Fig. 3.9 – CFD analysis under LC3: (a) PVA-SHCC; (b) PE-SHCC. Note difference in the horizontal axes (diagrams on the left) and color scales (pictures on the right).

In the case of PE-SHCC the resulting CFD are considerably smaller than those in PVA-SHCC. This might be a feature of the monitored crack and of the position of the virtual caliper. As indicated by the color code in Fig. 3.9b, this crack shows larger deformations closer to the edge. Also, in this case CFD III yielded dominant values, with CFD II and III occurring slightly later and showing lower magnitudes.

3.4.4. Combined torsion and axial tension (LC4)

Analogous to the previous load cases, the mechanical behavior of the specimens tested under LC4 is presented in terms of axial load-deformation and torque-rotation angle in Fig. 3.10. A summary of the corresponding experimental results is given in Table 3.7. The specimens yielded average axial forces at first crack formation of 2.4 kN and 2.8 kN for SHCC made with PVA and PE fibers, respectively. This means a decrease of 32 % and 27 %, respectively, in comparison to the values measured under LC1. Furthermore, PVA-SHCC showed a reduction of 34 % in axial deformation prior to softening and 28 % reduction in peak axial load in terms of average values. PE-SHCC was affected to a lesser extent, exhibiting reductions of 23 % and 12 %, respectively, for these parameters; see Fig. 3.10a.

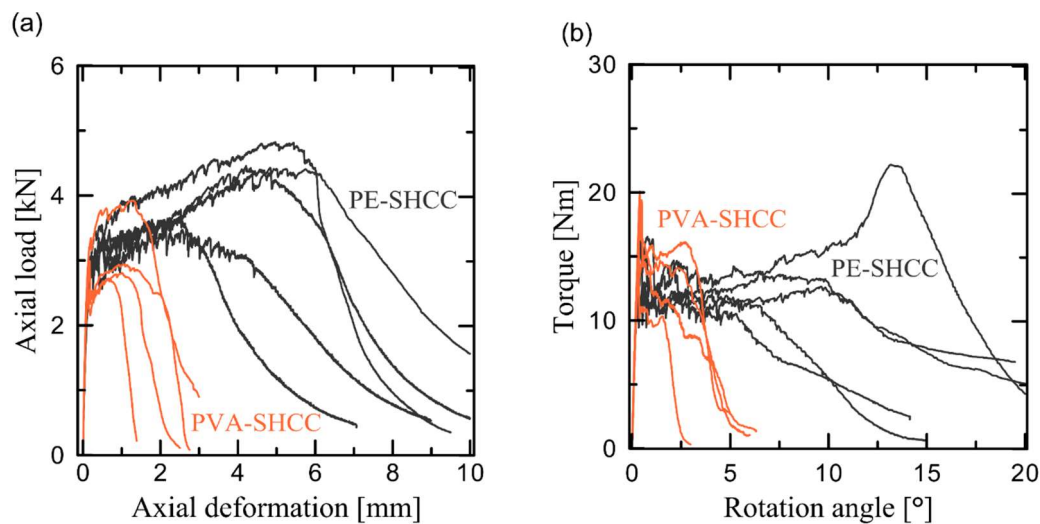


Fig. 3.10 – Behavior of PVA-SHCC and PE-SHCC under LC4: (a) axial load-deformation; (b) torque-rotation curves.

Table 3.7 – Mechanical parameters of PVA-SHCC and PE-SHCC under LC4.

Standard deviations are given parentheses.

	F_{1st} [MPa]	F_{max} [MPa]	T_{1st} [Nm]	θ_{1st} [°]	T_{max} [Nm]	θ_{Tmax} [°]
PVA-SHCC	2.4 (0.4)	2.9 (0.6)	17.6 (2.7)	0.5 (0.1)	12.2 (2.6)	2.4 (0.6)
PE-SHCC	2.8 (0.1)	4.4 (0.6)	13.2 (3.1)	0.3 (0.1)	12.9 (4.4)	10.0 (4.3)

The average maximum torque (prior to softening) was 12.2 Nm for PVA-SHCC and 12.9 Nm for PE-SHCC. The reduction in torsional capacity when compared with LC2 and LC3 was considerably more pronounced than that of the axial force corresponding to LC1. This may possibly be related to the strains in the

axial direction dominating over those in the transversal direction, as defined by the axial displacement rate of 0.05 mm/s and angular rate of 0.1 °/s. Although the CFD analysis provided some evidence in this respect, numerical simulations would be needed for a more reliable estimation of the principal stresses corresponding to the imposed displacement/angular rates.

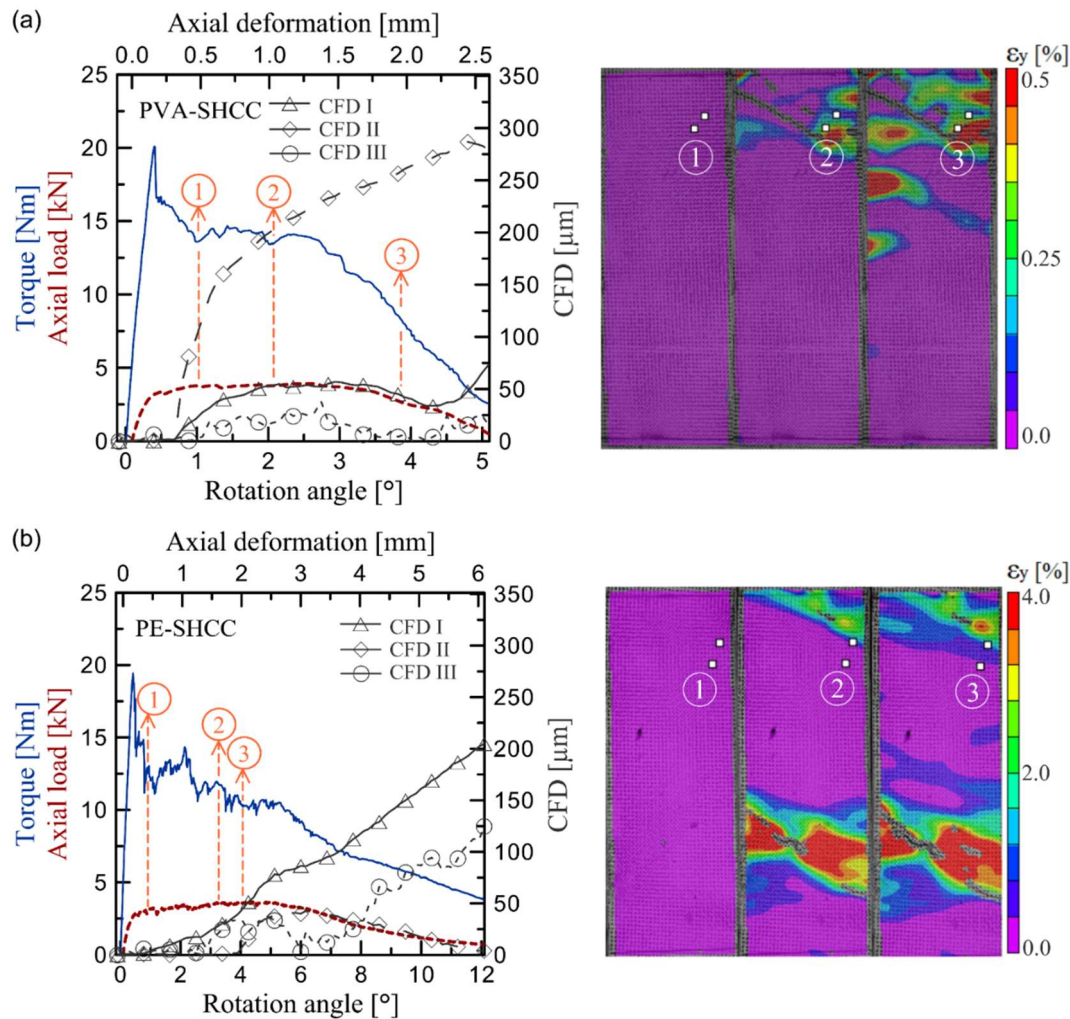


Fig. 3.11 – CFD-analysis of the specimens tested under LC4: (a) PVA-SHCC and (b) PE-SHCC. Note different axes (diagrams on the left) and different color scales (pictures on the right).

The combined loading in LC4 resulted in intermediary values for the average crack angle, i.e. between those obtained for LC1 and LC3. The average crack inclination angles were 33 % for PVA-SHCC and 27 % for PE-SHCC. Similar to the other load cases, PVA-SHCC showed broader scattering among the CFDs of different cracks, while crack localization occurred even more rapidly; see Fig. 3.11. The crack monitored in the case of PVA-SHCC yielded a dominating CFD II with

a value of approximately 200 μm at the initiation of softening. During the softening phase, CFD II continued increasing while CFD I and CFD II showed elastic recovery. In contrast, CFD I was dominant throughout the deformation history of PE-SHCC, whereas CFD III increased only after failure localization.

3.4.5. Concluding comparisons of all load cases

A generalized comparison of the material response under LC1 and LC4 is presented in Fig. 3.12 through the envelopes of the load-deformation curves of PVA-SHCC and PE-SHCC, respectively. The axial tensile strength and ductility decreased for both composites when the loading mode changed from LC1 to LC4. However, PVA-SHCC yielded a considerably more significant reduction, especially in axial deformation.

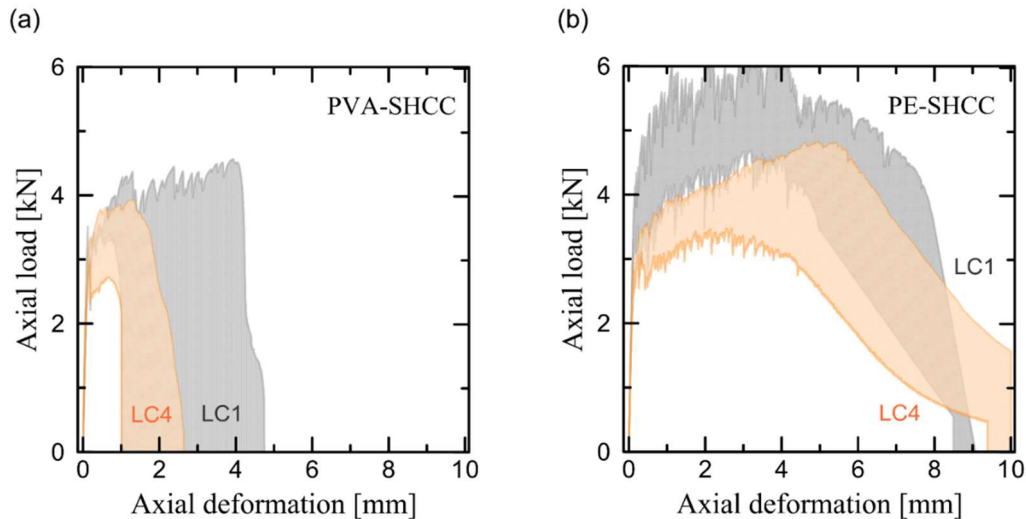


Fig. 3.12 – Envelopes of the axial load-deformation curves under LC1 (uniaxial tension) and LC4 (combined tension and torsion): (a) PVA-SHCC and (b) PE-SHCC.

Fig. 3.13 presents a general overview of the material response under the torsional load cases through the envelopes of the torque-rotation angle curves. Both SHCC compositions yielded the highest load-bearing capacity and deformability up to peak load under LC2, while under LC3 they showed shallower softening branches compared to LC2. Finally, LC4 induced a dramatic reduction in torsional resistance, which can be partly traced back to the axial displacement rate's being higher than the angular one.

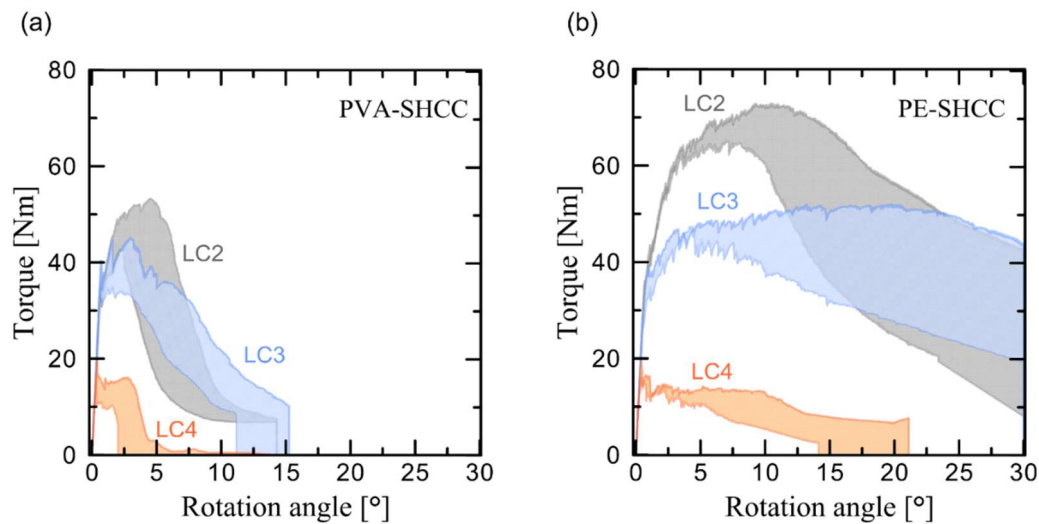


Fig. 3.13 – Influence of load case on the torsional response of (a) PVA-SHCC and (b) PE-SHCC.

Regarding the performance of SHCC under shear, the adopted setup holds large potential, providing not only the shear strength, focus of previous studies [69,70,84], but facilitating the assessment of the effect of combined loading in conjunction with a full-field strain and crack evaluation. With the four loading cases, important data is provided for eventual numerical studies related to SHCC performance. Even though the single-crack response could not be fully assessed due to limitations in the resolution of the available equipment and the pronounced scattering in the opening modes of different cracks, the obtained quantitative and qualitative data on the behavior of SHCC under various loading conditions serves as an extensive quantitative input for calibrating material laws in numerical simulations.

With respect to the fibers under investigation, the experimental results demonstrate that PE-SHCC yield superior mechanical properties compared to PVA-SHCC under all load cases. Whereas the pre-peak crack-bridging behavior of the PE fibers ensures more pronounced multiple cracking compared to PVA-SHCC, the post-peak, i.e., softening, crack-bridging action ensures considerable stress transfer even at large crack openings, which contributes to higher torsional load-bearing capacity and ductility; see Fig. 3.14. At the same time, the slip-hardening behavior of the PVA fibers affects not just the uniaxial tensile properties of PVA-SHCC but leads to a more pronounced reduction in mechanical performance under combined loading conditions.

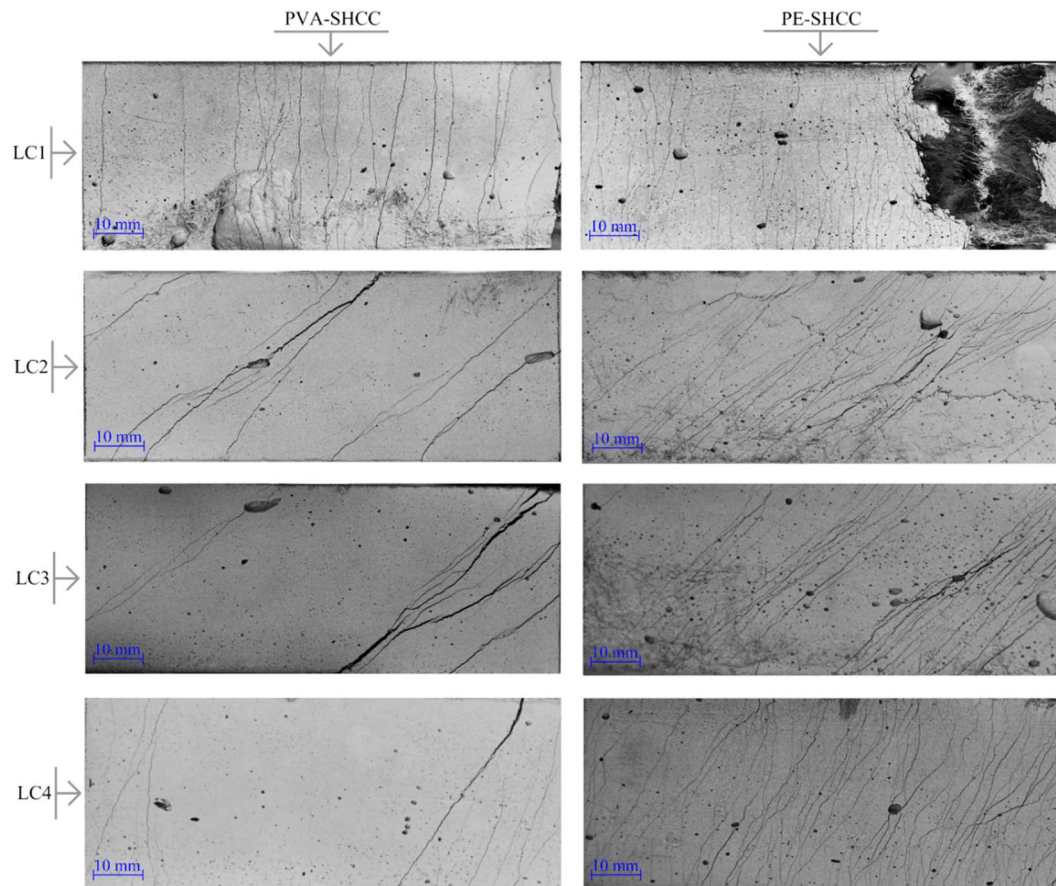


Fig. 3.14 – Multiple cracking patterns of representative specimens in each load case.

It is noteworthy that besides the different surface properties of the fibers and the resulting fiber-matrix interactions, the different aspect ratios of the fibers used play as well a decisive role in the performance of the SHCC under investigation. However, given the strong fiber-matrix interaction in the case of PVA, a reduction in their diameter, e.g., to that of PE fibers, would result in an even higher degree of fiber rupture, leveling out any advantage in terms of aspect ratio. In the same course of argumentation, use of PE fibers with larger diameter (close or equal to that of PVA fibers) would not facilitate the exploitation of their high tensile strength in the normal-strength matrix, but rather have an adverse effect on the mechanical performance of SHCC.

3.5. Conclusions

This chapter presents the results of an extensive experimental study on the mechanical behavior of two types of normal-strength SHCC under four different load cases: uniaxial tension, torsion with blocked axial deformation, torsion with

free axial deformation and combined tension-torsion. The difference in the analyzed SHCC consisted in the reinforcing fibers, which were made of PVA and UHMWPE, respectively.

It was shown that the SHCC made with UHMWPE fibers (PE-SHCC) demonstrated superior behavior under all load cases compared to the SHCC made with PVA fibers (PVA-SHCC). This was traced back to the superior pre-peak and post-peak crack-bridging behavior of the UHMWPE fibers and by their smaller diameter. The characteristic slip-hardening pullout behavior of PVA fibers in cementitious matrices resulted in fiber rupture at small crack openings and inferior multiple cracking of PVA-SHCC under uniaxial tensile loading.

Both types of SHCC yielded substantial axial expansion under torsion, the expansion being proportional to the degree of multiple cracking. The axial confinement of the specimens subject to torsion resulted in a higher torsional load bearing capacity, but also in a more abrupt softening phase in comparison to the specimens subject to torsion but with free axial deformation. Finally, the combined tension-torsional loading led to a dramatic reduction in torsional strength and deformability of both SHCC. However, the latter was partly attributed to the applied axial displacement rate, which seemed to dominate the angular rate.

The cracking process and the crack-flank kinematics in SHCC under various loading conditions were monitored with the help of a stereo camera system and quantitatively analyzed by means of DIC. Despite the detailed information on crack-flank displacements, the pronounced variation of the latter among various cracks in individual specimens did not allow quantification of the shear-transfer capacity in dependence on crack opening mode and magnitude. It may be assumed that the involvement of shorter samples and the purposeful integration of inclined notches would enable a restriction of the crack formation to the notched region and a more detailed crack analysis. This will facilitate the derivation of analytical constitutive models at the single-crack level and will be a matter of interest in future studies.

Ongoing studies involving the SHCC presented in this article include uniaxial tensile tests under impact loading, the investigation of the influence of the inclination angle on the fiber pullout mechanisms under quasi-static and impact loading regimes, and the application of SHCC as shear-strengthening layers on

structural elements subjected to impact. The experiments at the structural scale are complemented by numerical simulations using Finite Element Methods, in which the results presented in the chapter at hand serve as experimental basis for the calibration of the constitutive laws for SHCC.

3.6. Overview

The present study represents a strong indication of both assessed materials under shear stress fields. Although could be noticed a superior performance of the SHCC made with PE fibers at the material level, it was considered that the composite fabricated with PVA fibers still displayed a reasonable performance for structural applications. Moreover, the available state of the art indicated a more significant improvement of strain capacity for PVA-SHCC under high dynamic strain rates under direct tension. Thus, in addition to the SHCC made with PE fibers, it was decided to follow also with the one made with PVA fibers on the structural level evaluation, aiming the performance assessment of both composites as strengthening layers of members with critical shear under impact scenarios.

4 Effect of shear reinforcement and external strengthening with strain-hardening cement-based composites (SHCC) on the impact resistance of reinforced concrete beams

4.1. Introduction

Since the 1980's there is an increasing interest in the effects of the strain rate on the strength and fracture of reinforced concrete structures [104,136]. Reinforced Concrete (RC) has been widely used for almost two centuries due to its relatively low cost-benefit ratio when compared with other structural systems. Although most of the existing RC-structures were designed foreseeing mainly static scenarios, with eventual loads considering the human activity, or normal natural actions such as the wind, it has become clear the high probability that during service life these structures can also be subjected to other variations of dynamic loading such as earthquakes, blasts, or impact [124,142,160,198]. This prospect is worrisome because during these events structural stability requires large amounts of energy dissipation in a short period of time, which is constrained by concrete's intrinsic brittleness [104,132,136].

In respect of dynamic loading, the Model Code 2010 [120,121] implies a dynamic enhancement of material strength for both concrete and steel under compression and tension. At the same time, research studies report that quasi-brittle materials such as concrete display a tendency of change from failure mode I to mixed mode with the increase in loading rate [122–124], with normal-strength concrete being more rate-sensitive than high-strength ones [127–130]. At the structural level, additional energy-dissipation mechanisms arise, with the inertia forces most significantly inciting changes in the global behavior of the structural member [161]. The inertia effect disturbs the deflected shape of the RC-member subjected to impact loading, deviating it from its static configuration [132]. These attributes generally result in the change of failure from flexural to shear when shifting from quasi-static to dynamic loading, which offsets the positive effects related to structural inertia and material rate sensitivity [122,123,131,142,199–201].

Additionally, the occurrence of damage mechanisms as scabbing and spalling represents another concern from a safety perspective [120,121].

It was demonstrated that the inelastic deformational capacity of RC elements under dynamic loading could be improved with discrete fibers [124,127–130,132,159–162]. When shifting from quasi-static loading ($\dot{\epsilon} \approx 10^{-6}$) to impact loading ($\dot{\epsilon} \approx 10^0$; impactor velocity of 1.4 m/s) Fiber Reinforced Composite (FRC) beams yielded a decrease in the nonlinearity of the load-deflection curves [129,159] and the peak load and bending-energy increased from 20 to 100 times when compared with plain concrete [161]. However, nowadays the complete replacement of normal concrete for FRC in all new structures would be economically unfeasible [15,104]. Moreover, sustainability requires the rehabilitation of existing structures, with the development of cost-effective repair methods to extend their life [202]. Therefore, an effective solution of the mechanical features can be exploited to improve the resilience of RC structures to dynamic loading events by external strengthening.

Strain-Hardening Cement-based Composites (SHCC) are a special class of FRC that exhibit a high energy absorption capacity in tension, compression, and shear [18]. These composites are reinforced with high-performance polymer micro-fibers typically in volume fractions of 2%. SHCC may reach tensile strain up to 5% prior to failure localization due to the formation of multiple cracks not exceeding 100 μm in width [14,203]. SHCC are also highly suitable for applications as external strengthening layers by spraying or lamination, as enabled by their fresh-state properties [15]. Moreover, given their cementitious basis, SHCC exhibit a high physical and mechanical compatibility with concrete substrates, including the bond [17]. At last, although the cost of SHCC are about 2-3 times that of normal concrete (mainly ruled by the cost of the fibers), it is still far below the cost of the most commonly marketed repair materials [87].

This chapter presents the first part of the analysis of an experimental campaign designed to examine the influence of SHCC as transversal strengthening layers on the impact resistance and fracture behavior of RC beams. Higher levels of impact energies than the ones commonly reported in the literature were studied, with the impactor velocity ranging from 17 m/s to 30 m/s. Two RC beam configurations were adopted as reference cases: (1) beams with longitudinal and stirrup reinforcement (span-to-depth ratio of 2.3); (2) beams with longitudinal

reinforcement only. Both configurations implied a constant longitudinal reinforcement ratio of 0.72%. Two variations of normal-strength SHCC were analyzed as strengthening layers, one reinforced with polyvinyl alcohol (PVA) fibers, and the second with ultra-high molecular weight polyethylene (UHMWPE), shortly referred to as PE. The SHCC strengthening layers were applied manually by lamination on the lateral faces of the beams, in this way implying a shear strengthening.

4.2. Experimental program

4.2.1. Materials

The concrete of the RC beams consisted of ordinary Portland cement type III/A (42.5 N) and fly ash as binders, with water-to-binder ratio (w/b) of 0.35 and maximum aggregate size of 8 mm. The mix proportions by weight are given in Table 4.1. Concrete production and casting were done in a concrete plant. The compressive strength of the concrete was tested on 24 cubic specimens with a corner-size of 150 mm. The mean value of compressive strength was 49.5 MPa at 28 days and 50.9 MPa at 42 days, the latter being the average testing age of the RC beams. The internal reinforcement consisted of steel ribbed bars B500S ($f_y \approx 500$ MPa).

Table 4.1 – Mixture design of the ordinary concrete.

Component	Cement	Fly ash	Coarse aggregate	Fine aggregate	Water	Superplasticizer
Quantity	380	60	762	932	188	2.85

Following previous investigations on the shear and multi-axial mechanical properties of SHCC at the material level [18], two types of SHCC were investigated as shear strengthening layers in this study. The mixture compositions of the SHCCs used in this program were already addressed by the authors in previous works [10,64,204,205]. Both SHCCs held a fiber content of 2% by volume and an identical, normal-strength cementitious matrix ($f_{ck} \approx 42$ MPa), differing only in the type of dispersed fiber; see Table 4.2. One was reinforced with PVA fibers Kuralon REC15 (by Kuraray, Japan), and the other with PE fibers Dyneema SK62 (by DSM, the Netherlands). The composites were designated according to the reinforcing

fibers, i.e. PVA-SHCC and PE-SHCC, respectively. The geometric and mechanical properties of the used fibers are presented in Table 4.3.

Table 4.2 – Mixture compositions of the SHCC under investigation.

	PVA-SHCC	PE-SHCC
	[kg/m ³]	[kg/m ³]
Portland cement CEM I 42.5 R-HS	505	505
Fly ash Steamment H4	621	621
Quartz sand 60 – 200 µm	536	536
Water	338	333
Superplasticizer BASF Glenium ACE 30	10	25
Viscosity modifying agent	4.8	4.8
PVA fiber 2% by volume	26	–
UHMWPE fiber 2% by volume	–	20

Table 4.3 – Geometric and mechanical properties of PVA and PE fibers according to producers [187,206].

Fiber		PVA	PE
Nominal diameter	[µm]	40	20
Length	[mm]	12	12
Density	[g/cm ³]	1.26	0.97
Tensile strength	[MPa]	1600	2500
Young's modulus	[GPa]	40	80
Elongation at break	[%]	6.0	3.5

This rather typical normal-strength matrix was initially developed targeting a proper crack-bridging behavior of PVA fibers, which, despite their oil coating, yield a strong chemical bond with cementitious matrices due to their inherent hydrophilic properties [189–191]. The cementitious matrix was purposely designed in terms of strength and packing density to ensure an adequate (limited) fiber-matrix bond strength, thus, mitigating the occurrence of fiber rupture [10]. Meanwhile, PE fibers are hydrophobic, hence only frictionally/mechanically anchored in the matrix [193]. However, they have a twice smaller diameter, which ensures an even higher collective embedment surface and an adequate crack-bridging strength. A slightly higher dosage of superplasticizer as well as a higher mixing energy and duration were provided to PE-SHCC compared to PVA-SHCC in order to compensate for

the high aspect ratio of the PE fibers [10]. The studied SHCC with PVA and PE fibers presented an average strain capacity of 1.0% and 2.5% respectively; see Fig. 4.1.

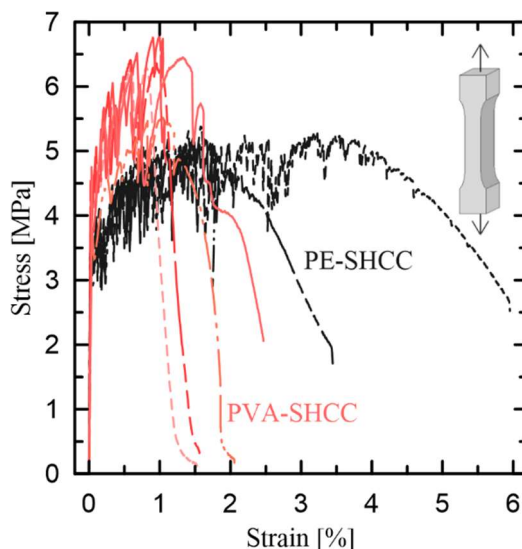


Fig. 4.1 – Representative tensile stress-strain curves of the studied SHCC tested under monotonic strain rates at 28 days.

4.2.2. RC beams production and strengthening

Although the casting of the 24 RC beams occurred in two events, one-week apart due to logistical considerations, each batch of specimens was subjected to the same protocol. The wood molds were previously internally dressed with the retarder paper WB-Paper type “grey” (by HEBAU, Germany) to optimize the process of preparation of the beams’ surfaces for strengthening. The casting was executed in layers and the densification was enabled by an electro-mechanical vibrator with 1" shaft. After casting, the upper side of the specimens was watered and sealed with a waterproof tarp fabric for 24 hours. At that time the wood molds were disassembled, and the beams were washed out with a high-pressure waterjet to expose the aggregates (Fig. 4.2a). Thereafter the RC specimens were simply stored in the laboratory environment until 24 hours before strengthening, during which the surfaces of the beams to be strengthened were continuously regularly sprayed with water.

From the 24 RC beams, 8 represented reference configurations and 16 were strengthened with SHCC when the RC beams had an average age of 21 days. The strengthening layers were applied on the surfaces parallel to the impactor’s trajectory (side surfaces), due to the expectation of critical shear failure under

impact strain rates (Fig. 2.22). Moreover, it was chosen because the first three-year term of the GRK 2250 (see Section 2.1), already addressed the strengthening on the front and rear surfaces, such as [207]. The 20 mm-thick reinforcement layer was casted-in, in a way that the strengthening of each specimen entailed the following steps: (1) Horizontally positioning of the beam; (2) Fixation of the wood forms used as the reinforcement thickness template (20 mm), while also preventing the SHCC leakage (Fig. 4.2b); (3) Casting of a volume of SHCC, enough to form the first layer with approximately 10 mm thickness; (4) Combing of the fibers in the transversal direction with a plastering trowel; (5) Casting of the second and final layer of SHCC, overflowing the wood frame (Fig. 4.2c); (6) Combing of the fibers in the longitudinal direction with a plastering trowel. (Fig. 4.2d); (7) Correction of the SHCC thickness with the cross-sectional passage of a finishing trowel throughout the length of the specimen; (8) 24 hours curing with watered plastic cover; (9) Removal of the wood frames, and backward positioning for the strengthening of the opposite surface. Although the strengthening layers were horizontally applied in the lab environment for logistic reasons, this technique was adopted due to the supposedly possibility to be fairly replicated in industrial applications through SHCC spraying (ensuring the proper rheology properties) associated with the passage of a plastering trowel, thus providing a reasonable alignment of the fibers.

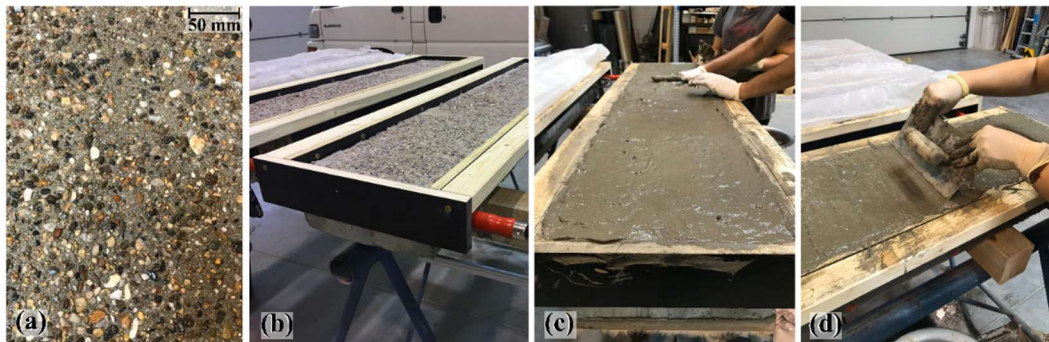


Fig. 4.2 – Casting procedures of the strengthening with SHCC: (a) Substrate preparation by washing the superficial cement-paste layer; (b) Fixation of the wood templates; (c) Molding process; (d) Surface correction.

Twenty-four hours after applying the final strengthening layers, the beams were stored outside the laboratory for 28 days under mild environmental conditions (average environmental temperature 16° C and humidity 65 %), protected with a waterproof tarp fabric. The specimens were returned to the laboratory 72 hours prior

to testing to dry, facilitating the surfaces painting for Digital Image Correlation (DIC) and fixation of sensors.

4.2.3. Specimens' details and setup

All the beams had a rectangular cross-section of 130 mm in width and 280 mm in depth, and a total length of 1450 mm; see Fig. 4.3. The span length was 1250 mm, and the shear-span ratio was 2.3. All the specimens were longitudinally reinforced with $\varnothing 8$ mm ribbed steel bars, with a constant upper and lower reinforcement of two and three rebars, respectively. Plastic spacers were used to ensure a constant concrete cover thickness of 10 mm for all beams. Two variations of shear reinforcement were assessed in the RC beams: with $\varnothing 8$ mm stirrups spaced at a distance of 150 mm, and without any type of transversal reinforcement. The design parameters of these two variations of the RC beams are listed in Table 4.4. The RC beams were labeled "Ce" and "Se" in reference to the presence or absence of stirrups, respectively.

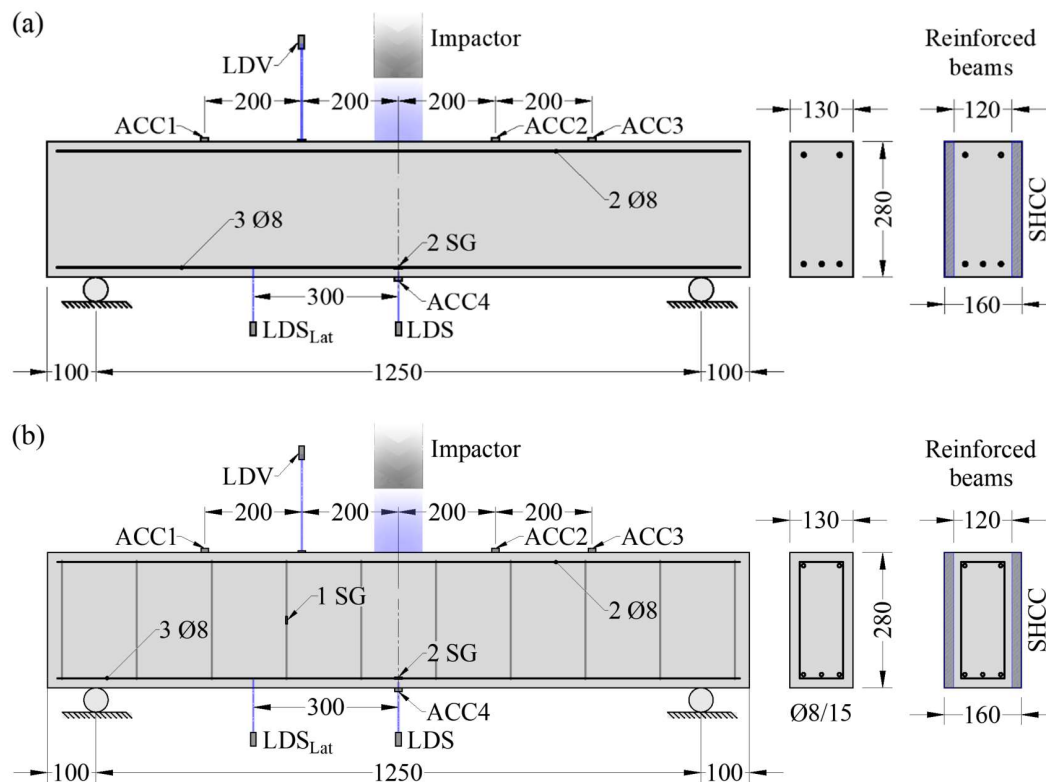


Fig. 4.3 – Geometry of the RC beams, layout of the steel reinforcement and location of the embodied instrumentation: (a) Beams without stirrups (Se); (b) Beams with stirrups (Ce). Dimensions in mm.

In this work only impact experiments were performed. The static flexural and shear resistances were calculated according to the Model Code 2010 [121]. As indicated in Table 4.4, all the specimens should have displayed a flexural failure in case of static loading. Analogous to other publications from IE (intended publication) that did not include static tests, these values are not reduced by safety values, thus giving an estimation for the ultimate strength of the specimens.

Table 4.4 – Static design values.

	Se	Ce
Longitudinal reinf. ratio [%]	0.72	0.72
Shear reinf. ratio [%]	0.00	0.53
Flexural resistance [kN]	48.2	48.2
Shear resistance [kN]	70.9	181.1
Shear to bending resistance ratio	1.5	3.8
Expected failure mode	Bending	Bending

The beams were simply supported and additionally braced at the ends to the supports; see Fig. 4.4. The braces did not affect the static system and allowed beam rotation. A rubber pad was used in the contact with the specimens' surface for clamping, helping to counterbalance the rebound effect. The impact load was applied vertically in the mid-span of the top surface of the beams by discharging of a flat-nose steel projectile with weight of 14.2 kg. The projectile was 250 mm long and 100 mm in diameter. Aside from the free-falling height of 10 m, the projectile speed was charged by an air-pressure system, with pressures varying from 0.2 to 1.2 bar, resulting in impact velocities in the range between 17.7 m/s and 29.9 m/s.

An overview of the entire program is presented in Fig. 4.5, including the specimens' designated nomenclature. In follow, the designation "Ref" was used for the reference beams, i.e. specimens without external strengthening. Comparably, "PVA" and "PE" indicate the beams laterally reinforced with SHCC made with the named fibers. Finally, the ending number refers to the charging gas pressure of the impactor. The last column refers to the number of tests effectively performed in each specimen. Generally the test consisted of a single impact, aside an intermediary series, where the impact loading was repeated until the complete depletion of load bearing capacity of the beam; this was done to assess the residual strength of the specimens reinforced with the SHCC layers.

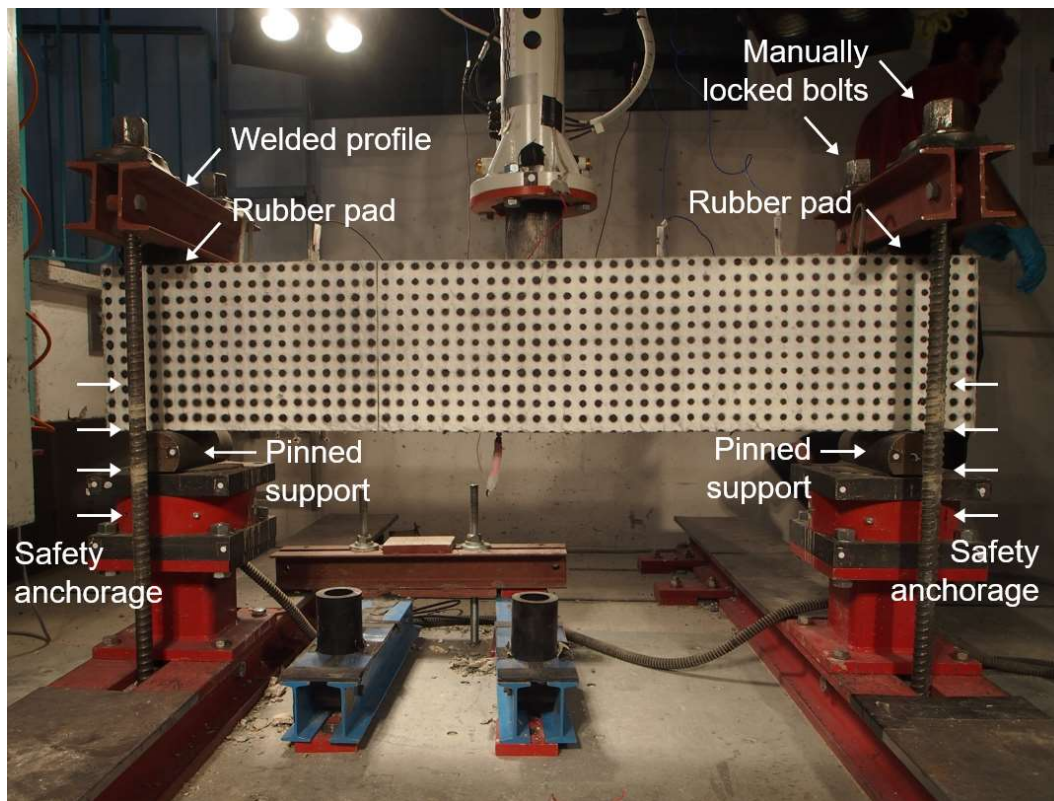


Fig. 4.4 – Testing setup's boundary conditions.



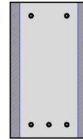
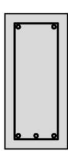
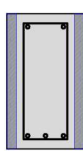
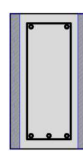
<p>(a) Se-Ref</p>  <p>0.2 bar – 1 impact 0.4 bar – 1 impact 0.8 bar – 1 impact 1.2 bar – 1 impact</p>	<p>(b) Se-PVA</p>  <p>0.4 bar – 1 impact 0.8 bar – 1 impact 0.8 bar – 2 impacts 1.2 bar – 1 impact</p>	<p>(c) Se-PE</p>  <p>0.4 bar – 1 impact 0.8 bar – 1 impact 0.8 bar – 2 impact 1.2 bar – 1 impact</p>
<p>(d) Ce-Ref</p>  <p>0.2 bar – 1 impact 0.4 bar – 1 impact 0.8 bar – 1 impact 1.2 bar – 1 impact</p>	<p>(e) Ce-PVA</p>  <p>0.4 bar – 1 impact 0.8 bar – 1 impact 0.8 bar – 2 impacts 1.2 bar – 1 impact</p>	<p>(f) Ce-PE</p>  <p>0.4 bar – 1 impact 0.8 bar – 1 impact 0.8 bar – 3 impacts 1.2 bar – 1 impact</p>

Fig. 4.5 – Configurations of the specimens, charging gas pressures and number of impacts.

The drop tower used for the investigations, in pressurized air-accelerated mode, is part of the Otto Mohr Laboratory [208]. It consisted of an aged three-story building to enclose the impact testing apparatus in the center of the plant; see Fig. 4.6. Aside from the test frame and other customary testing gadgets, the main feature of this testing setup is the moving base-platform, a slab with 110 cm thickness, seating in a foundation built with a reinforced base-spring system completely disconnected from the perimeter elements, ensuring improved absorption of the

momentum arising from the tests. Besides providing the test-energy secure dissipation, the moving test floor eased the beams positioning in the test frame.

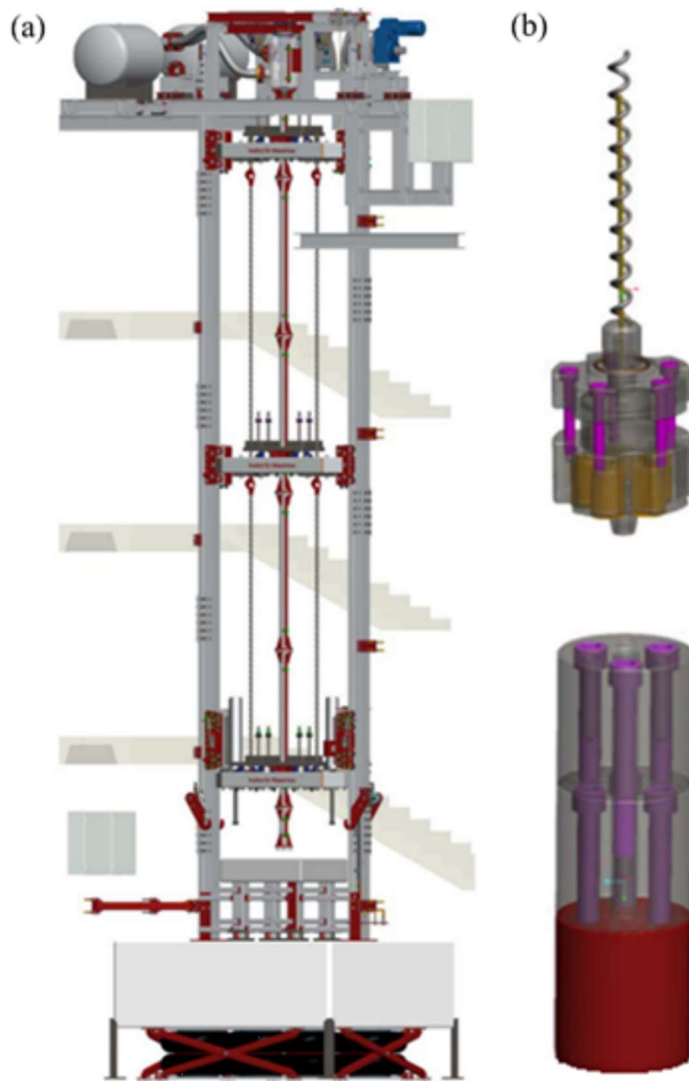


Fig. 4.6 – Accelerated configuration of the impact system [115]: (a) Schematic sketch of the testing facility; (b) Detailed image of the projectile including the retraction device.

The specimens were instrumented to capture the vertical displacements and accelerations of the beams, as well as the deformations on the internal steel rebars. The specimens' layout and instrumentation positioning are shown in Fig. 4.3. The specimens' deflections in the middle span and 300 mm to the left side were contactless obtained employing Laser Displacement Sensors (LDS and LDS_{Lat}) LAM-F-200 with a cut-off frequency of 100 kHz (by WayCon, Germany) and an overall measuring length of approximately 200 mm. In order to quantify the

dynamic response of the beams, four acceleration sensors PCB-M350C04 (by PCB Piezotronics, USA) were used, three of which were placed on the impact front-surface (ACC1, ACC2, and ACC3) and one at the rear-surface (ACC4). These sensors had a measuring range of ± 5000 G. Furthermore, two semi-conductor strain gauges (SG) SB-500-3-P-3 with a working strain of $600 \mu\epsilon$ (by BCM Sensor Technologies, Belgium) were applied to record the strains in the mid-span of the longitudinal rebars located at the bottom of the specimens. An additional strain gauge was used to assess the strains on the stirrups. A Laser Doppler Vibrometer (LDV) Nova-Speed-DF with a cut-off frequency of 2.5 MHz (by OptoMET, Germany) was used to detect the particle speed next to the point of impact.

Aside the instrumentation embodied in the specimen, the system enfolded two load-cells in the supports with bearing-capacity of 10 MN, two light barriers located 380 mm apart at the end of the acceleration tube to capture the impactor speed (see next section), and a high-speed camera FASTCAM SA5 (by Photron, Japan) used to monitor the displacements field and crack patterns in one of the lateral surfaces through DIC. Additional images from the opposite side-surface were captured with a digital camera of 12 megapixels at the end of each test, for optical evaluation of the cracking patterns. The LDSs, vibrometer, accelerometers, and bearing loads were collected at a sampling rate of 200 kHz, while the sampling rate of the FASTCAM and strain gauge data was 10 kHz.

4.2.4. Methodology for indirect parameters estimation

Different from parallel research studies, due to the magnitude of the speed of the impactor, the utilization of a load cell in the impact front-surface (see Fig. 2.22) would be unfeasible. Based on preliminary tests the impact load was indirectly computed through the estimation of the impulse, which in turn was determined by the measured velocity of the impactor [115,209]. As aforementioned, the impactor velocity (v_{imp}) was calculated based on the time (Δt) needed by the impactor to cover the distance between the two light barriers positioned at the end of the acceleration tube (d_{lb}): $v_{imp} = d_{lb}/\Delta t$ (Eq. 7).

Considering negligible the energy lost between the time that the impactor exits the acceleration tube and strikes the specimen, it can be considered that the impulse generated by the impactor (I_{imp}) is entirely sourced by its momentum

change: $I_{imp} = m_{imp} \cdot v_{imp}$ (Eq. 8), where m_{imp} is the mass of the impactor and v_{imp} is the velocity of the impactor immediately before striking the beam surface.

The loading function was assumedly described as a trapezoidal wave, considering each time-span corresponding to one-third of the total period of transfer of the impact energy (Fig. 4.7). This simplification of the maximum applied load (P_{max}) represented as a plateau facilitates future numerical simulations [209]. The time between t_0 and t_3 can be forwardly obtained using the contact time $t_{contact} = L_{imp}/c_{imp}$ [210], where L_{imp} is the impactor's length and c_{imp} is the wave propagation velocity in steel [207]. Thereby, the impulse transferred to the specimen could be formulated as:

$$I_{beam} = \left[(t_1 - t_0) \cdot \frac{1}{2} + (t_2 - t_1) + (t_3 - t_2) \cdot \frac{1}{2} \right] \cdot P_{max} \quad (\text{Eq. 9})$$

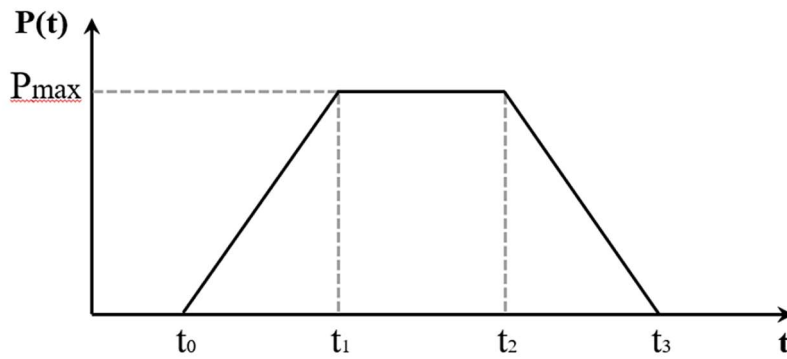


Fig. 4.7 – Assumed shape of the loading pulse.

Finally, for the determination of the maximum applied load, it was assumed that the entire impulse was transferred from the impactor to the specimen ($I_{imp} = I_{beam}$). Thus, the impact load is directly obtained:

$$P_{max} = \frac{m_{imp} \cdot v_{imp}}{\left[(t_1 - t_0) \cdot \frac{1}{2} + (t_2 - t_1) + (t_3 - t_2) \cdot \frac{1}{2} \right]} \quad (\text{Eq. 10})$$

4.3. Results and discussion

Fig. 4.8 shows the relation between the acceleration pressure and the velocity of the impactor shortly before striking the beam. An almost linear relation between the increments of pressure and the impactor speed was observed. It is noticeable the good agreement between the measurements throughout the experimental program,

signaling a robust response of the system and providing a low deviation of values of impulse and thus, impact load (P_{\max}).

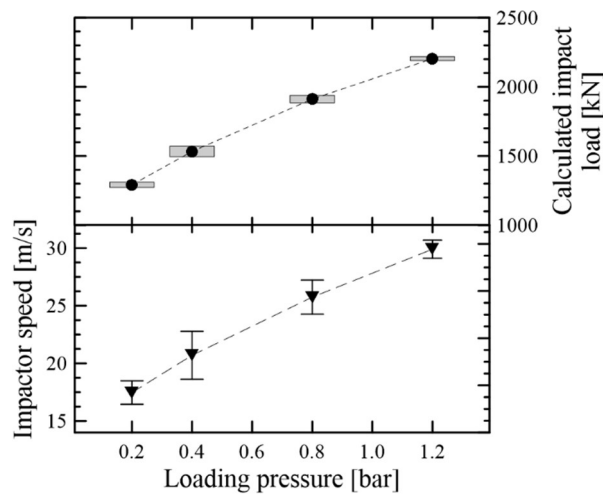


Fig. 4.8 – Impactor velocity and calculated impact load obtained for each loading pressure.

The impulse of the impactor and the associated impact load were determined through the routine described in 4.2.4 considering the contact time of 0.0417 ms. A summary of these results and the ones presented in the following sections is related in Table 4.5. Additional information is available on the appendixes at the end of this thesis.

4.3.1. Non-strengthened beams

The time histories of the reaction forces measured by the load cells and the displacements obtained through the LDV during the experiment are shown in Fig. 4.9 within a range of 15 ms. The maximum values of these forces are summarized in Table 4.5. The curves describe the overlapped behavior of the response-waves obtained from the supports. Almost all the curves tended to display a sinusoidal wave with a rapid, almost linear increase in the initial ascending branch, followed by a multi-peaked unloading branch with residual beam oscillations after unloading. The exception was the specimen Ce-Ref-0.8 which damping behavior was quite divergent from its peers, thus, considered undependable and not represented. Typically for high loading rates [160], it was observed a delay to the stress wave to propagate from the impact point to the supports, corresponding to an average travel time of about 2.1 ms. After the first peak, the reaction forces took around 6.1 ms to be counterbalanced.

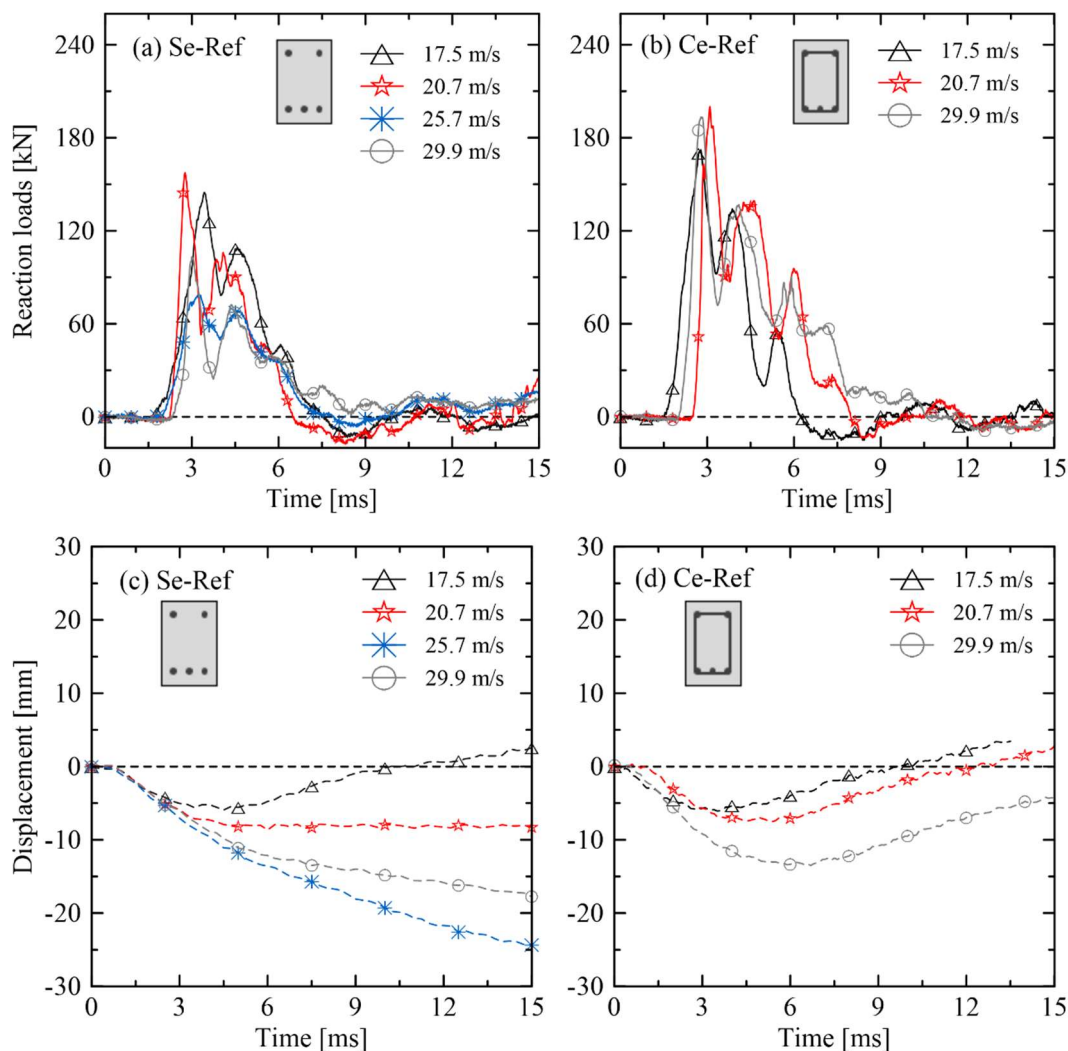


Fig. 4.9 – Time histories of the summed reaction forces measured by the load cells and the displacements obtained through the LDV during the experiments of the non-strengthened beams.

Analogously to lower impact velocities [141,142], the RC-beams displayed an increase in the maximum bearing load with the increase of the average impact velocity from 17.5 m/s to 20.7 m/s. The specimens without transversal reinforcement showed considerably lower peak loads compared to those with stirrups; see Fig. 4.9a. Besides, a new enhancement was observed for an even higher average impact velocity (29.9 m/s). This last behavior entailed a drop of only 34.3% and 3.4% with the average increment of the speed of the impactor from 20.7 m/s to 29.7 m/s, raising doubts against the previously related reduction of bearing-strength, and anomalous performance from the RC-beams tested under 25.7 m/s. Indeed, the referred specimens held a slightly distinct preparation process; due to logistics during the casting, these beams also were molded with the retarder paper

(see Fig. 4.13c and 4.13g), causing the weakening of the cement paste cover, which probably jeopardized the coarse aggregates' confinement, and thus the interlock process. Regardless of this discrepant response of the specimens tested under an impactor velocity of 25.7 m/s, the observed decline of the bearing loads at 29.7 m/s appears to indicate the real behavior of the specimens. This performance contrasts with the available literature, considering lower loading rates, where a direct relation between the loading rate and the bearing loads could be observed (1 – 6 m/s) [141,142]. This behavior seems to be related to the depletion of deformation, hence, the strength of the specimen, after it fails, completely loses its load-bearing capacity.

The displacements were measured with two LDS positioned on the bottom of the beams, by optical measurements of one of the lateral surfaces, and by an LDV positioned on the top surface. The last was positioned orthogonally to the specimens' superior face, around 15 cm from the edge of the impactor, thereby, its signal was correspondent to the frequency of the specimen, allowing the deformation sourcing [211]. The redundancy on monitoring by different instruments was a prudential approach with the intent to diminish the eventuality of data-loss during acquisition and was used for relative validation of the results.

The MatLab's Signal Analyzer toolbox (by MathWorks, USA) was used to sample and filter the data and evaluate the best fit to represent the results with minimum information loss. A quadratic regression with a smoothing factor of 0.2 was used in all analyses. This protocol was chosen because it could assure a sound fit without detracting from the primary shape of the original signal. In contrast, the measurements derived from the LDV were relatively free of noise, although slightly smaller in magnitude than the values obtained through DIC; see the supplementary Fig. 4.10. Moreover, except for the specimen Se-Ref-1.2, which displayed an elevated level of damage, it was observed that the displacement-time curves related to the LDS positioned in the bottom mid-span of the beams were similar to the ones provided by LDV, being also in the same order of magnitude of the values obtained through DIC. Therefore, the LDV displacements were used on the following evaluations. Their time histories are displayed in Fig. 4.9. The observed beam response is probably related to the visible small bending displacements in almost all specimens, despite the substantial damage, with emphasis on the ones externally reinforced with SHCC.

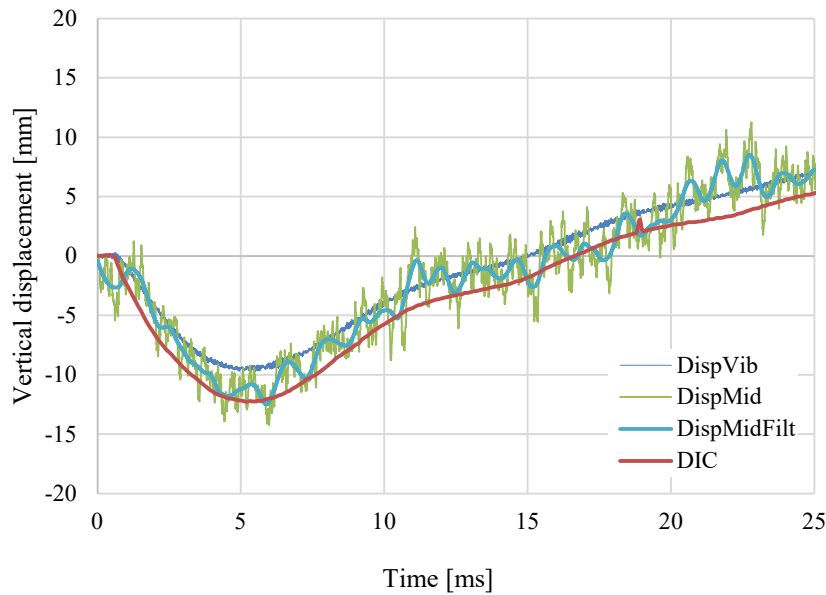


Fig. 4.10 – Time histories of the LDV displacements during the experiment for the specimen Ce-PVA-0.8.

In general, the displacements increased with the enhancement of the impactor velocity. All the transversally reinforced beams tended to display a deformation recovery on the graphs, which is actually due to the tendency of rigid body movement on the rebound engaged by the higher global stiffness. The RC-beams Se-Ref, without any type of shear reinforcement (Fig. 4.9c) presented a similar performance at the lowest impactor velocity (17.5 m/s), switching to drift at the instant correspondent to the bearings' peak loads (≈ 5 ms) at higher levels. This suggests the yielding of the longitudinal metallic reinforcement, combined with concrete crushing on the top side and the development of wide diagonal cracks (punching cone).

The specimen Se-Ref-0.2, as all the beams with some type of transversal reinforcement (internal and/or external), tended to display a minor residual flexural-deflection. However, this remark does not necessarily reflect the performance during the impact events, when large displacements were visually observed. As more clearly evidenced in Fig. 4.11, it is clear that the residual deflections, as the deflections during the tests, were directly related to the loading rate. Moreover, the magnitude of the immediate deflections, the deformations that occurred shortly after the impactor contact, and before the beginning of load transferring to the bearings, also seem related to the impact energy.

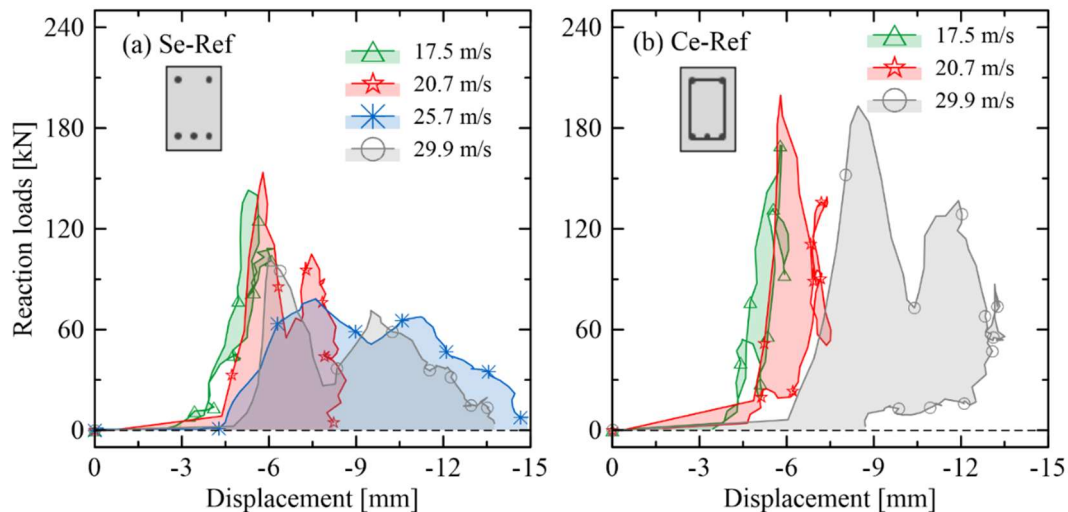


Fig. 4.11 – Load-deflection curves of the RC-beams during the experiments.

Usually load-deflection curves based on the applied load and the mid-span deflection enabled a deeper understanding of the mechanical behavior of materials under three-point bending tests, providing the energy expended in deflecting and fracturing of the specimens [136]. Here it seems that higher absorbed energies are related to higher levels of the impactor speed, albeit this also does not necessarily entail the residual structural stability of the specimen, or at least a safe absorption capacity. For instance, the larger areas were obtained with the Ce-Ref specimens, which also presented substantial fragmentation and scabbing (see Table 4.5). The Se-Ref beams also presented sizable areas, as shown in Fig. 4.13a, but they yielded structural failure.

No clear correlation was observed between the impact-energies and the amplitudes of the wave signals derived from the acceleration measurements, yet a dependency between the amplitude values and the positioning of the sensors was detected (see Fig. 4.12). Higher values were obtained in the sensors ACC4, ACC3, ACC2, and ACC1, respectively. Moreover, it can be noticed that no representative resemblance was observed between the signals ACC1 and ACC3, as would be expected as these sensors were equally distant from the point of loading. This issue, of the deviation of the theoretical and experimental behavior, was already addressed in previous studies [174,212]. As pointed out, the main reason behind this difference could be directly accounted on the misplacing of the specimen, but in truth, many variables can locally intervene with the damping, as the internal tridimensional porous structure. As such, these results should not be discredited.

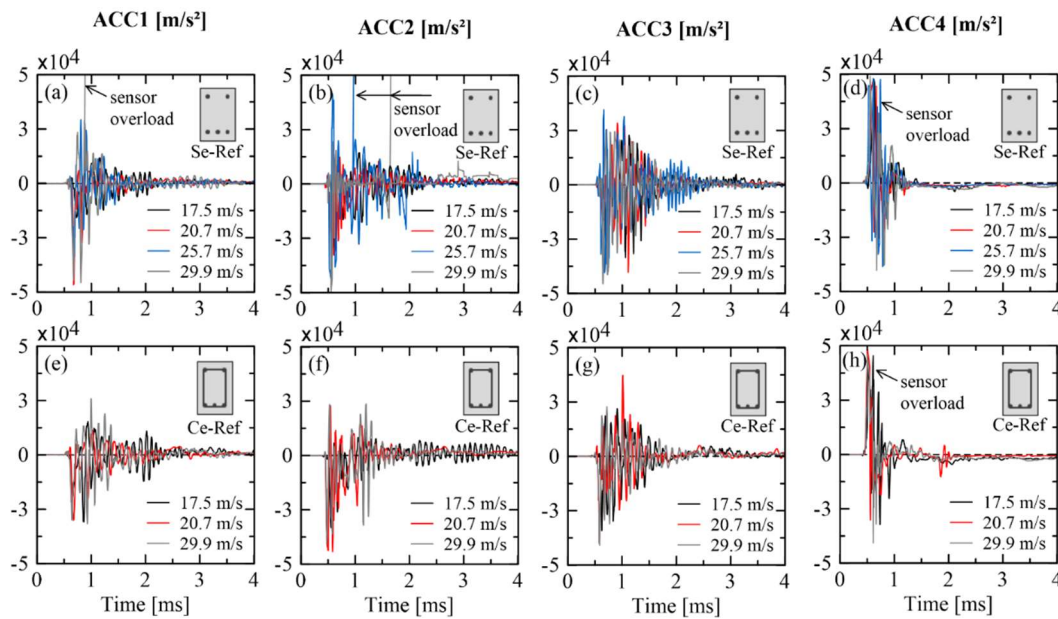


Fig. 4.12 – Acceleration histories of the specimens with and without stirrups during the experiment.

Although exhibiting the higher magnitude, the signals deriving from ACC4 were the ones that were most rapidly diminished. After the peak, the waves were virtually stabilized after 0.8 ms and 1.2 ms in the case of the Se-Ref and Ce-Ref specimens, respectively. The SHCC reinforced beams also displayed strong damping for the first 0.5 ms but seemed to present a slower decay after that, with remaining oscillations. The most delayed attenuation (1.5 ms in total) was observed for the Ce-PE specimens, which also presented the lower level of damage of the mid-span cross-section.

All tested specimens presented a significant level of damage. The evaluation of the cracking patterns is an important comparative criterion in structural tests [174]. A leaning towards a direct relation with the impactor velocity could be detected. As the program included beams with a non-negligible relative variation of self-weight due to the differences in the internal reinforcement and the SHCC layers, the mass reduction due to impact was handled as a percentage of the original weight of the intact specimens. These values of loosened material are available in Table 4.5. The strain gauges' signals will be addressed in the next section for comparison purposes.

The RC beams presented significant scabbing and spalling. The specimens without transversal reinforcement displayed marked punching cones, characteristic of shear failure (see Fig. 4.13a-d). Thus, a change in the failure mode with the

enhancement of the loading rate from static to impact levels was observed, following previous research studies [122,123,131,142,199–201]. However, this cracking pattern was not noticed on the RC specimens with stirrups, which in turn yielded a combination of bending and shear cracks with no evident punching cone (Fig. 4.13e-h).

From the cracking pattern of the RC specimens, it can be noticed that the stirrups contributed to the confinement of the upper reinforcement, influencing the deterioration on the top side and improving the perforation strength. Notably, the specimens Se-Ref and Ce-Ref exhibited somewhat rounded holes sized close to the impactor's diameter at projectile velocities of 17.5 m/s and 20.7 m/s respectively. Under greater speeds, craters were observed, related to the elevated levels of breakdown material. Moreover, an hourglass aspect could be detected in the lateral cracking patterns. Although the studied range of impact energy was not enough to produce vertical segmentation (horizontal cracks), disengagements could be noticed just below the impactor's contact point. These upper segments stood out by the resounding difference from the original substrate, presenting themselves as highly fragile, with a powdery bias related to the substrate concrete crushing.

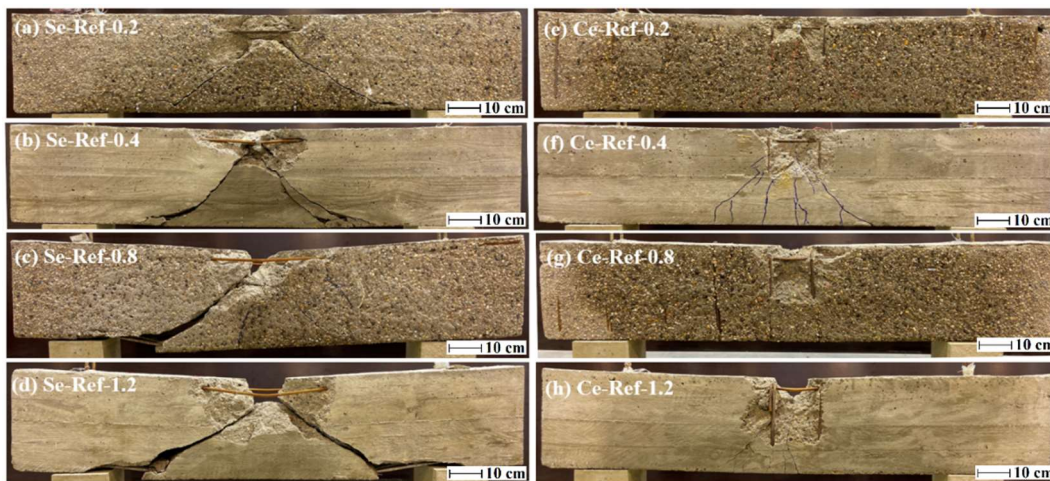
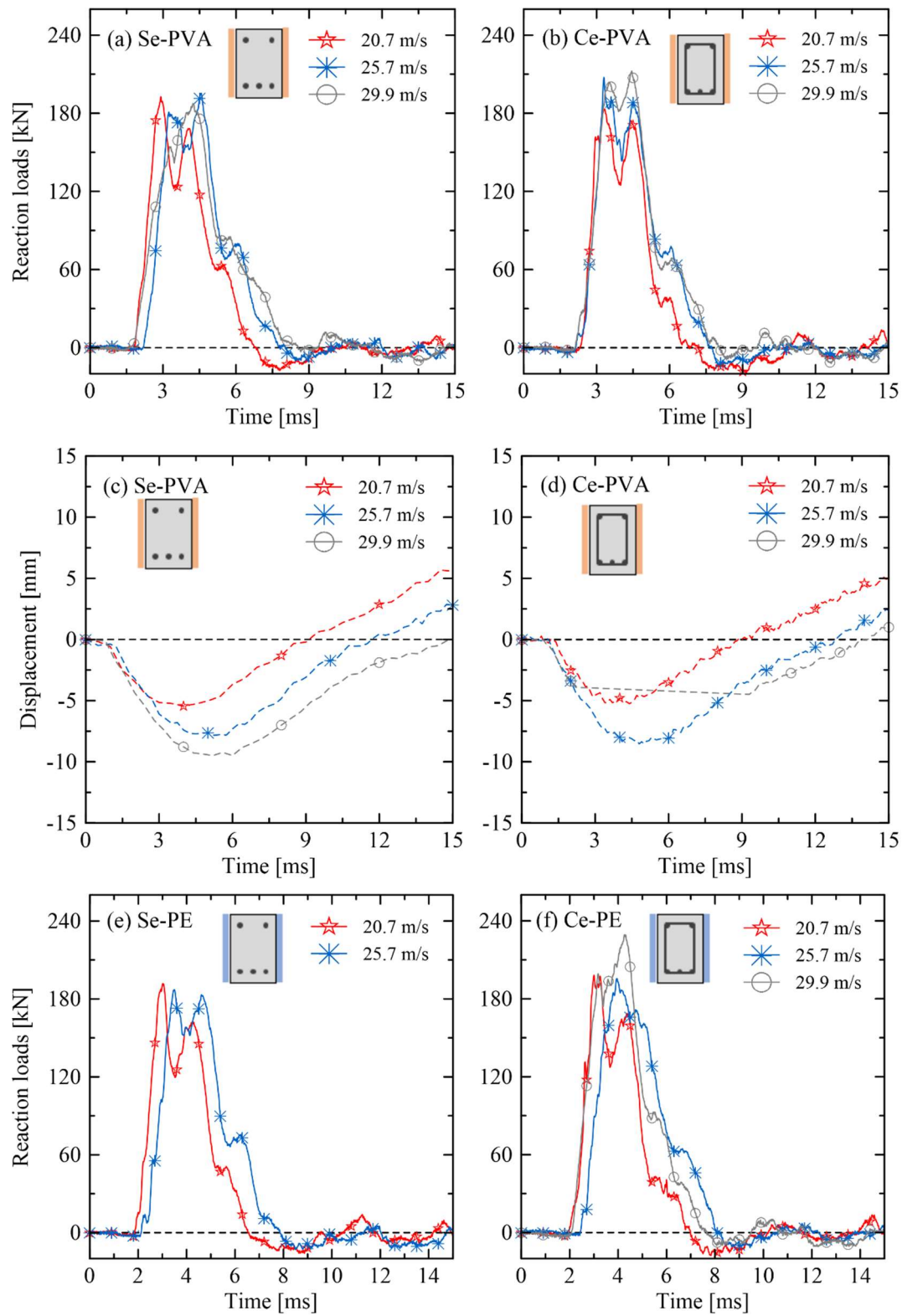


Fig. 4.13 – Damage extent in the RC beams after the impact tests with different charges.

4.3.2. Beams strengthened with SHCC

The time histories of the summed reaction forces are shown in Fig. 4.14. The maximum values of these forces are summarized in Table 4.5. All the curves tended to display a trapezoidal wave with a rapid and almost linear increase in the initial

ascending branch similar to the non-strengthened specimens, followed by a plateau and unloading with evident oscillations.



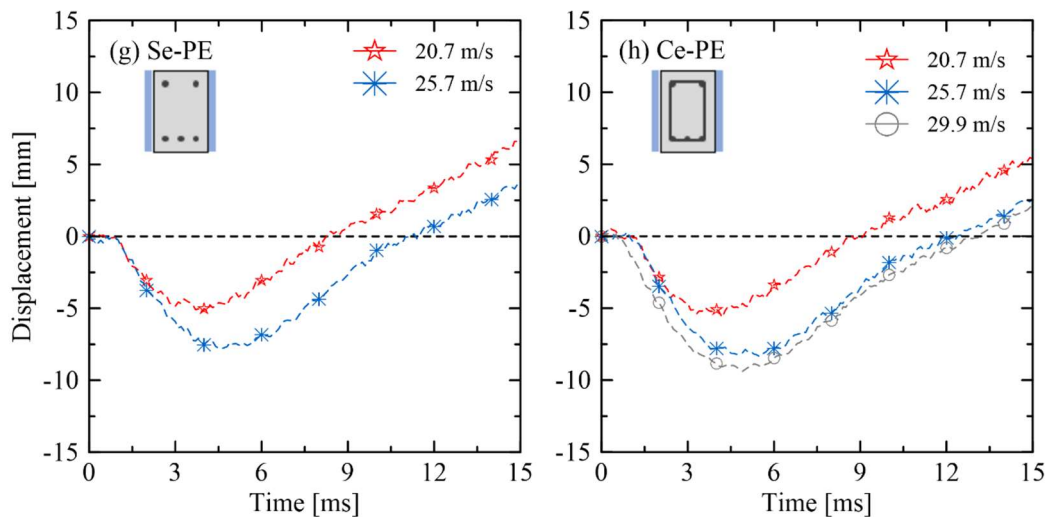


Fig. 4.14 – Time histories of the summed reaction forces measured by the load cells and the displacements obtained through the LDV during the experiments of the strengthened beams.

The external reinforcement with SHCC approximated the behavior of the specimens with and without stirrups, enhancing the magnitude of the reaction loads even for the Se specimens; see Fig. 4.15. A subtle tendency of the rise of the support loads with the increase of the loading rate could be observed.

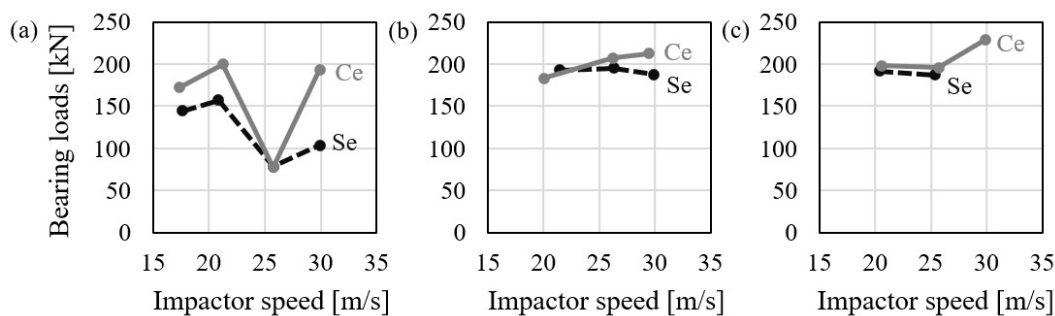


Fig. 4.15 – Maximum reaction loads: (a) reference beams; (b) beams strengthened with PVA-SHCC; (c) beams strengthened with PE-SHCC.

With the intent of studying the residual strength provided by the SHCC reinforcement, four additional specimens of the intermediary series (25.7 m/s) were subjected to repeated impact events. At the second strike, the amount of load acknowledged by the bearings is significantly reduced for the specimens reinforced without internal transversal reinforcement and externally reinforced with PVA-SHCC (37.4%) and PE-SHCC (31.4%); see Fig. 4.16 a and c. This reduction is probably due to concrete crushing under the impactor. The presence of the stirrups

apparently contributed to the tridimensional confinement of the substrate, noticed by the compliance of the curves obtained from the subsequent strikes (Fig. 4.16 b and d). The shear strengthening covers, especially the one made with PE-SHCC, ensured a higher specimen rigidity and damage tolerance. This subject will be further addressed in the end of this section.

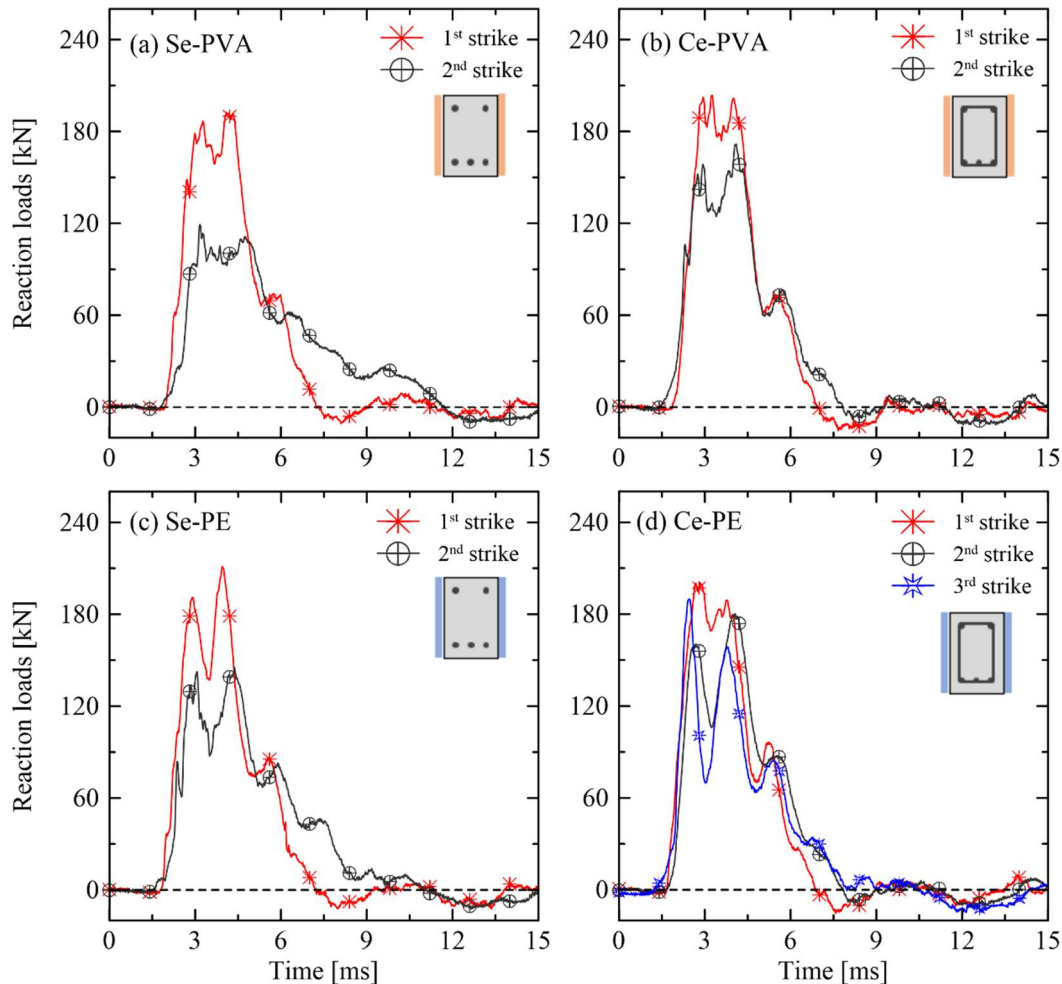


Fig. 4.16 – Time histories of the bearing loads of the specimens subjected to repeated impact loads.

Analogously to the RC-beams, the data here referred was based on the LDV data. In general, the displacements increased with the enhancement of the loading rate. All the transversally reinforced beams yielded a considerably higher deformation recovery compared to the non-strengthened beams. Again, as it was observed in Fig. 4.14, it is noticeable that the behavior of the beams reinforced with SHCC seems independent of the internal transversal reinforcement (Fig. 4.14 c, d, g, and h). This response strongly suggests that the SHCC improves the stiffness of

the beams without or with insufficient transversal reinforcement at least for impact energies until 6.4 kJ.

Following the findings of the last section all the beams with some type of transversal reinforcement (internal and/or external), tended to display a limited residual flexural-deflection. However, as more clearly evidenced in Fig. 4.17, it is salient that the residual deflections, as the deflections during the tests, were directly related to the loading rate. Moreover, the magnitude of the immediate deflections, i.e., the deformations that occurred shortly after the impactor contact also seem related to the impact energy. It also seems that higher absorbed energies are related to higher levels of the impactor speed.

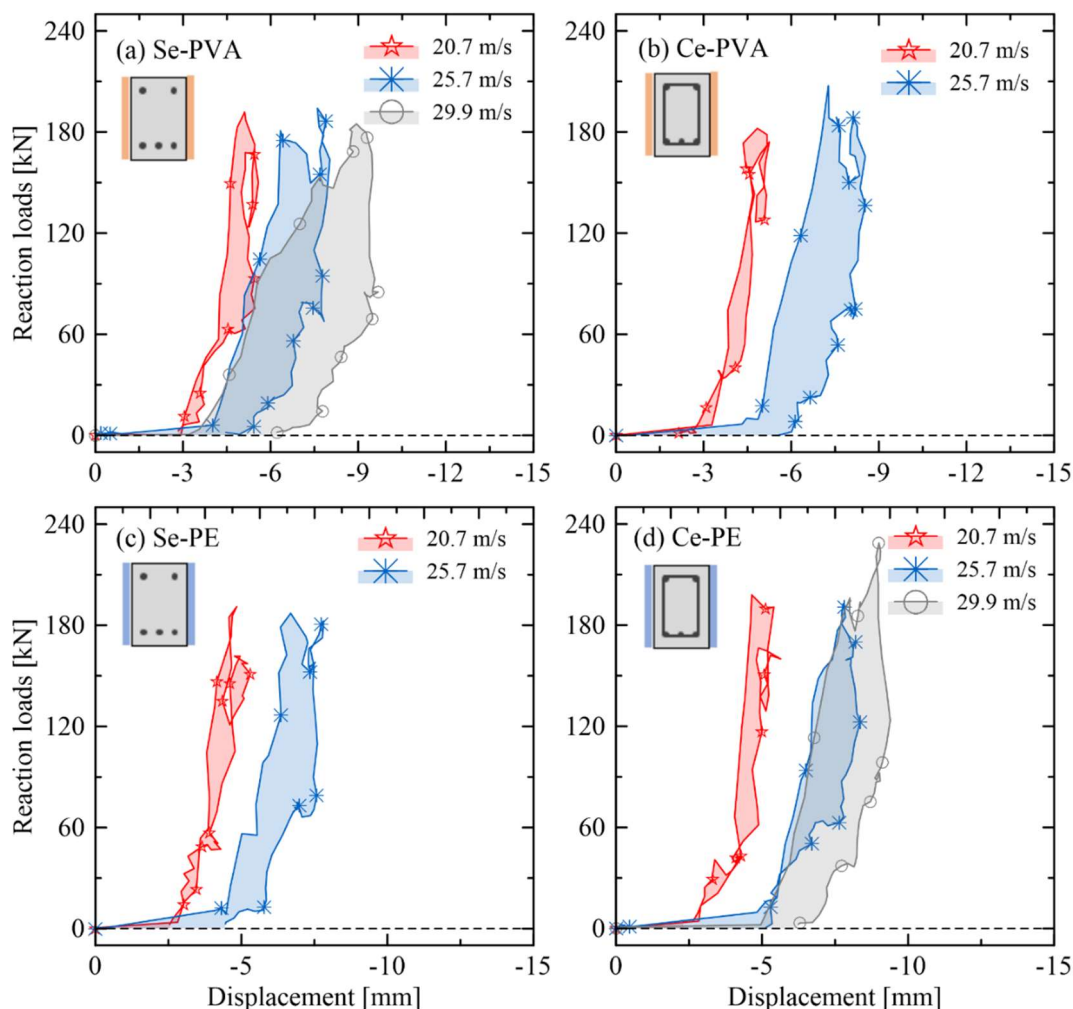


Fig. 4.17 – Load-deflection curves of impacted beams strengthened with SHCC.

Indeed, it appears that the broader areas obtained with the reference specimens (Fig. 4.11) do not necessarily reflect a greater energy absorption capacity, probably on account of the way the specimens were fixed and the fact that the SHCC reinforcement has contributed to an increase of rigidity. Normally,

sudden drops would reflect that the ultimate capacity was reached, but as aforementioned in the previous section, the observed declines of deflection of the specimens that maintained some structural integrity were in truth due to the rigid-body rebound. This behavior was noted in all beams reinforced with SHCC (Fig. 4.17), which did not yield shear failure but maintained their structural integrity with pronounced multiple cracking in the SHCC covers. Also, the beams reinforced with both types of SHCC exhibited an analogous behavior in all velocity levels and for both variations of internal reinforcement. At last, it is also noticeable the resemblance of the curves of the specimens with and without stirrups, once again indicating the improved performance supplied by the external reinforcement with SHCC.

Table 4.5 – Resume of the results regarding loads and detached mass for the specimens subjected to a singular impact event.

Specimen code	Detached material [%]	v [m/s]	Imp [kg.m/s]	P _{max} [kN]	R _{max} [kN]	Dissipated load [kN]	Dissipated load [%]
Se-Ref-0.2	1.15	17.65	250.98	9036.88	144.65	8892.23	98.4
Ce-Ref-0.2	0.65	17.29	245.86	8852.56	172.18	8680.38	98.1
Se-Ref-0.4	3.41	20.86	301.32	10680.41	157.38	10523.03	98.5
Ce-Ref-0.4	1.92	21.19	296.63	10849.37	199.97	10649.40	98.2
Se-PVA-0.4	0.00	21.41	289.80	10962.01	192.65	10769.36	98.2
Ce-PVA-0.4	0.00	20.02	292.08	10250.33	183.23	10067.10	98.2
Se-PE-0.4	0.00	20.38	304.45	10434.65	191.78	10242.87	98.2
Ce-PE-0.4	0.00	20.54	284.68	10516.57	198.15	10318.42	98.1
Se-Ref-0.8	5.53	25.76	365.60	13189.23	78.40	13110.83	99.4
Ce-Ref-0.8	2.26	25.73	360.19	13173.87	77.74	13096.13	99.4
Se-PVA-0.8	0.01	26.30	373.99	13465.72	195.42	13270.30	98.6
Ce-PVA-0.8	0.04	26.26	373.42	13445.24	207.51	13237.73	98.5
Se-PE-0.8	0.03	25.33	366.31	12969.07	187.13	12781.94	98.6
Ce-PE-0.8	0.00	25.71	365.88	13163.63	195.64	12967.99	98.5
Se-Ref-1.2	8.24	29.90	425.18	15308.93	103.33	15205.60	99.3
Ce-Ref-1.2	2.39	29.90	425.18	15308.93	193.27	15115.66	98.7
Se-PVA-1.2	0.07	29.85	418.78	15283.33	187.57	15095.76	98.8
Ce-PVA-1.2	0.00	29.45	425.18	15078.53	212.39	14866.14	98.6
Se-PE-1.2	0.30	–	–	–	–	–	–
Ce-PE-1.2	0.06	29.90	424.47	15308.93	229.29	15079.64	98.5

Analogously with what was observed for the RC-beams, no correspondence could be detected between the impact-energies and the amplitudes of the wave

signals (see the supplementary Fig. 4.18). However, a dependency between the amplitude values and the positioning of the sensors could be observed. Higher values were obtained respectively for the sensors ACC4, ACC3, ACC2, and ACC1. Also, again no representative resemblance was observed between the signals ACC1 and ACC3, as would be expected due to the positioning of these sensors. Although exhibiting the higher magnitude, the signals deriving from ACC4 were the ones that were most rapidly diminished. After the peak, the waves displayed strong damping for the first 0.5 ms but seemed to present a slower decay after that, with residual oscillations. The most delayed attenuation (1.5 ms on total) was observed for the Ce-PE specimens, which also presented the lower level of damage of the mid-span cross-section.

Strain gauges were used to track the development of strain on the internal rebars. The transducers were applied on the specimens of the series tested by a single impact-event under the initial charges of 0.2, 0.8, and 1.2 bar. The measuring points were already addressed in Fig. 4.3. Considering the entire program, the presented results were based on 92.9% of the installed transducers, as some of them provided false or no recordings. Almost all the strain gauges (96.4%) presented a step-type of signal response. Hence, a graphic representation was employed to facilitate possible comparisons and give a better understanding of the results. The peak values of strain are available in supplementary Fig. 4.19. Most of the readings (53.6%) were limited by the transducers' measurement range. Except for one of the strain gauges positioned on the longitudinal rebars of the specimen Se-Ref-0.2, all the specimens without shear reinforcement and strengthening layers presented an overload of the monitored signals. Considering the yield stress of 500 MPa of the metallic rebars and the standard steel's Young modulus of 210 GPa, the threshold of 2.38‰ could be adopted as the reference yielding strain. Thus, an overload suggests significantly elevated levels of plastic deformations. While this finding is thoroughly in agreement with the visual aspect of the tested specimens, it also raises doubts about the possibility of localized yielding in regions outside the monitored region, or either a false-response due to the compromise of the strain gages wiring.

It was found that the RC beams with stirrups tended to reduce the strain level in the longitudinal rebars ($\approx 91.6\%$) and stirrups ($\approx 68.0\%$) with the increase of the impactor velocity from 17.5 m/s to 29.9 m/s. Despite the fact that the beams subjected to the higher level of impact energy displayed extremely elevated levels

of plastic deformations of the superior rebars, these results indicate that these specimens failed due to the loss of structural integrity issued by the substantial amount of material disintegrated during the event. This type of failure is considerably less stable than the one obtained through the reinforcements yielding.

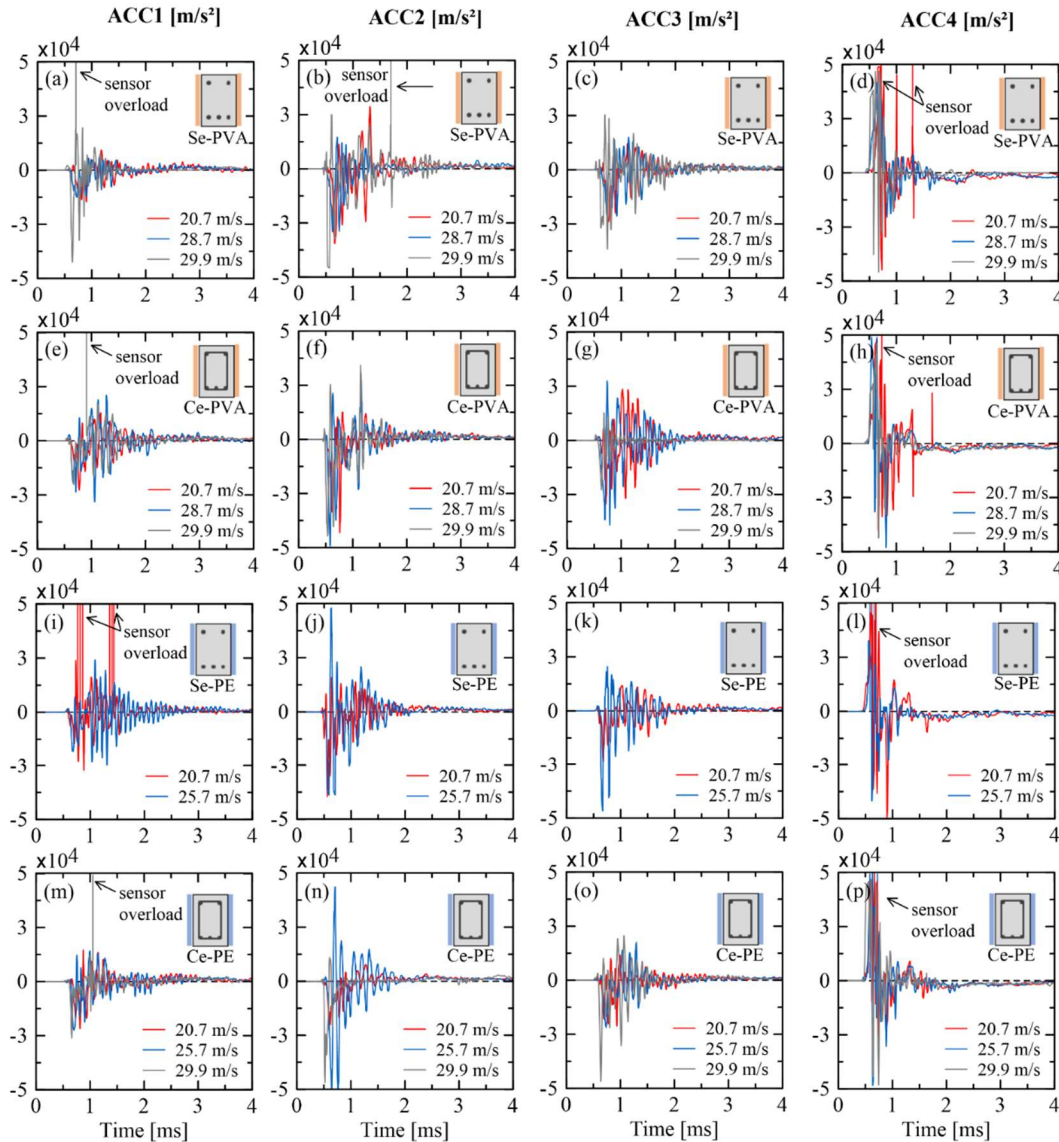


Fig. 4.18 – Acceleration histories of the specimens reinforced with SHCC with and without stirrups during the experiment.

Overall, no correspondence could be observed between the loading rate and the strain level, nor an influence of the SHCC strengthening on the strains of the longitudinal rebars. It is surprising though, that the strengthened beams did not exhibit severe damage based on the optical analysis of the lateral surface but the concrete region below the impactor crushed and the rebars yielded great deformations. Concerning the internal transversal reinforcement, PVA-SHCC

specimens seemed to present the same effect as the reference beams fully prepared with original RC substrate, tending towards a reduction of the strain to a level underling the yielding strain for higher loading rates. In turn, PE-SHCC seemed to improve the participation of the transversal reinforcement on higher impact energies scenarios.

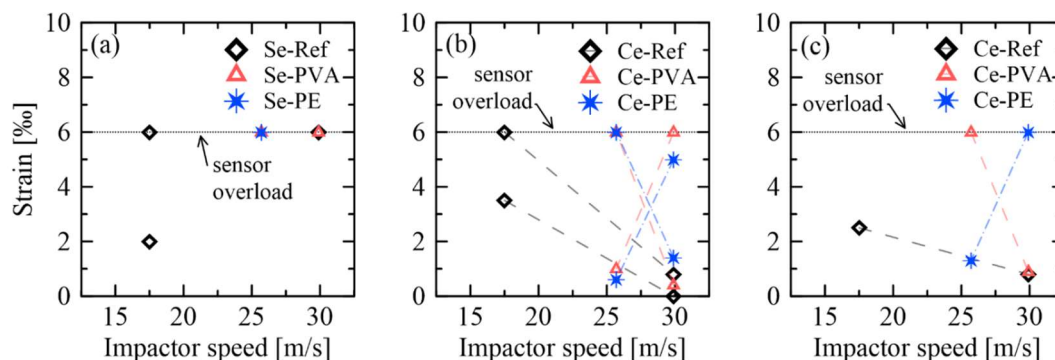


Fig. 4.19 – Peak values of strain on the: (a) longitudinal rebars, in the specimens without stirrups; (b) longitudinal rebars, in the specimens with stirrups; (c) stirrups.

The SHCC strengthening contributed to the increased rigidity of the specimens and also substantially reduced the amount of breakout material. The beams strengthened with SHCC did not entirely lose their structural integrity, with apparent multiple fine cracks with widths varying between 20 μm and 100 μm on the lateral surfaces. The multiple-cracking formation is an intrinsic characteristic of SHCC, necessary to the achievement of the composite's high macroscopic ductility under tensile and shear stresses [213,214]. This outstanding width control, in turn, is one of the top desirable qualities for reinforcing materials, being a contributing factor to the durability of structural members [88].

The damage assessment of these beams also included the evaluation of the cracking patterns of the mid-span cross-section. Fig. 4.20 displays one of the lateral, and the cross-sectional cracking patterns of the four strengthened beams of the 1.2 bar series, which corresponds to the higher level of impact energy of the present program. Under this evaluation, the internal damage of the original substrate is quite visible. A propensity of a cone cracking pattern can be detected, with the internal rebars acting as stress concentrators, luring the fracture path. It is notable the excellent adhesion between the SHCC reinforcement and the concrete, supporting

the SHCC function as a strengthening material for structural elements with cement-based substrates.

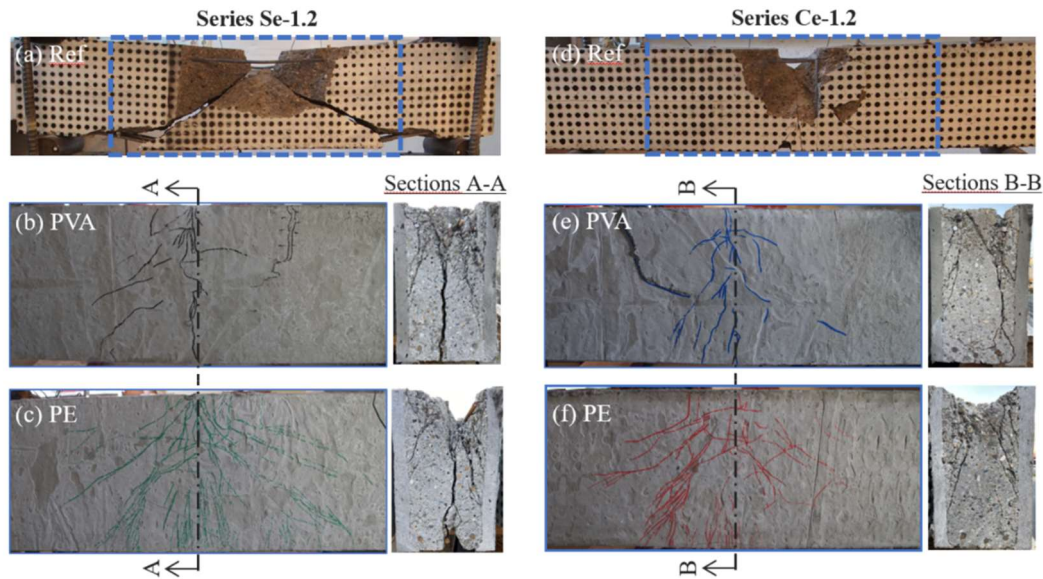


Fig. 4.20 – Comparative damage assessment of the specimens tested under 29.9 m/s: influence of the stirrups and the SHCC reinforcement: (a) Cracking pattern of the reference specimen without stirrups; (b) Highlighted cracking pattern and middle cross-section of the specimen without stirrups and strengthened with PVA-SHCC; (c) Highlighted cracking pattern and middle cross-section of the specimen without stirrups and reinforced with PE-SHCC; (d) Cracking pattern of the reference specimen with stirrups; (e) Highlighted cracking pattern and middle cross-section of the specimen with stirrups and reinforced with PVA-SHCC; (f) Highlighted cracking pattern and middle cross-section of the specimen with stirrups and strengthened with PE-SHCC.

Analogous to the RC beams, those strengthened with SHCC presented a marked deterioration of the impacted surface, even though no sizeable scabbing could be detected. In particular, the condition of the upper part of the punching cone displayed a divergent behavior, tending towards a much more consolidated state. The main reason behind this behavior is probably because the penetration resistance is ruled by the rigidity of the targeted substrate and the strength of the surfaces parallel to the impactor's path [57]. On account of the way the testing setup was contemplated, with the impactor diameter reaching only the specimens' core, the SHCC layers were loaded both in shear as in bending tension, significantly improving the confinement of the substrate. For instance, even with the cross-

section cuts, only the specimen Se-PVA-1.2 presented the absolute separation of the upper-cone volume; an integrated mass of 0.427 kg.

The contribution of the SHCC reinforcement can be better illustrated with the damage assessment of the specimens subjected to more than one single impact event (see Fig. 4.21). Both types of SHCC secured an afterlife to the original RC specimens, evidenced by the existence of a considerable residual load-bearing capacity. Although during the second and third events (the last about Ce-PE specimen; see Fig. 4.21) the concrete substrate initially presented itself highly cracked, it was still able to transmit the kinetic energy of the impactor to the SHCC covers, evidenced by the enhancement of crack density. Despite the damage of the substrate, the SHCC reinforcement was still capable to limit the detached fragments. The damage assessment of these specimens, as well as the contribution of the SHCC covers on the impact dumping, is the topic of an ongoing study.

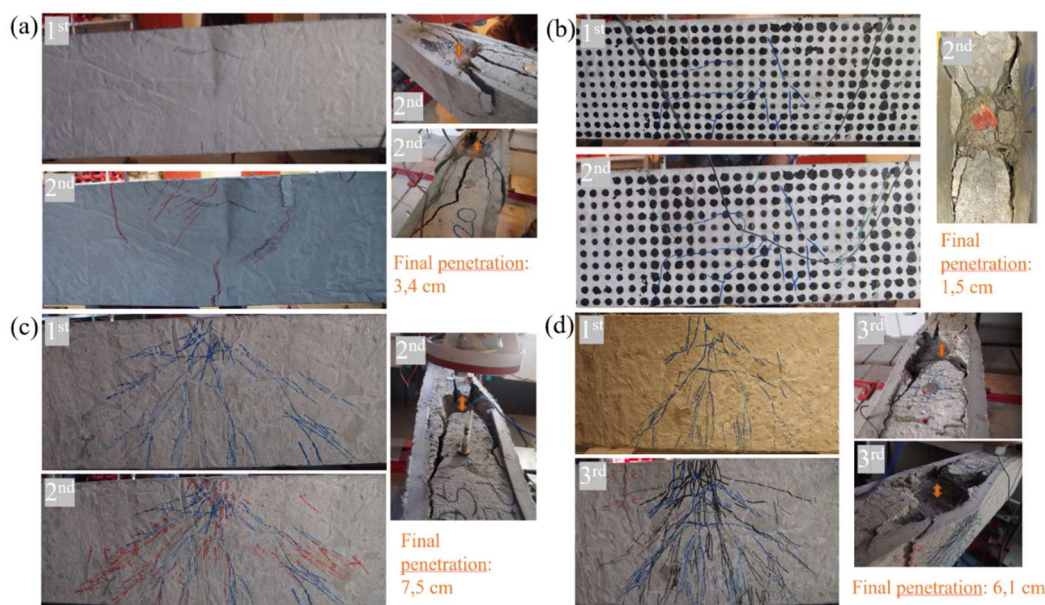


Fig. 4.21 – Lateral and upper view of the specimens impacted more than one time.

Photo report of the cracking patterns after the first and the last impact: (a) Se-PVA; (b) Ce-PVA; (c) Se-PE; (d) Ce-PE.

4.4. Conclusions

An extensive experimental program on the impact performance of RC-beams reinforced with different types of transversal reinforcement was carried out by combining two configurations of internal rebars, with two variations of external reinforcement made with SHCC, under levels of kinetic energy varying between

2.1 kJ and 6.4 kJ. Based on the presented results, the following conclusions can be drawn:

1. Both types of transversal reinforcement, internally with stirrups and externally with the SHCC achieved similar contribution in terms of stress-transference to the bearings and residual stability. All the specimens reinforced with SHCC displayed an even more significant after-event stability, with residual bodies able to endure additional impact events (impactor velocities ≈ 26 m/s)
2. The load-displacement hysteresis were found to be not sufficient for a quantitative evaluation of the dissipated energy due to the rigid-body tendency of motion of the specimens with greater rigidity, which impaired a comparative correlation.
3. SHCC presented a strong synergetic composite action with the concrete-substrate, presenting outstanding adhesion and deformation compliance. It also restated its elevated damage tolerance under extreme scenarios, excelling on the breakout material control, significantly reducing the detritus deriving from scabbing and spalling (≈ 0 %). Moreover, it also displayed a remarkable cracking control, with crack widths varying between $20 \mu\text{m}$ and $100 \mu\text{m}$.

5 Experimental modal analysis of RC beams strengthened with SHCC subjected to shear under impact strain rates

5.1. Introduction

Strain-Hardening Cement-based Composites (SHCC), also known as Engineered Cementitious Composites (ECC), are a class of building material that exhibits elevated strain capacity (1-5 %) under tension when compared with plain concrete [193,215,216]. This distinct strain capacity prior to failure localization is related to the formation of very fine multiple cracks (max. 100 μm of width) [14,49,203], which are controlled by dispersed polymeric microfibers (3-12 mm long), typically employed with volume fractions of 2 %. Although SHCC nomenclature is remitted to its direct-tension behavior, it also displays advantageous performances under compressive and shear stresses, especially with regard to its energy absorption capacity [18,213]. Aside from its awesome mechanical response, the complete substitution of normal concrete for SHCC in new structures poses as economically unfeasible mainly due to the cost of the fibers [15,87,104]. However, it holds great potential for applications as external strengthening layers due to its fresh-state properties which enable spraying or lamination [15]. Moreover, SHCC easily overcomes one of the main problems regarding strengthening materials, the bond between the patch-material and the substrate as long as the properly rough application surface is ensured [17]. It also presents comparatively a much lower cost than the most commonly marketed strengthen materials [87].

Reinforced Concrete (RC) structures are, in general, in constant deterioration due to erosive actions resulting from environmental exposure conditions (volumetric dilatation, moisture, wind, sea air, etc), air pollution (CO_2), and variations on the service loads [117,145,217]. Quite often this accumulation of damage requires the rehabilitation of the structure to hold its serviceability, commonly adding new concrete covers. In the long-term, it is also to be expected the degradation of these reinforcement layers, which unfortunately makes the task of damage detection harder, especially with regard to the state of the substrate, as

the strengthening layers impair any visual inspection [145,218]. On the other hand, reinforcements made of Fiber-Reinforced Polymers (FRP) are subjected to transverse cracking, interlaminar delamination, fiber breakage, fiber-matrix debonding, and cavitation, representing a damage-detection challenge by themselves [145,217–219]. FRP made with cement-based composites, let alone the ones reinforced with dispersed fibers such as SHCC, are exposed to similar deterioration mechanisms than the concrete substrate, thus can be examined using the same methods.

One advantageous technique to detect the damage in cement-based systems is the evaluation of their vibrational response, more specifically their change in mode shapes, natural frequencies, and damping ratios [117,133,145–150]. For instance, it was already reported that undamaged reinforced concrete members display damping values of $\sim 0.85\%$, while cracked ones can provide larger coefficients, with values varying between $0.5 - 4.0\%$ [152–154]. Thus, although experimental modal analysis is intrinsically a non-destructive evaluation, it can also be used to assess the residual response of damaged systems when considering an intact referential, thus being useful to evaluate the residual stability provided by strengthening layers [146,151]. The technique consists of measuring the frequency(ies) at which a structural member would oscillate when disturbed by an external stimulus and allowed to vibrate freely [151]. Therefore, its dynamic response comes from an interaction between its inertial and elastic forces, constrained by the undercritically-damped system, which in turn arises from the substrate and reinforcement internal molecular friction, viscosity, and cracking, thus providing an understanding of the structural integrity of the examined specimen, being an important technique of structural health monitoring [133,151,220–228]. To the best of the authors' knowledge, there are still limited experiments on RC beams subjected to structural damage focusing on impact scenarios, previously and subsequently monitored through vibration analysis to detect the enhancement of deterioration [223,225]. The topic has been even more discreetly addressed on fiber reinforced composites (FRC) structural elements [220,226,227], let alone members strengthened with SHCC.

In this way, this chapter presents the second-part analysis of an experimental campaign designed to examine the influence of transversal reinforcement and strengthening layers on the impact resistance and fracture behavior of RC beams

(chapter 4). The influence of the strengthening layers made out of SHCC on the intact specimens, as the contribution to their residual performance, were evaluated through the assessment of their modal parameters i.e. mode shapes, natural frequencies, and damping. A total of 24 structural beams were tested. Their experimental modal results were obtained using two independent routines implemented on Matlab (by MathWorks, USA). Comparisons among the experimental results coming from the RC beams with theoretically calculated values and a numerical model implemented on Abaqus (By Dassault Systèmes Simulia, USA) were used to evaluate the agreement of the vibration modes. Finally, the numerical routines implemented on Matlab were extrapolated for the beams strengthened with SHCC, providing the means for a comparative damage evaluation of these specimens. While this research consists of a very special structural case, it represents an important step forward the understanding on the contribution of SHCC strengthening covers on the impact resistance of existing structures.

5.2. Materials and methods

The present program entailed the modal evaluation of 24 specimens that were subjected to increasing levels of impact energy varying from 2.1 kJ to 6.4 kJ. Two variations of RC beams with outer dimensions of 0.13 m \times 0.28 m \times 1.45 m (width \times height \times length) were studied: the first group considered the specimens without transversal reinforcement whereas the second one with stirrups on a shear reinforcement ratio of 0.53 %. Both variations had the same longitudinal reinforcement ratio of 0.72 %, and a concrete cover of 10 mm. The investigation focused on the improvement of the impact resistance and residual stability through the use of externally applied strengthening layers of SHCC. Eight beams from each reinforcement configuration (without and with stirrups) received a 20 mm thickness layer of two variations of SHCC, totalizing 16 strengthened specimens. More details regarding the experimental program can be found in chapter 4.

5.2.1. Materials

All the beams were built with the same normal-weight concrete with a water-to-binder ratio (w/b) of 0.35 and a maximum aggregate size of 8 mm. Besides

Portland cement type III (42.5N), a discrete amount of fly ash was also used as a binder for rheological improvement purposes. The mix design by weight is given in Table 5.1. The mean compressive strength measured on 150 mm cubes was 49.5 MPa at 28 days and 50.9 MPa at 42 days, which was the average testing age. The beams were reinforced with Ø8 mm ribbed bars of steel B500S ($f_y \approx 500$ MPa).

Table 5.1 – Concrete composition (kg/m³).

Component	Cement	Fly ash	Coarse aggregate	Fine aggregate	Water	Superplasticizer
Quantity	380	60	762	932	188	2.85

Two types of normal-strength SHCC ($f_{ck} \approx 42$ MPa) were assessed in this study, as already described on chapter 4; see also Fig. 5.1. Following previous investigations by the authors, both held a fiber content of 2% in volume [18]. One was produced with polyvinyl alcohol (PVA) fibers (by Kuraray, Japan), and the other with ultra-high molecular weight polyethylene (UHMWPE), shortly referred as PE fibers (by DSM, the Netherlands). The geometric and mechanical properties of these fibers are listed in Table 5.2.

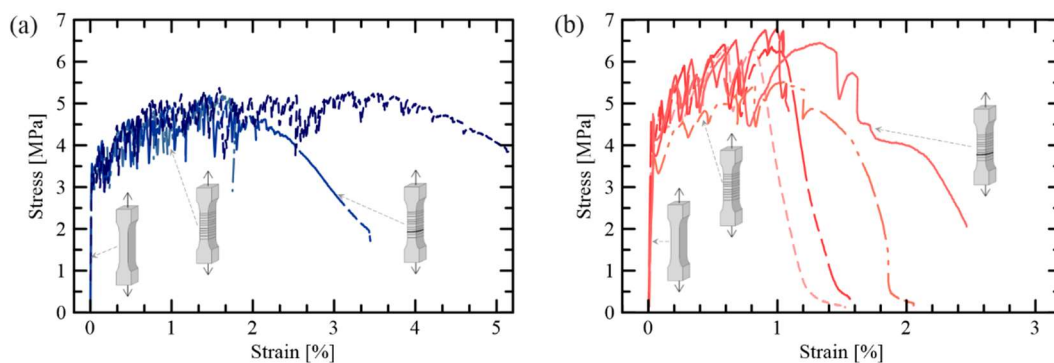


Fig. 5.1 – Direct tensile behavior of the studied SHCC at 28 days: (a) PE-SHCC; (b) PVA-SHCC. Note different scale of the x-axes.

The compositions of the SHCC made with PVA and PE fibers are practically identical, having an average strain capacity of 1.0% and 2.5% respectively. The mixture was previously developed by the authors Curosu and Mechtcherine [10,64,204,205] to ensure proper crack-bridging behavior for PVA-SHCC. Due to PVA inherent hydrophilic properties [189–191], it yields a strong chemical bond with cementitious matrices. The matrix in reference was purposely conditioned to afford limited bond-strength between the fibers and the matrix, therefore reducing the occurrence of fiber-rupture during the pullout process [10].

Table 5.2 – Geometric and mechanical properties of PVA and PE fibers according to producers [187,206].

Fiber		PVA	PE
Specification		REC15	SK62
Diameter	[μm]	40	20
Length	[mm]	12	12
Density	[g/cm ³]	1.26	0.97
Tensile strength	[MPa]	1600	2500
Young's modulus	[GPa]	40	80
Elongation at break	[%]	6.0	3.5

PE fibers are intrinsically hydrophobic, hence mainly frictionally anchored to cementitious matrices [193]. Consequently, the pullout behavior of PE-SHCC would be favored by the matrix compactness. However, it was chosen to maintain the same matrix, which was primarily developed to PVA-SHCC for comparison purposes with minor adjustments. The modifications were implemented to ensure the proper workability for PE-SHCC since its relative higher aspect ratio represents a drawback in terms of fiber dispersion. The proper rheology was achieved with a small increase in the superplasticizer content and with a combination of higher energy and duration of mixing [10]. Both SHCC compositions are listed in Table 5.3.

Table 5.3 – Compositions of the SHCC under investigation.

	PVA-SHCC	PE-SHCC
	[kg/m ³]	[kg/m ³]
Portland cement CEM I 42.5 R-HS	505	505
Fly ash Steament H4	621	621
Quartz sand 60 – 200 μm	536	536
Water	338	333
Superplasticizer BASF Glenium ACE 30	10	25
Viscosity modifying agent	4.8	4.8
PVA fiber 2 % by volume	26	–
UHMWPE fiber 2 % by volume	–	20

5.2.2. Test specimens and setup

All the specimens were subject to impact load by using the accelerated configuration of the drop tower facility located at the Otto-Mohr Laboratory of the Technische Universität Dresden [208]. The RC beams were positioned over rollers

and vertically braced at ends so that the supports enabled only the rotation in the plane of loading (Fig. 5.2a). Each brace consisted of a neoprene pad fastened by a pair of manually adjusted metallic clamps. The impact load was applied by a flat-nose steel impactor with 100 mm of diameter, and 14.2 kg of weight. This projectile was initially charged with pressures varying from 0.2 bar (200 kPa) to 1.2 bar (1200 kPa), resulting in impact velocities from 17.7 m/s to 29.9 m/s, and corresponding to a kinetic energy varying from 2.1 kJ to 6.4 kJ, respectively. The specimens were instrumented with four piezoelectric accelerometers model PCB-M350C04 (by PCB Piezotronics, USA), with a sensitivity of 0.10 mV/(m/s²), and a bandwidth varying from 0.2 Hz to 25 kHz. The data acquisition system worked on a sampling rate of 200 kHz. Three of the sensors were positioned on the impact front-surface – top of the beams (ACC1, ACC2, and ACC3), and one at the rear-surface – bottom of the beams (ACC4); see Fig. 5.2b.

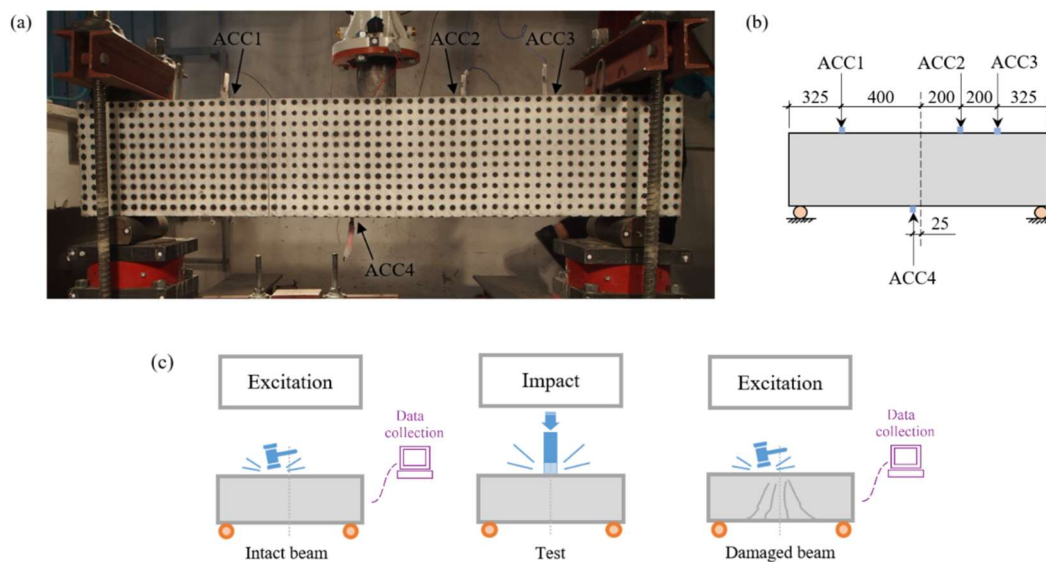


Fig. 5.2 – Test configuration: (a) View of the test set-up; (b) Illustration of the boundary conditions and positioning of the transducers (dimensions in mm); (c) Schematic representation of the measuring steps considered on the experimental modal analysis.

The damage assessment was enabled by the modal analysis of the data collected by a non-destructive excitation before and after each test; see Fig. 5.2c. A metallic half-round impactor head was struck by hand by the same operator in all tests, hitting the specimen always at the same position: on the left front-side of the beam considering the projectile's penetration path. The data of the accelerometers

lasting 2 s in time domain was recorded while the specimens were still clamped on the load cells. It should be noted that only the accelerometer signals (output-only) were considered in the following analysis of Sections 3 and 4.

Fig. 5.3 relates the nomenclature of the specimens, the pressure and velocity of the steel impactor, and the number of destructive impacts. Most of the beams were subjected to a single event. However, with the intention to assess the residual strength provided by the SHCC layers, additional impacts were performed on some of the strengthened specimens of the intermediate (0.8 bar) series. The specimens were labelled according to their configuration of reinforcement ("WS" and "WOS" in reference to the presence or absence of stirrups, respectively), of the strengthening layer material ("Ref" was used for the reference beams, i.e. specimens without external strengthening, and "PVA" and "PE" indicate the beams which lateral surfaces received the SHCC made with these fibers), and to the initial charging pressure of the impactor (0.2 – 1.2 bar). Thus, the test set-up results in a total of 116 dynamic responses in terms of acceleration.

Acceleration pressure / Impactor's velocity				
	0.2 bar (17.7 m/s)	0.4 bar (20.8 m/s)	0.8 bar (26.1 m/s)	1.2 bar (29.9 m/s)
Reinforcement	Without stirrups With stirrups	Without stirrups With stirrups	Without stirrups With stirrups	Without stirrups With stirrups
Strengthening	Without	Without PVA-SHCC PE-SHCC	Without PVA-SHCC PE-SHCC	Without PVA-SHCC PE-SHCC
Number of impacts	1 impact	1 impact	1 impact 2, or 3 impacts	1 impact

Fig. 5.3 – Summary of the specimen characteristics and loading conditions.

5.3. Analysis methodology

The damage assessment was based on the analysis of the variations of the natural frequencies and damping values of the undamaged and damaged specimens. Both were obtained through the time and frequency domain (TD and FD respectively). The selection of the natural frequencies corresponding to the first three theoretical modes was based on the peaks obtained through FD, on the results of analytical formulations, numerical modeling (Fig. 5.4a), and supported by the shapes of the normalized modal coordinates (NMC) to unity based only on the TD

response (Fig. 5.4b). Although the results were obtained through two independent protocols, they were intricately related: the peaks visualization was based on an FD routine, as will be further discussed, while the validation data was obtained through TD proceedings. The motivation that driven these parallel studies was the enhancement of reliability on the results.

The analytical evaluation was guided by the expression $f = C \cdot \pi \sqrt{EI/m'l^4}$ that describes the natural frequency of simply supported beams in Hz [152,154], where EI represents the stiffness of the specimen, being E its Young's modulus, and I its moment of inertia. The variable m' represents the modal mass of the specimen, which is half the value of its total measured mass in case of simply supported beams, and l is the free span of the set. The variable C is a constant that assumes the values 0.5, 2.0, or 4.5 for the first, second and third theoretical modes, respectively [152,154].

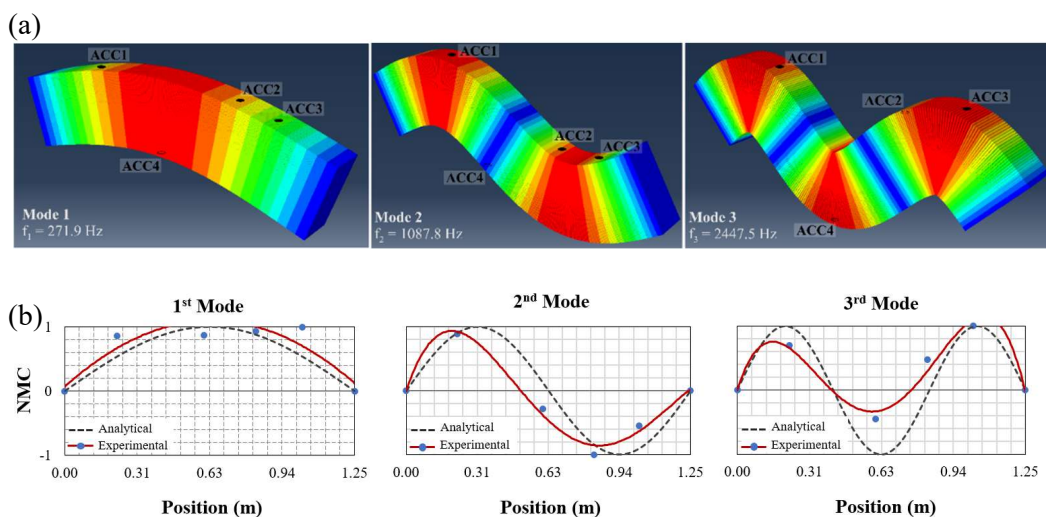


Fig. 5.4 – Three first theoretical vibrational modes with indication of the transducers' positioning (e.g. WOS-Ref): (a) mode shapes and corresponding natural frequencies obtained through numerical modeling; (b) correlation example of the NMC with the analytical formulations.

Analogous to other dynamic evaluations, the detection of the natural frequencies of each specimen is not an easy task, being considerably hampered on the damaged specimens. The calculation by simple observation of the natural period of the TD free vibration response (Fig. 5.5a) is almost impossible because of the contribution of several vibration modes. Consequently, a Fast Fourier Transformation (FFT) is typically adopted (Fig. 5.5b). In this sense, a routine was

also implemented in Matlab as part of the FD procedures to facilitate the identification of the natural frequencies, easing especially the recognition of the peaks related to the lowest frequencies and the damaged specimens. Thereby, the determination of the natural frequencies was based on the peak values of the Averaged Normalized Power Spectral Density plot (ANPSD) [117,229], which corresponds to the sum of the normalized square magnitude of the spectral density functions obtained from the four accelerometers (see Fig. 5.5c). For this, the Power Spectral Density (PSD) of each signal was first computed using Welch's method [154]. Additionally, the ANPSD values are also shown in decibels (dB) to improve the visualization of the peaks (Fig. 5.5d).

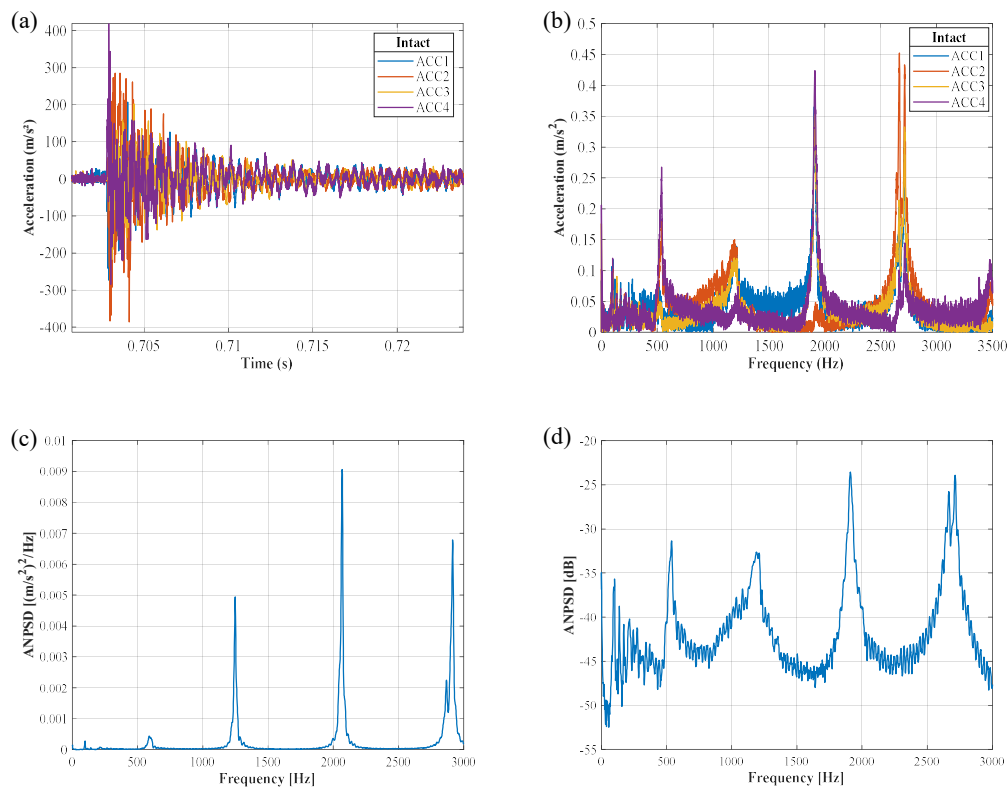


Fig. 5.5 – Typical vibration spectrums for an intact specimen (e.g. WOS-Ref): (a) acceleration-time response considering the four accelerometers; (b) acceleration-frequency response coming from the FFT; (c) ANPSD-frequency response; (d) ANPSD-frequency response on decibel scale.

Afterward, a combination of low and highpass Butterworth filters to form a bandpass filter was used on the TD signals to isolate the contribution of the vibration modes of interest considering appropriate cutoff frequencies. This procedure allowed the estimation of the modal damping ratios in TD by the

automatic curve fitting of the exponential free decay from each accelerometer signal. Furthermore, as each peak in FD was well approximated by a single degree of freedom response, the damping ratios were also determined from the ANPSD plots using the well-known half-power bandwidth method [229,230].

Normalized damage indices based on [222] were also adopted to evaluate the overall cracking progression associated with each impact velocity on the strengthened beams. Damage indexes are a well-known method to qualitatively assess changes in structural modal strain energy of elements without significant variations of the modal mass [117]. The stiffness degradation index (DI_f) was estimated by the change of the natural frequency of a specific vibrational mode of a specimen from its intact state (f_0) and after the damage (f_i): $DI_f = (f_0 - f_i)/f_0$ (1). Analogously, the damping degradation index (DI_ζ) was based on the variation on the damping coefficients of a specimen on its intact (ζ_0) and damaged state (ζ_i) for each vibrational mode: $DI_\zeta = (\zeta_i - \zeta_0)/\zeta_0$ (2).

5.4. Results and discussion

5.4.1. RC-beams

Typical vibration spectra of the RC beams coming from the FFT are shown in Fig. 5.6 before and after the damage. While the peaks referent to the frequencies greater than 500 Hz could be clearly detected, an uncertainty hovered the detection of the first peaks. Thus, as detailed in Section 6.3, the spectra based on the ANPSD, as part of the FD protocol, were used to support the observations from the TD routine. This way, all the significant peaks until 2000 Hz were initially investigated and the filtered data in the TD was used to plot their NMC. Based on this routine, it was possible to verify for all intact specimens that the peak associated with frequencies around 500 Hz represented an experimental mode without correlation with the first three theoretical vibration modes presented in Fig. 5.4. These would be spurious modes, that according to the numerical model, wouldn't be able to be performed by real specimens. For this reason, these peaks were not considered in the analysis. The main graphs produced for the analysis of each specimen are available in the second appendix of this thesis.

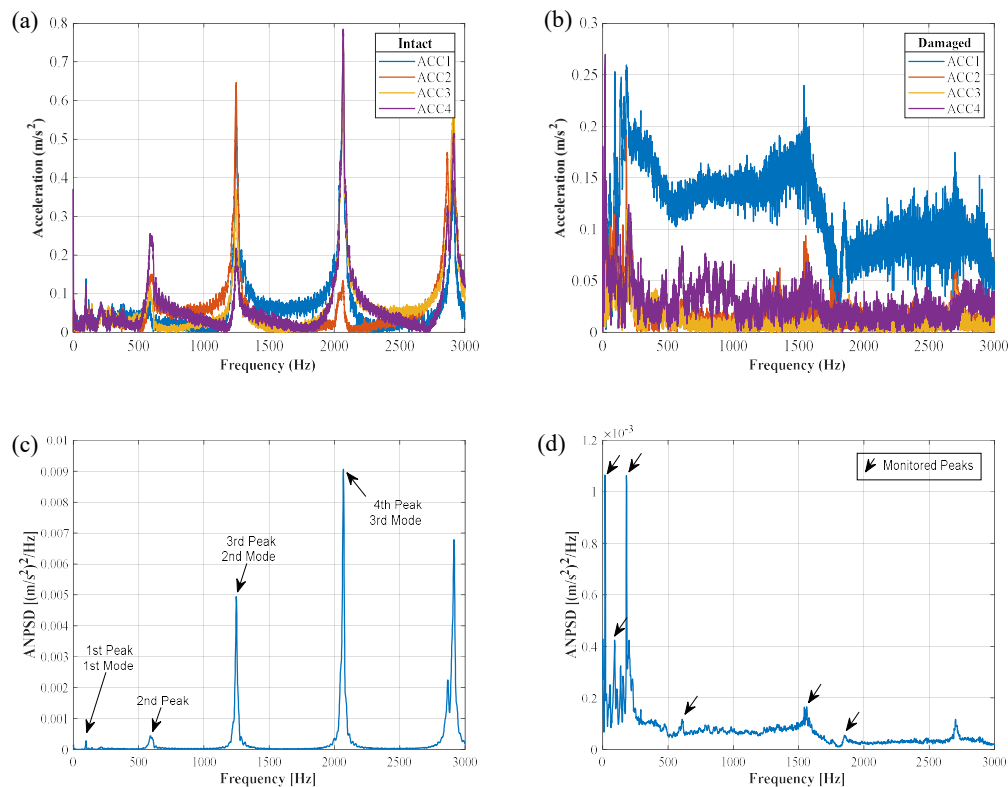


Fig. 5.6 – Typical vibration spectra for the RC specimens and natural frequencies associated with the three first vibrational modes (e.g. WOS-Ref): (a) FFT before the impact; (b) FFT after the impact; (c) ANPSD before the impact; (d) ANPSD after the impact.

The identified natural frequencies (f) and damping values (ζ) based on the FD and TD to the first three vibration modes are shown in the supplementary Table 5.4 for the intact beams. As the level of damage does not interfere with the values at this instance (analysis based on the data before the damage), the specimens were grouped into two major groups: specimens without transversal reinforcement (WOS) and specimens with transversal reinforcement (WS). It is possible to notice that the natural frequencies associated with each mode showed a very low dispersion on the results obtained through TD or FD for both WOS ($\sim 2.3\%$) and WS ($\sim 2.7\%$) configurations, with the specimens without stirrups presenting superior values for the first (4.7%), second (1.5%), and third (1.2%) modes when compared with the specimens with stirrups. These results point out that although the WS specimens presented a small enhancement of stiffness due to the presence of stirrups, the representativity of the relatively higher amount of reinforcement

steel was even more significant in terms of mass, leading to a reduction in the values of the natural frequencies.

Table 5.4 – Natural frequencies and damping values of the undamaged RC beams obtained through TD and FD for the first three theoretical modes regarding the specimens without transversal reinforcement (WOS) and specimens with transversal reinforcement (WS). Standard-deviation in parenthesis.

	Mode 1				Mode 2				Mode 3			
	f _{FD} 1 [Hz]	f _{TD} 1 [Hz]	ζ _{FD} 1 [%]	ζ _{TD} 1 [%]	f _{FD} 2 [Hz]	f _{TD} 2 [Hz]	ζ _{FD} 2 [%]	ζ _{TD} 2 [%]	f _{FD} 3 [Hz]	f _{TD} 3 [Hz]	ζ _{FD} 3 [%]	ζ _{TD} 3 [%]
WOS	97.78 (7.32)	93.54 (6.78)	5.08 (2.57)	3.28 (1.39)	1210.23 (25.52)	1215.91 (27.51)	0.82 (0.29)	1.14 (0.48)	2016.23 (39.75)	2001.30 (57.21)	0.50 (0.09)	0.57 (0.04)
WS	94.71 (6.84)	87.96 (2.65)	6.43 (1.62)	5.77 (1.45)	1196.10 (26.49)	1194.84 (25.85)	1.10 (0.34)	1.49 (0.79)	1988.30 (36.34)	1982.41 (35.92)	0.65 (0.07)	0.84 (0.14)

The damping values, in turn, displayed discreetly higher values of dispersion between the results obtained through TD or FD for both WOS (~ 31.8 %) and WS (~ 20.1 %) configurations, with the specimens with stirrups presenting superior values for the first (31.5 %), second (24.6 %), and third (28.0 %) modes when compared with the specimens without stirrups. It means that most probably the inclusion of stirrups enhanced the number of microstructural defects on the WS specimens, leading to a larger number of crack initiation points, even if visually the crack pattern of the damaged specimens is significantly more discrete (chapter 4).

As the values of natural frequencies are widely dependent on a specimen's modal mass, stiffness, and boundary conditions, comparisons of the values obtained on the present program with other studies become impractical. Yet, overall benchmarks can be drawn based on the results of the damping coefficients. The undamaged RC beams presented values fairly in agreement with the examined references [152,153], with a maximum dispersion of 52.3% (WS) on the second mode and 36.5% on the third (WOS). However, the values obtained for the first mode deeply contrasted, matching the results of damaged specimens. This behavior is a strong indicator that the first vibrational mode is markedly more controlled by a friction damping, being more affected by the defects (microcracks, voids) intrinsically present on RC members, even under negligible stress states [152]. The second and third modes, in turn, appear to assume a larger portion of the viscous damping typically related to uncracked specimens.

The natural frequencies and damping values according to the first three vibration modes based on the FD and TD analysis for the damaged beams with stirrups considering an impactor speed until 25.73 m/s are available in Table 5.5. It should be noted that the beams of the WOS configuration, as the WS specimens tested on speeds of 29.9 m/s did not preserve any beam stability, preventing the observation of their modal parameters. As aforementioned, the modal analysis of the damaged specimens in general entailed a great difficulty of identification of the natural frequencies peaks even counting with the ANPSD spectrums (see also Fig. 5.6b); the dismissed parameters were also related to the acknowledgement of “mixed-mode” NMC plots on the monitored peaks, i.e. it was not possible to clearly distinguish the mode shapes from the theoretical ones.

Table 5.5 – Natural frequencies and damping values of the damaged RC beams with stirrups obtained through TD and FD for the first three theoretical modes.

Speed [m/s]	Mode 1				Mode 2				Mode 3			
	f _{FD} 1 [Hz]	f _{TD} 1 [Hz]	ζ _{FD} 1 [%]	ζ _{TD} 1 [%]	f _{FD} 2 [Hz]	f _{TD} 2 [Hz]	ζ _{FD} 2 [%]	ζ _{TD} 2 [%]	f _{FD} 3 [Hz]	f _{TD} 3 [Hz]	ζ _{FD} 3 [%]	ζ _{TD} 3 [%]
17.29	74.84	—	3.78	—	—	—	—	—	—	—	—	—
21.79	79.48	79.42	7.16	8.11	539.57	530.98	3.33	8.63	1338.70	1336.20	1.41	4.33
25.73	88.19	88.98	7.47	3.74	235.46	242.18	7.48	11.53	1169.50	1030.90	1.66	10.00

The parameters referred to the damaged RC beams displayed much more significant dispersion, especially on the damping values, with average values ever exceeding the maximum reference value of 4 % [152,153,231]. It was found a maximum average dispersion of 91.0 % (21.9 m/s), 137.8 % (25.7 m/s), and 45.8 % (25.7 m/s) for the first, second, and third modes, respectively.

Unexpectedly, the greater damage was observed on the beam subjected to 17.29 m/s of impactor speed, which presented the larger reduction in the natural frequency of the first mode while presenting negligible enhancement on the damping value as would be expected for cracked specimens. This is most probably caused by a greater content of internal defects on this beam due to problems during the specimen preparation, which led to an intact state internally much more impaired than what was expected by visual inspection. Indeed, this specimen already presented a natural frequency for the first mode on the intact state quite below the average (7.3 %), representing a reduction of 18.4 % while on the damaged

state. This reduction, as of the other specimens here referred, will be better illustrated on the next section.

5.4.2. RC-beams strengthened with SHCC

The analysis of the strengthened specimens followed the same protocol as the reference beams. The values were listed in the Table 5.6 to Table 5.8, so that they were sorted by type of reinforcement and strengthening. As well as the RC beams, the intact strengthened specimens also entailed an uncertainty regarding the detection of the peaks lower than 500 Hz (Fig. 5.7), justifying the auxiliary plot of the spectrums based on the ANPSD. At first, all significant peaks were monitored. Only when identified a resemblance between an NMC shape and one of the first three theoretical modes, that the peak was properly labeled.

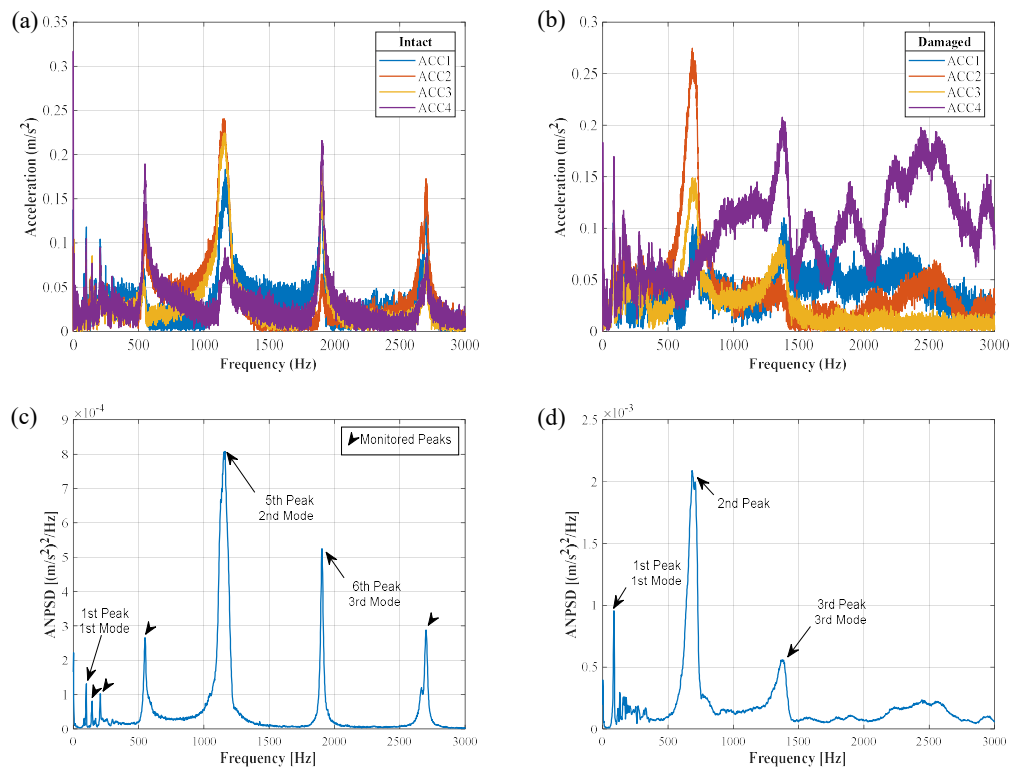


Fig. 5.7 – Typical vibration spectra for the strengthened specimens and natural frequencies associated with the three first vibrational modes (e.g. WOS-PVA): (a) FFT before the impact; (b) FFT after the impact; (a) ANPSD before the impact; (b) ANPSD after the impact.

The intact strengthened beams also presented an experimental mode without correlation with the first three theoretical vibration modes on the peak associated with the frequencies around 500 Hz. In fact, when comparing the correspondent

natural frequencies of the peaks selected through NMC of the reference specimens (RC beams) with the ones that received the SHCC layers, it is possible to observe that these values corresponding to the three vibration modes are similar to each other, as shown in Fig. 5.8. This finding indicates that the SHCC initially only slightly affects the natural frequencies of the intact beams.

Table 5.6 – Natural frequencies and damping values of the intact strengthened beams obtained through TD and FD for the first three theoretical modes.

	Mode 1				Mode 2				Mode 3			
	f_{FD} 1 [Hz]	f_{TD} 1 [Hz]	ζ_{FD} 1 [%]	ζ_{TD} 1 [%]	f_{FD} 2 [Hz]	f_{TD} 2 [Hz]	ζ_{FD} 2 [%]	ζ_{TD} 2 [%]	f_{FD} 3 [Hz]	f_{TD} 3 [Hz]	ζ_{FD} 3 [%]	ζ_{TD} 3 [%]
WOS-PVA	98.13 (1.59)	87.64 (15.85)	3.03 (1.15)	2.73 (0.81)	1159.43 (4.19)	1156.99 (1.71)	1.54 (0.29)	1.83 (0.48)	1908.63 (10.69)	1906.96 (12.97)	0.55 (0.10)	0.68 (0.06)
WOS-PE	98.30 (1.39)	109.05 (19.66)	4.92 (1.89)	2.49 (1.56)	1168.13 (15.88)	1166.91 (18.83)	1.46 (0.80)	1.75 (1.10)	1906.35 (11.94)	1904.58 (12.34)	0.61 (0.08)	1.10 (0.96)
WS-PVA	97.81 (2.75)	93.09 (7.34)	3.25 (0.67)	2.67 (1.63)	1140.05 (19.42)	1138.39 (18.85)	1.37 (0.17)	1.59 (0.39)	1878.75 (26.43)	1877.48 (26.30)	0.63 (0.11)	0.84 (0.22)
WS-PE	92.69 (4.23)	91.83 (10.08)	4.19 (1.25)	3.26 (1.49)	1142.90 (4.85)	1140.74 (4.84)	1.21 (0.36)	1.31 (0.18)	1879.33 (7.71)	1875.91 (9.52)	0.54 (0.16)	1.57 (1.17)

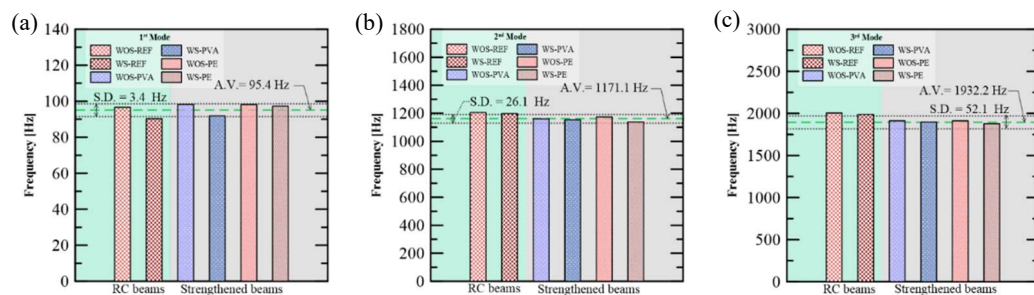


Fig. 5.8 – Average values (A.V.) and standard-deviation (S.D.) of the natural frequencies obtained through TD and FD on the intact specimens classified by type: (a) Mode 1; (b) Mode 2; (c) Mode 3. Note different y-axes.

In turn, the SHCC contribution could be fully noticed after the damage. As illustrated in Fig. 5.9, the strengthening contributed to the maintenance of the values of natural frequencies after de impact, even for the highest levels of damage (impactor speed of 29.9 m/s) on the three monitored vibrational modes. This observation agrees with the residual stability observed on the specimens that received the SHCC layers (chapter 4), and is a strong indicator of limited progression of damage [222]. On the non-strengthened specimens, none of the RC beams without stirrups outlasted any level of impact, and some specimens with

stirrups withstood some vibrational response even if with the substantial average reduction of 37 % on the values of natural frequencies. In contrast, almost all the strengthened beams overcame the reference values (WOS-PVA, 25.0 %; WS-PVA, 23.5 %; WS-PE, 24.7 %) corresponding to damaged RC beams with stirrups (see also Table 5.4), except for the beams without stirrups strengthened with PE-SHCC, which seemed to present a higher density of cracks though with a smaller opening width (chapter 4). This higher global deformation most probably impaired the WOS-PE specimens internal integrity, and thus their vibrational response on Mode 2 (see Fig. 5.9b) resulting in an average global decrease of 46.4 %, even if no significant deterioration could be optically observed.

Table 5.7 – Natural frequencies of the damaged strengthened beams for the first three theoretical modes.

Config.	Speed [m/s]	f,FD_1 [Hz]	f,TD_1 [Hz]	f,FD_2 [Hz]	f,TD_2 [Hz]	f,FD_3 [Hz]	f,TD_3 [Hz]
WOS-PVA	21.41	85.09	86.25	700.08	–	1374.80	1380.10
	26.30	87.28	85.61	572.80	565.84	1281.05	1220.33
		(1.31)	(4.39)	(16.88)	(17.44)	(150.40)	(141.32)
	29.85	81.66	81.16	–	–	–	–
WOS-PE	20.38	82.92	83.69	660.28	656.37	1197.10	1246.10
	25.33	80.50	76.09	434.84	430.28	1192.00	1184.10
		(3.13)	(8.73)	(142.55)	(136.15)	–	–
	29.90	88.46	88.97	330.33	320.75	1615.00	1559.45
WS-PVA	20.02	98.34	91.27	778.28	772.64	1437.70	1432.95
	26.26	89.61	77.62	679.70	658.44	1372.60	1375.80
		(3.18)	(10.30)	(50.53)	(32.56)	–	–
	29.45	86.98	87.14	675.34	672.04	1390.10	1381.70
WS-PE	20.54	81.98	70.16	699.32	691.27	1743.00	1740.40
	25.71	87.30	87.23	641.01	633.95	1263.90	1283.75
		(7.48)	(7.53)	(6.46)	(3.38)	–	–
	29.90	86.98	87.04	675.34	672.54	1394.90	1383.30

The maintenance of the values of natural frequencies, as the level of deterioration of the specimens, is antagonistic to the enhancement of the damping coefficient values since the cracking process usually enlarges a structural element's capacity to absorb energy through the development of elastic and plastic (new surfaces, for cement-based materials) deformations [152]. Therefore, not surprisingly the RC specimens with stirrups, notably the ones that poorly outlasted the impact events, presented the greatest increase in the global damping coefficient

(55.2 %), which takes into account only the values corresponding to an established vibrational performance on the undamaged and damaged states; see Table 5.9. Nevertheless, with the exception of the WOS-PVA specimens that presented a discrete increase in this value (14.8 %) attributed to the rapid crack localization of the strengthening layers observed on these specimens (see chapter 4), the beams of the remaining configurations displayed substantial enhancements on the same parameter (WOS-PE, 55.4%; WS-PVA, 40.3 %; WS-PE, 43.9%), notoriously without compromising their residual stability (see chapter 4). From these findings it is clear that PVA-SHCC is more sensitive to the internal reinforcement configuration since the absence of stirrups seemed to jeopardize the internal stresses path. PE-SHCC appeared to better hold the transferred energy, presenting an extremely dense cracking pattern with cracks of small width while the substrate presented itself with severe levels of deterioration (chapter 4).

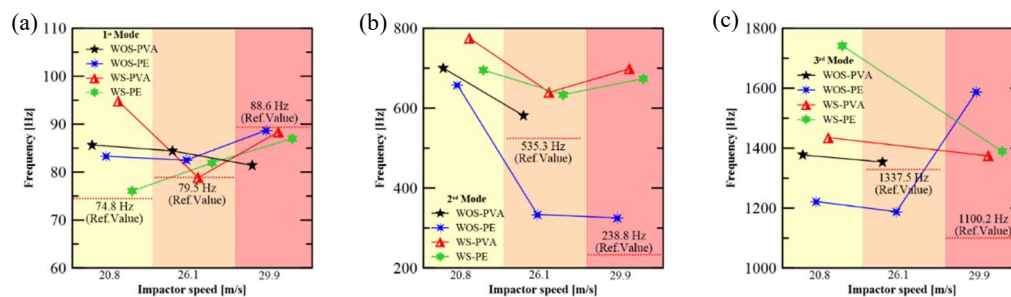


Fig. 5.9 – Average values of the natural frequencies obtained through TD and FD in function of the impactor speed regarding the SHCC damaged specimens classified by type: (a) Mode 1; (b) Mode 2; (c) Mode 3. Note different y-axes. Values on the x-axis are out of phase to improve the visualization. The reference values (Ref. Value) corresponds to the average value obtained on the damaged RC beams with stirrups (see also Table 5.5).

Another outstanding contribution of the SHCC strengthening layers was its participation concerning the modal parameters maintenance while ensuring residual structural stability in the occasion of multiple impact events. As presented in Fig. 5.10, the strengthened beams were able to repeatedly endure average impact energies of 4.8 kJ. The values of natural frequencies on the undamaged state (0 impacts) are compared with the values obtained after 1, 2, and 3 impacts. The dotted reference values emphasize the magnitude of the natural frequencies of the reference specimens with stirrups, the only RC-only configuration that displayed residual vibrational response after one impact event. Despite the reduction of the

natural frequencies associated with the three analytical vibrational modes, especially pronounced for the second and third modes, it is notorious the afterlife capability provided by the strengthening layers. Emphasis is given to PE-SHCC which was able to stand up to two additional impact events on the WS configuration.

Table 5.8 – Damping values of the damaged strengthened beams for the first three theoretical modes.

Config.	Speed [m/s]	ζ_{FD_1} [%]	ζ_{TD_1} [%]	ζ_{FD_2} [%]	ζ_{TD_2} [%]	ζ_{FD_3} [%]	ζ_{TD_3} [%]
WOS-PVA	21.41	5.48	4.08	3.23	—	1.38	3.25
	26.30	4.88	2.57	3.20	4.73	1.50	6.89
		(0.91)	(0.04)	(0.25)	(0.30)	(0.21)	(0.88)
WOS-PE	20.38	10.56	6.56	5.53	7.07	10.05	8.96
	25.33	4.16	2.94	3.64	5.88	1.33	3.83
		(0.63)	(0.31)	(0.44)	(0.46)	—	—
WS-PVA	29.90	3.77	2.38	2.15	3.07	1.04	9.83
	20.02	4.57	1.54	1.00	3.18	0.49	3.19
	26.26	6.43	5.15	2.53	4.02	1.34	2.30
WS-PE		(0.49)	(0.93)	(0.04)	(1.15)	—	—
	29.45	3.33	1.56	2.59	4.62	1.66	4.24
	20.54	7.22	7.24	3.28	4.97	1.56	4.22
	25.71	3.99	2.22	2.72	4.17	1.49	2.53
		(0.25)	(0.41)	(0.12)	(0.11)	—	—
	29.90	3.33	1.45	2.59	4.62	1.37	4.32

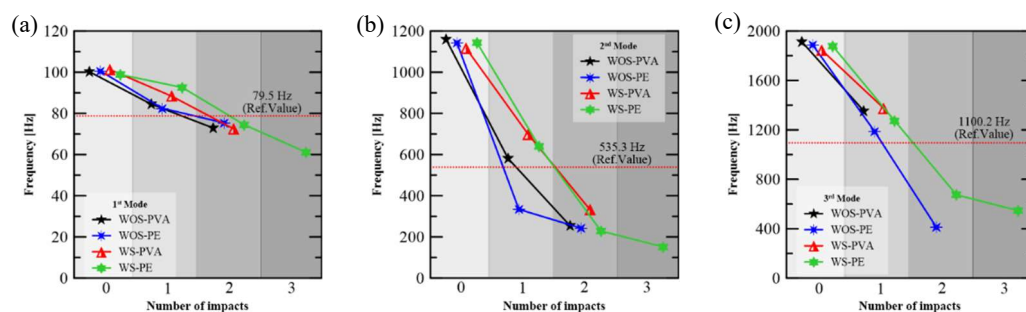


Fig. 5.10 – Average values of the natural frequencies of the SHCC specimens subjected to more than one impact at the speed of 26.1 m/s: (a) Mode 1; (b) Mode 2; (c) Mode 3. Note different y-axes. Values on the x-axis are out of phase to improve the visualization.

As illustrated in Fig. 5.11, the values of the average damping coefficients displayed the opposite tendency, significantly increasing with the additional impact

events. The results tended to exceed the regular reference value of 4 % related to building beams [152,153], almost achieving levels ~10% associated to beam-slabs usable in bridges when subjected to cyclic loading [231]. The configuration WOS-PE exhibited the highest global level of damping when comparing the three modes, enhancing the damping coefficient on 144 % after the first impact, and an additional 107 % after the second, when the level of deterioration detected by visual inspection was considered overly substantial and the loading was interrupted. Both configurations of internal reinforcement which specimens were strengthened with PVA-SHCC held a similar performance, presenting an increase in the damping coefficient of 92 % and 112 % on the first impact event, and 15 % compared to 7 % on the second event for WOS-PVA and WS-PVA, respectively. The configuration WS-PE, that was able to endure more events, displayed a mildly discrete increase on the same parameter presenting enhancements of 60 %, 84 %, and 19 % from the undamaged state to the first, second, and third impact events, respectively.

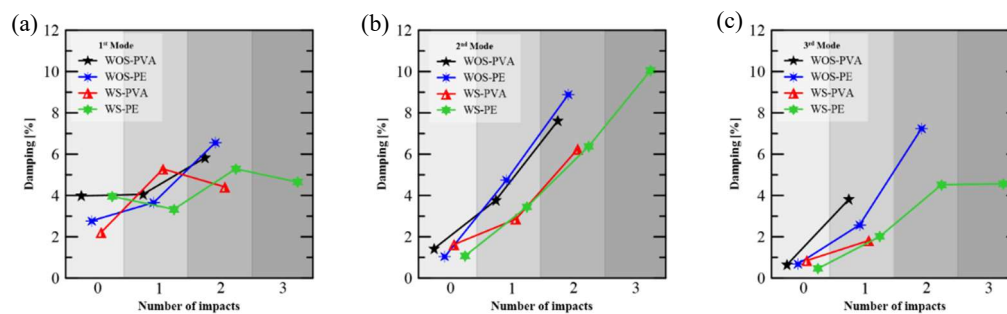


Fig. 5.11 – Average values of damping on the specimens subjected to more than one impact at the speed of 26.1 m/s: (a) Mode 1; (b) Mode 2; (c) Mode 3. Note different y-axes. Values on the x-axis are out of phase to improve the visualization.

The analysis of the damage indices [see Eqs. (1) and (2)] enabled a better assessment of the overall behavior of the tested specimens. These values were summarized in Table 5.9, where the absent values correspond to combinations where no vibrational response could be detected after the damage, preventing the determination of the indices. Positive values of both indices indicate the expected increase in the progression of structural damage, while negative values suggest a pseudo global hardening surely associated with the multiple-cracking process of the SHCC strengthening covers. In accordance with the reference [222] the results of

the RC beams displayed a crescent correlation between the level of damage (i.e., impactor velocity) and the indices values in all the monitored vibrational modes. The results coming from the strengthened beams presented meaningful distinctions. In general, the strengthened beams displayed similar values of DI_f for all levels of damage, specially considering the second and third vibrational modes. These values are on average 30.8 % below the reference specimens (WS-Ref). Although the indexes of the strengthened specimens could not be directly compared with the results obtained for the RC-beams, as these specimens displayed a sizable mass loss during the impact event (see Chapter 5), these results are a strong indicator on the inferior reduction of stiffness on the beams strengthened with SHCC. The DI_f values related to the first mode presented a considerable variation for the beams strengthened with PVA-SHCC; while it seems to be a small stiffness disturbance, no conclusions could be drawn for certain. In contrast, the specimens strengthened with PE-SHCC tended to display higher values of stiffness degradation for the first mode than the reference specimens, even if with smaller values on the WS configuration. This could be an indication that this composite significantly contributed to the beams' global hardening during the impact event, an assumption backed by the reduction observed on the DI_ζ parameter.

Table 5.9 – Stiffness degradation (DI_f) and damping degradation (DI_ζ) indices.

Specimen variation	Impact speed [m/s]	DI_f [%]			DI_ζ [%]		
		Mode 1	Mode 2	Mode 3	Mode 1	Mode 2	Mode 3
WOS-PVA	20.7	-3.9	39.6	27.6	86.3	-9.5	287.4
	25.9	2.5	51.7	39.4	78.9	178.3	627.0
	29.8	17.1	–	–	22.7	–	–
WS-PVA	20.7	-4.4	31.5	23.3	-33.9	75.3	107.6
	25.9	19.4	44.5	–	187.9	108.8	–
	29.8	5.3	41.8	27.1	-13.7	175.2	374.8
WOS-PE	20.7	29.5	44.4	36.1	122.4	109.0	493.0
	25.9	24.5	54.7	–	-38.0	256.9	–
	29.8	9.3	72.2	17.1	16.4	150.2	794.7
WS-PE	20.7	21.8	38.9	7.0	72.5	179.3	58.4
	25.9	3.8	44.8	–	-35.8	145.5	–
	29.8	0.9	40.8	26.5	4.7	236.5	386.1

5.5. Conclusions

A modal analysis was carried out to investigate experimentally the changes in the dynamic properties of 24 full-sized RC beams subjected to impact. The program entailed the examination of the acceleration signals provided by four accelerometers installed in each specimen, assessing a combination of variables such as two configurations of transversal steel reinforcement, two configurations of shear strengthening layers made with SHCC, and increasing levels of kinetic energy varying between 2.1 kJ and 6.4 kJ. Based on the presented results, the following conclusions can be drawn:

1. The internal transversal reinforcement represents a small, but nevertheless relevant influence on the dynamic behavior of RC beams. The RC beams with the total absence of stirrups did not preserve any structural behavior regarding their vibrational response in terms of natural frequencies and vibrational modes after the damage, while the specimens with stirrups withstood a residual dynamic performance until average impact speeds of 4.8 kJ (26.1 m/s), with increased levels of the damping coefficient.

2. In general, the specimens strengthened with SHCC excelled on enduring a residual dynamic response, even standing multiple impact events while preserving the beams modal mass.

3. Both types of SHCC presented a similar dynamic performance when considering the specimens with internal transversal reinforcement. The beams without stirrups strengthened with PVA-SHCC were not able to work out higher frequencies as the ones associated with the third theoretical vibrational mode. Moreover, these specimens did not endure higher levels of impact damage (6.4 kJ, corresponding to the impactor velocity of 29.9 m/s).

4. PE-SHCC appears more suitable for application as strengthening layers of existing structural elements in case of dynamic scenarios where there is a deficient, or content uncertainty, regarding the internal shear reinforcement.

6 Conclusions and outlook

6.1. Conclusions

The contribution of SHCC as strengthening layers to improve the afterlife of existing structural beams under impact scenarios was assessed. Two variations of normal-strength SHCC were investigated, differing mainly in the type of reinforcing fiber: PVA, and PE. On the material-scale, were performed multiaxial tests combining tensile and shear stresses at quasi-static strain rates. The quasi-static tests were carried in a closed-loop servo-hydraulic system, under displacement control. On the structural scale, SHCC's effectiveness as a strengthening material to prevent shear failure in case of high-speed impact loading was evaluated with the aid of a 4-story drop-weight testing facility set to permit accelerated strikes with kinetic energy levels varying between 2.1 kJ and 6.4 kJ.

Under a quasi-static regime, PE-SHCC demonstrated superior mechanical performance under all combinations of loading when compared with PVA-SHCC. This was attributed to the superior pre- and post-peak macroscopic crack-bridging behavior of the PE fibers, which led to substantially more extensive cracking patterns. It is related in part to their smaller diameter (half of PVA fibers) which provides relatively higher fiber content acting on the crack width control, and their well-known pullout behavior with cementitious matrices, tending to the fibers being pulled out, which favors the overall stable cracking.

The monitored crack-flank displacements (CFD) showed that, even under direct tensile loading, both types of SHCC yielded significant crack-flank sliding, both in-plane and out-of-plane. This was partly traced back to the small crack inclination of the fibers bridging the already opened cracks, being initially (during the multiple-cracking stage) more significant on the PVA-SHCC specimens, which presented a relatively lower crack-width opening control. These slide-modes become more significant during the softening phase on PE-SHCC specimens (mostly in-plane), contributing to the subtle load-bearing capacity decay of this composite. PE-SHCC also excelled in the case of the shear stresses related to

torsion, and in the case of combined torsion and tension loading, enduring significantly higher deformations and displaying a more uniform distribution of cracks throughout the gauge portion when compared to PVA-SHCC.

The reported crack-bridging capacity at all CFD variations on both types of SHCC, but especially noteworthy in the case of PE-SHCC, is a reasonable indication of the potential of these composites for structural applications, where the stress states generally include a combination of normal and shear stresses. Despite the relatively limited strain-capacity displayed by the composite fabricated with PVA fibers in comparison with the one made with PE fibers in this program, which entailed a material-level evaluation under quasi-static strain-rates, its performance was considered quite reasonable for structural applications, where the local deformations are limited by the global stability of the structural member. In addition, the expected (according to the state of the art and exploratory program) strain capacity improvement of PVA-SHCC under very high strain rates (such as of impact) under direct tension stress states, encouraged the decision to follow with the evaluation of both composites on the structural level evaluation. Especially thinking on industrial applications, the SHCC produced with PVA fibers presents a less-sensible rheology, even presenting many dosages already updated for spraying, which is a differential thinking on the overall performance as strengthening layers for shear reinforcement of existing members, that could be favored by this methodology of casting.

In relation to the structural tests, it was found that both types of SHCC presented a strong synergetic composite action with the concrete-substrate, presenting outstanding adhesion and deformation compliance, eliminating the need for additional bond-bridges such as polymeric resins when provided a proper level of roughness of the substrate, a standard requirement in all types of strengthening. Both composites also achieved similar contributions in terms of stress-transference to the supports and residual stability of the specimens, while demonstrating elevated damage tolerance when excelling on the breakout material control, significantly reducing the detritus deriving from scabbing and spalling ($\approx 0\%$). PE-SHCC stood out displaying a remarkable cracking control (crack widths varying between 20 μm and 100 μm) even at post-failure, up to the highest levels of impact energy.

Although it was not one of the main objectives of the research at hand, the role of stirrups on RC beams alone (without strengthening) under impact loads

could also be assessed. The stirrups play a decisive role in the stress transference to the supports while limiting the defragmentation of the specimens during the event, significantly reducing the level of global damage for the studied levels of energy. Some residual stability was noticed on these specimens after the tests, although markedly inferior to the strengthened ones, mainly due to the amount of breakout material and severity of cracks. The contribution of the stirrups in the case of impact scenarios was also supported by modal analysis since the specimens without transversal reinforcement did not preserve any vibrational response in terms of natural frequencies and vibrational modes after the damage, while the specimens with stirrups withstood a residual dynamic performance until average impact energies of 4.8 kJ (26.1 m/s).

When comparing the vibrational response of the intact RC beams with the strengthened ones before the impact event, it was found that the SHCC layers represent an insignificant interference on the vibrational response of the undamaged specimens, even while considering the average enhancement of mass due to the patch's weight ($\sim 17.4\%$). The contribution of the composite could be clearly acknowledged after the impact events, considering that the specimens strengthened with SHCC excelled on enduring a residual dynamic response, even standing multiple impacts (under kinetic energy of 4.8 kJ, corresponding to an average velocity of the impactor of 26.1 m/s) while preserving the modal mass of the specimens. In contrast to the ones strengthened with PE-SHCC, the beams without stirrups strengthened with PVA-SHCC were not able to work out a dynamic response correspondent to the second and third theoretical vibrational modes under higher levels of damage (6.4 kJ, corresponding to the impactor velocity of 29.9 m/s).

To sum all, although the SHCC made with PE fibers excelled on the strain capacity on the material level at quasi-static strain rates, both types of SHCC presented similar contributions in terms of stress-transference and residual stability of the strengthened specimens under impact strain rates. Both the SHCC made with PVA, as the one made with PE fibers overly improved the breakout material scabbing and spalling, thus being validated as strengthening layers for shear reinforcement for the improvement of the impact resistance of existing structural members. When considering their dynamic, residual response, the beams with stirrups strengthened with both variations of SHCC exhibited comparable

preservation of their dynamic performance after the impact tests. However, when considering the specimens without stirrups, only the ones strengthened with PE-SHCC displayed a clear modal response. Thus, PE-SHCC would be more suitable for shear strengthening applications within dynamic scenarios where there is a deficient, or content uncertainty, about the internal transversal reinforcement of the existing members.

6.2. Suggestions for future works

While the present research presented novel results concerning the multiaxial response of SHCC and its application as strengthening layers of RC members, it also highlighted new demands for specific investigations, such as:

- The performance of the already developed tests combining tension and torsion on high-strength SHCC, as a step to better understand their performance under multiaxial stress states, aiming a future structural application.
- The calibration of a numerical model able to describe the behavior of the studied normal-strength SHCC produced with PVA and PE fibers, based on the results of the monitored CFD, which would enable future numerical enterprises under quasi-static strain rates.
- The development and performance of multiaxial tests combining tension and torsion on SHCC under high-speed regimes, also focusing on the monitoring of the CFD, thus establishing a reliable database for numerical simulations using the Finite Element Method.
- The conduction of triaxial tests under different confining pressures of the concrete used on the fabrication of the structural beams, focusing on the influence of confinement on the plastification properties of the substrate region just below the contact point, and how these parameters affect the perforation depth on the reference and strengthened specimens.

References

- [1] Y. Yao, F.A. Silva, M. Butler, V. Mechtcherine, B. Mobasher, M. Butler, V. Mechtcherine, Failure Localization and Correlation of High-Speed Tension and Impact Tests of Strain-Hardening Cement-Based Composites, *J. Mater. Civ. Eng.* 29 (2017) 04017212. [https://doi.org/10.1061/\(ASCE\)MT.1943-5533.0002056](https://doi.org/10.1061/(ASCE)MT.1943-5533.0002056).
- [2] X. Li, X. Zhou, Y. Tian, M. Li, A modified cyclic constitutive model for engineered cementitious composites, *Eng. Struct.* 179 (2019) 398–411. <https://doi.org/10.1016/j.engstruct.2018.09.030>.
- [3] S. Mindess, L. Zhang, Impact resistance of fibre-reinforced concrete, *Proc. Inst. Civ. Eng. - Struct. Build.* 162 (2009) 69–76. <https://doi.org/10.1680/stbu.2009.162.1.69>.
- [4] X.H. Vu, L. Daudeville, Y. Malecot, Effect of coarse aggregate size and cement paste volume on concrete behavior under high triaxial compression loading, *Constr. Build. Mater.* 25 (2011) 3941–3949. <https://doi.org/10.1016/j.conbuildmat.2011.04.026>.
- [5] J.C. Walraven, Symposium Eurocodes: Backgrounds and Applications. Brussels, (2008).
- [6] RILEM TC 162-TDF: “Test and design methods for steel fibre reinforced concrete,” Stress-strain design method: Final Recommendation, *Mater. Struct.* 36 (2003) 560–567.
- [7] A.E. Naaman, Engineered Steel Fibers with Optimal Properties for Reinforcement of Cement Composites, *J. Adv. Concr. Technol.* 1(3) (2003) 241–252.
- [8] H. Ma, E. Herbert, M. Ohno, V.C. Li, Scale-linking model of self-healing and stiffness recovery in Engineered Cementitious Composites (ECC), *Cem. Concr. Compos.* 95 (2019) 1–9.
- [9] C. Lu, J. Yu, C.K.Y.Y. Leung, Tensile performance and impact resistance of Strain Hardening Cementitious Composites (SHCC) with recycled fibers, *Constr. Build. Mater.* 171 (2018) 566–576.

- [10] I. Curosu, Influence of Fiber Type and Matrix Composition on the Tensile Behavior of Strain-Hardening Cement-Based Composites (SHCC) Under Impact Loading, Technischen Universität Dresden (TU Dresden), 2017.
- [11] D.-Y. Yoo, N. Banthia, Impact resistance of fiber-reinforced concrete – A review, *Cem. Concr. Compos.* 104 (2019) 103389. <https://doi.org/10.1016/j.cemconcomp.2019.103389>.
- [12] C.E. Chalioris, Torsional strengthening of rectangular and flanged beams using carbon fibre-reinforced-polymers - Experimental study, *Constr. Build. Mater.* 22 (2008) 21–29. <https://doi.org/10.1016/j.conbuildmat.2006.09.003>.
- [13] K. Rokugo, T. Kanda, Strain Hardening Cement Composites: Structural Design and Performance, 2013. <https://doi.org/10.1017/CBO9781107415324.004>.
- [14] V.C. Li, On Engineered Cementitious Composites (ECC) - A Review of the material and its applications, *J. Adv. Concr. Technol.* 1(3) (2003) 215–230.
- [15] B.T. Huang, Q.H. Li, S.L. Xu, B. Zhou, Strengthening of reinforced concrete structure using sprayable fiber-reinforced cementitious composites with high ductility, *Compos. Struct.* 220 (2019) 940–952.
- [16] V. Mechtcherine, V. Slowik, P. Kabele, Strain-hardening cement-based composites: SHCC4, RILEM Bookseries. 15 (2018) iii–iv. <https://doi.org/10.1007/978-94-024-1194-2>.
- [17] A.E.H. Khalil, E. Etman, A. Atta, M. Essam, Behavior of RC beams strengthened with strain hardening cementitious composites (SHCC) subjected to monotonic and repeated loads, *Eng. Struct.* 140 (2017) 151–163. <https://doi.org/10.1016/j.engstruct.2017.02.049>.
- [18] T.C.S.P. Figueiredo, I. Curosu, G.L.G. Gonzáles, M. Hering, F.A. Silva, M. Curbach, V. Mechtcherine, Mechanical behavior of strain-hardening cement- based composites (SHCC) subjected to torsional loading and to combined torsional and axial loading, *Mater. Des.* 198 (2021) 14. <https://doi.org/https://doi.org/10.1016/j.matdes.2020.109371>.
- [19] A.E. Naaman, Fiber Reinforced Concrete: Five Decades of Progress, in: BCCM4 - 4th Brazilian Conf. Compos. Mater., Rio de Janeiro, Brasil, 2018.
- [20] A.E. Naaman, Half a Century of Progress Leading to Ultra-High Performance Fiber Reinforced Concrete: Part 2 - Tensile Stress-Strain Response, in: Proc. 2nd Int. RILEM Conf. Strain Hardening Cem. Compos.,

- Rio de Janeiro, Brasil, 2011: pp. 17–26.
- [21] A.M. De Oliveira, F.D.A. Silva, E. De Moraes, R. Fairbairn, R. Dias, T. Filho, Coupled temperature and moisture effects on the tensile behavior of strain hardening cementitious composites (SHCC) reinforced with PVA fibers, *Mater. Struct.* (2018) 51–65.
 - [22] V. Mechtcherine, O. Millon, M. Butler, K. Thoma, Mechanical behaviour of strain hardening cement-based composites under impact loading, *Cem. Concr. Compos.* 33 (2011) 1–11. <https://doi.org/10.1016/j.cemconcomp.2010.09.018>.
 - [23] V. Mechtcherine, F.D.A. Silva, M. Butler, D. Zhu, B. Mobasher, S.-L. Gao, E. Mäder, Behaviour of Strain-Hardening Cement-Based Composites Under High Strain Rates, *J. Adv. Concr. Technol.* 9 (2011) 51–62. <https://doi.org/10.3151/jact.9.51>.
 - [24] A.M. Oliveira, F.A. Silva, E.M. Fairbairn, R.D.T. Filho, Temperature and internal moisture effects on the tensile behavior of strain-hardening cement-based composites (SHCC) reinforced with PVA fibers, in: 3rd Int. RILEM Conf. Strain Hardening Cem. Compos., Dordrecht, Netherlands, 2014. <https://doi.org/10.13140/2.1.4566.7522>.
 - [25] Y. Chen, J. Yu, C.K.Y. Leung, Use of high strength Strain-Hardening Cementitious Composites for flexural repair of concrete structures with significant steel corrosion, *Constr. Build. Mater.* 167 (2018) 325–337. <https://doi.org/10.1016/j.conbuildmat.2018.02.009>.
 - [26] V. Mechtcherine, F.D.A. Silva, S. Müller, P. Jun, R.D.T. Filho, Coupled strain rate and temperature effects on the tensile behavior of strain-hardening cement-based composites (SHCC) with PVA fibers, *Cem. Concr. Res.* 42 (2012) 1417–1427. <https://doi.org/10.1016/j.cemconres.2012.08.011>.
 - [27] E. Secieru, V. Mechtcherine, C. Schröfl, D. Borin, Rheological characterisation and prediction of pumpability of strain-hardening cement-based-composites (SHCC) with and without addition of superabsorbent polymers (SAP) at various temperatures, *Constr. Build. Mater.* 112 (2016) 581–594. <https://doi.org/10.1016/j.conbuildmat.2016.02.161>.
 - [28] K.Q. Yu, J.G. Dai, Z.D. Lu, C.S. Poon, Rate-dependent tensile properties of ultra-high performance engineered cementitious composites (UHP-ECC), *Cem. Concr. Compos.* (2018).

- [29] M. Deng, Y. Zhang, Q. Li, Shear strengthening of RC short columns with ECC jacket: Cyclic behavior tests, *Eng. Struct.* 160 (2018) 535–545. <https://doi.org/10.1016/j.engstruct.2018.01.061>.
- [30] Y. Zheng, L.F. Zhang, L.P. Xia, Investigation of the behaviour of flexible and ductile ECC link slab reinforced with FRP, *Constr. Build. Mater.* 166 (2018) 694–711. <https://doi.org/10.1016/j.conbuildmat.2018.01.188>.
- [31] S. Müller, V. Mechtcherine, Fatigue behaviour of strain-hardening cement-based composites (SHCC), *Cem. Concr. Res.* (2017).
- [32] K. Kobayashi, Y. Asano, K. Rokugo, Application of HPFRCC as a patching repair material for RC-members exposed to chloride attack, in: 2nd Int. RILEM Conf. Strain Hardening Cem. Compos., Rio de Janeiro, Brasil, 2011: pp. 173–180.
- [33] J. Cai, J. Pan, X. Li, Behavior of ECC-encased CFST columns under axial compression, *Eng. Struct.* 171 (2018) 1–9. <https://doi.org/10.1016/j.engstruct.2018.05.090>.
- [34] F.A. Silva, Cementitious materials and Fiber reinforced composites courses – Class notes, (2017).
- [35] K. Kobayashi, D. Le Ahn, K. Rokugo, Effects of crack properties and water-cement ratio on the chloride proofing performance of cracked SHCC suffering from chloride attack, *Cem. Concr. Compos.* 69 (2016) 18–27. <https://doi.org/10.1016/j.cemconcomp.2016.03.002>.
- [36] G.P.A.G. van Zijl, S.C. Paul, Crack distribution linked to chloride-induced corrosion in R/SHCC, in: BEFIB 2016 - RILEM Int. Symp. FIBER Reinf. Concr., RILEM BEFIB 2016, 2016.
- [37] K. Kobayashi, M. Suzuki, L.A. Dung, H. do Yun, K. Rokugo, The effects of PE and PVA fiber and water cement ratio on chloride penetration and rebar corrosion protection performance of cracked SHCC, *Constr. Build. Mater.* 178 (2018) 372–383.
- [38] K. Kobayashi, Y. Kojima, Effect of fine crack width and water cement ratio of SHCC on chloride ingress and rebar corrosion, *Cem. Concr. Compos.* 80 (2017) 235–244. <https://doi.org/10.1016/j.cemconcomp.2017.03.006>.
- [39] I. Curosu, M. Liebscher, V. Mechtcherine, C. Bellmann, S. Michel, Tensile behavior of high-strength strain-hardening cement-based composites (HS-SHCC) made with high-performance polyethylene, aramid and PBO fibers,

- Cem. Concr. Res. 98 (2017) 71–81.
<https://doi.org/10.1016/j.cemconres.2017.04.004>.
- [40] I. Curosu, V. Mechtcherine, D. Forni, E. Cadoni, Performance of various strain-hardening cement-based composites (SHCC) subject to uniaxial impact tensile loading, *Cem. Concr. Res.* (2017).
- [41] A.A. Heravi, O. Smirnova, V. Mechtcherine, Effect of Strain Rate and Fiber Type on Tensile Behavior of High-Strength Strain-Hardening Cement-Based Composites (HS-SHCC), *RILEM Bookseries*. 15 (2018) 266–274.
<https://doi.org/10.1007/978-94-024-1194-2>.
- [42] J. Yu, J. Yao, X. Lin, H. Li, J.Y.K. Lam, C.K.Y. Leung, I.M.L. Sham, K. Shih, Tensile performance of sustainable Strain-Hardening Cementitious Composites with hybrid PVA and recycled PET fibers, *Cem. Concr. Res.* 107 (2018) 110–123. <https://doi.org/10.1016/j.cemconres.2018.02.013>.
- [43] A.M. Oliveira, High temperature creep, fiber-matrix adhesion and mechanical behavior under hygrothermal actions of cementitious composites reinforced with PVA fibers (in Portuguese), Universidade Federal do Rio de Janeiro, 2015.
- [44] M.S. Magalhães, Experimental characterization of fiber reinforced composites made with PVA fibers: fracture process, thermal properties, deferred deformations and thermal stability (in Portuguese), UFRJ/COPPE, 2010.
- [45] H. Fakhri, Y. Han, R. Ranade, Influence of Damage on the Effectiveness of SHCC Covers for Reducing Corrosion Rates in Reinforced-Concrete Structural Elements, *RILEM Bookseries*. 15 (2017) iii–iv.
<https://doi.org/10.1007/978-94-024-1194-2>.
- [46] V.C. Li, C. Wu, S. Wang, A. Ogawa, T. Saito, Interface tailoring for strain-hardening polyvinyl alcohol-engineered cementitious composite (PVA-ECC), *ACI Mater. J.* 99(5) (2002) 463–472.
- [47] T. Kanda, V.C. Li, Practical Design Criteria for Saturated Pseudo Strain Hardening Behavior in ECC, *J. Adv. Concr. Technol.* 4 (2006) 59–72.
<https://doi.org/10.3151/jact.4.59>.
- [48] Z. Zhang, Q. Zhang, Matrix tailoring of Engineered Cementitious Composites (ECC) with non-oil-coated, low tensile strength PVA fiber, *Constr. Build. Mater.* 161 (2018) 420–431.

- <https://doi.org/10.1016/j.conbuildmat.2017.11.072>.
- [49] V.C. Li, C.K.Y. Leung, Steady-State and Multiple Cracking of Short Random Fiber Composites, *J. Eng. Mech.* 118 (1992) 2246–2264. [https://doi.org/10.1061/\(ASCE\)0733-9399\(1992\)118:11\(2246\)](https://doi.org/10.1061/(ASCE)0733-9399(1992)118:11(2246)).
 - [50] V.C. Li, H.-C. Wu, Conditions for pseudo strain-hardening in fiber reinforced brittle matrix composites, in: V.C. Li (Ed.), *Micromechanical Model. Quasi-Brittle Mater. Behav.*, ASCE, 1992: pp. 390–398.
 - [51] H. Ma, S. Qian, Z. Zhang, Z. Lin, V.C. Li, Tailoring Engineered Cementitious Composites with local ingredients, *Constr. Build. Mater.* 101 (2015) 584–595.
 - [52] R.P. Batista, INTERFERÊNCIA DA COMPOSIÇÃO DA MATRIZ NO DESEMPENHO MECÂNICO DE COMPÓSITOS ÁLCALI-ATIVADOS REFORÇADOS COM FIBRAS CURTAS DE PVA, CEFET-MG, 2018.
 - [53] D.B. Marshall, B.N. Cox, A J-Integral method for calculating steady-state matrix cracking stresses in composites, *Mech. Mater.* 7 (1988) 127–133.
 - [54] C. Li, V.C., Wang, S. and Wu, Tensile strain-hardening behaviour of Polyvinyl Alcohol Engineered Cementitious Composites (PVA-ECC), *ACI Mater. J.* (2001) 483–492. <https://doi.org/10.14359/10851>.
 - [55] Z. Pan, C. Wu, J. Liu, W. Wang, J. Liu, Study on mechanical properties of cost-effective polyvinyl alcohol engineered cementitious composites (PVA-ECC), *Constr. Build. Mater.* 78 (2015) 397–404. <https://doi.org/10.1016/j.conbuildmat.2014.12.071>.
 - [56] Steady-state and Griffith's types of crack, (n.d.). <https://images.app.goo.gl/6qeVRHYajzSzjq6QA> (accessed January 10, 2021).
 - [57] S. Abrate, *Impact on composite structures*, Cambridge University Press, 1998.
 - [58] I. Curosu, V. Mechtcherine, O. Millon, Effect of fiber properties and matrix composition on the tensile behavior of strain-hardening cement-based composites (SHCC) subject to impact loading, *Cem. Concr. Res.* (2016).
 - [59] W.P. Boshoff, V. Mechtcherine, G.P.A.G. van Zijl, Characterising the time-dependant behaviour on the single fibre level of SHCC: Part 1: Mechanism of fibre pull-out creep, *Cem. Concr. Res.* 39 (2009) 779–786. <https://doi.org/10.1016/j.cemconres.2009.06.007>.

- [60] W.P. Boshoff, G.P.A.G. van Zijl, Time-dependent response of ECC: Characterisation of creep and rate dependence, *Cem. Concr. Res.* 37 (2007) 725–734. <https://doi.org/10.1016/j.cemconres.2007.02.001>.
- [61] W.P. Boshoff, C.J. Adendorff, Effect of sustained tensile loading on SHCC crack widths, *Cem. Concr. Compos.* 37 (2013) 119–125.
- [62] E. Yang, V.C. Li, Strain-rate effects on the tensile behavior of strain-hardening cementitious composites, *Constr. Build. Mater.* 52 (2014) 96–104. <https://doi.org/10.1016/j.conbuildmat.2013.11.013>.
- [63] I. Curosu, V. Mechtcherine, D. Forni, E. Cadoni, Dynamic Tensile Behaviour of Strain-Hardening Cement-Based Composites (SHCC), *EPJ Web Conf.* 183 (2018) 02015. <https://doi.org/10.1051/epjconf/201818302015>.
- [64] I. Curosu, V. Mechtcherine, O. Millon, Effect of fiber properties and matrix composition on the tensile behavior of strain-hardening cement-based composites (SHCCs) subject to impact loading, *Cem. Concr. Res.* 82 (2016) 23–35. <https://doi.org/10.1016/j.cemconres.2015.12.008>.
- [65] J. Yu, J. Lin, Z. Zhang, V.C. Li, Mechanical performance of ECC with high-volume fly ash after sub-elevated temperatures, *Constr. Build. Mater.* 99 (2015) 82–89. <https://doi.org/10.1016/j.conbuildmat.2015.09.002>.
- [66] M.T. Taghizadeh, N. Sabouri, Thermal Degradation Behavior of Polyvinyl Alcohol/Starch/Carboxymethyl Cellulose/ Clay Nanocomposites, *Univers. J. Chem.* 1 (2013) 21–29. <https://doi.org/10.13189/ujc.2013.010202>.
- [67] T. Soetens, S. Matthys, Shear-stress transfer across a crack in steel fibre-reinforced concrete, *Cem. Concr. Compos.* 82 (2017) 1–13. <https://doi.org/10.1016/j.cemconcomp.2017.05.010>.
- [68] W. Kaufmann, A. Amin, A. Beck, M. Lee, Shear transfer across cracks in steel fibre reinforced concrete, *Eng. Struct.* 186 (2019) 508–524. <https://doi.org/10.1016/j.engstruct.2019.02.027>.
- [69] V. Li, D. Mishra, A. Naaman, J. Wigh, J. LaFave, H. Wu, Y. Inada, On the shear behavior of engineered cementitious composites, *Adv. Cem. Based Mater.* (1994) 142–149.
- [70] G.P.A.G. van Zijl, Improved mechanical performance: Shear behaviour of strain-hardening cement-based composites (SHCC), *Cem. Concr. Res.* 37 (2007) 1241–1247.

- [71] Y.X. Zhang, N. Ueda, Y. Umeda, H. Nakamura, M. Kunieda, Evaluation of shear failure of Strain Hardening Cementitious Composite beams, *Procedia Eng.* 14 (2011) 2048–2057. <https://doi.org/10.1016/j.proeng.2011.07.257>.
- [72] S. Xu, L.-J. Hou, X.-F. Zhang, Shear Behavior of Reinforced Ultrahigh Toughness Cementitious Composite Beams without Transverse Reinforcement, *J. Mater. Civ. Eng.* 24 (2012) 1283–1294. [https://doi.org/10.1061/\(asce\)mt.1943-5533.0000505](https://doi.org/10.1061/(asce)mt.1943-5533.0000505).
- [73] L. Hou, S. Xu, X. Zhang, D. Chen, Shear Behaviors of Reinforced Ultrahigh Toughness Cementitious Composite Slender Beams with Stirrups, *J. Mater. Civ. Eng.* 26 (2013) 466–475. [https://doi.org/10.1061/\(asce\)mt.1943-5533.0000833](https://doi.org/10.1061/(asce)mt.1943-5533.0000833).
- [74] L. Yin, C. Yan, S. Liu, J. Zhang, M. Liang, Shear behavior of a strain hardening cementitious composites (SHCC)-Grooved steel composite deck, *Compos. Part B Eng.* 160 (2019) 195–204. <https://doi.org/10.1016/j.compositesb.2018.10.025>.
- [75] K. Shimizu, T. Kanakubo, T. Kanda, S. Nagai, SHEAR BEHAVIOR OF STEEL REINFORCED PVA-ECC BEAMS, in: 13th World Conf. Earthq. Eng. (Vancouver, Canada), 2004: pp. 74–76. [https://doi.org/10.1016/0093-6413\(82\)90023-4](https://doi.org/10.1016/0093-6413(82)90023-4).
- [76] H. Baghi, J.A.O. Barros, M. Rezazadeh, Shear strengthening of damaged reinforced concrete beams with Hybrid Composite Plates, *Compos. Struct.* 178 (2017) 353–371. <https://doi.org/10.1016/j.compstruct.2017.07.039>.
- [77] E. Esmaeeli, F. Danesh, K.F. Tee, S. Eshghi, A combination of GFRP sheets and steel cage for seismic strengthening of shear-deficient corner RC beam-column joints, *Compos. Struct.* 159 (2017) 206–219. <https://doi.org/10.1016/j.compstruct.2016.09.064>.
- [78] Y. Zhang, H. Peng, W. Lv, Shear stress transfer model for evaluating the fracture behaviour of SHCCs for RC shear strengthening, *Mag. Concr. Res.* 70 (2018) 512–518. <https://doi.org/10.1680/jmacr.17.00104>.
- [79] G. Wang, C. Yang, Y. Pan, F. Zhu, K. Jin, K. Li, A. Nanni, Shear behaviors of RC beams externally strengthened with engineered cementitious, *Materials (Basel)*. 12(2163) (2019) 1–16.
- [80] J. Wei, Y. Chen, C. Wu, C.K.Y. Leung, Shear strengthening of reinforced concrete beams with high strength strain-hardening cementitious composites

- (HS-SHCC), in: Proc. Fram. Bayonne, 2019: pp. 1–9.
- [81] J. Tian, X. Wu, Y. Zheng, S. Hu, Y. Du, W. Wang, C. Sun, L. Zhang, Investigation of interface shear properties and mechanical model between ECC and concrete, *Constr. Build. Mater.* 223 (2019) 12–27. <https://doi.org/10.1016/j.conbuildmat.2019.06.188>.
 - [82] A. Hassan, A.M. Atta, T.F. El-Shafiey, Restoration of the shear capacity for RC beams with web openings using precast SHCC plates, *Structures*. 25 (2020) 603–612. <https://doi.org/10.1016/j.istruc.2020.03.046>.
 - [83] Q. Shang, G.P.A.G. Van Zijl, Characterising the shear behaviour of strainhardening fibre-reinforced cement-based composites, *J. South African Inst. Civ. Eng.* 49(2) (2007) 16–23.
 - [84] T. Kanakubo, K. Shimizu, S. Nagai, T. Kanda, Shear transmission on crack surface of ECC, *Proc. Fram. Jeju.* (2010) 1623–1630.
 - [85] H. Baghi, J.A.O. Barros, Shear properties of the strain hardening cementitious composite material, *J. Mater. Civ. Eng.* 28(10) (2016) 1–13. [https://doi.org/10.1061/\(ASCE\)MT.1943-5533.0001603](https://doi.org/10.1061/(ASCE)MT.1943-5533.0001603).
 - [86] A.A. Heravi, O. Mosig, A. Tawfik, M. Curbach, An Experimental Investigation of the Behavior of under Impact Compression and Shear Loading, (2020).
 - [87] V.C. Li, High performance fiber reinforced cementitious composites as durable material for concrete structure repair, *Restor. Build. Monum. an Int. J.* 10 (2004) 163–180.
 - [88] V. Mechtcherine, Towards a durability framework for structural elements and structures made of or strengthened with high-performance fibre-reinforced composites, *Constr. Build. Mater.* 31 (2012) 94–104. <https://doi.org/10.1016/j.conbuildmat.2011.12.072>.
 - [89] F.H. Wittmann, P. Wang, P. Zhang, T. Zhao, F. Beltzung, Capillary absorption and chloride penetration into neat and water repellent shcc under imposed strain, in: 2nd Int. RILEM Conf. Strain Hardening Cem. Compos., 2011: pp. 165–172.
 - [90] C. Wagner, V. Slowik, On the water permeability of cracked strain hardening cement-based composites, in: 2nd Int. RILEM Conf. Strain Hardening Cem. Compos., 2011: pp. 181–188.
 - [91] W.P. Boshoff, P.D. Nieuwoudt, Tensile crack widths of strain hardening

- cement-based composites, in: 2nd Int. RILEM Conf. Strain Hardening Cem. Compos., 2011: pp. 199–206.
- [92] C. Wagner, B. Villmann, V. Slowik, V. Mechtcherine, Water permeability of cracked strain-hardening cement-based composites, *Cem. Concr. Compos.* 82 (2017) 234–241. <https://doi.org/10.1016/j.cemconcomp.2017.06.003>.
- [93] Y.M. Lima, V.C. Lib, Durable Repair of Aged Infrastructures Using Trapping Mechanism of Engineered Cementitious Composites, *Cem. Concr. Compos.* 19 (1997) 373–385.
- [94] ACI, 544.5R Report on the Physical Properties and Durability of Fiber-Reinforced Concrete, 2010.
- [95] A. Neville, Chloride attack of reinforced concrete: an overview, *Mater. Struct.* 28 (1995) 63–70. <https://doi.org/10.1007/BF02473172>.
- [96] A. Oliveira, Performance evaluation of concretes with mineral additions with regards to chloride-induced reinforcement corrosion (in Portuguese), UFG, 2007.
- [97] S.C. Paul, G.P.A.G. Van Zijl, A.J. Babafemi, M.J. Tan, Chloride ingress in cracked and uncracked SHCC under cyclic wetting-drying exposure, *Constr. Build. Mater.* 114 (2016) 232–240. <https://doi.org/10.1016/j.conbuildmat.2016.03.206>.
- [98] R. Ranade, C. Basaran, F. Hamidreza, Ductile Fiber-reinforced Concrete for Corrosion Mitigation in Reinforced Concrete Structures : Experiments and Theory, in: 2017.
- [99] Y. Chen, J. Yu, H. Younas, C.K. Leung, Experimental and numerical investigation on bond between steel rebar and high-strength Strain-Hardening Cementitious Composite (SHCC) under direct tension, *Cem. Concr. Compos.* 112 (2020) 103666. <https://doi.org/10.1016/j.cemconcomp.2020.103666>.
- [100] Y. Chen, J. Yu, H. Younas, C.K. Leung, Experimental and numerical investigation on bond between steel rebar and high-strength Strain-Hardening Cementitious Composite (SHCC) under direct tension, *Cem. Concr. Compos.* 112 (2020) 103666. <https://doi.org/10.1016/j.cemconcomp.2020.103666>.
- [101] S. Das Adhikary, L.R. Chandra, A. Christian, K.C.G. Ong, SHCC-

- strengthened RC panels under near-field explosions, *Constr. Build. Mater.* 183 (2018) 675–692. <https://doi.org/10.1016/j.conbuildmat.2018.06.199>.
- [102] A. V. Georgiou, S.J. Pantazopoulou, Effect of fiber length and surface characteristics on the mechanical properties of cementitious composites, *Constr. Build. Mater.* 125 (2016) 1216–1228. <https://doi.org/10.1016/j.conbuildmat.2016.09.009>.
- [103] A. Hassan, A.M. Atta, T.F. El-Shafiey, Restoration of the shear capacity for RC beams with web openings using precast SHCC plates, *Structures* 25 (2020) 603–612. <https://doi.org/10.1016/j.istruc.2020.03.046>.
- [104] J. Wei, Shear strengthening of reinforced concrete beams with High Strength Strain-Hardening Cementitious Composites (HS-SHCC), *Mater. Struct.* 53 (2020) 1–15. <https://doi.org/10.21012/fc10.233281>.
- [105] T.C.S.P. Figueiredo, Estudo experimental do reforço à torção de vigas de concreto armado com compósitos de fibras de carbono, PUC-Rio, 2014.
- [106] G. Al-Bayati, R. Al-Mahaidi, R. Kalfat, Torsional strengthening of reinforced concrete beams using different configurations of NSM FRP with epoxy resins and cement-based adhesives, *Compos. Struct.* 168 (2017) 569–581.
- [107] R. Narayanan, A.S. Kareem-Palanjian, Steel fibre reinforced concrete beams in torsion, *Int. J. Cem. Compos. Light. Concr.* 5(4) (1983) 235–246.
- [108] J.J.H. Silva Filho, Reforço à Torção de Vigas de Concreto Armado com Compósitos de Fibras de Carbono, PUC-Rio, 2007.
- [109] M.A. Mansur, P. Paramasivam, Steel fibre reinforced concrete beams in pure torsion, *Int. J. Cem. Compos. Light. Concr.* 4(1) (1982) 39–45.
- [110] S.P. Patil, K.K. Sangle, Tests of steel fibre reinforced concrete beams under predominant torsion, *J. Build. Eng.* 6 (2016) 157–162.
- [111] T.D.G. Rao, D.R. Seshu, Torsion of steel fiber reinforced concrete members, *Cem. Concr. Res.* 33 (2003) 1783–1788.
- [112] H. Ju, K.S. Kim, D.H. Lee, J.H. Hwang, S.H. Choi, Y.H. Oh, Torsional responses of steel fiber-reinforced concrete members, *Compos. Struct.* 129 (2015) 143–156.
- [113] S. Bentur, Arnon; Mindess, Cementitious Composites, *Civ. Eng.* (2007) 625.
- [114] Rediscover Concrete, The Benefits of Concrete, (n.d.). <http://rediscoverconcrete.com/en/sustainability/a-better-building->

material/the-benefits-of-concrete.html.

- [115] M. Just, M. Curbach, T.K. Kapitel, M. Hering, Final report of the first phase of the project regarding the component behavior under shock loading by aircraft fuel tanks: scale effect evaluation (in German), Dresden, 2015.
- [116] H. Aoude, F.P. Dagenais, R.P. Burrell, M. Saatcioglu, Behavior of ultra-high performance fiber reinforced concrete columns under blast loading, *Int. J. Impact Eng.* 80 (2015) 185–202.
<https://doi.org/10.1016/j.ijimpeng.2015.02.006>.
- [117] D.M. Prado, I.D.G. Araujo, V.G. Haach, R. Carrazedo, Assessment of shear damaged and NSM CFRP retrofitted reinforced concrete beams based on modal analysis, *Eng. Struct.* 129 (2016) 54–66.
<https://doi.org/10.1016/j.engstruct.2016.09.058>.
- [118] V. Mechtcherine, I. Curosu, Mineral-Bonded Composites for Enhanced Structural Impact Safety - A New Research Training Group GRK 2250 of the German Research Society, *Procedia Eng.* 210 (2017) 182–185.
<https://doi.org/10.1016/j.proeng.2017.11.064>.
- [119] M.Y.H. Bangash, Shock, impact and explosion: Structural analysis and design, 2009.
- [120] Model Code 2010 Vol.1, *Fib Bull.* No. 65. (2012) 350.
- [121] Model Code 2010 Vol.2, *Fib Bull.* No. 66. (2012) 370.
- [122] J. Ožbolt, A. Sharma, Numerical simulation of reinforced concrete beams with different shear reinforcements under dynamic impact loads, *Int. J. Impact Eng.* 38 (2011) 940–950.
<https://doi.org/10.1016/j.ijimpeng.2011.08.003>.
- [123] J. Ožbolt, A. Sharma, H.W. Reinhardt, Dynamic fracture of concrete - Compact tension specimen, *Int. J. Solids Struct.* 48 (2011) 1534–1543.
<https://doi.org/10.1016/j.ijsolstr.2011.01.033>.
- [124] G. Ruiz, A. de la Rosa, L.C. Almeida, E. Poveda, X.X. Zhang, M. Tarifa, Z.M. Wu, R.C. Yu, Dynamic mixed-mode fracture in SCC reinforced with steel fibers: an experimental study, *Int. J. Impact Eng.* 129 (2019) 101–111.
<https://doi.org/10.1016/j.ijimpeng.2019.03.003>.
- [125] P.H. Bischoff, Tension Stiffening and Cracking of Steel Fiber-Reinforced Concrete, *J. Mater. Civ. Eng.* 15 (2003) 174–182.
[https://doi.org/10.1061/\(ASCE\)0899-1561\(2003\)15:2\(174\)](https://doi.org/10.1061/(ASCE)0899-1561(2003)15:2(174)).

- [126] F. Richard, C. Poilâne, H. Yang, F. Gehring, E. Renner, A viscoelastoplastic stiffening model for plant fibre unidirectional reinforced composite behaviour under monotonic and cyclic tensile loading, *Compos. Sci. Technol.* 167 (2018) 396–403. <https://doi.org/10.1016/j.compscitech.2018.08.020>.
- [127] A.E. Naaman, V.S. Gopalaratnam, Impact properties of steel fibre reinforced concrete in bending, *Int. J. Cem. Compos. Light. Concr.* 5 (1983) 225–233. [https://doi.org/10.1016/0262-5075\(83\)90064-7](https://doi.org/10.1016/0262-5075(83)90064-7).
- [128] V.S. Gopalaratnam, S.P. Shah, R. John, A modified instrumented charpy test for cement-based composites, *Exp. Mech.* 24 (1984) 102–111. <https://doi.org/10.1007/BF02324991>.
- [129] V.S. Gopalaratnam, S.P. Shah, Properties of Steel Fiber Reinforced Concrete Subjected To Impact Loading., *J. Am. Concr. Inst.* 83 (1986) 117–126. <https://doi.org/10.14359/1750>.
- [130] A. Caverzan, E. Cadoni, M. Di Prisco, Tensile behaviour of high performance fibre-reinforced cementitious composites at high strain rates, *Int. J. Impact Eng.* 45 (2012) 28–38. <https://doi.org/10.1016/j.ijimpeng.2012.01.006>.
- [131] S. Saatci, F.J. Vecchio, Effects of shear mechanisms on impact behavior of reinforced concrete beams, *ACI Struct. J.* 106 (2009) 78–86. <https://doi.org/10.14359/56286>.
- [132] N. Banthia, Impact resistance of concrete, University of British Columbia, 1987.
- [133] M. Hering, F. Bracklow, S. Scheerer, M. Curbach, Reinforced concrete plates under impact load—damage quantification, *Materials (Basel)*. 13 (2020) 1–13. <https://doi.org/10.3390/ma13204554>.
- [134] D.J. Kim, K. Wille, S. El-Tawil, A.E. Naaman, Testing of Cementitious Materials under High-Strain-Rate Tensile Loading Using Elastic Strain Energy, *J. Eng. Mech.* 137 (2011) 268–275. [https://doi.org/10.1061/\(asce\)em.1943-7889.0000224](https://doi.org/10.1061/(asce)em.1943-7889.0000224).
- [135] M. Hering, Investigation of mineral-bonded reinforcing layers for reinforced concrete slabs against impact loads (in German), Technische Universität Dresden, 2020.
- [136] A. Bentur, S. Mindess, N. Banthia, The behaviour of concrete under impact

- loading: Experimental procedures and method of analysis, *Mater. Struct.* 19 (1986) 371–378. <https://doi.org/10.1007/BF02472127>.
- [137] T.S. Lok, P.J. Zhao, Impact Response of Steel Fiber-Reinforced Concrete Using a Split Hopkinson Pressure Bar, *J. Mater. Civ. Eng.* 16 (2004) 54–59. [https://doi.org/10.1061/\(asce\)0899-1561\(2004\)16:1\(54\)](https://doi.org/10.1061/(asce)0899-1561(2004)16:1(54)).
- [138] A.C.C. Trindade, A.A. Heravi, I. Curosu, M. Liebscher, F. de Andrade Silva, V. Mechtcherine, Tensile behavior of strain-hardening geopolymer composites (SHGC) under impact loading, *Cem. Concr. Compos.* 113 (2020) 103703. <https://doi.org/10.1016/j.cemconcomp.2020.103703>.
- [139] A.A. Heravi, T. Gong, V. Mechtcherine, Mechanical characterization of textile reinforced concrete (TRC) subject to dynamic tensile loading, (2019) 1–11.
- [140] A.L.I.A. Heravi, V. Mechtcherine, Mechanical characterization of strain-hardening cement-based composite (SHCC) under dynamic tensile load, in: 10th Int. Conf. Fract. Mech. Concr. Concr. Struct., 2019.
- [141] N. Kishi, H. Mikami, K.G. Matsuoka, T. Ando, Impact behavior of shear-failure-type RC beams without shear rebar, *Int. J. Impact Eng.* 27 (2002) 955–968. [https://doi.org/10.1016/S0734-743X\(01\)00149-X](https://doi.org/10.1016/S0734-743X(01)00149-X).
- [142] S. Das Adhikary, B. Li, K. Fujikake, Dynamic behavior of reinforced concrete beams under varying rates of concentrated loading, *Int. J. Impact Eng.* 47 (2012) 24–38. <https://doi.org/10.1016/j.ijimpeng.2012.02.001>.
- [143] S.M. Soleimani, N. Banthia, A novel drop weight impact setup for testing reinforced concrete beams, *Exp. Tech.* 38 (2014) 72–79. <https://doi.org/10.1111/j.1747-1567.2012.00810.x>.
- [144] T.M. Pham, Y. Hao, H. Hao, Sensitivity of impact behaviour of RC beams to contact stiffness, *Int. J. Impact Eng.* 112 (2018) 155–164. <https://doi.org/10.1016/j.ijimpeng.2017.09.015>.
- [145] D.R. Sanders, Y.I. Kim, N. Stubbs, Nondestructive evaluation of damage in composite structures using modal parameters, *Exp. Mech.* 32 (1992) 240–251. <https://doi.org/10.1007/BF02319362>.
- [146] A. Katunin, Nondestructive damage assessment of composite structures based on wavelet analysis of modal curvatures: State-of-the-art review and description of wavelet-based damage assessment benchmark, *Shock Vib.* 2015 (2015). <https://doi.org/10.1155/2015/735219>.

- [147] K.S. Lee, J. Il Choi, S.E. Park, J.S. Hwang, B.Y. Lee, Damping property of prepacked concrete incorporating coarse aggregates coated with polyurethane, *Cem. Concr. Compos.* 93 (2018) 301–308. <https://doi.org/10.1016/j.cemconcomp.2018.06.018>.
- [148] D. Yang, C. Kang, Z. Hu, B. Ye, P. Xiang, On the study of element modal strain energy sensitivity for damage detection of functionally graded beams, *Compos. Struct.* 224 (2019) 110989. <https://doi.org/10.1016/j.compstruct.2019.110989>.
- [149] M.M. Nasery, M. Hüsem, F.Y. Okur, A.C. Altunişik, Numerical and Experimental Investigation on Dynamic Characteristic Changes of Encased Steel Profile Before and After Cyclic Loading Tests, *Int. J. Civ. Eng.* 18 (2020) 1411–1431. <https://doi.org/10.1007/s40999-020-00545-0>.
- [150] A. Yadav, M. Amabili, S.K. Panda, T. Dey, R. Kumar, Nonlinear damped vibrations of three-phase CNT-FRC circular cylindrical shell, *Compos. Struct.* 255 (2021) 112939. <https://doi.org/10.1016/j.compstruct.2020.112939>.
- [151] S. Walunj Prashant, V.N. Chougule, A.C. Mitra, Investigation on Modal Parameters of Rectangular Cantilever Beam Using Experimental Modal Analysis, *Mater. Today Proc.* 2 (2015) 2121–2130. <https://doi.org/10.1016/j.matpr.2015.07.214>.
- [152] H. BACHMANN, W.J. AMMANN, F. DEISCHL, J. EISENMANN, I. FLOEGL, G.H. HIRSCH, G.K. KLEIN, G.J. LANDE, O. MAHRENHOLTZ, H.G. NATKE, H. NUSSBAUMER, A.J. PRFTIOVE, J.H. RAINER, E.-U. SAEMANN, L. STFINBEISSER, *Vibration problems in structures: Practical guidelines*, 1997. <https://doi.org/10.1139/196-116>.
- [153] H.L. Soriano, *Introdução à Dinâmica das Estruturas*, 2014.
- [154] A. Brandt, *Noise and Vibration Analysis*, John Wiley and Sons Ltd., 2011.
- [155] S.M. N. Banthia, V. Bindiganavile, Impact resistance of fiber reinforced concrete: a progress report, in: *Proc. High Perform. Fiber Reinf. Concr.* 4, RILEM, Cachan Cedex, France, 2003: pp. 117–131.
- [156] X. Zhang, G. Ruiz, A.M. Abd Elazim, Loading rate effect on crack velocities in steel fiber-reinforced concrete, *Int. J. Impact Eng.* 76 (2015) 60–66. <https://doi.org/10.1016/j.ijimpeng.2014.09.004>.
- [157] M. Nili, A.H. Ghorbankhani, A. Alavinia, M. Zolfaghari, Assessing the

- impact strength of steel fibre-reinforced concrete under quasi-static and high velocity dynamic impacts, *Constr. Build. Mater.* (2016). <https://doi.org/10.1016/j.conbuildmat.2015.12.161>.
- [158] Z.S. Tabatabaei, J.S. Volz, D.I. Keener, B.P. Gliha, Comparative impact behavior of four long carbon fiber reinforced concretes, *Mater. Des.* 55 (2014) 212–223. <https://doi.org/10.1016/j.matdes.2013.09.048>.
- [159] W. Suaris, S.P. Shah, Properties of concrete subjected to impact, *J. Struct. Eng.* (United States). 109 (1983) 1727–1741. [https://doi.org/10.1061/\(ASCE\)0733-9445\(1983\)109:7\(1727\)](https://doi.org/10.1061/(ASCE)0733-9445(1983)109:7(1727)).
- [160] X.X. Zhang, A.M. Abd Elazim, G. Ruiz, R.C. Yu, Fracture behaviour of steel fibre-reinforced concrete at a wide range of loading rates, *Int. J. Impact Eng.* 71 (2014) 89–96. <https://doi.org/10.1016/j.ijimpeng.2014.04.009>.
- [161] W. Suaris, S.P. Shah, Strain-rate effects in fibre-reinforced concrete subjected to impact and impulsive loading, *Composites.* (1982) 153–159.
- [162] N. Banthia, J.F. Trottier, Deformed steel fiber-cementitious matrix bond under impact, *Cem. Concr. Res.* 21 (1991) 158–168. [https://doi.org/10.1016/0008-8846\(91\)90042-G](https://doi.org/10.1016/0008-8846(91)90042-G).
- [163] V. Bindiganavile, Generating Dynamic Crack Growth Resistance Curves for Fiber-reinforced Concrete, *Exp. Mech.* 45 (2005) 112–122. <https://doi.org/10.1177/0014485105052321>.
- [164] L. Jin, R. Zhang, L. Li, X. Du, Y. Yao, Impact behavior of SFRC beams at elevated temperatures: Experimental and analytical studies, *Eng. Struct.* 197 (2019) 109401. <https://doi.org/10.1016/j.engstruct.2019.109401>.
- [165] N. Banthia, C. Yan, K. Sakai, Impact resistance of fiber reinforced concrete at subnormal temperatures, *Cem. Concr. Compos.* 20 (1998) 393–404. [https://doi.org/10.1016/S0958-9465\(98\)00015-8](https://doi.org/10.1016/S0958-9465(98)00015-8).
- [166] W. Zhang, S. Chen, Y. Liu, Effect of weight and drop height of hammer on the flexural impact performance of fiber-reinforced concrete, *Constr. Build. Mater.* 140 (2017) 31–35. <https://doi.org/10.1016/j.conbuildmat.2017.02.098>.
- [167] Y. Hao, H. Hao, G. Chen, Experimental investigation of the behaviour of spiral steel fibre reinforced concrete beams subjected to drop-weight impact loads, *Mater. Struct. Constr.* 49 (2016) 353–370. <https://doi.org/10.1617/s11527-014-0502-5>.

- [168] P. Sukontasukkul, Impact resistance of laterally confined fibre reinforced concrete plates, *Mater. Struct.* 34 (2001) 612–618. <https://doi.org/10.1617/13689>.
- [169] A.B. Elnagar, H.M. Afefy, A.T. Baraghith, M.H. Mahmoud, Experimental and numerical investigations on the impact resistance of SHCC-strengthened RC slabs subjected to drop weight loading, *Constr. Build. Mater.* 229 (2019) 116866. <https://doi.org/10.1016/j.conbuildmat.2019.116866>.
- [170] Y. Zhang, S. Bai, Q. Zhang, H. Xie, X. Zhang, Failure behavior of strain hardening cementitious composites for shear strengthening RC member, *Constr. Build. Mater.* 78 (2015) 470–473. <https://doi.org/10.1016/j.conbuildmat.2015.01.037>.
- [171] T. Paulay, Displacement-based design approach to earthquake-induced torsion in ductile buildings, *Eng. Struct.* 19 (9) (1997) 699–707.
- [172] S. Tachibana, H. Masuya, S. Nakamura, Performance based design of reinforced concrete beams under impact, *Nat. Hazards Earth Syst. Sci.* 10 (2010) 1069–1078. <https://doi.org/10.5194/nhess-10-1069-2010>.
- [173] Q.X. Ren, L.H. Han, C. Hou, Z. Tao, S. Li, Concrete-encased CFST columns under combined compression and torsion: Experimental investigation, *J. Constr. Steel Res.* 138 (2017) 729–741. <https://doi.org/10.1016/j.jcsr.2017.08.016>.
- [174] T. Kühn, M. Hering, U. Häußler, M. Curbach, Dynamic behaviour of reinforced slabs – blast testing, in: *ICPS5 2018 - 5th Int. Conf. Prot. Struct.*, Poznan, Poland, 2018: pp. 485–493.
- [175] A. Goswami, S. Das Adhikary, Retrofitting materials for enhanced blast performance of Structures: Recent advancement and challenges ahead, *Constr. Build. Mater.* 204 (2019) 224–243. <https://doi.org/10.1016/j.conbuildmat.2019.01.188>.
- [176] A. Ghobarah, M.N. Ghorbel, S.E. Chidiac, Upgrading torsional resistance of reinforced concrete beams using fiber-reinforced polymer, *J. Compos. Constr.* 6 (2002) 257–263. [https://doi.org/10.1061/\(ASCE\)1090-0268\(2002\)6:4\(257\)](https://doi.org/10.1061/(ASCE)1090-0268(2002)6:4(257)).
- [177] M. Ameli, H. Ronagh, P. Dux, Behavior of FRP Strengthened Reinforced Concrete Beams under Torsion, *J. Compos. Constr.* 11(2) (2007) 192–200.
- [178] N. Nikoloutsopoulos, D. Passa, S. Gavela, A. Sotiropoulou, Comparison of

- shear strengthening techniques of reinforced concrete beams with carbon fibre reinforced polymers (CFRPs), *Procedia Struct. Integr.* 10 (2018) 141–147. <https://doi.org/10.1016/j.prostr.2018.09.021>.
- [179] F. Schladitz, M. Curbach, Torsion tests on textile-reinforced concrete strengthened specimens, *Mater. Struct. Constr.* 45 (2012) 31–40. <https://doi.org/10.1617/s11527-011-9746-5>.
- [180] A. Brückner, R. Ortlepp, M. Curbach, Textile reinforced concrete for strengthening in bending and shear, *Mater. Struct. Constr.* 39 (2006) 741–748. <https://doi.org/10.1617/s11527-005-9027-2>.
- [181] Z.C. Tetta, L.N. Koutas, D.A. Bournas, Textile-reinforced mortar (TRM) versus fiber-reinforced polymers (FRP) in shear strengthening of concrete beams, *Compos. Part B Eng.* 77 (2015) 338–348. <https://doi.org/10.1016/j.compositesb.2015.03.055>.
- [182] G. Loreto, S. Babaeidarabad, L. Leardini, A. Nanni, RC beams shear-strengthened with fabric-reinforced-cementitious-matrix (FRCM) composite, *Int. J. Adv. Struct. Eng.* 7 (2015) 341–352. <https://doi.org/10.1007/s40091-015-0102-9>.
- [183] M.Y. Alabdulhady, L.H. Sneed, C. Carloni, Torsional behavior of RC beams strengthened with PBO-FRCM composite – An experimental study, *Eng. Struct.* 136 (2017) 393–405. <https://doi.org/10.1016/j.engstruct.2017.01.044>.
- [184] C. Wu, C.K.Y. Leung, V.C. Li, Derivation of crack bridging stresses in engineered cementitious composites under combined opening and shear displacements, *Cem. Concr. Res.* 107 (2018) 253–263. <https://doi.org/10.1016/j.cemconres.2018.02.027>.
- [185] I. Curosu, S. Pirskawetz, V. Mechtcherine, Characterizing the crack development in strain-hardening cement-based composites (SHCC) by means of acoustic emission, (2016).
- [186] I. Curosu, Influence of Fiber Type and Matrix Composition on the Tensile Behavior of Strain-Hardening Cement-Based Composites (SHCC) Under Impact Loading, *Technischen Universität Dresden (TU Dresden)*, 2017.
- [187] Kuralon RECS15/RECS100L/RFS400 Standard Properties, (2020). <http://kuralon-frc.kuraray.com/product-application/for-mortar/recs>.
- [188] D. Dyneema, Ultra High Molecular Weight Polyethylene Fiber - Technical

- Data Sheet, 2016. www.dyneema.com.
- [189] T. Kanda, V.C. Li, Interface Property and Apparent Strength of High-Strength Hydrophilic Fiber in Cement Matrix, *J. Mater. Civ. Eng.* 10(1) (1998) 5–13.
 - [190] V.C. Li, C. Wu, S. Wang, A. Ogawa, T. Saito, Interface tailoring for strain-hardening polyvinyl alcohol-engineered cementitious composite (PVA-ECC), *ACI Mater. J.* 99 (2002) 463–472. <https://doi.org/10.14359/12325>.
 - [191] M.F. Arain, M. Wang, J. Chen, H. Zhang, Experimental and numerical study on tensile behavior of surface modified PVA fiber reinforced strain-hardening cementitious composites, *Constr. Build. Mater.* 217 (2019) 403–415. <https://doi.org/10.1016/j.conbuildmat.2019.05.083>.
 - [192] M. Ranjbarian, V. Mechtcherine, Z. Zhang, I. Curosu, J. Storm, M. Kaliske, Locking Front Model for pull-out behaviour of PVA microfibre embedded in cementitious matrix, *Cem. Concr. Compos.* 103 (2019) 318–330. <https://doi.org/10.1016/j.cemconcomp.2019.04.031>.
 - [193] I. Curosu, M. Liebscher, V. Mechtcherine, C. Bellmann, S. Michel, Tensile behavior of high-strength strain-hardening cement-based composites (HS-SHCC) made with high-performance polyethylene, aramid and PBO fibers, *Cem. Concr. Res.* 98 (2017) 71–81. <https://doi.org/10.1016/j.cemconres.2017.04.004>.
 - [194] R. Ranade, V.C. Li, M.D. Stults, T.S. Rushing, J. Roth, W.F. Heard, *Micromechanics of High-Strength, High-Ductility Concrete*, (2014).
 - [195] T. Klink, F. Stegmann, V. Slowik, Age dependence of cracking and deformability of a strain-hardening cement-based composite, *Constr. Build. Mater.* 214 (2019) 641–647. <https://doi.org/10.1016/j.conbuildmat.2019.04.047>.
 - [196] I. Curosu, V. Mechtcherine, O. Millon, Effect of Fiber Properties and Embedment Conditions, *Cem. Concr. Res.* 82 (2016) 23–35.
 - [197] S. Müller, V. Mechtcherine, Fatigue behaviour of strain-hardening cement-based composites (SHCC), *Cem. Concr. Res.* 92 (2017) 75–83. <https://doi.org/10.1016/j.cemconres.2016.11.003>.
 - [198] S.C. Lin, D. Li, B. Yang, Experimental study and numerical simulation on damage assessment of reinforced concrete beams, *Int. J. Impact Eng.* 132 (2019). <https://doi.org/10.1016/j.ijimpeng.2019.103323>.

- [199] J. Magnusson, M. Hallgreny, A. Ansell, Air-blast-loaded, high-strength concrete beams. Part I: Experimental investigation, *Mag. Concr. Res.* 62 (2010) 127–136. <https://doi.org/10.1680/mac.2008.62.2.127>.
- [200] K. Micallef, J. Sagaseta, M. Fernández Ruiz, A. Muttoni, Assessing punching shear failure in reinforced concrete flat slabs subjected to localised impact loading, *Int. J. Impact Eng.* 71 (2014) 17–33. <https://doi.org/10.1016/j.ijimpeng.2014.04.003>.
- [201] T.M. Pham, H. Hao, Prediction of the impact force on reinforced concrete beams from a drop weight, *Adv. Struct. Eng.* 19 (2016) 1710–1722. <https://doi.org/10.1177/1369433216649384>.
- [202] M. Safdar, T. Matsumoto, K. Kakuma, Flexural behavior of reinforced concrete beams repaired with ultra-high performance fiber reinforced concrete (UHPFRC), *Compos. Struct.* 157 (2016) 448–460.
- [203] Y. Yao, F.A. Silva, M. Butler, V. Mechtcherine, B. Mobasher, Failure Localization and Correlation of High-Speed Tension and Impact Tests of Strain-Hardening Cement-Based Composites, *J. Mater. Civ. Eng.* 29 (2017) 04017212. [https://doi.org/10.1061/\(ASCE\)MT.1943-5533.0002056](https://doi.org/10.1061/(ASCE)MT.1943-5533.0002056).
- [204] I. Curosu, S. Pirskawetz, V. Mechtcherine, Characterizing the crack development in strain-hardening cement-based composites (SHCC) by means of acoustic emission, *Proc. Fram. Calif.* (2016) 1–10. <https://doi.org/10.21012/fc9.207>.
- [205] I. Curosu, V. Mechtcherine, D. Forni, E. Cadoni, Performance of various strain-hardening cement-based composites (SHCC) subject to uniaxial impact tensile loading, *Cem. Concr. Res.* 102 (2017) 16–28.
- [206] D. Dyneema, Ultra High Molecular Weight Polyethylene Fiber from DSM Dyneema, *Tech. DataSheet.* 49 (2016). <https://issuu.com/eurofibers/docs/name8f0d44>.
- [207] M. Hering, Untersuchung von mineralisch gebundenen Verstärkungsschichten für Stahlbetonplatten gegen Impaktbeanspruchungen, (2020).
- [208] M.D.E. La, R. Du, Size effect method for determining fracture energy and process zone size of concrete, *Int. J. Rock Mech. Min. Sci. Geomech. Abstr.* 28 (1991) A198. [https://doi.org/10.1016/0148-9062\(91\)93225-u](https://doi.org/10.1016/0148-9062(91)93225-u).
- [209] M. Hering, Einfaches Bemessungsmodell für die Darstellung des Verhaltens

- von Stahlbetonplatten unter Impaktbelastung, TU Dresden, 2015.
- [210] S. Timoshenko, J.N. Goodier, Theory of Elasticity, 1951. <https://doi.org/10.2307/3613011>.
- [211] P. Garg, Displacement Measurement Using a Laser Doppler Vibrometer Mounted on an Unmanned Aerial Vehicles, University of New Mexico, USA, 2018.
- [212] M. Hering, F. Bracklow, T. Kühn, M. Curbach, Impact experiments with reinforced concrete plates of different thicknesses, Struct. Concr. 21 (2019) 12. <https://doi.org/10.1002/suco.201900195>.
- [213] V.C. Li, Damage tolerant ECC for integrity of structures under extreme loads, Proc. 2009 Struct. Congr. - Don't Mess with Struct. Eng. Expand. Our Role. (2009) 2209–2218. [https://doi.org/10.1061/41031\(341\)242](https://doi.org/10.1061/41031(341)242).
- [214] T.C.S.P. Figueiredo, I. Curosu, G.L.G. Gonzales, M. Hering, F.A. Silva, M. Curbach, V. Mechtcherine, Mechanical behavior of strain-hardening cement-based composites (SHCC) subjected to torsional loading and to combined torsional and axial loading, (2020).
- [215] V.C. Li, D.K. Mishra, H.C. Wu, Matrix design for pseudo-strain-hardening fibre reinforced cementitious composites, Mater. Struct. 28 (1995) 586–595. <https://doi.org/10.1007/BF02473191>.
- [216] H. Ma, S. Qian, Z. Zhang, Z. Lin, V.C. Li, Tailoring Engineered Cementitious Composites with local ingredients, Constr. Build. Mater. 101 (2015) 584–595. <https://doi.org/10.1016/j.conbuildmat.2015.10.146>.
- [217] M. Govindasamy, G. Kamalakannan, C. Kesavan, G.K. Meenashisundaram, Damage Detection in Glass / Epoxy Laminated Composite Plates Using Modal Curvature for Structural Health Monitoring Applications, J. Compos. Sci. 4 (2020) 27. <https://doi.org/10.3390/jcs4040185>.
- [218] H. Song, J.S. Popovics, Characterization of steel-concrete interface bonding conditions using attenuation characteristics of guided waves, Cem. Concr. Compos. 83 (2017) 111–124. <https://doi.org/10.1016/j.cemconcomp.2017.07.001>.
- [219] M. Lezgy-Nazargah, E. Etemadi, Reduced modal state-space approach for low-velocity impact analysis of sandwich beams, Compos. Struct. 206 (2018) 762–773. <https://doi.org/10.1016/j.compstruct.2018.08.081>.
- [220] H. Li, Z. Wang, H. Lv, Z. Zhou, Q. Han, J. Liu, Z. Qin, Nonlinear vibration

- analysis of fiber reinforced composite cylindrical shells with partial constrained layer damping treatment, *Thin-Walled Struct.* 157 (2020) 107000. <https://doi.org/10.1016/j.tws.2020.107000>.
- [221] S.D. Panteliou, T.G. Chondros, V.C. Argyrakis, A.D. Dimarogonas, Damping factor as an indicator of crack severity, *J. Sound Vib.* 241 (2001) 235–245. <https://doi.org/10.1006/jsvi.2000.3299>.
- [222] H. Othman, H. Marzouk, Dynamic identification of damage control characteristics of ultra-high performance fiber reinforced concrete, *Constr. Build. Mater.* 157 (2017) 899–908. <https://doi.org/10.1016/j.conbuildmat.2017.09.169>.
- [223] G. Bernagozzi, S. Mukhopadhyay, R. Betti, L. Landi, P.P. Diotallevi, Output-only damage detection in buildings using proportional modal flexibility-based deflections in unknown mass scenarios, *Eng. Struct.* 167 (2018) 549–566. <https://doi.org/10.1016/j.engstruct.2018.04.036>.
- [224] A. Andersson, J. Östlund, M. Ülker-kaustell, J. Battini, R. Karoumi, *Experimental Vibration Analysis for Civil Structures*, 2018. <http://link.springer.com/10.1007/978-3-319-67443-8>.
- [225] M. Morgantini, R. Betti, L. Balsamo, Structural damage assessment through features in quefreny domain, *Mech. Syst. Signal Process.* 147 (2021) 107017. <https://doi.org/10.1016/j.ymssp.2020.107017>.
- [226] L. Li, Y. Guo, F. Liu, Test analysis for FRC beams strengthened with externally bonded FRP sheets, *Constr. Build. Mater.* 22 (2008) 315–323. <https://doi.org/10.1016/j.conbuildmat.2006.08.016>.
- [227] C.A. Geweth, F.S. Khosroshahi, K. Sepahvand, C. Kerkeling, S. Marburg, Damage Detection of Fibre-Reinforced Composite Structures Using Experimental Modal Analysis, *Procedia Eng.* 199 (2017) 1900–1905. <https://doi.org/10.1016/j.proeng.2017.09.128>.
- [228] R. Bachoo, J. Bridge, The modal density of composite beams incorporating the effects of shear deformation and rotary inertia, *J. Sound Vib.* 423 (2018) 459–471. <https://doi.org/10.1016/j.jsv.2018.01.013>.
- [229] A.J. Felber, *Development of a hybrid bridge evaluation system*, University of British Columbia, 1993.
- [230] A. k. Chopra, *Dynamics of Structures: Theory and Applications to Earthquake Engineering*, Prentice-Hall, 2020.

<http://dx.doi.org/10.1016/j.tws.2012.02.007>.

- [231] A.E. Daneshjoo, F., & Gharighoran, Investigation of Damping in Cracked Concrete Beams Usable in bridges, (2006).
<https://doi.org/10.13140/RG.2.1.2997.2567>.

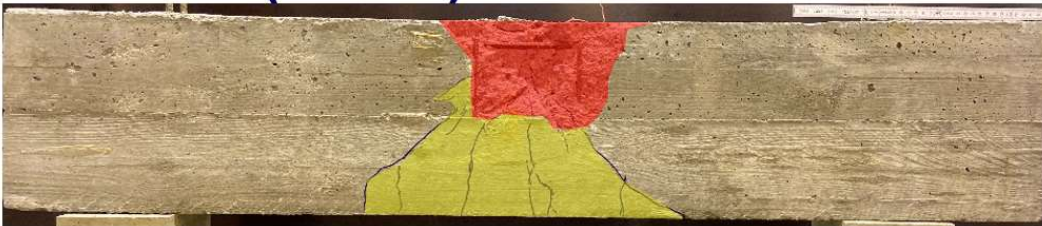
Appendix 1 – Cracking patterns of the structural tests

Reference beams (RC only), with stirrups (Ce/WS series)

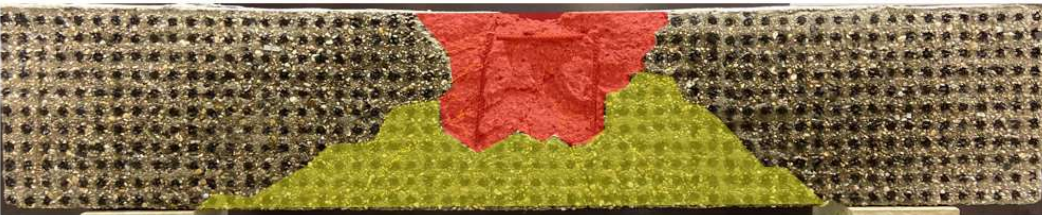
Impactor velocity 17.5 m/s (2.1 kJ)



Impactor velocity 20.7 m/s (3.1 kJ)



Impactor velocity 25.9 m/s (4.8 kJ)



Impactor velocity 29.8 m/s (6.4 kJ)



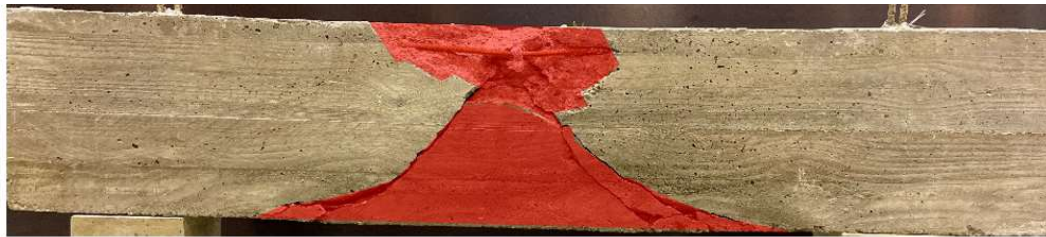
 Fragmentation region  Cracking region

Reference beams (RC only), without stirrups (Se/WOS series)

Impactor velocity 17.5 m/s (2.1 kJ)



Impactor velocity 20.7 m/s (3.1 kJ)



Impactor velocity 25.9 m/s (4.8 kJ)



Impactor velocity 29.8 m/s (6.4 kJ)

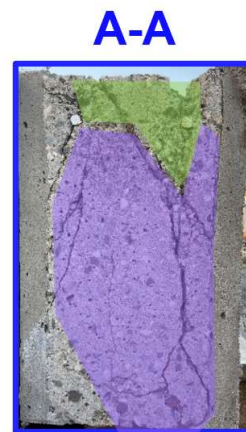
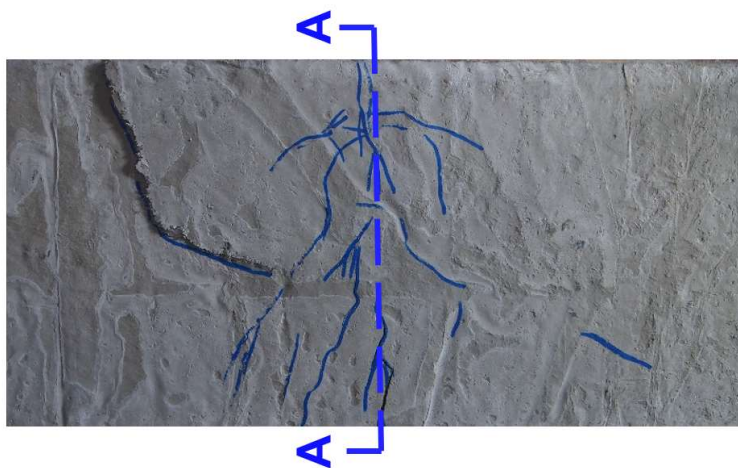


 Fragmentation region  Cracking region

Strengthened beams with stirrups (Se/WOS series), impactor velocity 29.8 m/s

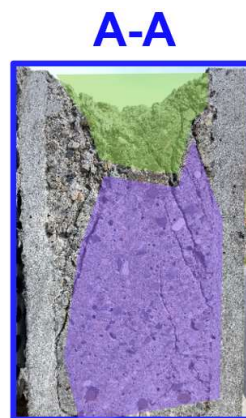
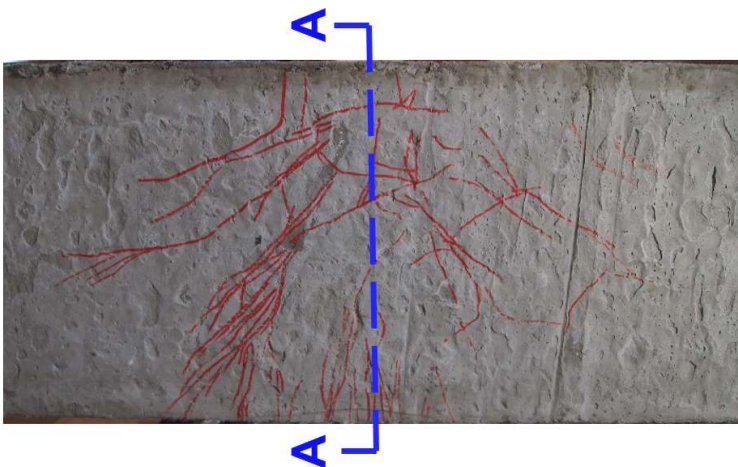
Strengthening material: PVA-SHCC

(lateral surface / mid-span cross-section)



Strengthening material: PE-SHCC

(lateral surface / mid-span cross-section)

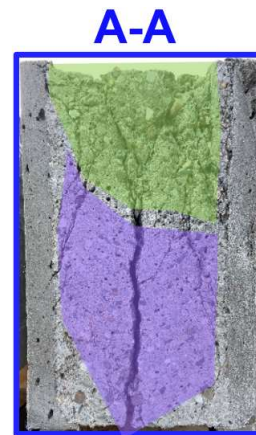
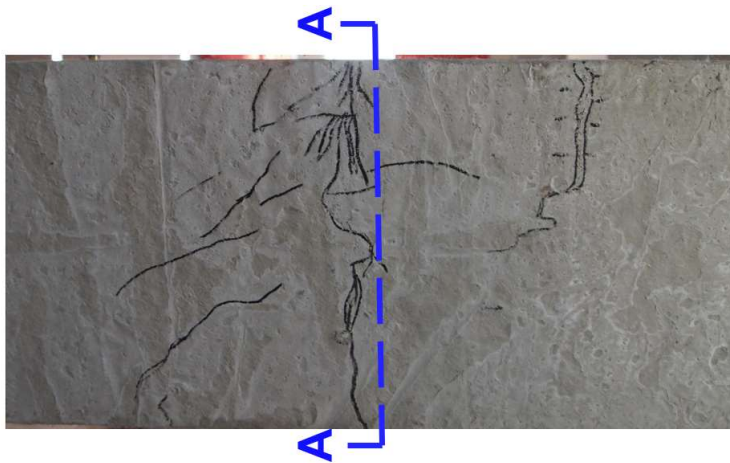


 Fragmentation region
  Cracking region

Strengthened beams without stirrups (Ce/WS series), impactor velocity 29.8 m/s

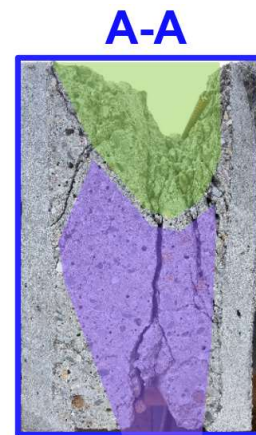
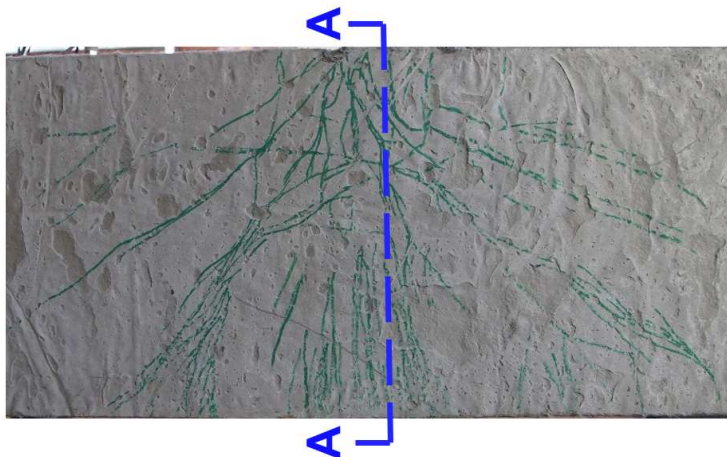
Strengthening material: PVA-SHCC

(lateral surface / mid-span cross-section)



Strengthening material: PE-SHCC

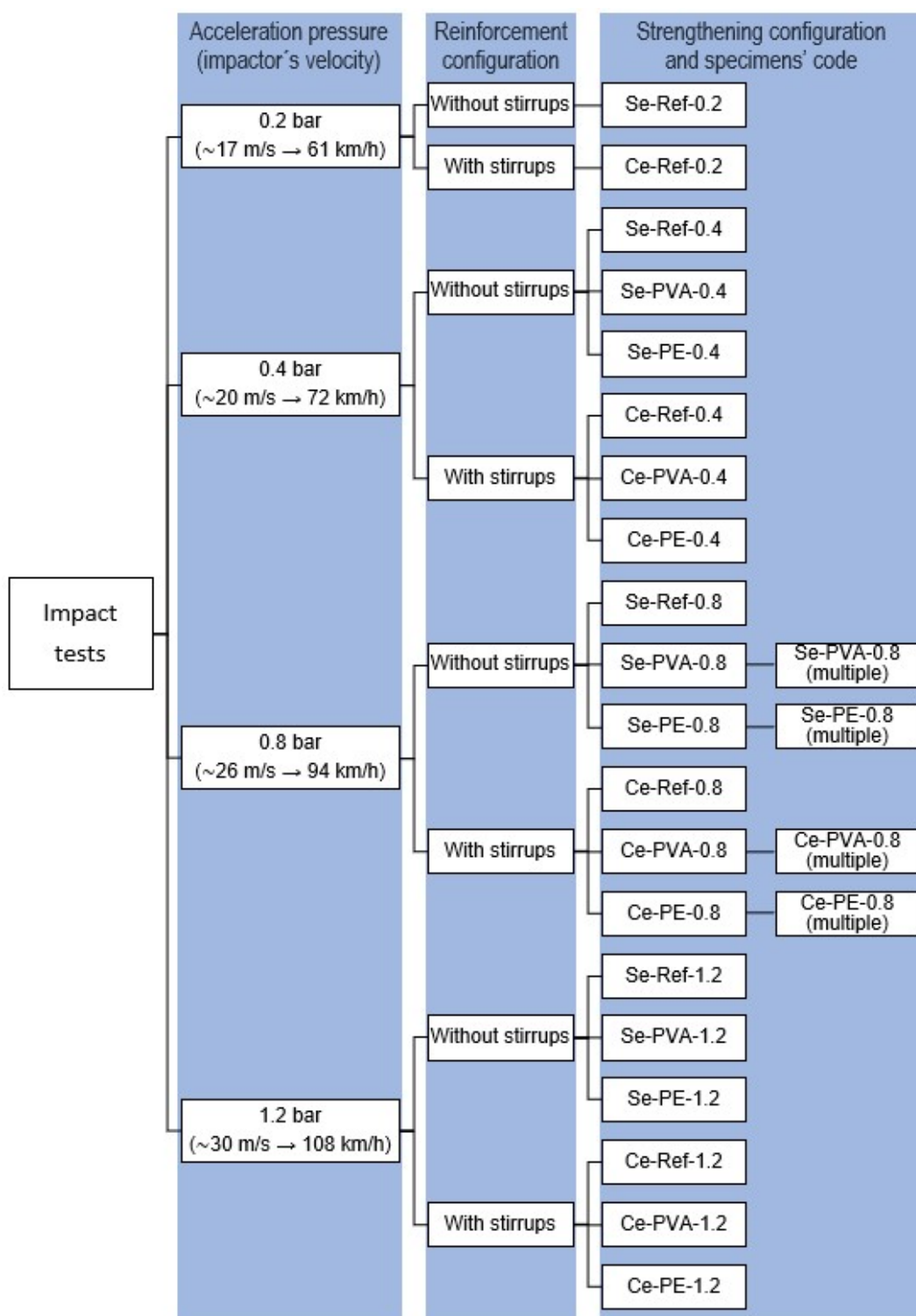
(lateral surface / mid-span cross-section)



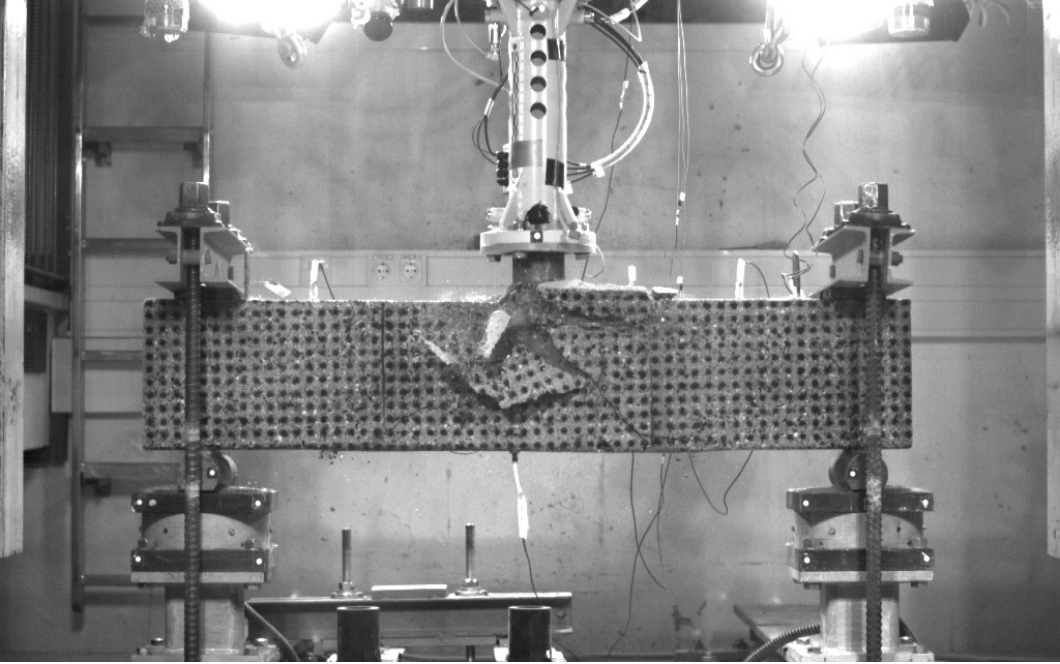
 Fragmentation region  Cracking region

Appendix 2 – Datasheets of the structural tests

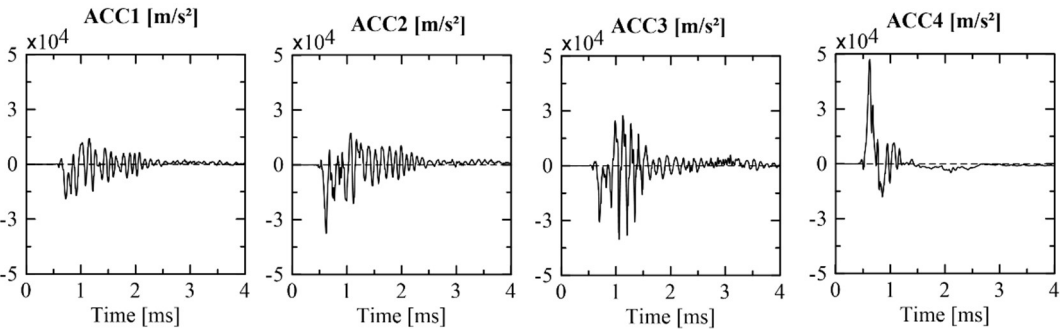
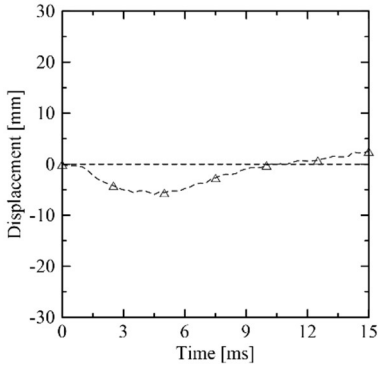
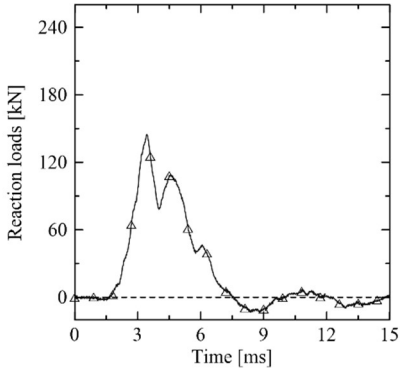
Structural program chart



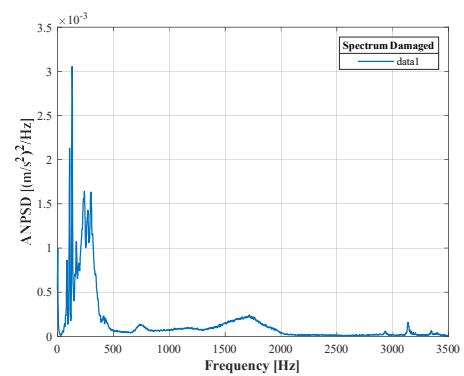
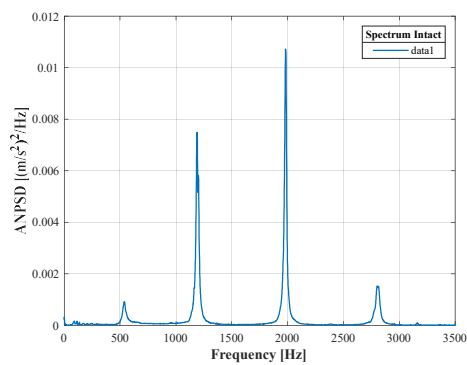
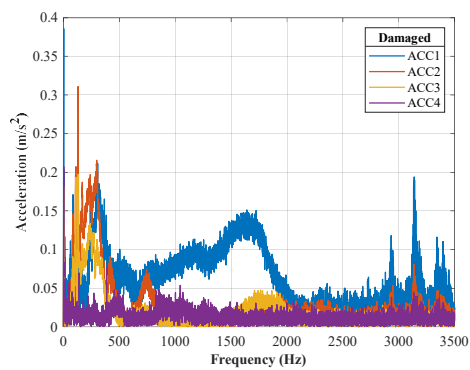
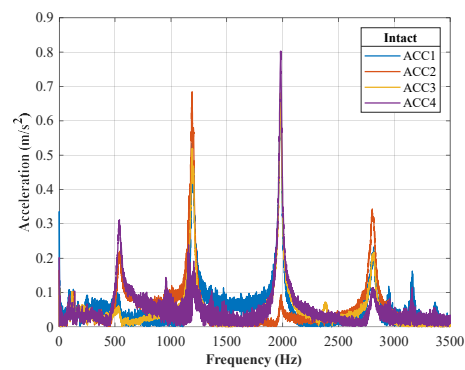
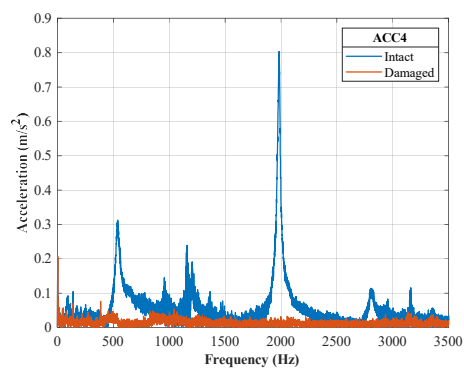
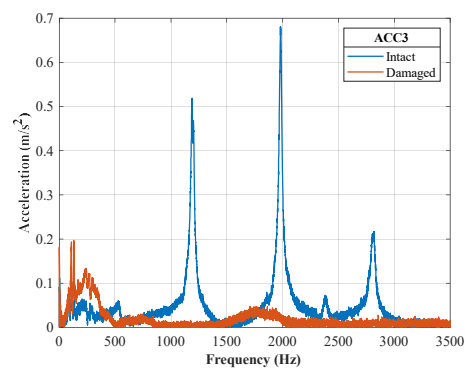
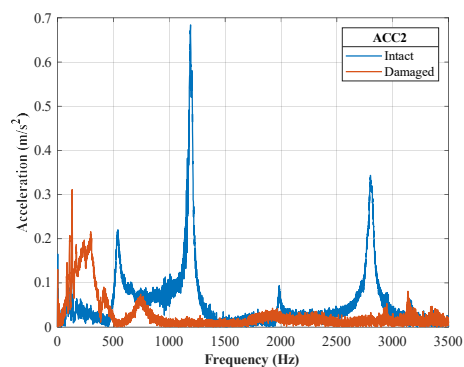
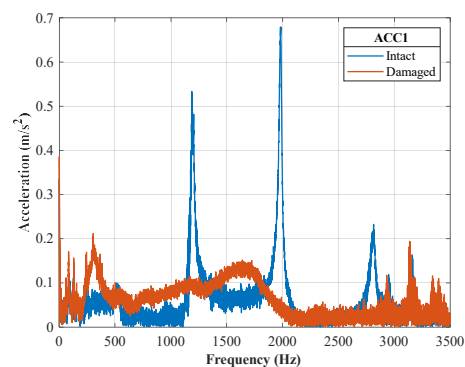
Se-Ref-0.2 (V01) – single impact test data



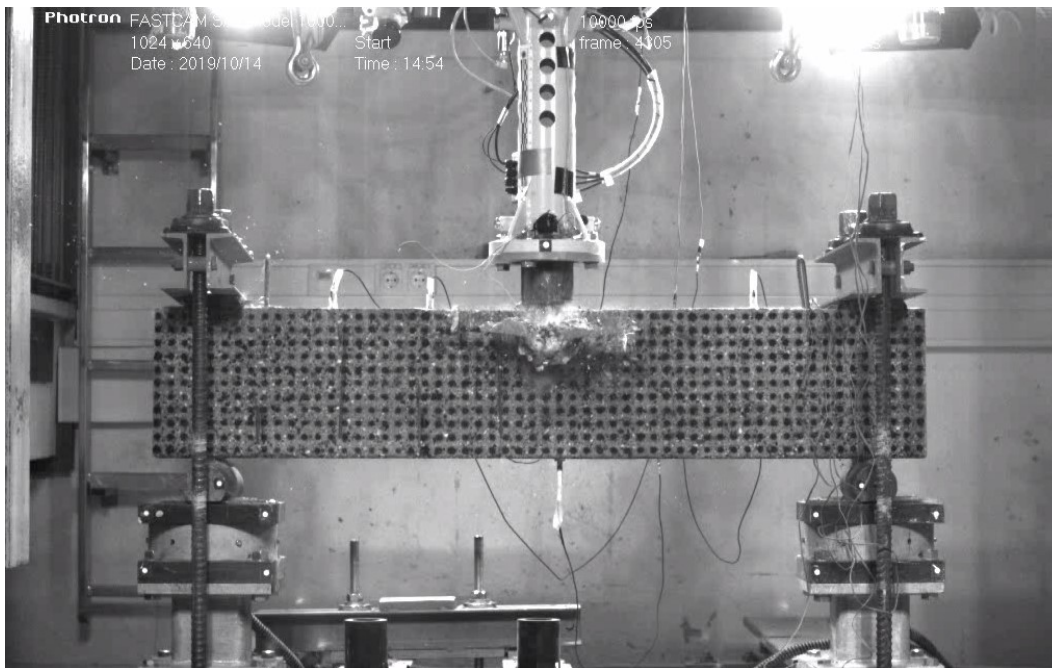
Transversal reinforcement configuration	Without stirrups
Strengthening specification	Reference beam
Acceleration pressure [bar]	0.2
Age substrate [days]	40
Age SHCC [days]	N/A
Impactor velocity [m/s]	17.7
Kinetic energy [J]	2214.9
Specimen mass before the test [kg]	105.8
Specimen mass after the test [kg]	104.6
Accountable breakout material [kg]	1.2



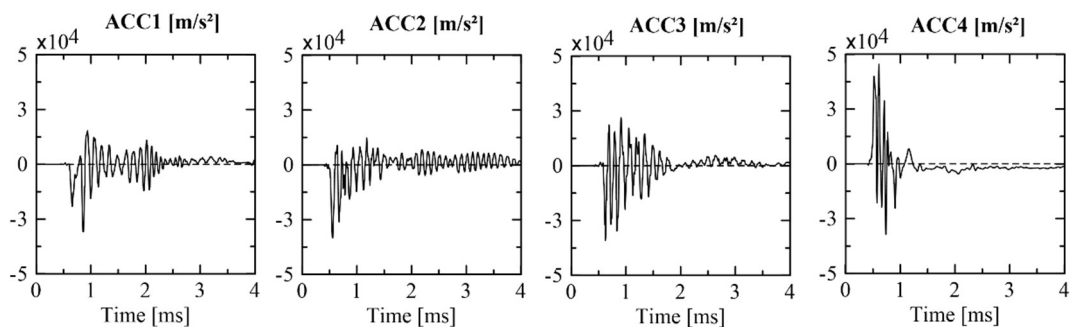
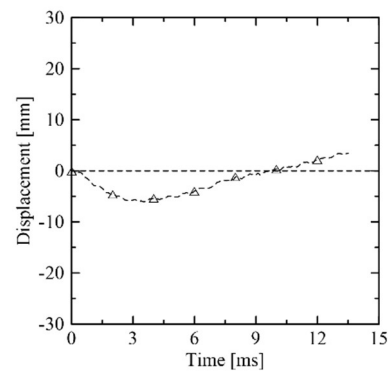
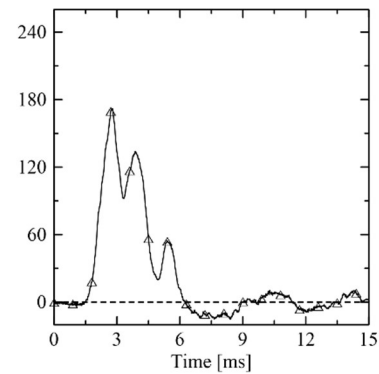
Se-Ref-0.2 (V01) – data collected before and after the impact



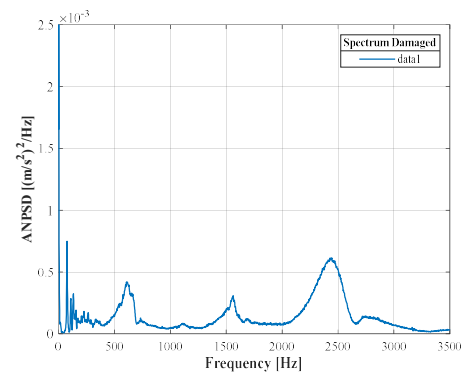
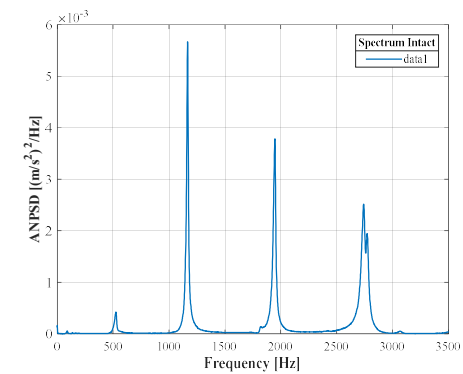
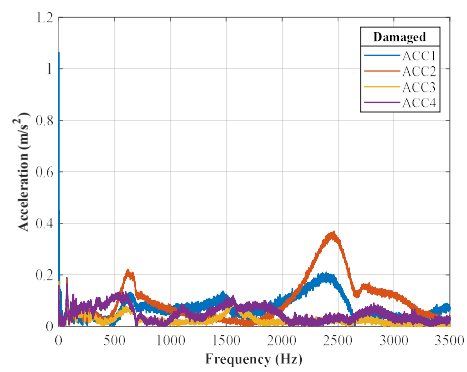
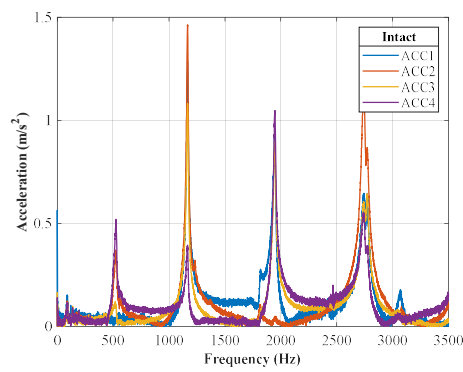
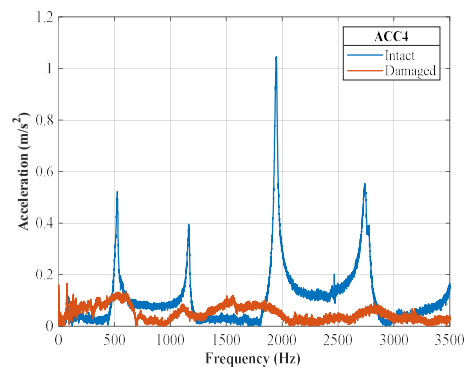
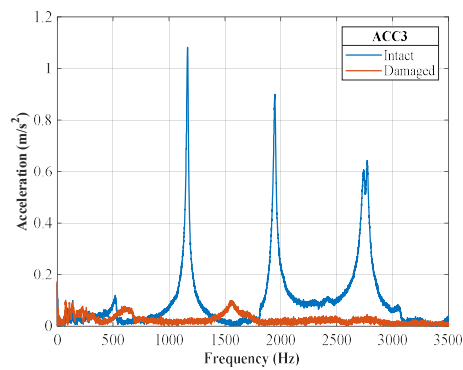
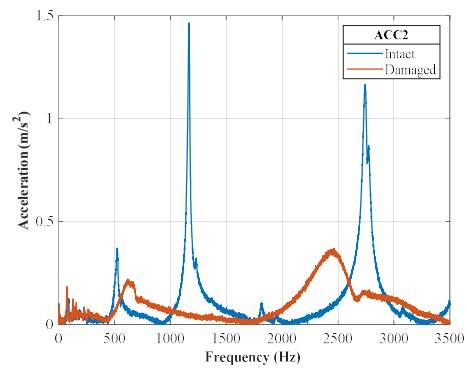
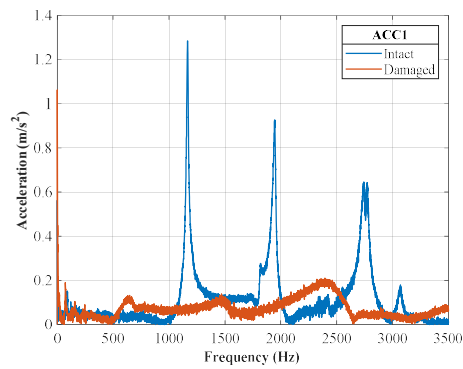
Ce-Ref-0.2 (V02) – single impact test data



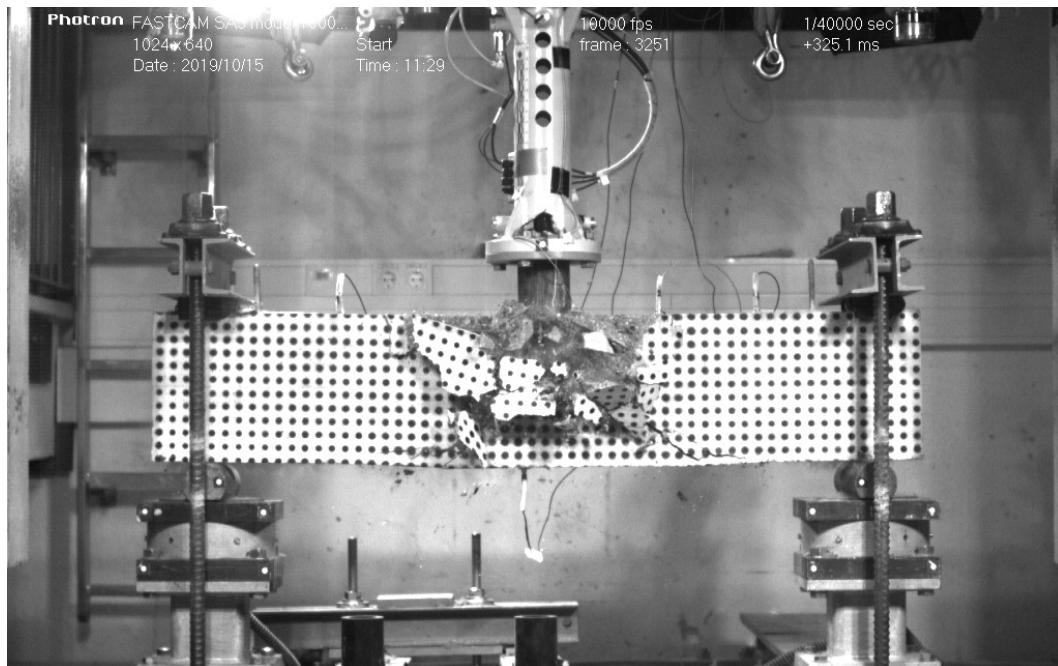
Transversal reinforcement configuration	With stirrups
Strengthening specification	Reference beam
Acceleration pressure [bar]	0.2
Age substrate [days]	40
Age SHCC [days]	N/A
Impactor velocity [m/s]	17.3
Kinetic energy [J]	2125.5
Specimen mass before the test [kg]	104.9
Specimen mass after the test [kg]	104.2
Accountable breakout material [kg]	0.7



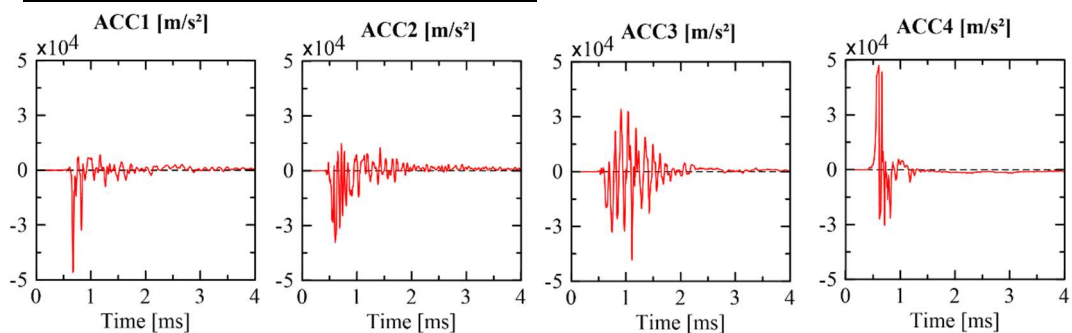
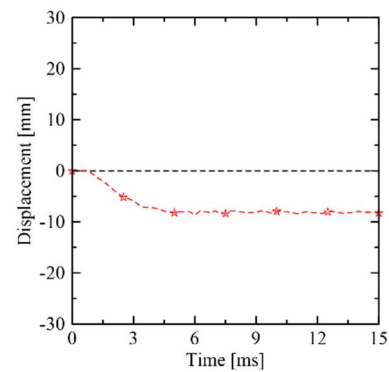
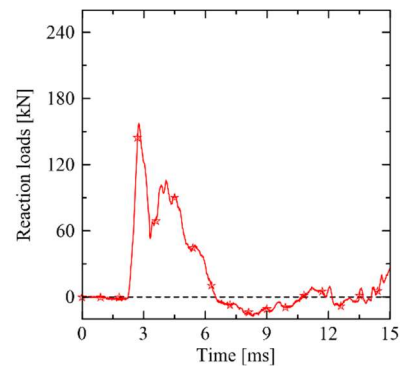
Ce-Ref-0.2 (V02) – data collected before and after the impact



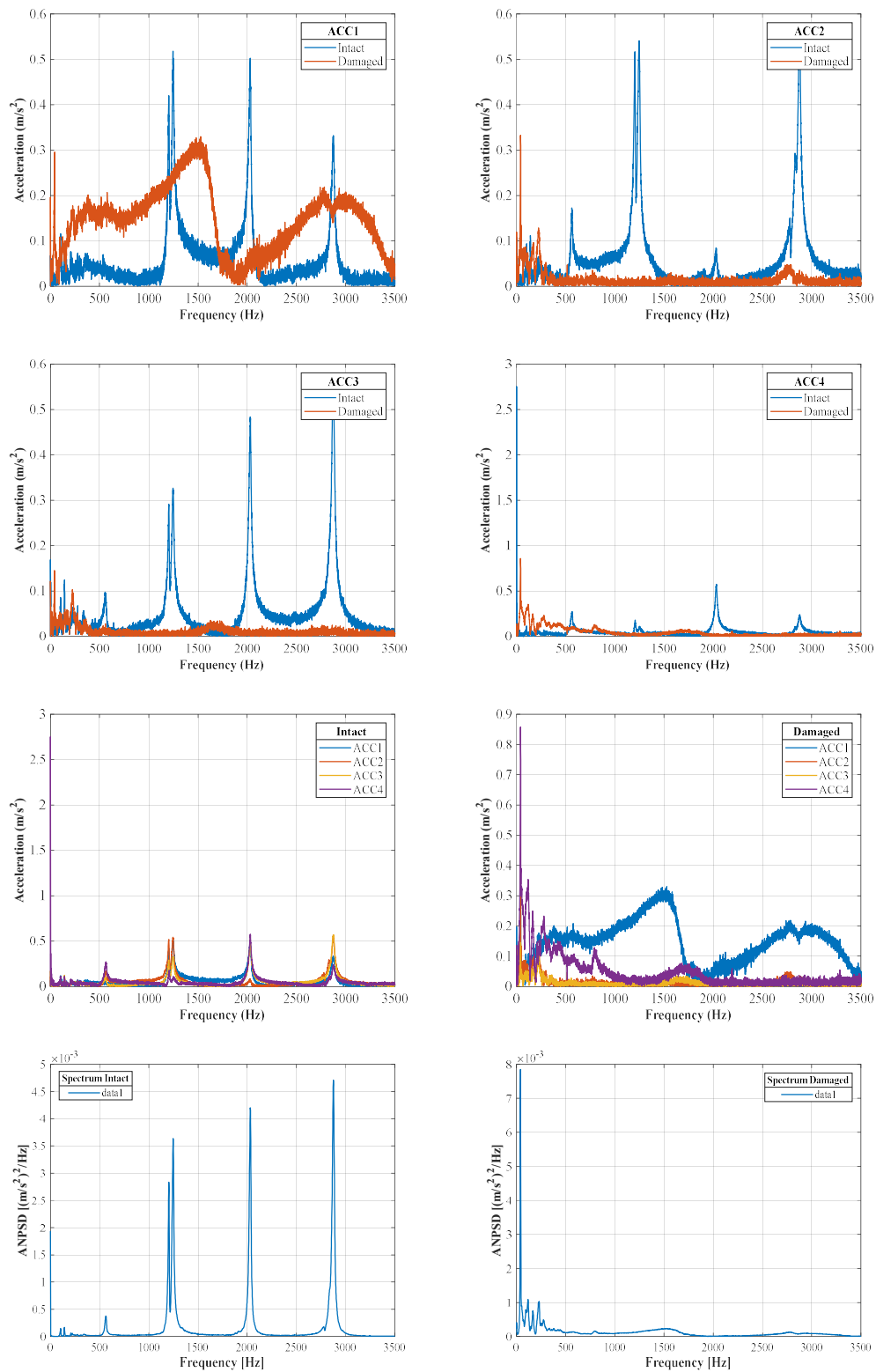
Se-Ref-0.4 (V04) – single impact test data



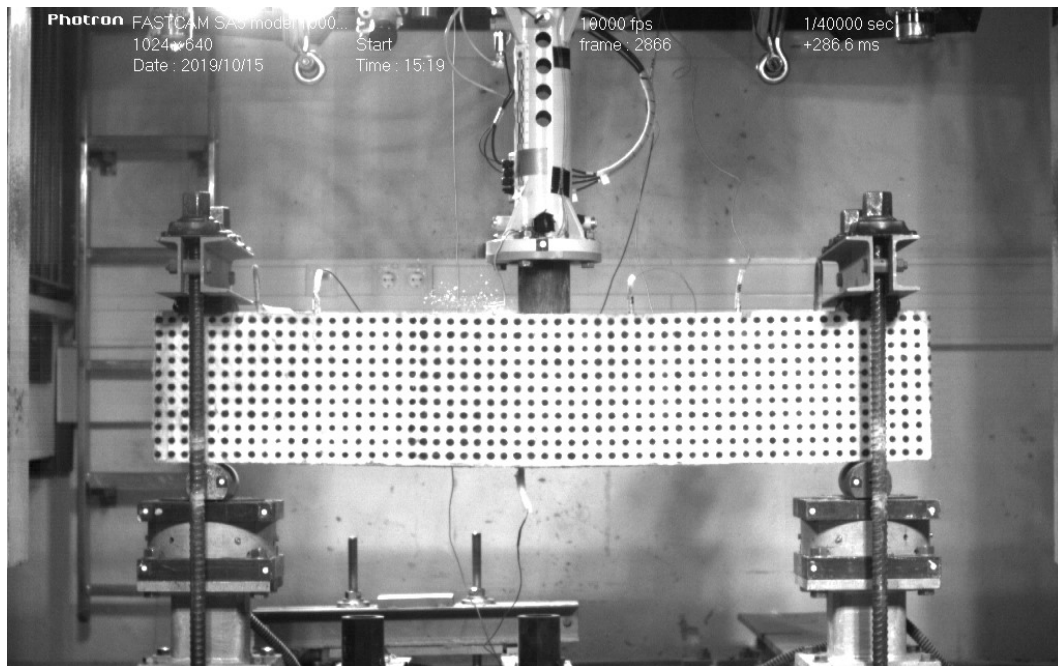
Transversal reinforcement configuration	Without stirrups
Strengthening specification	Reference beam
Acceleration pressure [bar]	0.4
Age substrate [days]	42
Age SHCC [days]	N/A
Impactor velocity [m/s]	20.9
Kinetic energy [J]	3093.8
Specimen mass before the test [kg]	107.8
Specimen mass after the test [kg]	104.1
Accountable breakout material [kg]	3.7



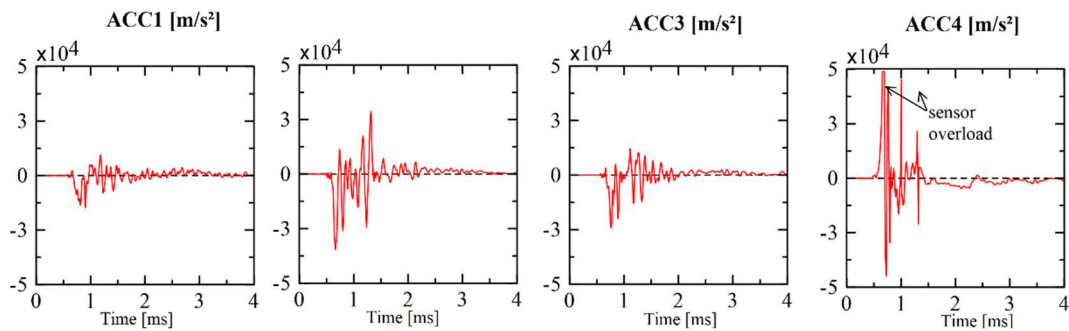
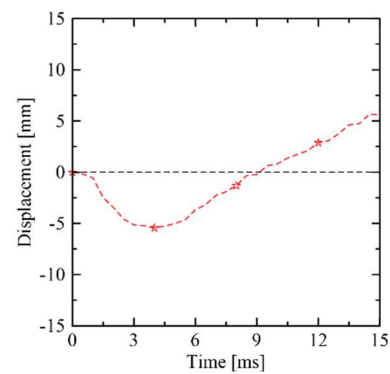
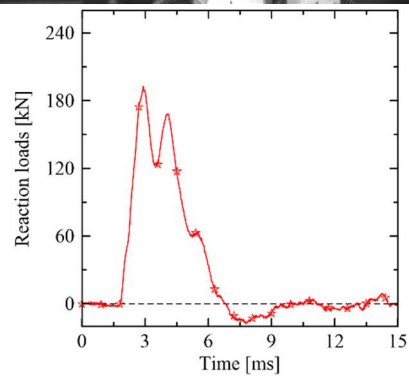
Se-Ref-0.4 (V04) – data collected before and after the impact



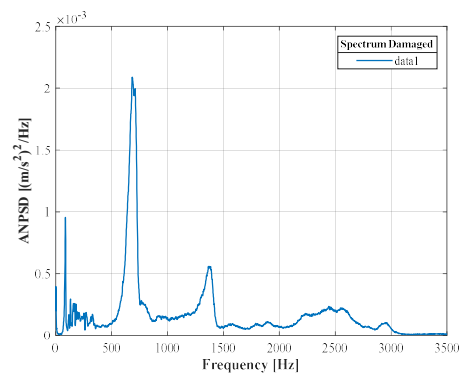
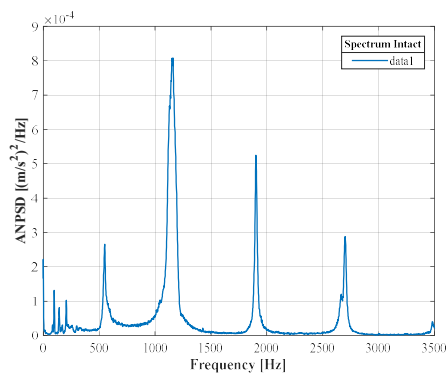
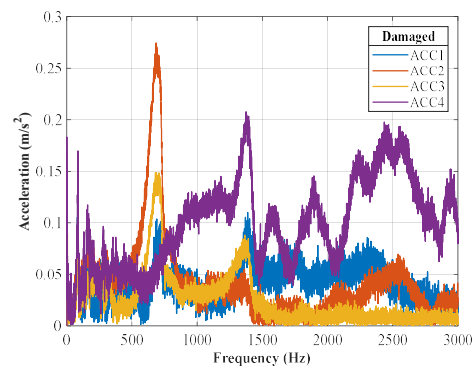
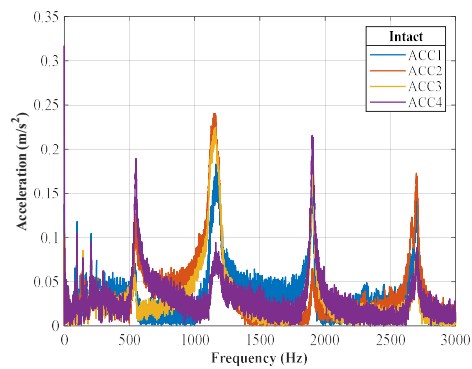
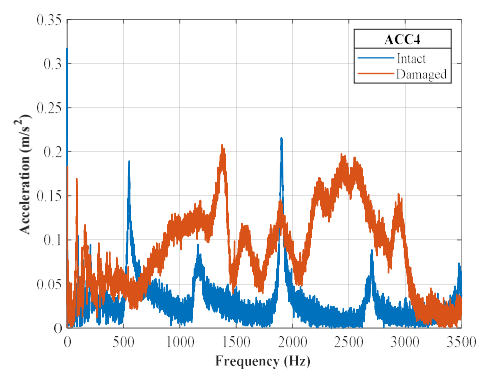
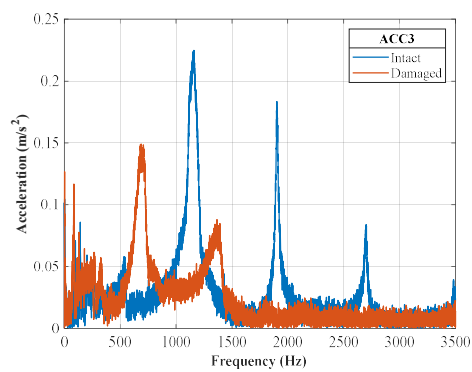
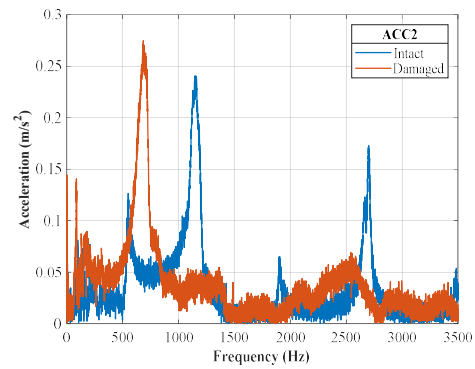
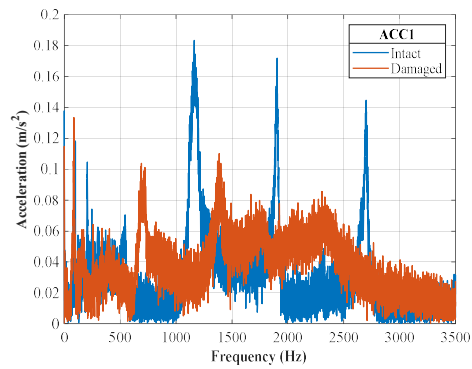
Se-PVA-0.4 (V07) – single impact test data



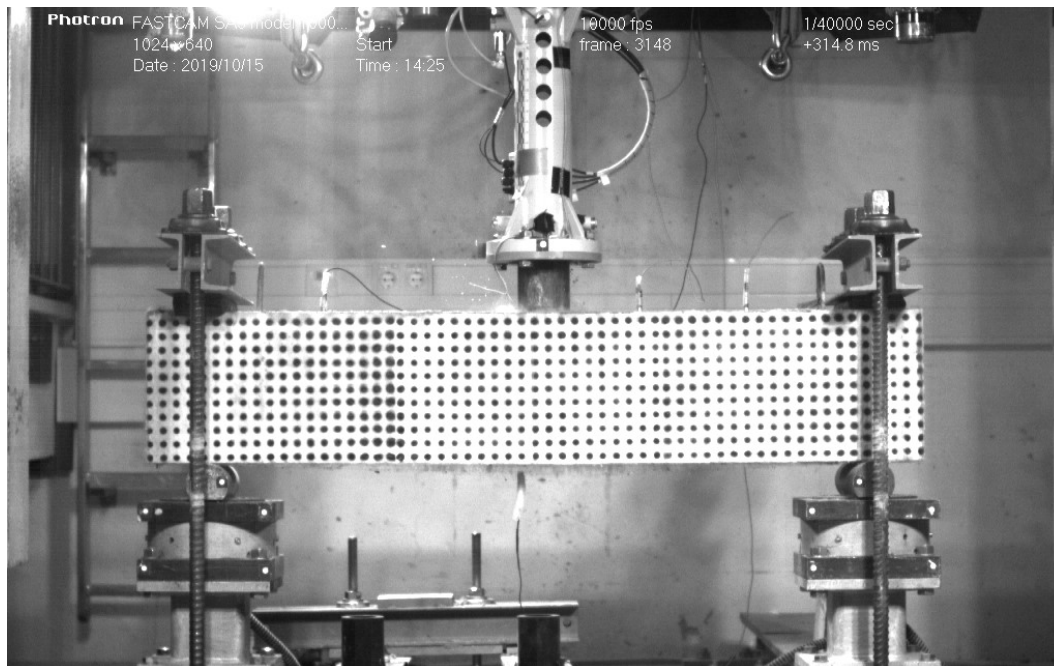
Transversal reinforcement configuration	Without stirrups
Strengthening specification	PVA
Acceleration pressure [bar]	0.4
Age substrate [days]	42
Age SHCC [days]	29
Impactor velocity [m/s]	21.4
Kinetic energy [J]	3259.1
Specimen mass before the test [kg]	135.1
Specimen mass after the test [kg]	135.1
Accountable breakout material [kg]	0.0



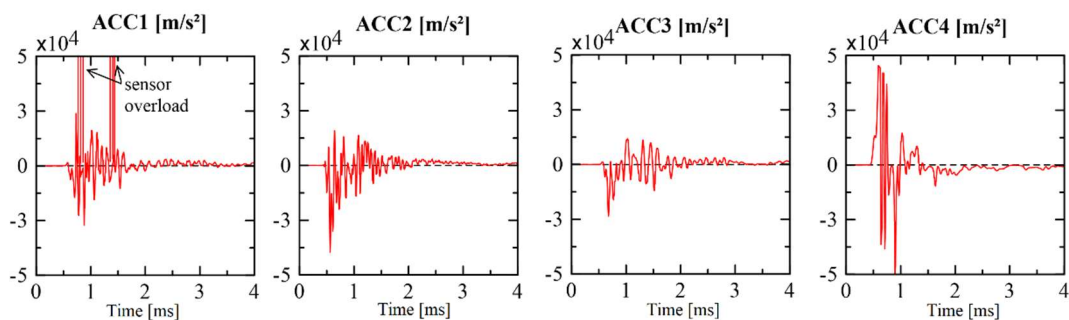
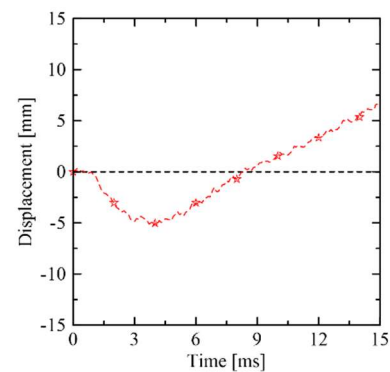
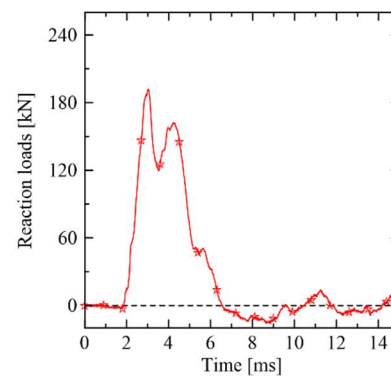
Se-PVA-0.4 (V07) – data collected before and after the impact



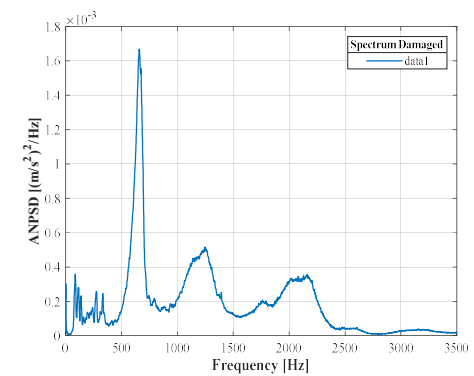
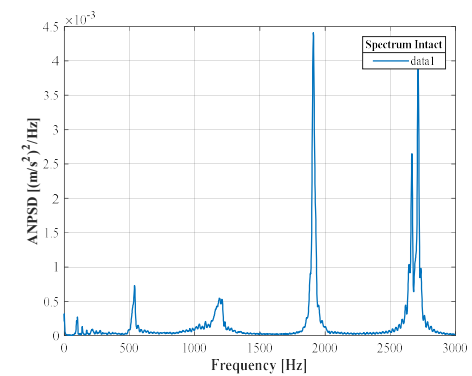
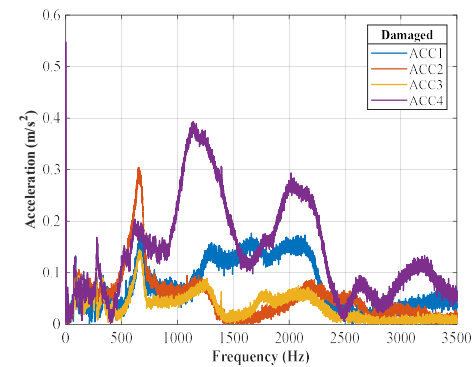
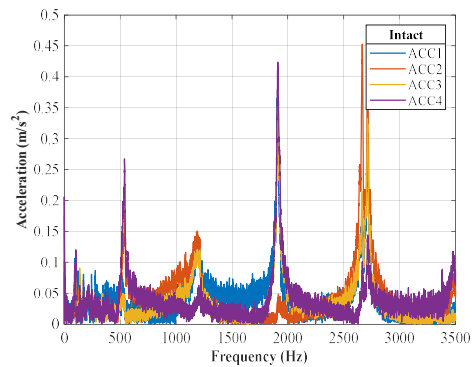
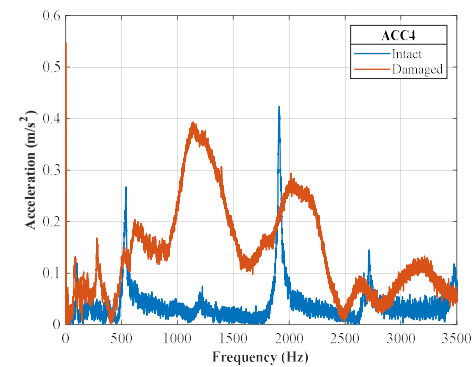
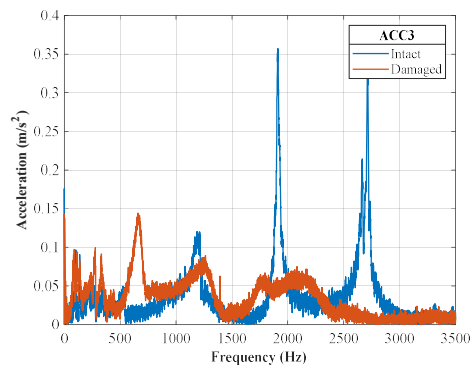
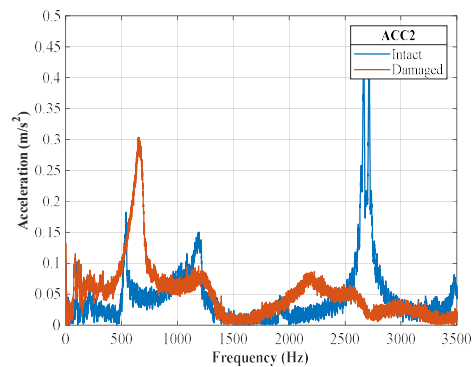
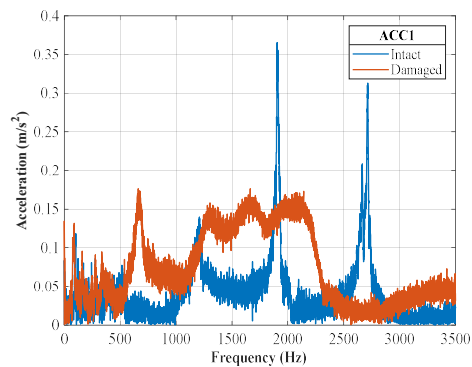
Se-PE-0.4 (V05) – single impact test data



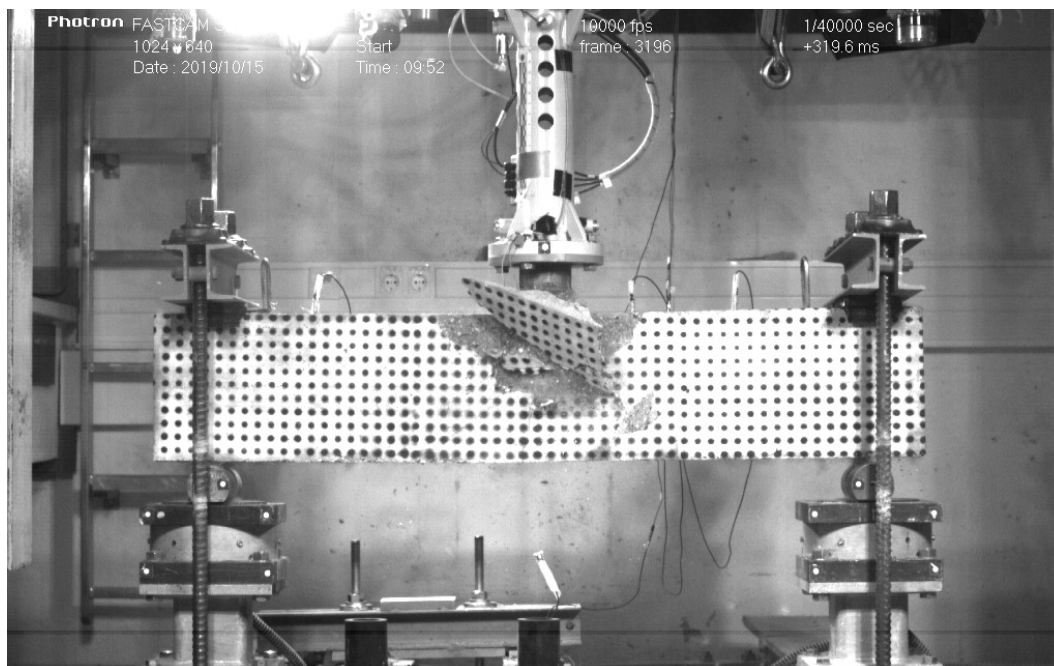
Transversal reinforcement configuration	Without stirrups
Strengthening specification	PE
Acceleration pressure [bar]	0.4
Age substrate [days]	42
Age SHCC [days]	29
Impactor velocity [m/s]	20.4
Kinetic energy [J]	2953.1
Specimen mass before the test [kg]	140.7
Specimen mass after the test [kg]	140.7
Accountable breakout material [kg]	0.0



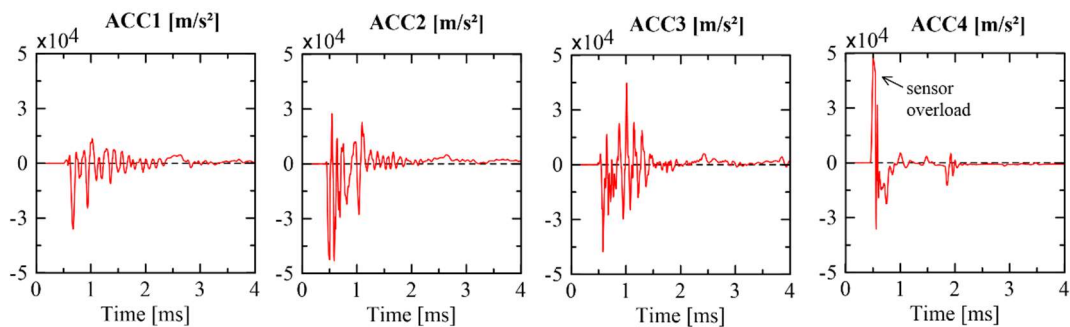
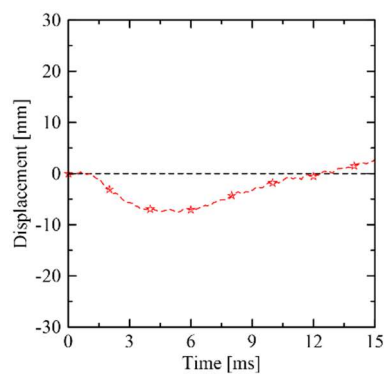
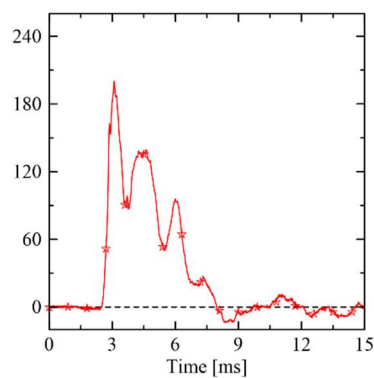
Se-PE-0.4 (V05) – data collected before and after the impact



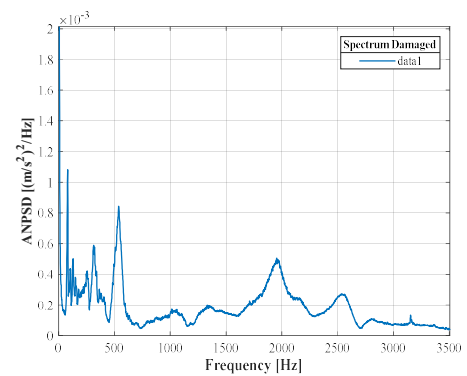
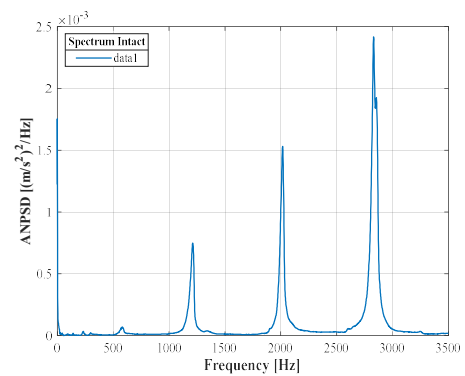
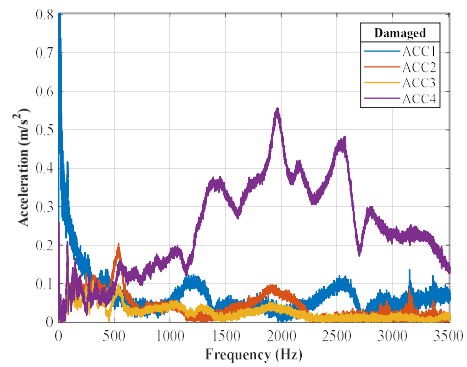
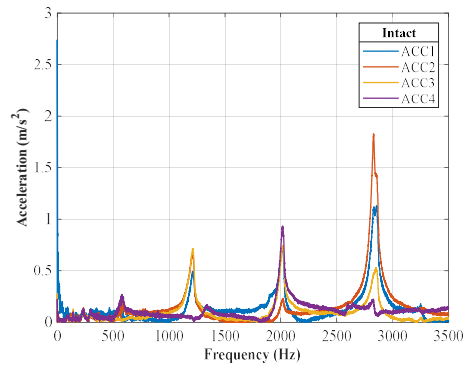
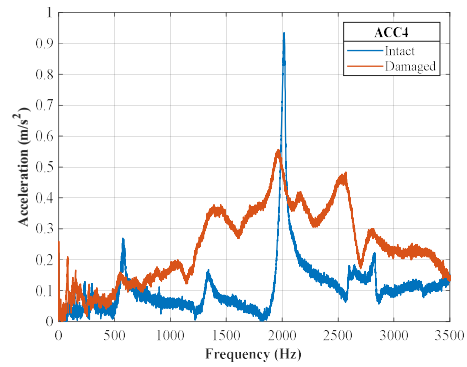
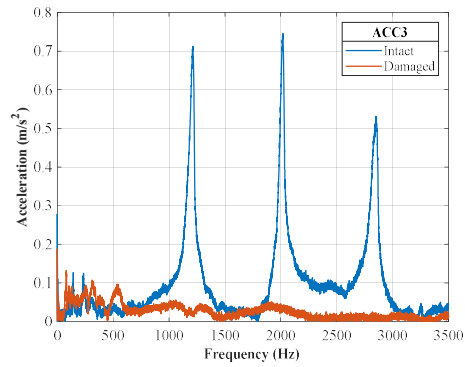
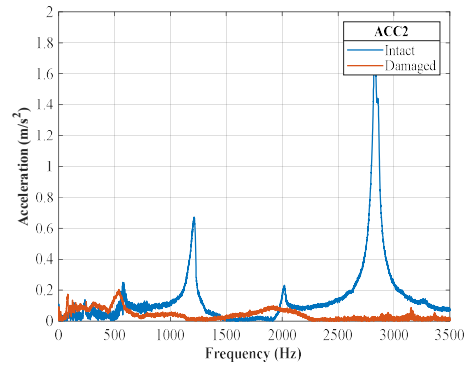
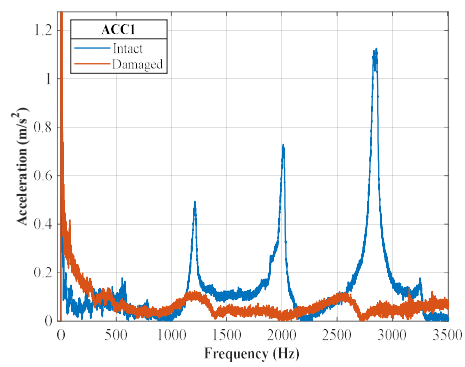
Ce-Ref-0.4 (V03) – single impact test data



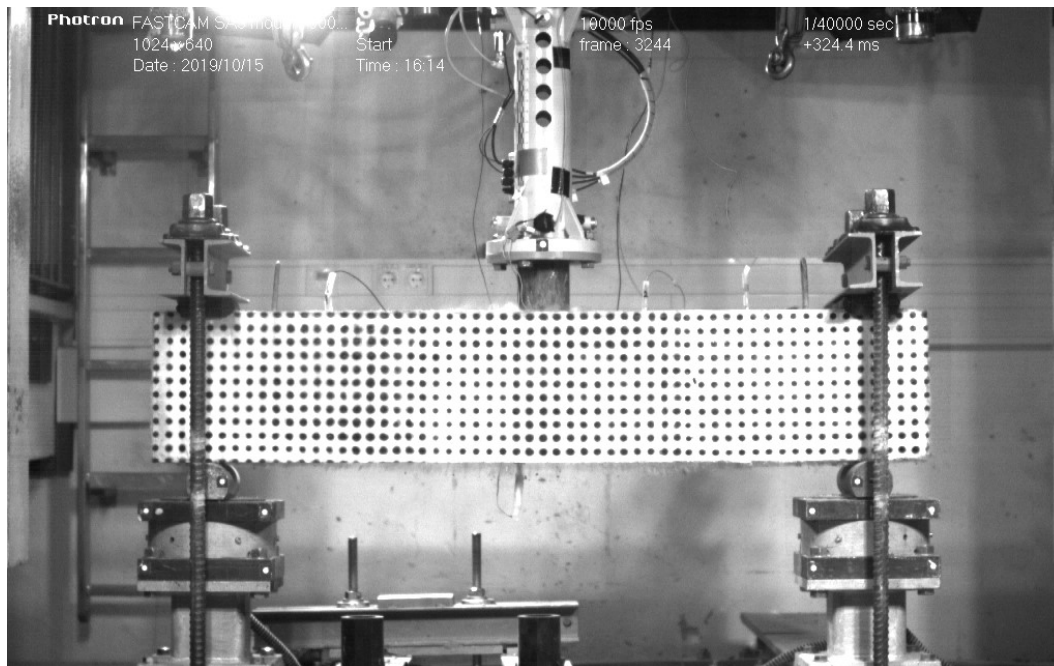
Transversal reinforcement configuration	With stirrups
Strengthening specification	Reference beam
Acceleration pressure [bar]	0.4
Age substrate [days]	42
Age SHCC [days]	N/A
Impactor velocity [m/s]	21.2
Kinetic energy [J]	3192.5
Specimen mass before the test [kg]	111.4
Specimen mass after the test [kg]	109.3
Accountable breakout material [kg]	2.1



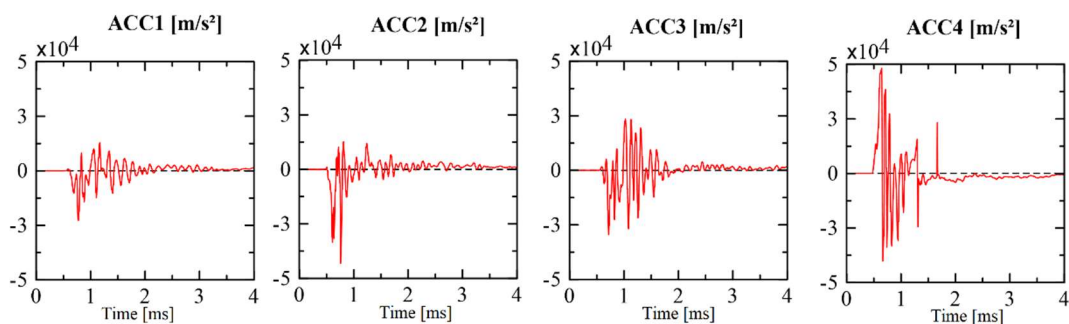
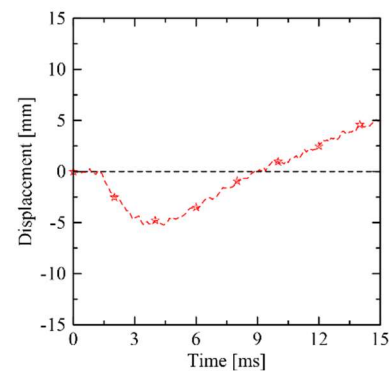
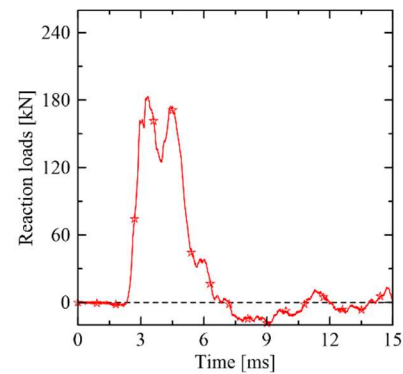
Ce-Ref-0.4 (V03) – data collected before and after the impact



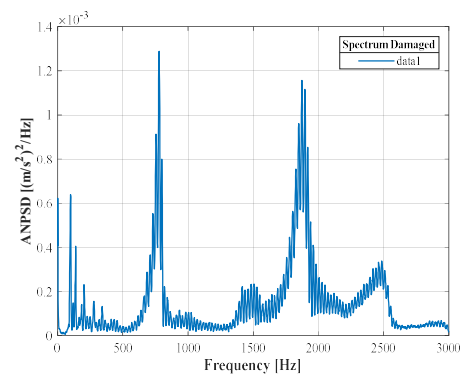
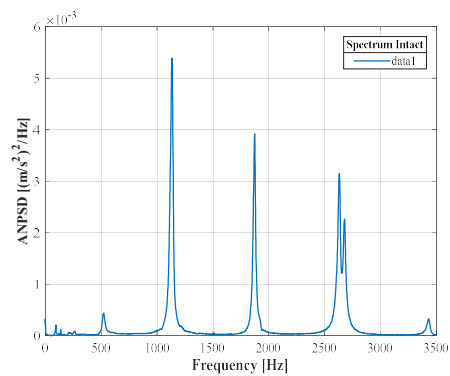
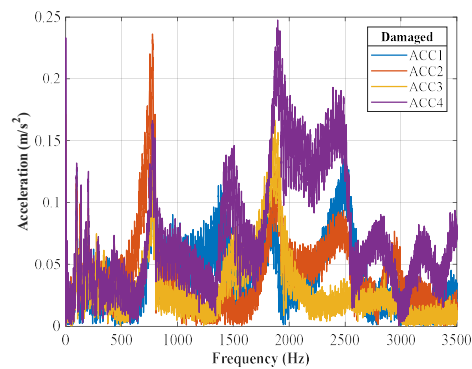
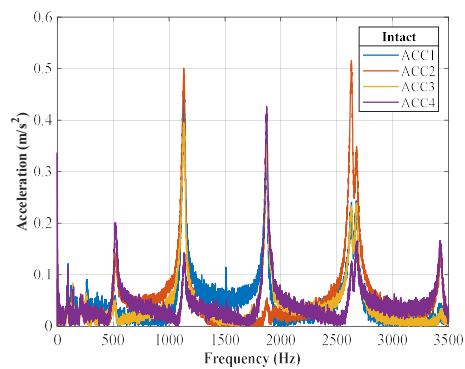
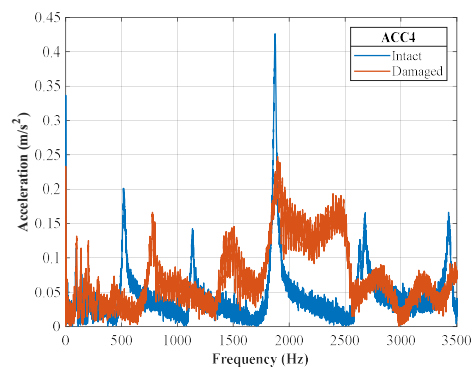
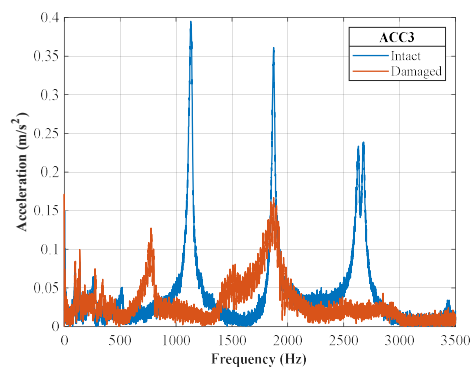
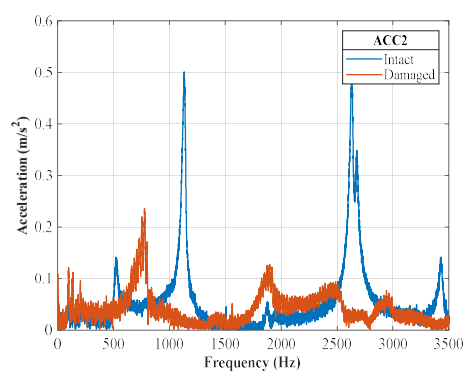
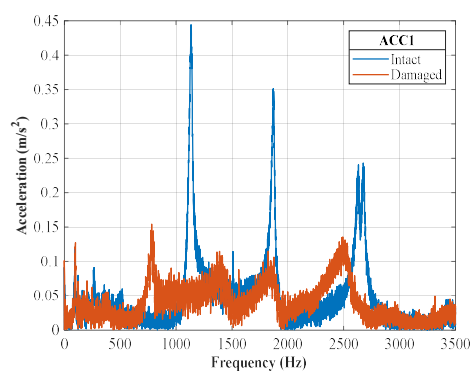
Ce-PVA-0.4 (V09) – single impact test data



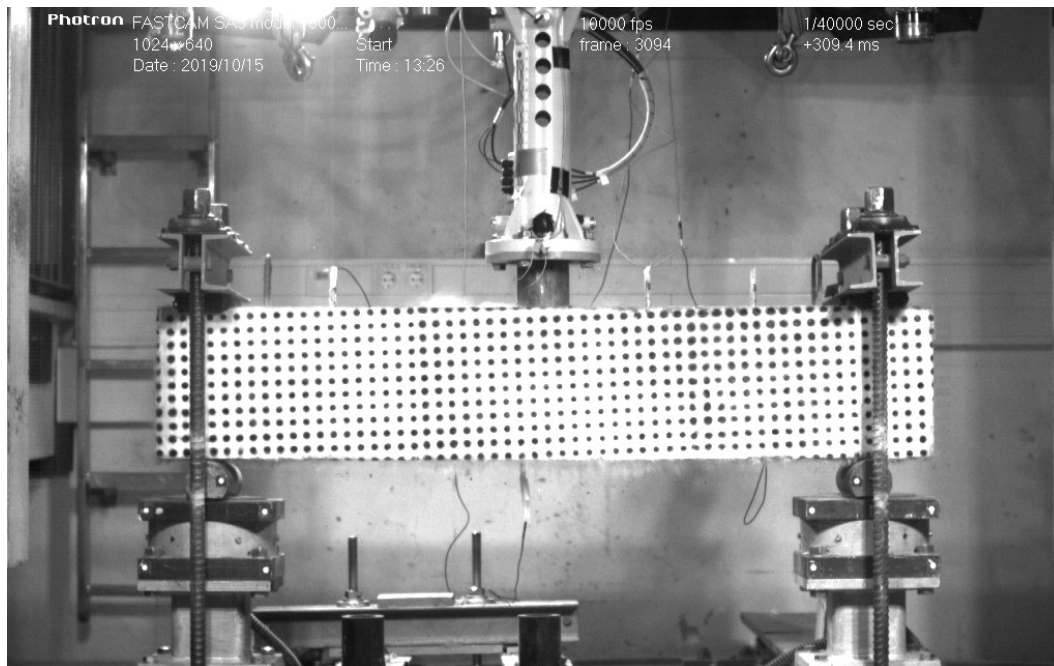
Transversal reinforcement configuration	With stirrups
Strengthening specification	PVA
Acceleration pressure [bar]	0.4
Age substrate [days]	42
Age SHCC [days]	29
Impactor velocity [m/s]	20.0
Kinetic energy [J]	2849.7
Specimen mass before the test [kg]	135.1
Specimen mass after the test [kg]	135.1
Accountable breakout material [kg]	0.0



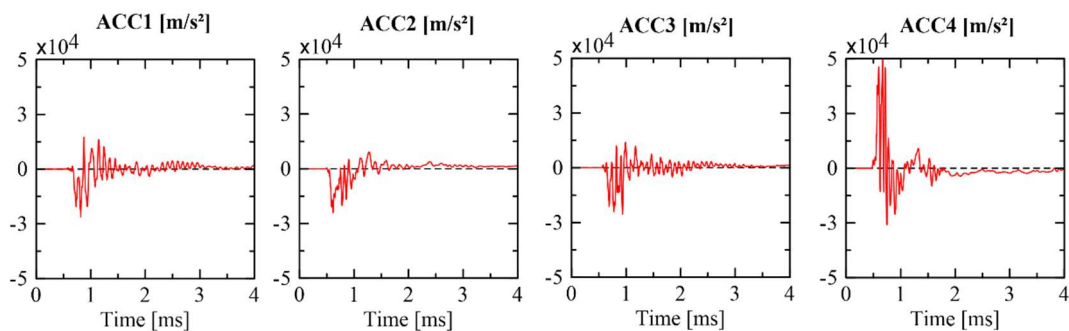
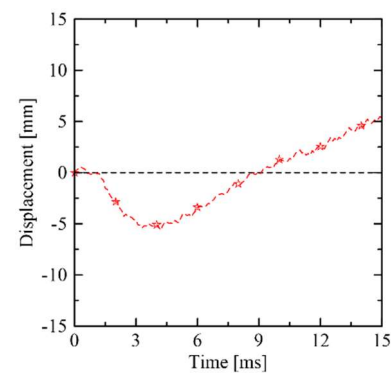
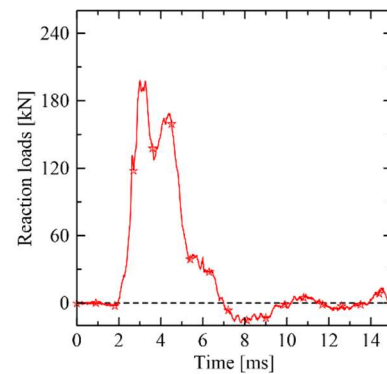
Ce-PVA-0.4 (V09) – data collected before and after the impact



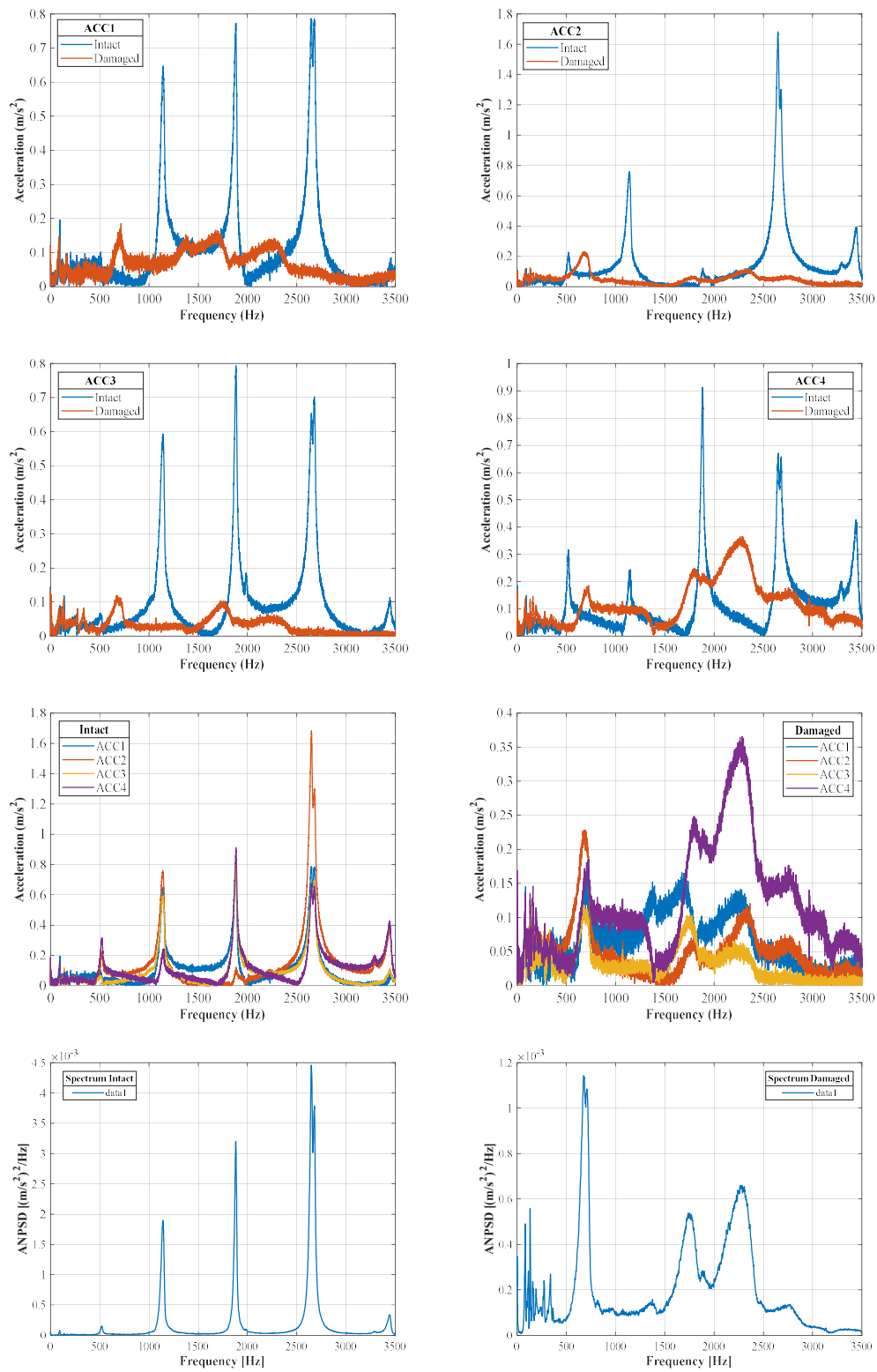
Ce-PE-0.4 (V06) – single impact test data



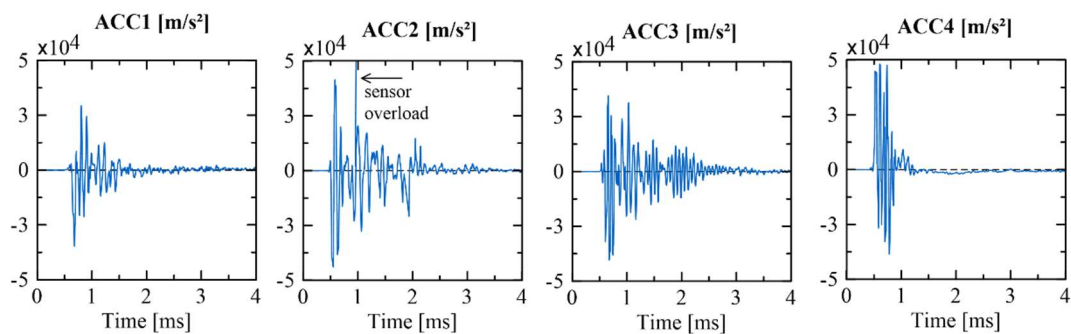
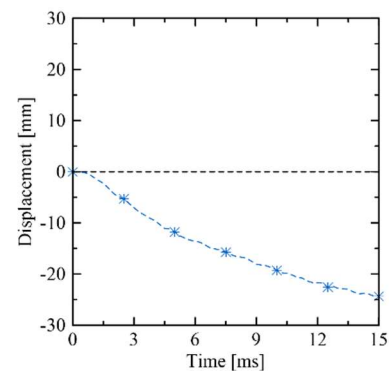
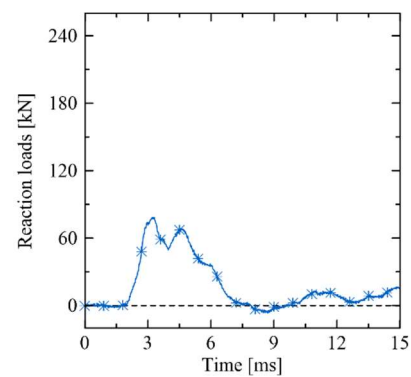
Transversal reinforcement configuration	With stirrups
Strengthening specification	PE
Acceleration pressure [bar]	0.4
Age substrate [days]	42
Age SHCC [days]	29
Impactor velocity [m/s]	20.5
Kinetic energy [J]	2999.6
Specimen mass before the test [kg]	140.9
Specimen mass after the test [kg]	140.9
Accountable breakout material [kg]	0.0



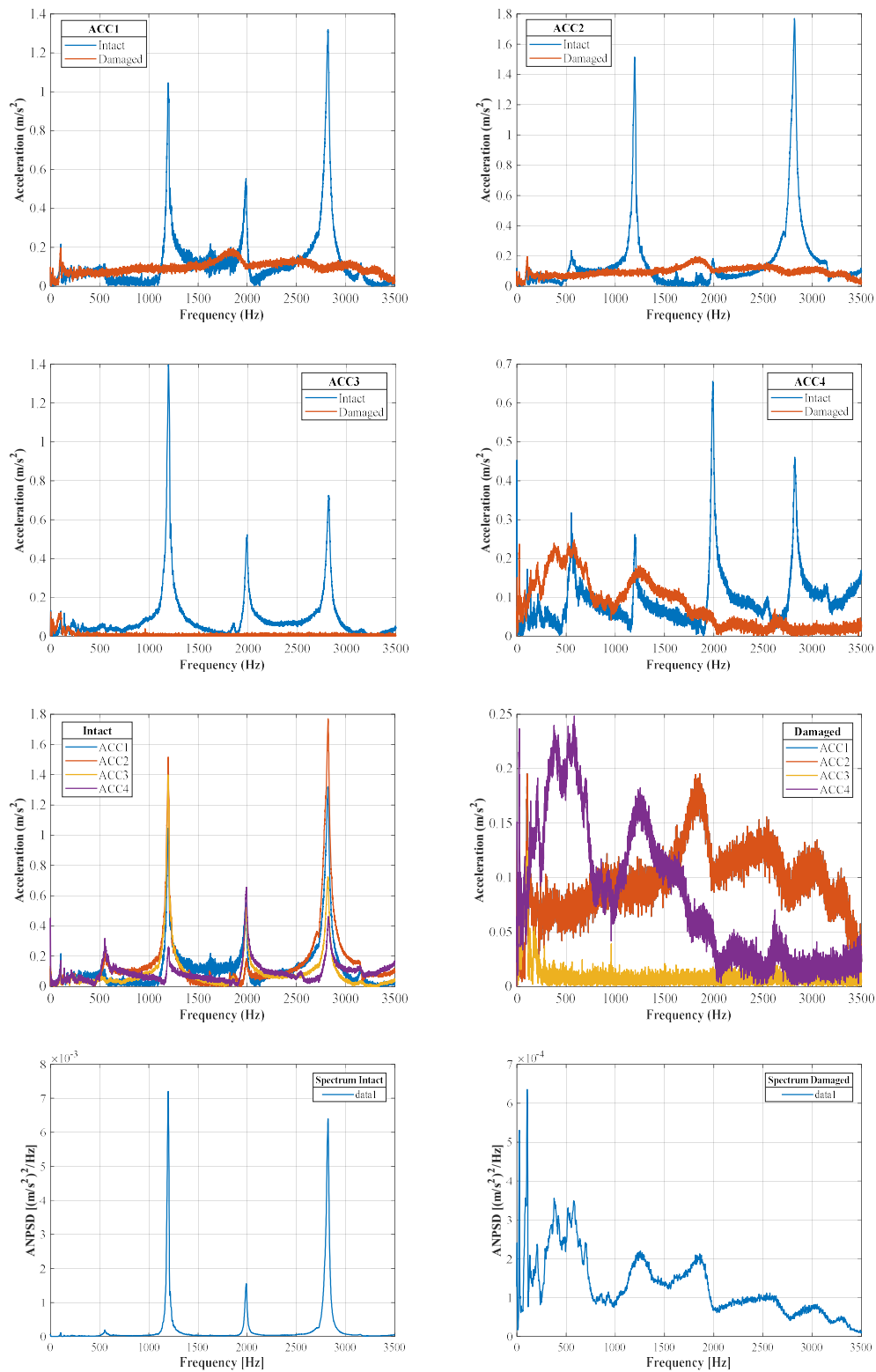
Ce-PE-0.4 (V06) – data collected before and after the impact



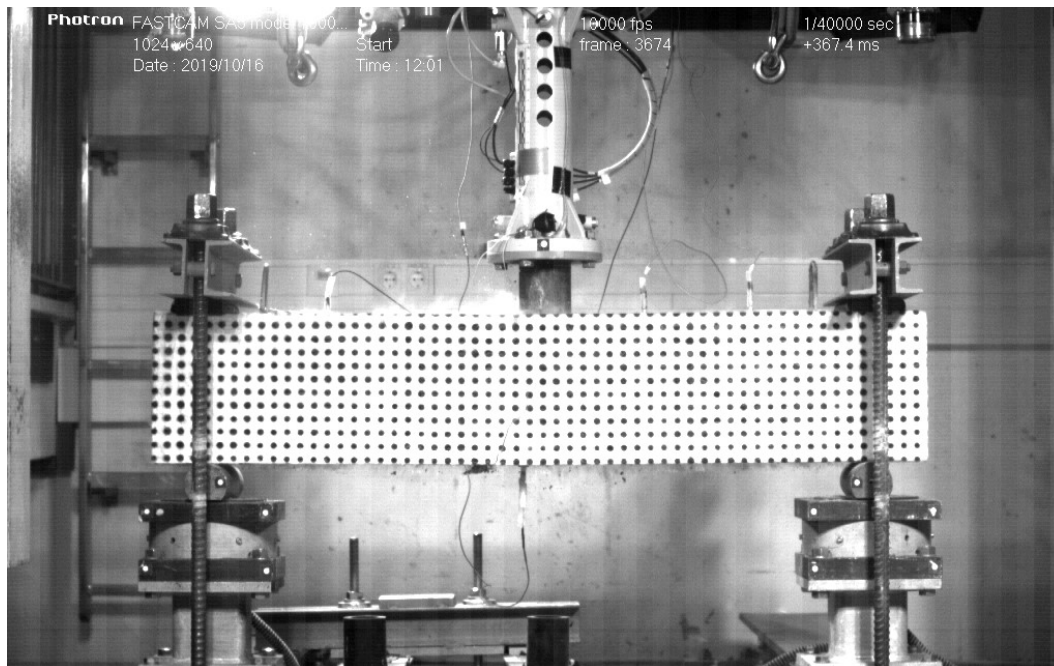
Transversal reinforcement configuration	Without stirrups
Strengthening specification	Reference beam
Acceleration pressure [bar]	0.8
Age substrate [days]	43
Age SHCC [days]	N/A
Impactor velocity [m/s]	25.8
Kinetic energy [J]	4718.0
Specimen mass before the test [kg]	103.8
Specimen mass after the test [kg]	98.1
Accountable breakout material [kg]	5.7



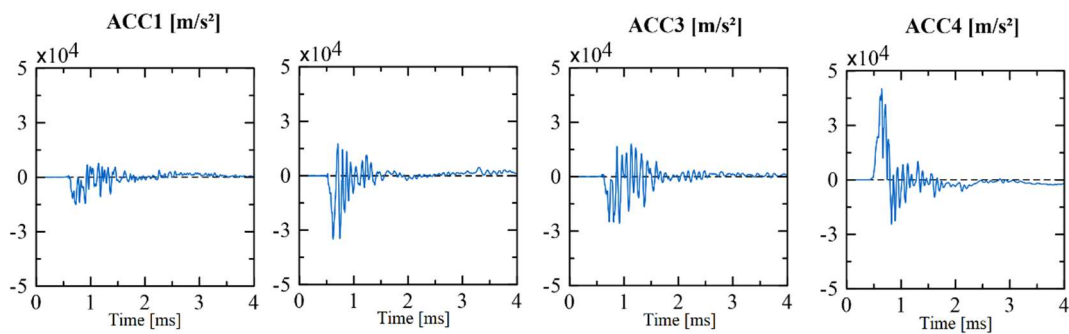
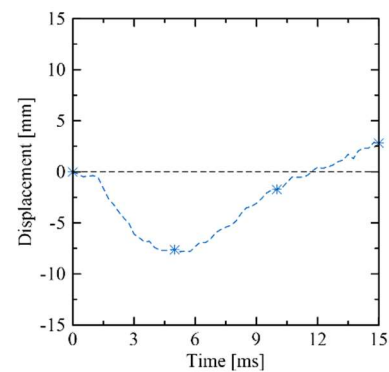
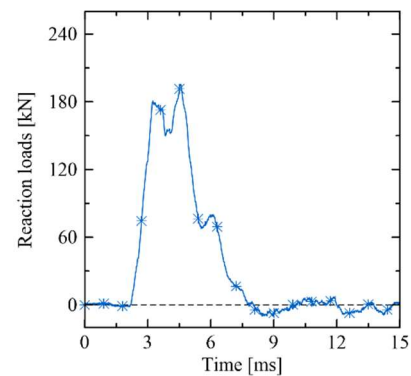
Se-Ref-0.8 (V13) – data collected before and after the impact



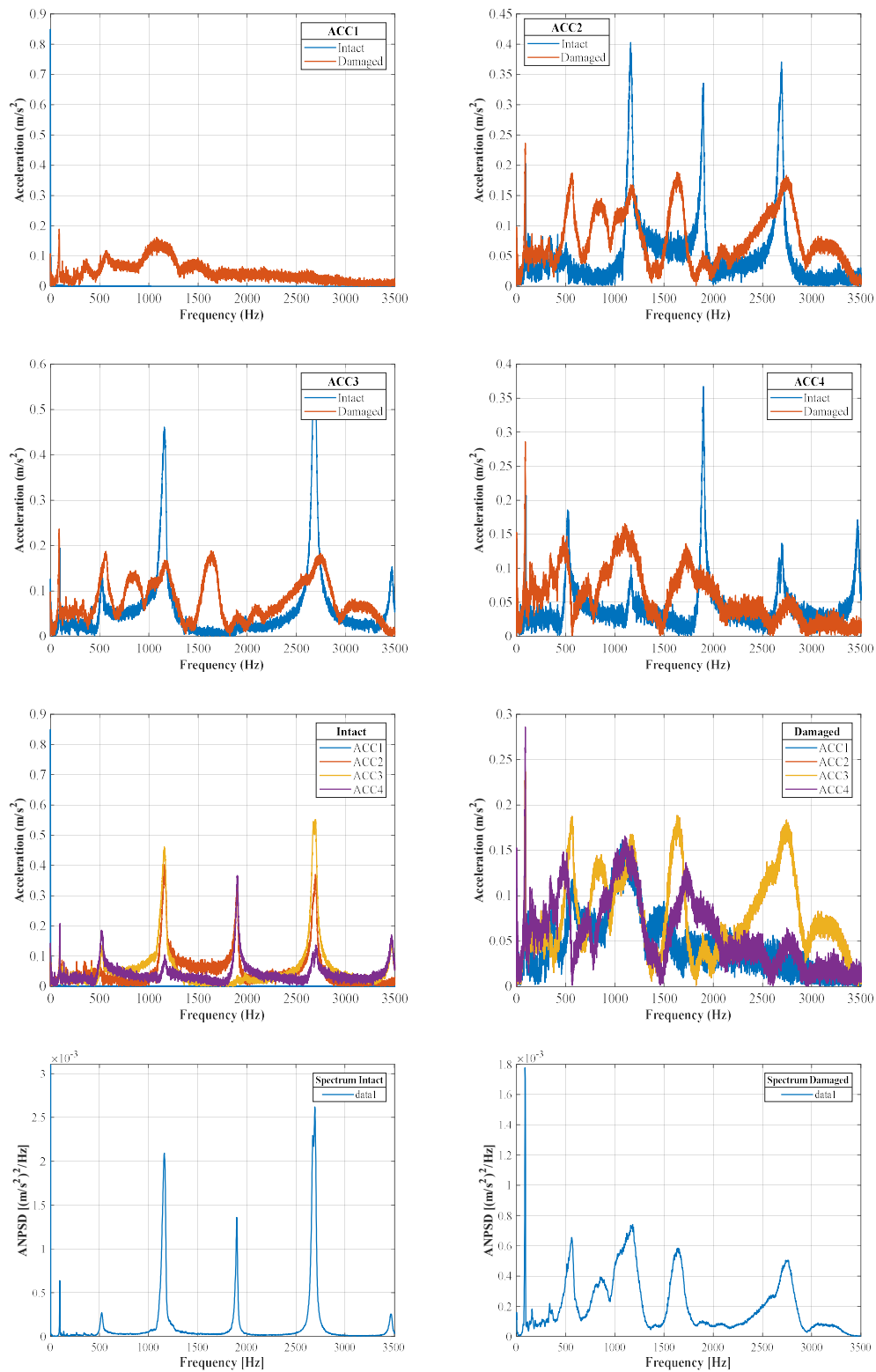
Se-PVA-0.8 (V11) – single impact test data



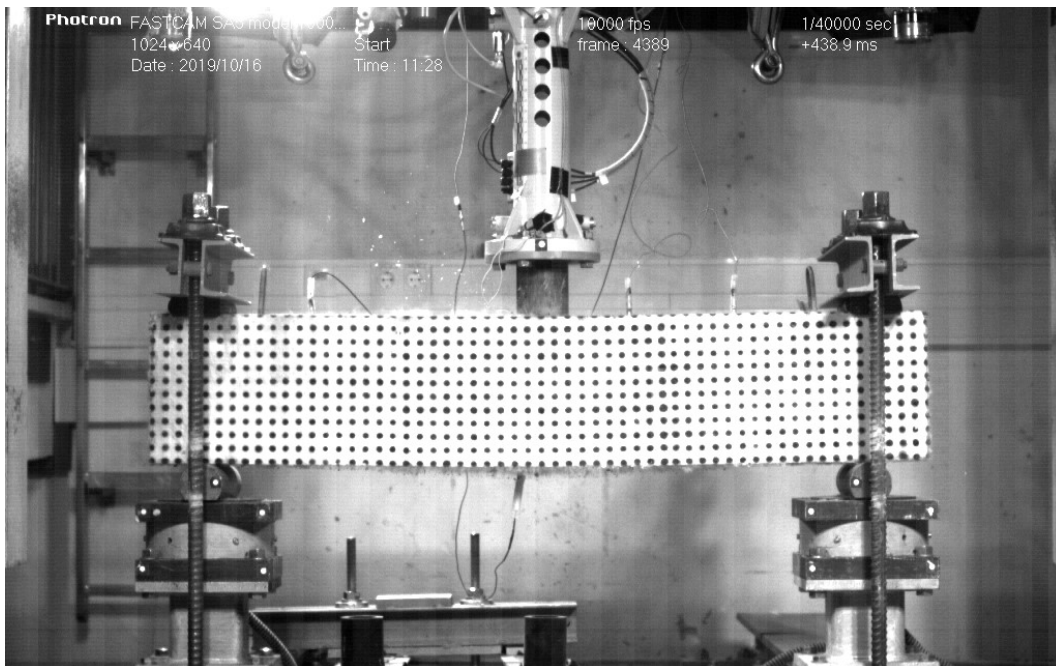
Transversal reinforcement configuration	Without stirrups
Strengthening specification	PVA
Acceleration pressure [bar]	0.8
Age substrate [days]	43
Age SHCC [days]	28
Impactor velocity [m/s]	26.3
Kinetic energy [J]	4917.9
Specimen mass before the test [kg]	137.4
Specimen mass after the test [kg]	137.4
Accountable breakout material [kg]	0.0



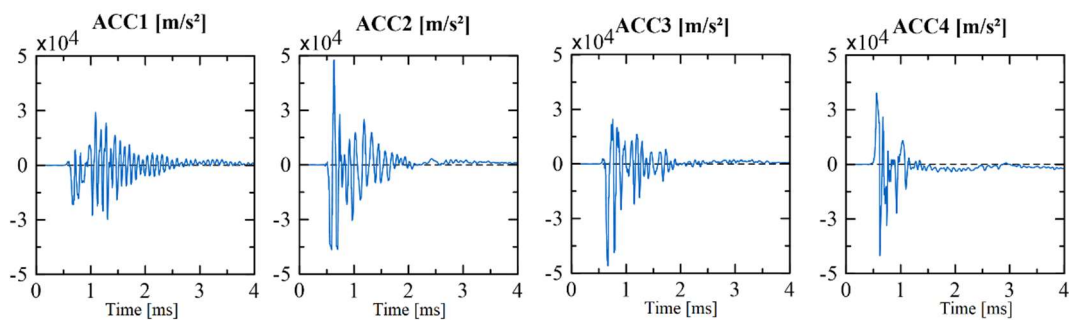
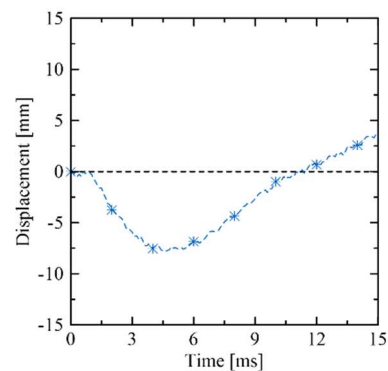
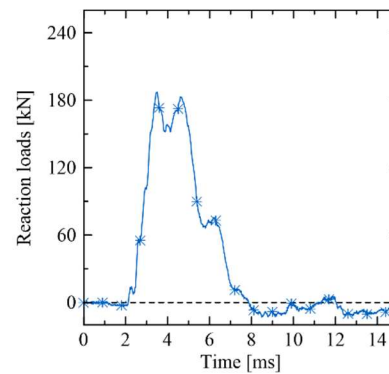
Se-PVA-0.8 (V11) – data collected before and after the impact



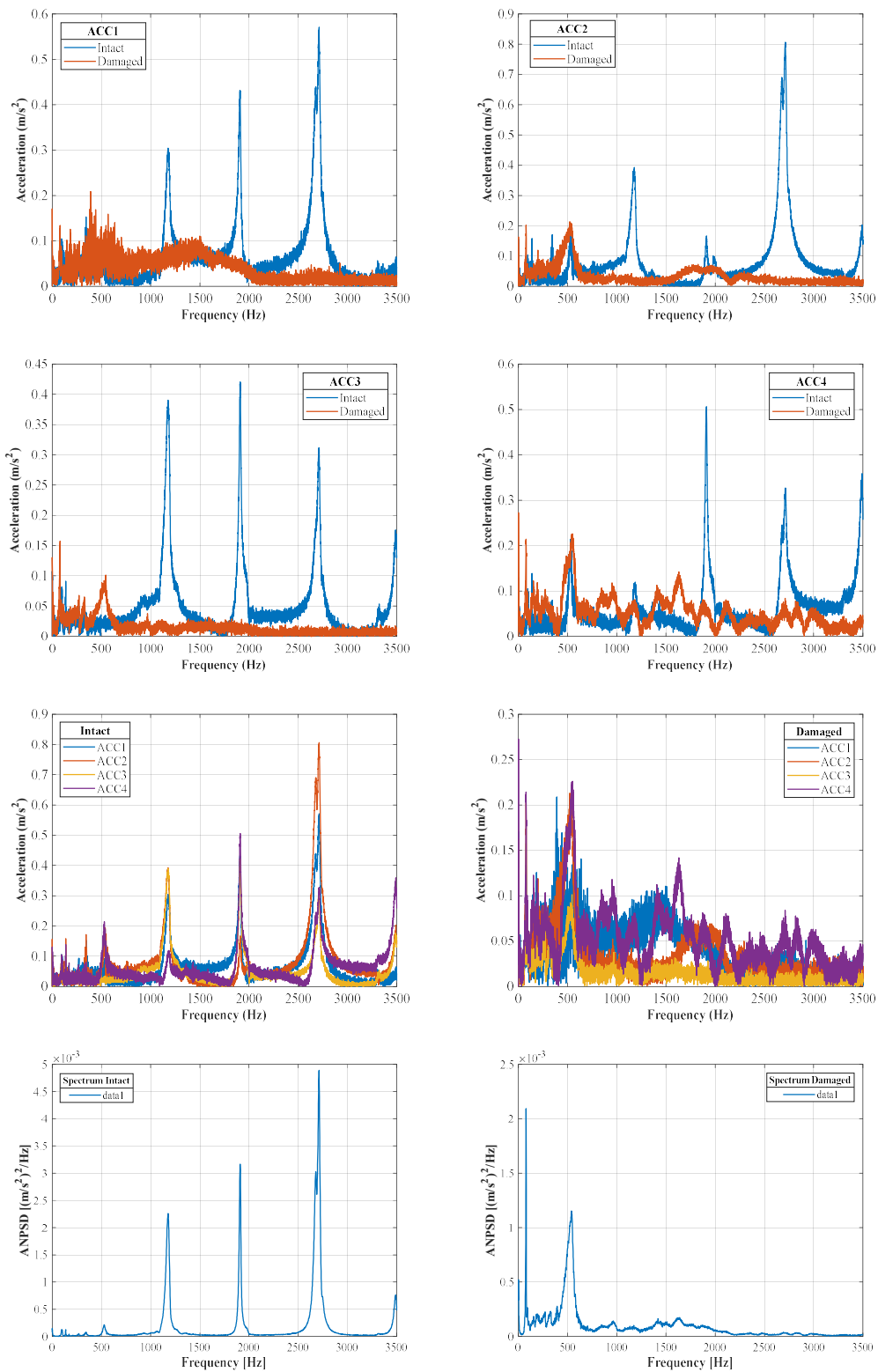
Se-PE-0.8 (V10) – single impact test data



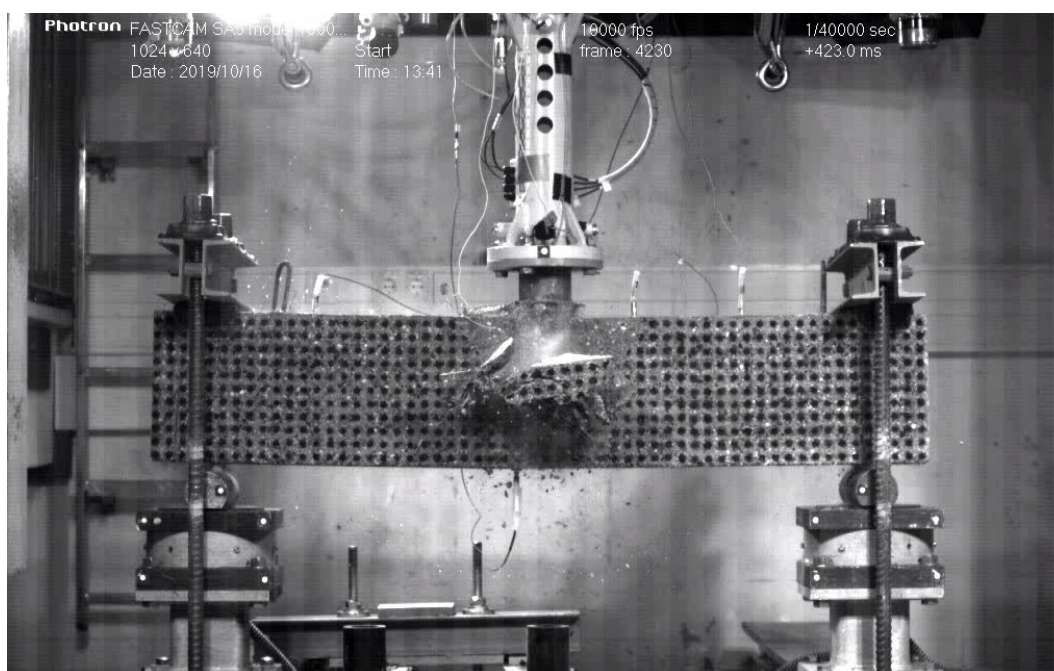
Transversal reinforcement configuration	Without stirrups
Strengthening specification	PE
Acceleration pressure [bar]	0.8
Age substrate [days]	43
Age SHCC [days]	28
Impactor velocity [m/s]	25.3
Kinetic energy [J]	4561.8
Specimen mass before the test [kg]	137.3
Specimen mass after the test [kg]	137.3
Accountable breakout material [kg]	0.0



Se-PE-0.8 (V10) – data collected before and after the impact

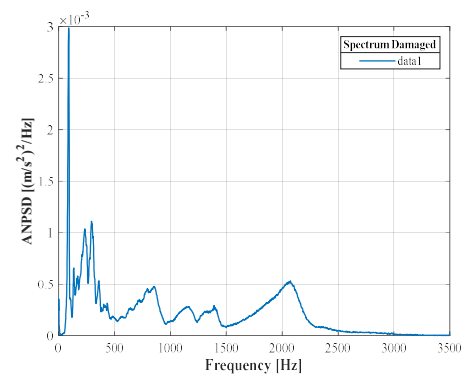
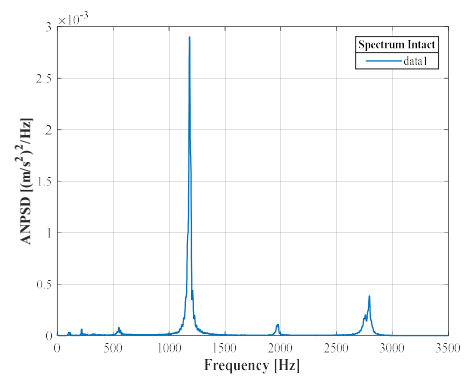
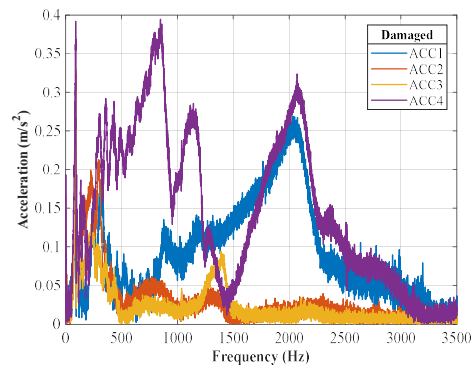
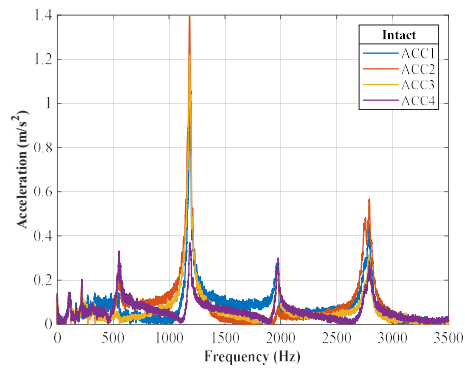
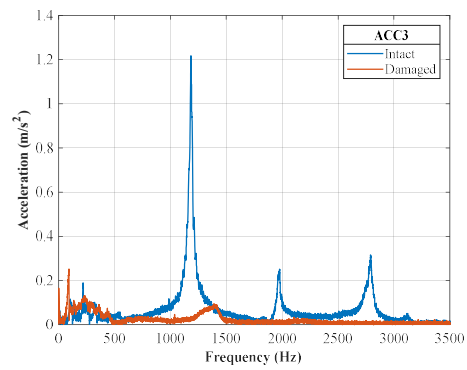
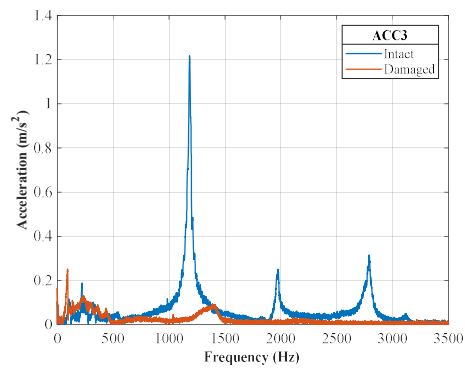
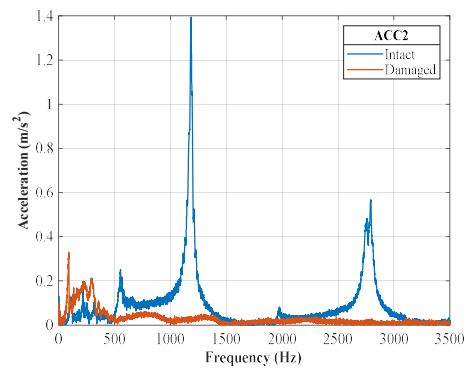
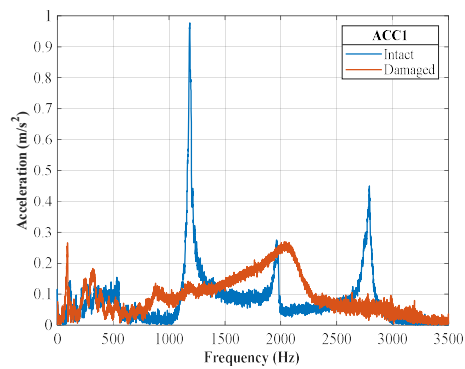


Ce-Ref-0.8 (V14) – single impact test data

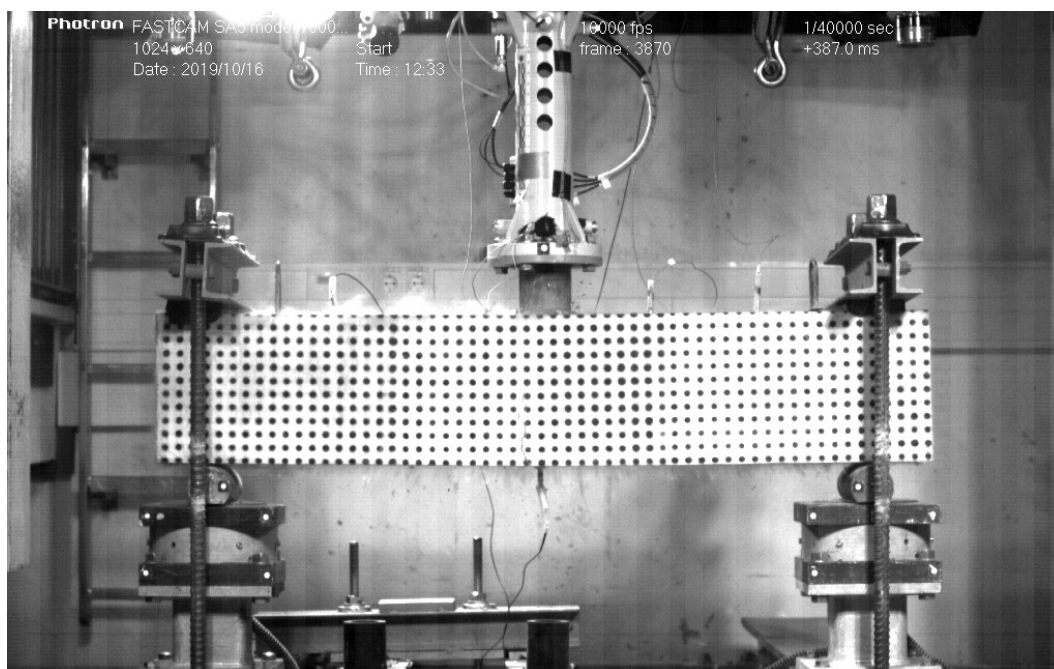


Transversal reinforcement configuration	With stirrups	
Strengthening specification	Reference beam	
Acceleration pressure [bar]	0.8	
Age substrate [days]	43	
Age SHCC [days]	N/A	Plots not available
Impactor velocity [m/s]	25.7	
Kinetic energy [J]	4707.1	
Specimen mass before the test [kg]	106.3	
Specimen mass after the test [kg]	103.9	
Accountable breakout material [kg]	2.4	

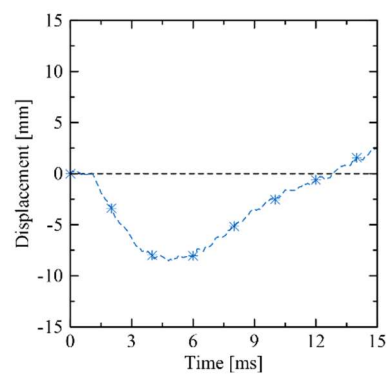
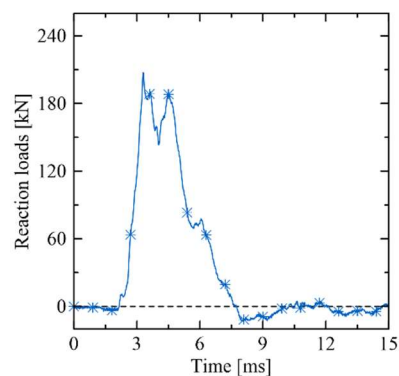
Ce-Ref-0.8 (V14) – data collected before and after the impact



Ce-PVA-0.8 (V12) – single impact test data

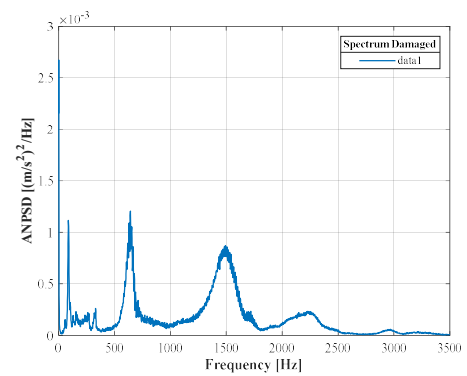
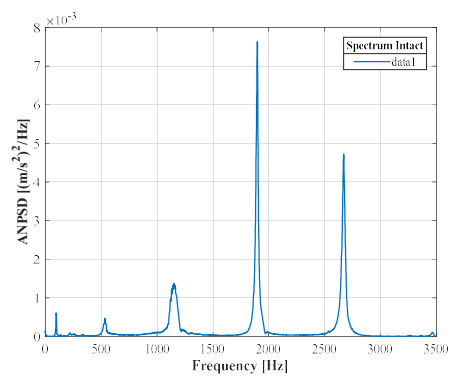
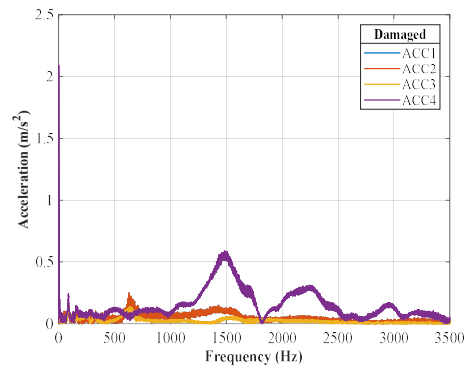
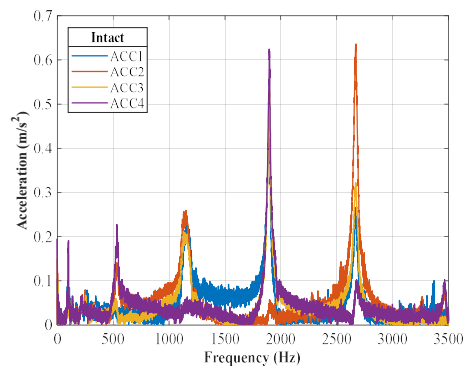
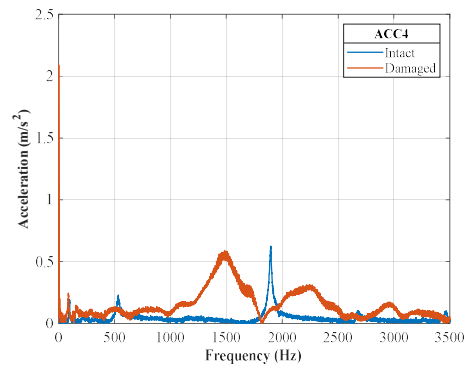
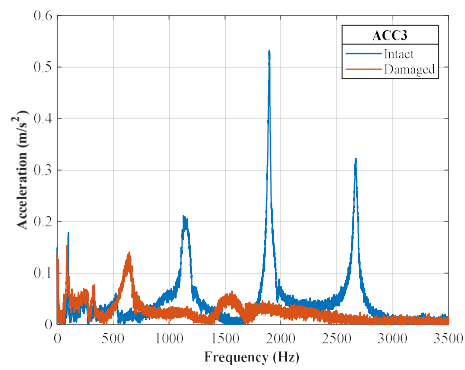
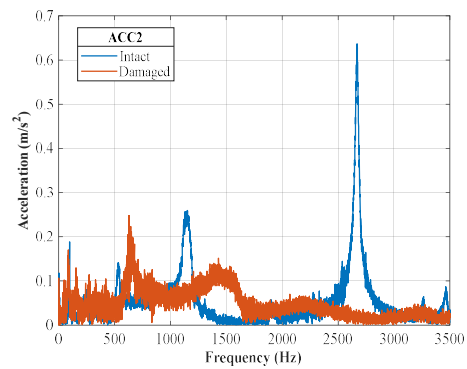
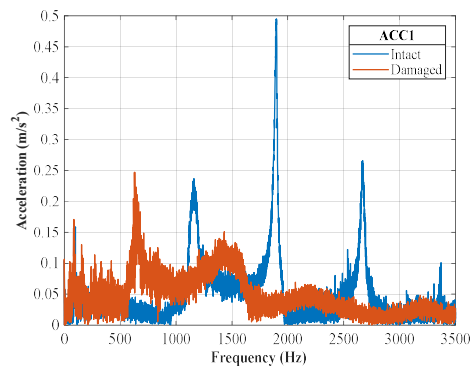


Transversal reinforcement configuration	With stirrups
Strengthening specification	PVA
Acceleration pressure [bar]	0.8
Age substrate [days]	43
Age SHCC [days]	28
Impactor velocity [m/s]	26.3
Kinetic energy [J]	4903.0
Specimen mass before the test [kg]	136.2
Specimen mass after the test [kg]	136.2
Accountable breakout material [kg]	0.0

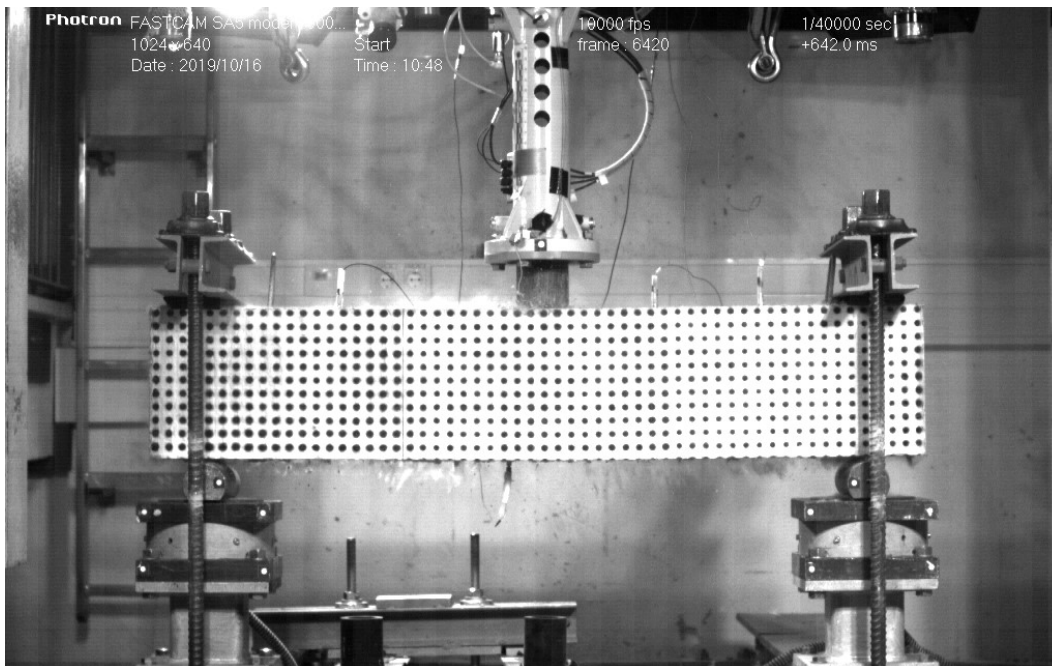


Accelerometers' plots not available

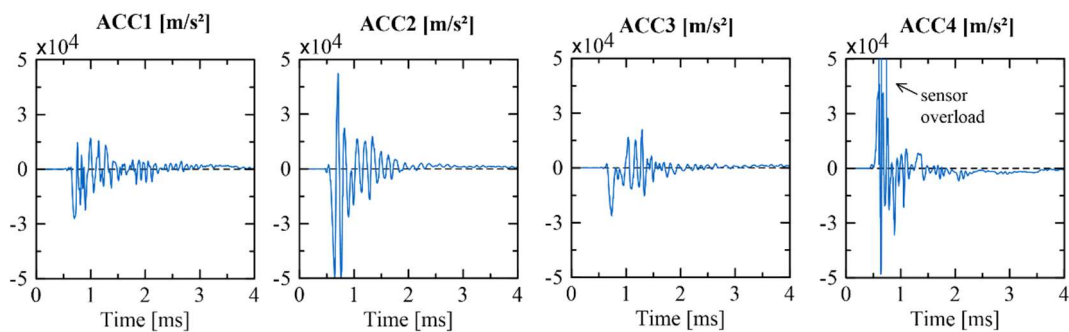
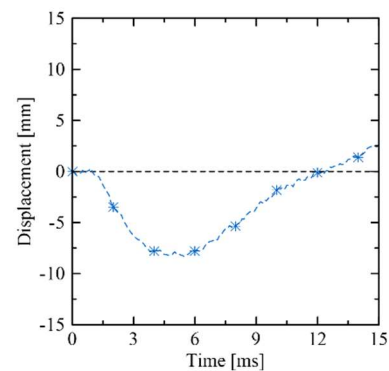
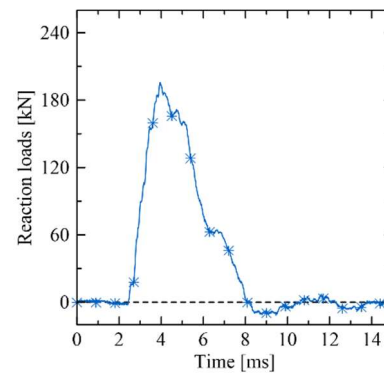
Ce-PVA-0.8 (V12) – data collected before and after the impact



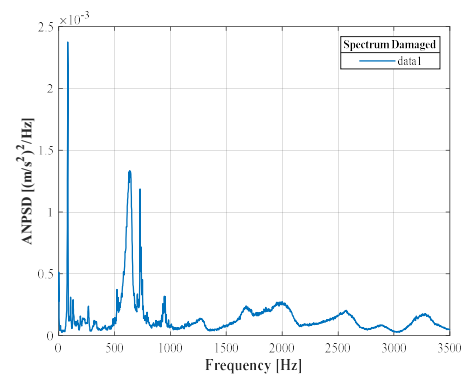
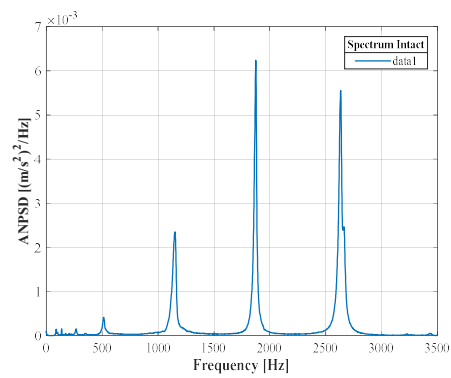
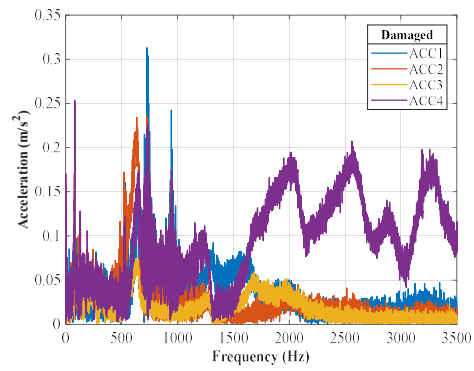
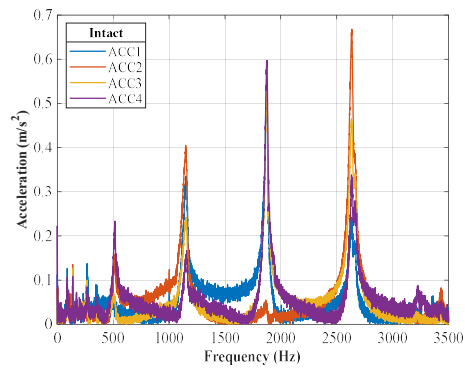
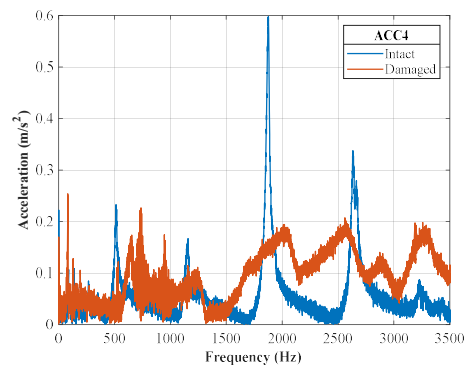
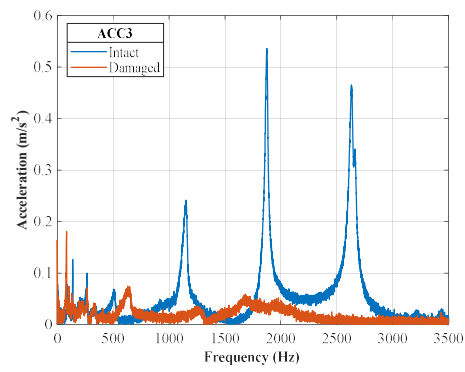
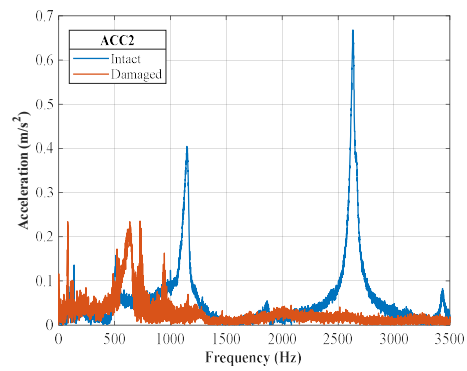
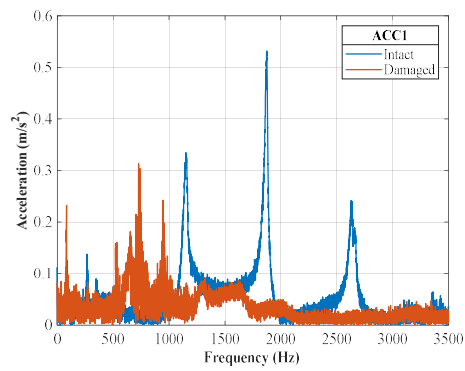
Ce-PE-0.8 (V08) – single impact test data



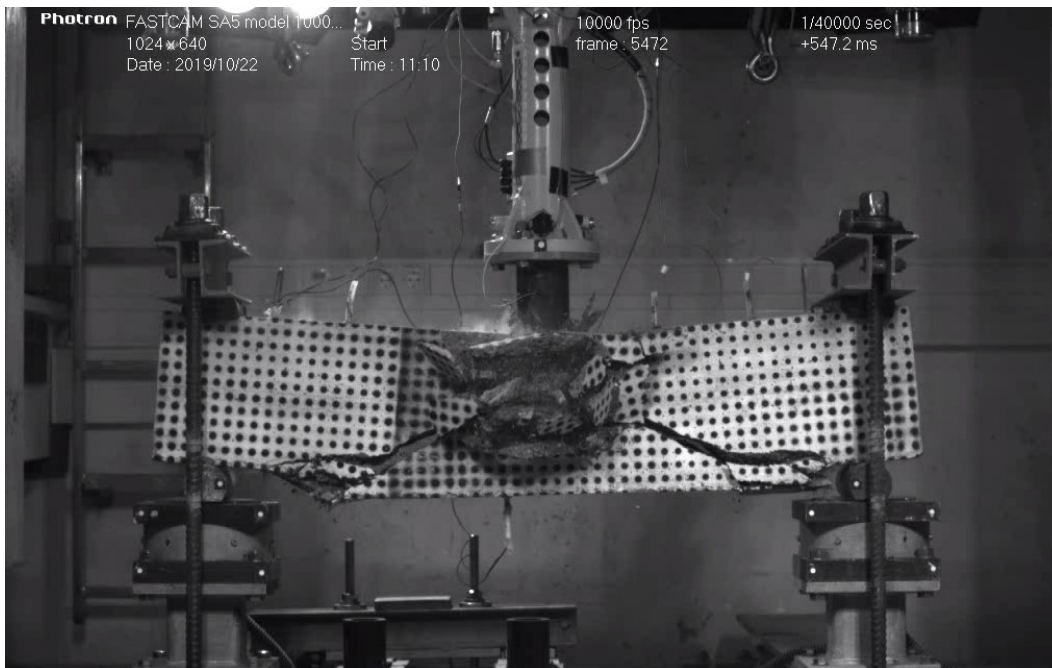
Transversal reinforcement configuration	With stirrups
Strengthening specification	PE
Acceleration pressure [bar]	0.8
Age substrate [days]	43
Age SHCC [days]	28
Impactor velocity [m/s]	25.7
Kinetic energy [J]	4699.7
Specimen mass before the test [kg]	141.2
Specimen mass after the test [kg]	141.2
Accountable breakout material [kg]	0.0



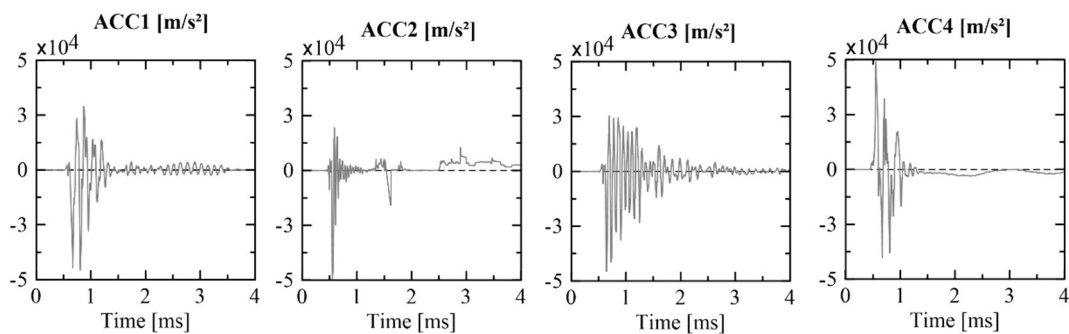
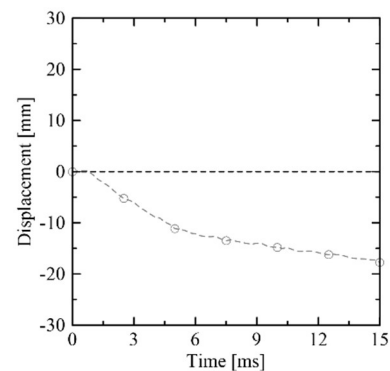
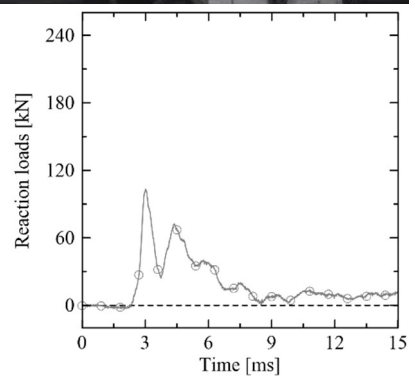
Ce-PE-0.8 (V08) – data collected before and after the impact



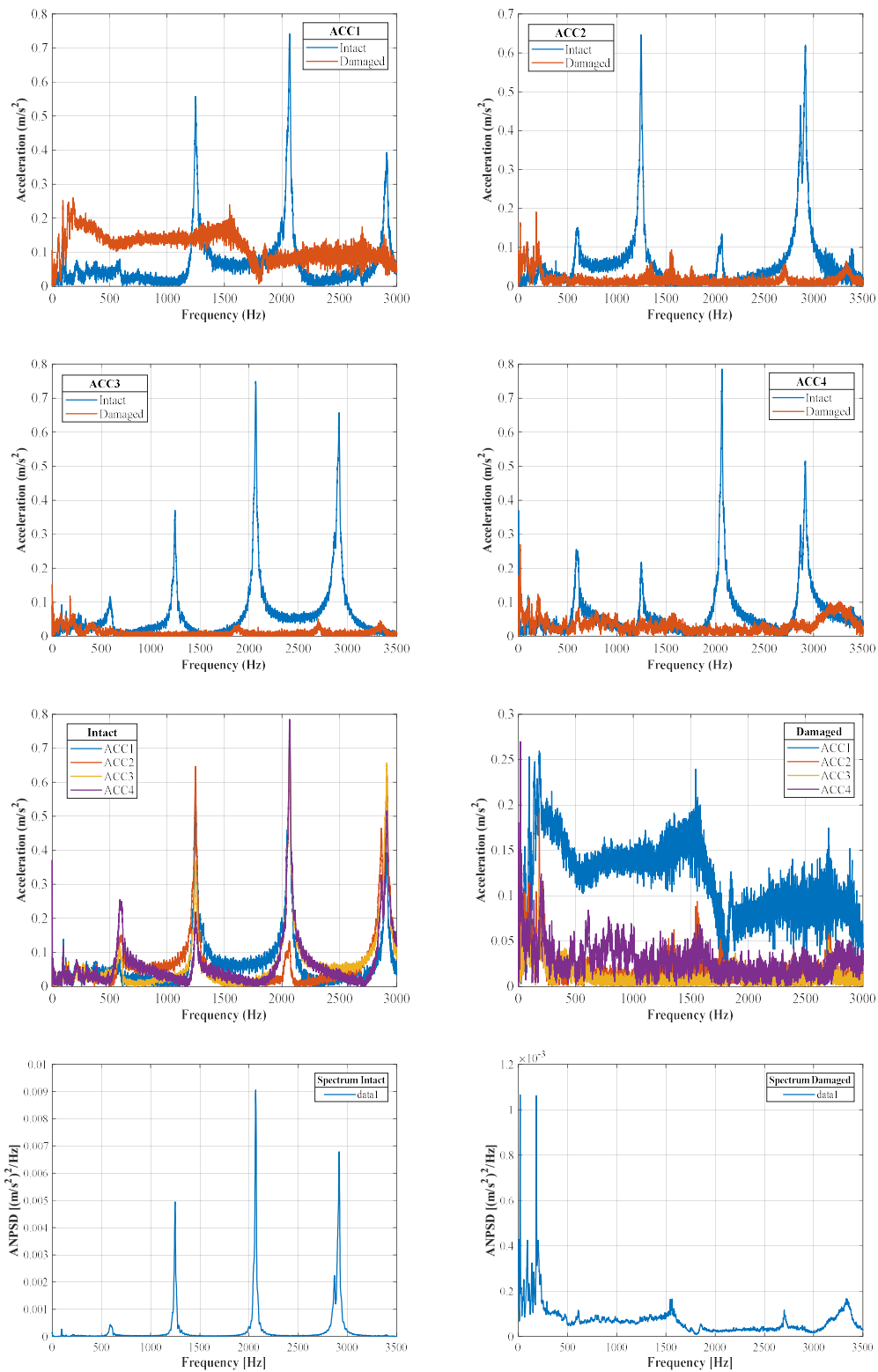
Se-Ref-1.2 (V17) – single impact test data



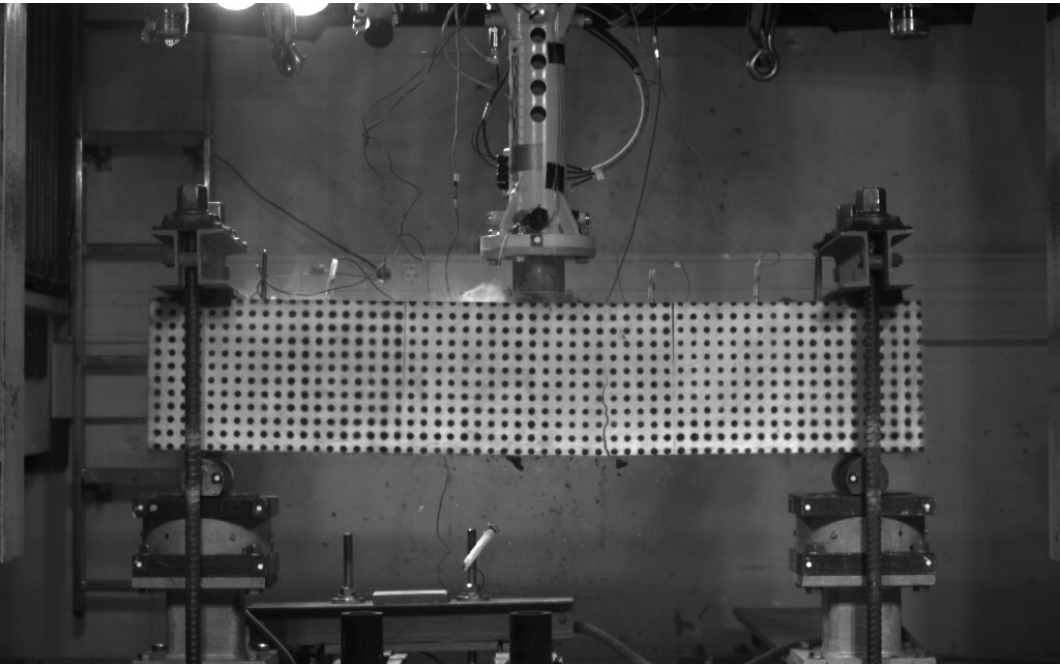
Transversal reinforcement configuration	Without stirrups
Strengthening specification	Reference beam
Acceleration pressure [bar]	1.2
Age substrate [days]	42
Age SHCC [days]	N/A
Impactor velocity [m/s]	29.9
Kinetic energy [J]	6356.4
Specimen mass before the test [kg]	115.6
Specimen mass after the test [kg]	106.1
Accountable breakout material [kg]	9.5



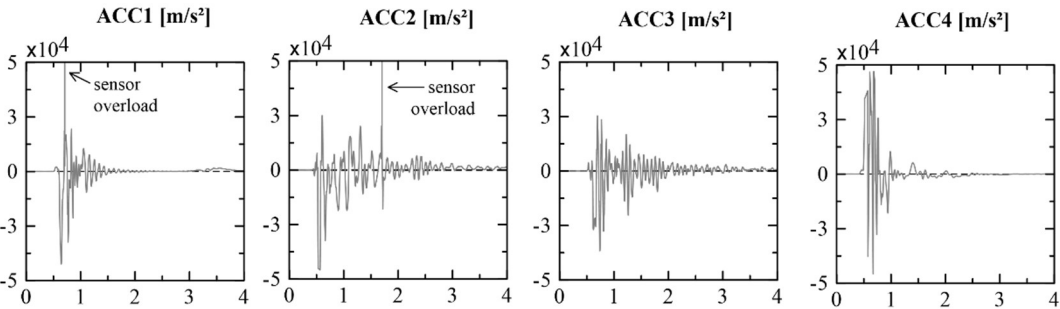
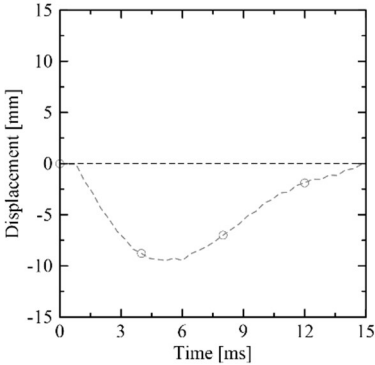
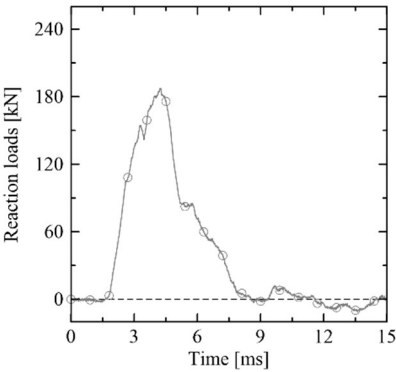
Se-Ref-1.2 (V17) – data collected before and after the impact



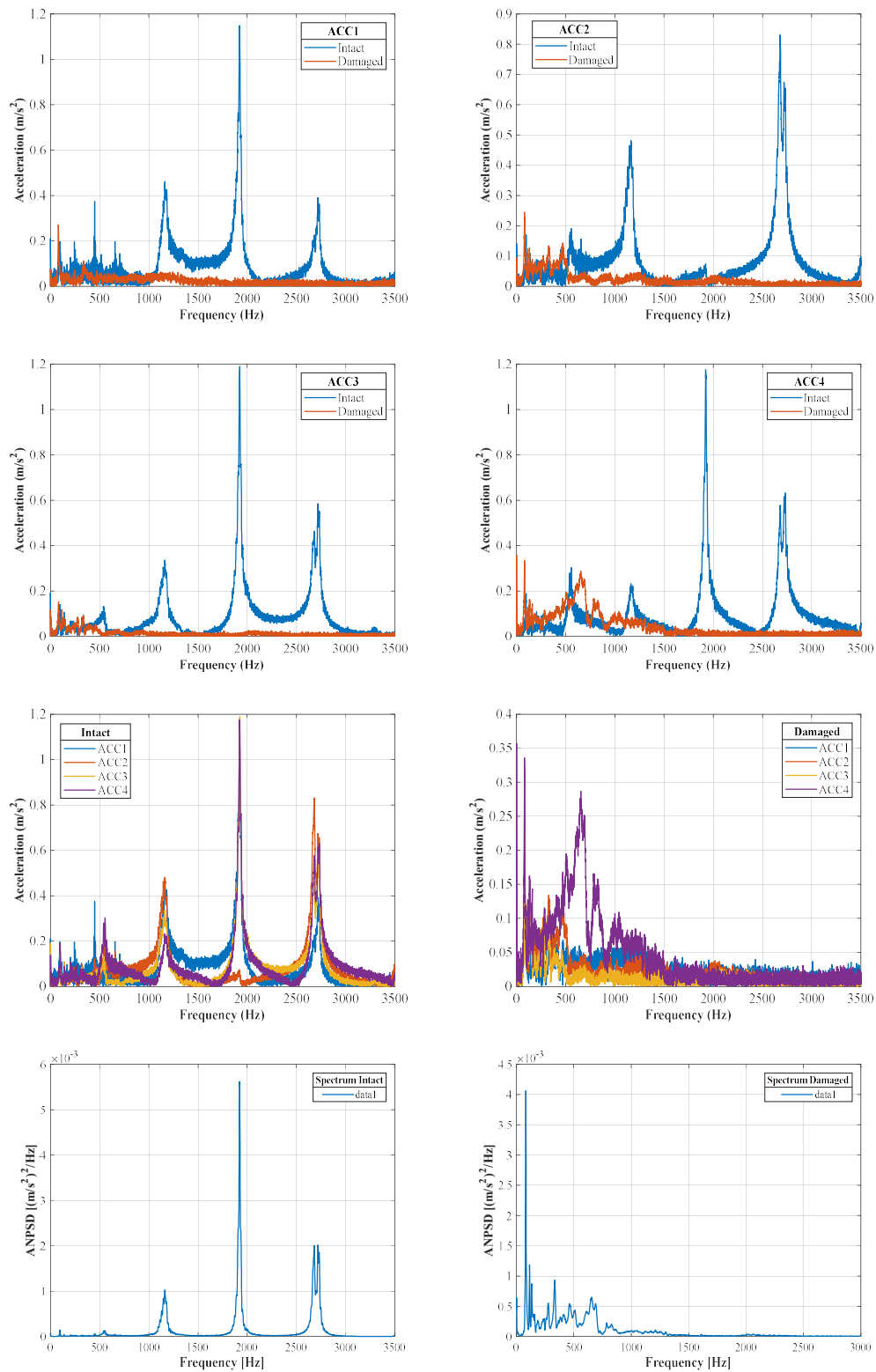
Se-PVA-1.2 (V24) – single impact test data



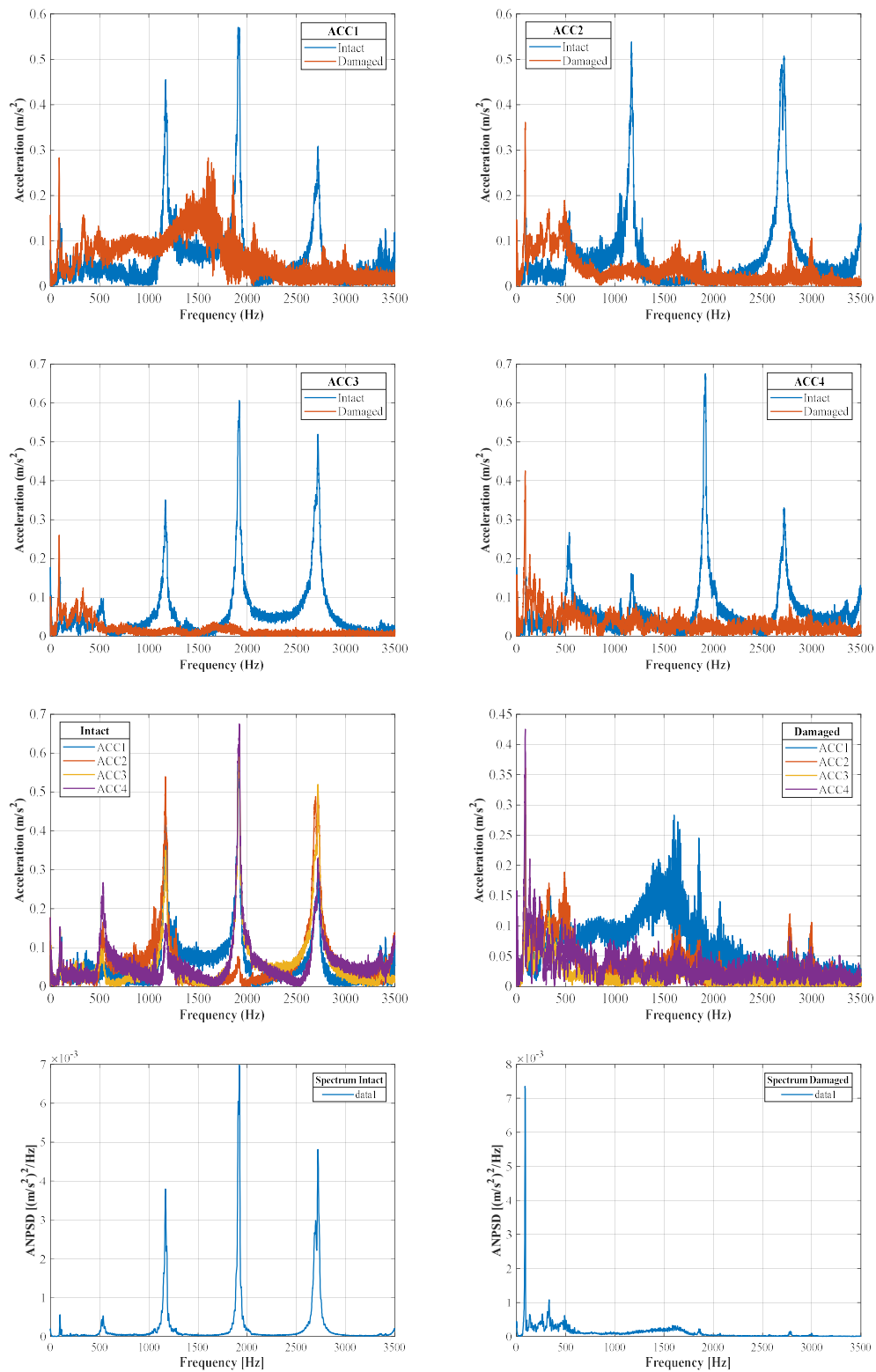
Transversal reinforcement configuration	Without stirrups
Strengthening specification	PVA
Acceleration pressure [bar]	1.2
Age substrate [days]	42
Age SHCC [days]	30
Impactor velocity [m/s]	29.9
Kinetic energy [J]	6335.2
Specimen mass before the test [kg]	141.6
Specimen mass after the test [kg]	141.5
Accountable breakout material [kg]	0.1



Se-PVA-1.2 (V24) – data collected before and after the impact

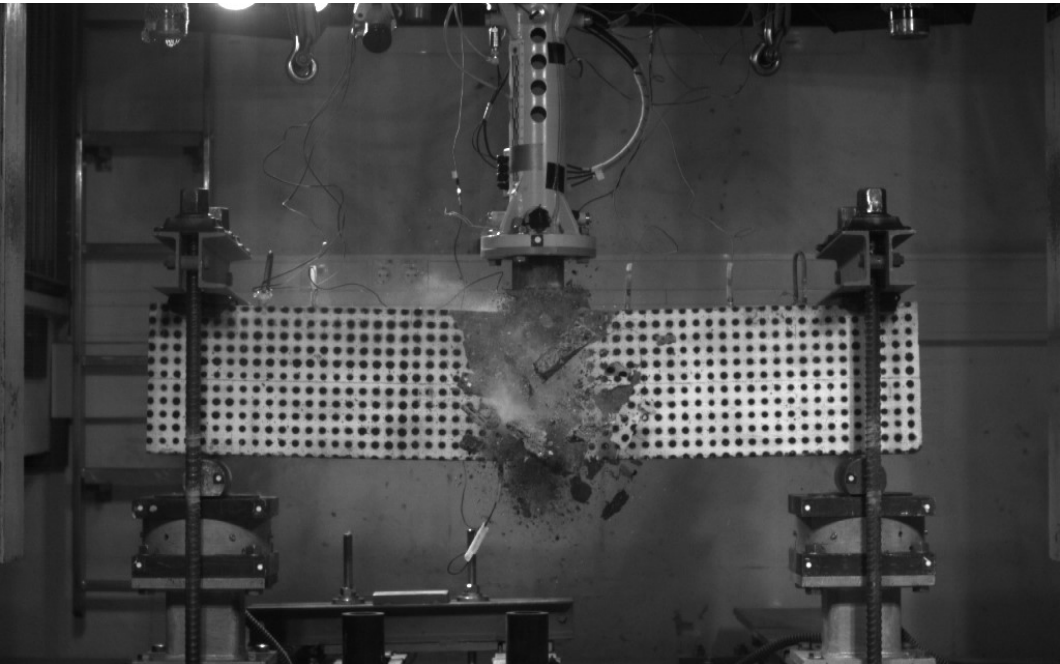


Se-PE-1.2 (V23) – data collected before and after the impact ⁹

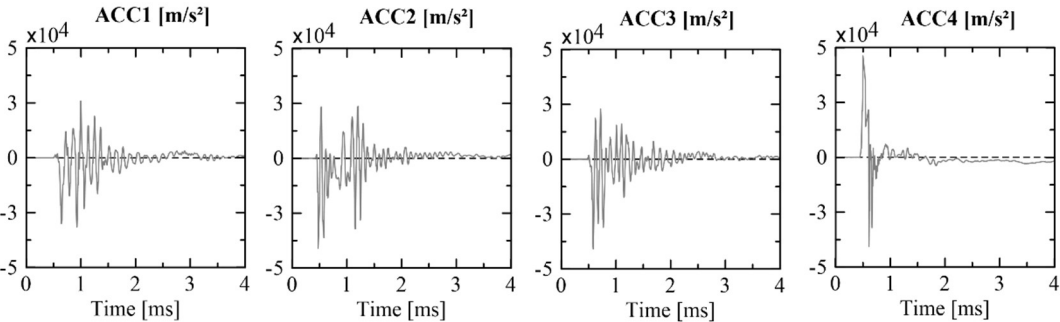
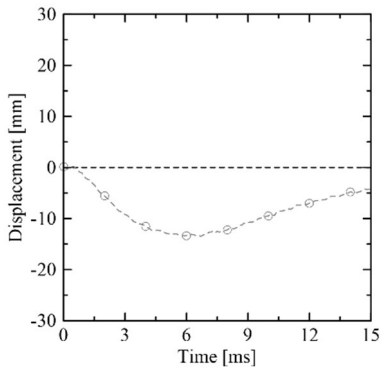
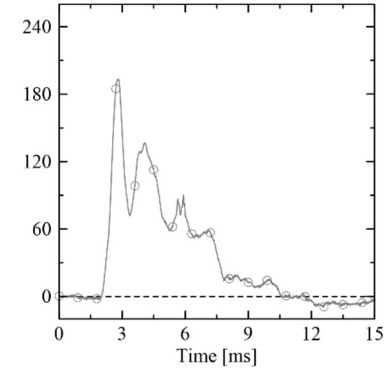


⁹ Due to acquisition problems, the datasheet regarding the impact test is not available.

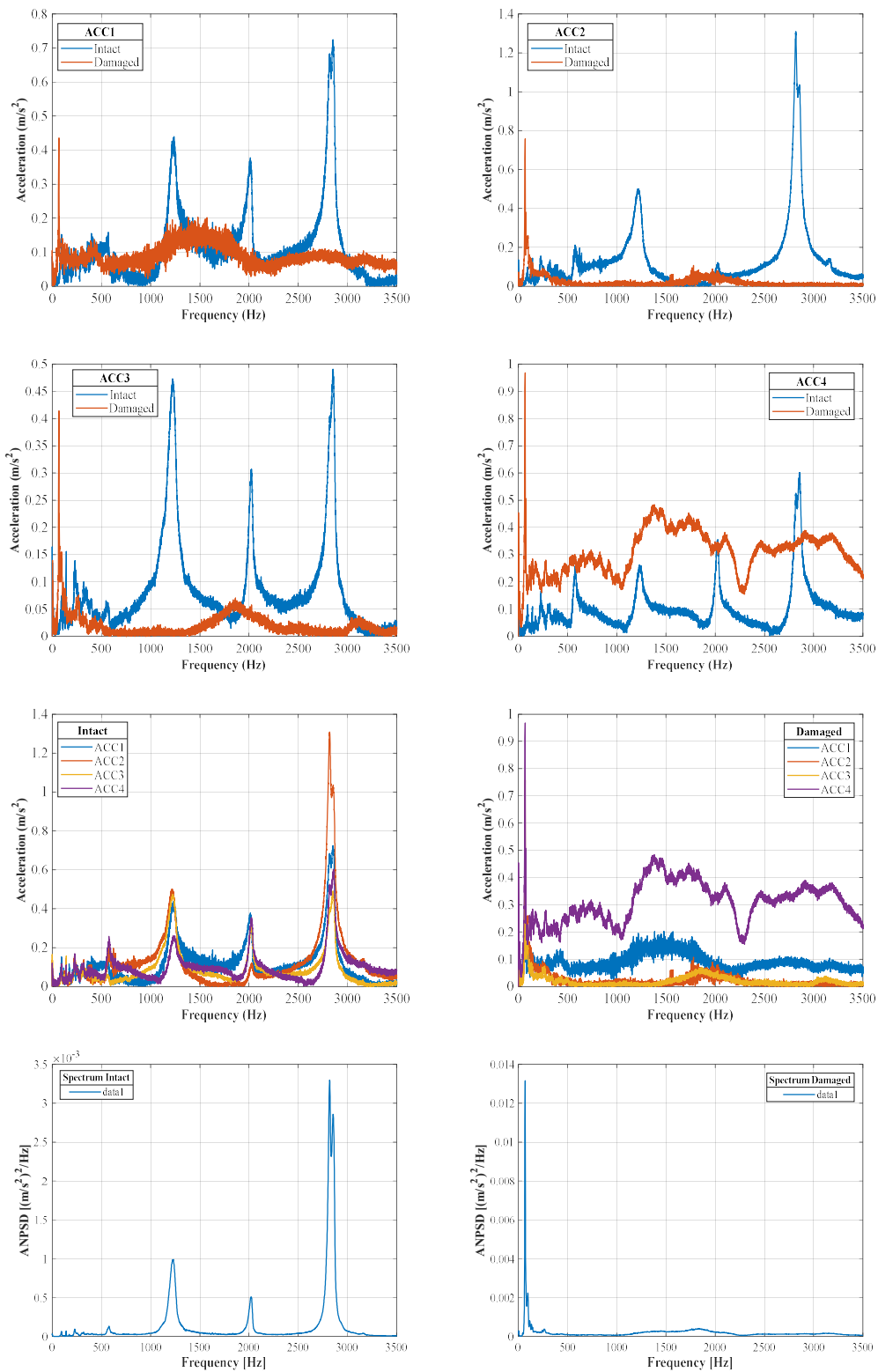
Ce-Ref-1.2 (V18) – single impact test data



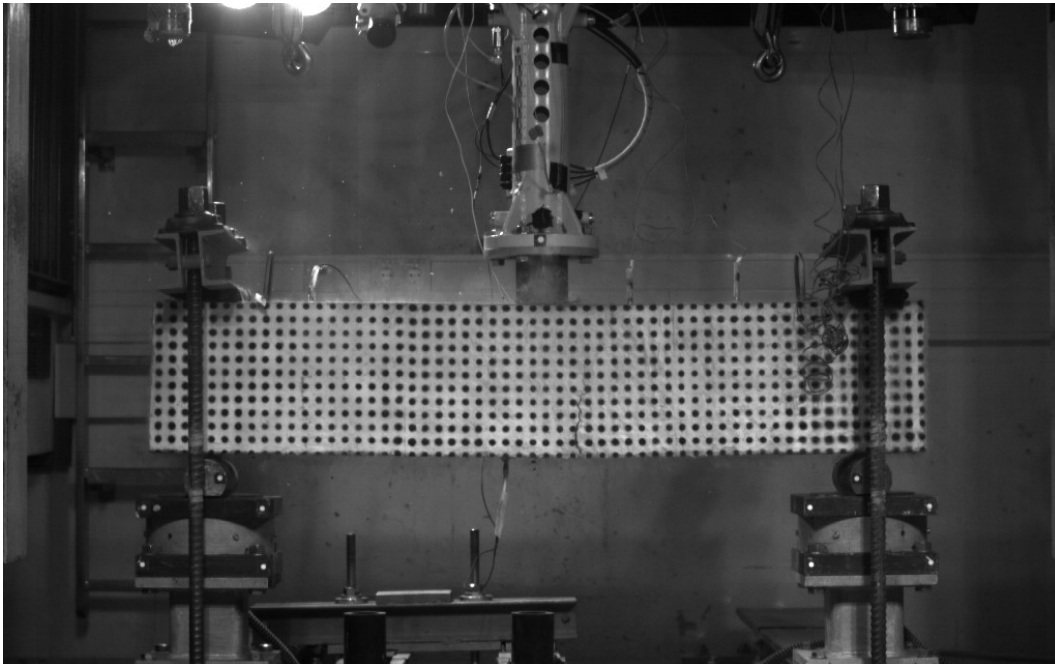
Transversal reinforcement configuration	With stirrups
Strengthening specification	Reference beam
Acceleration pressure [bar]	1.2
Age substrate [days]	42
Age SHCC [days]	N/A
Impactor velocity [m/s]	29.9
Kinetic energy [J]	6356.4
Specimen mass before the test [kg]	109.6
Specimen mass after the test [kg]	107.0
Accountable breakout material [kg]	2.6



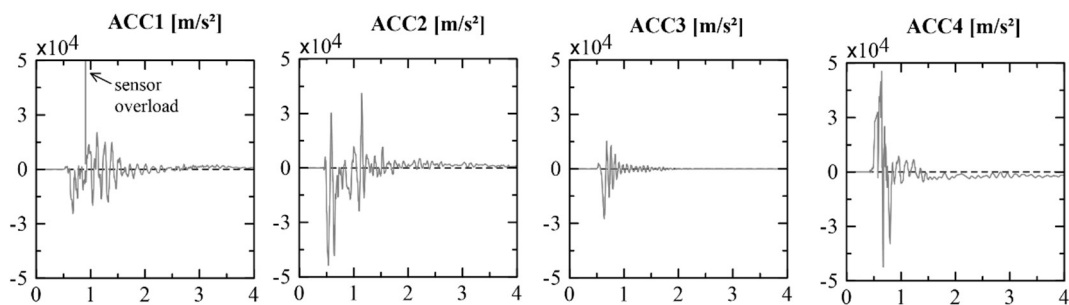
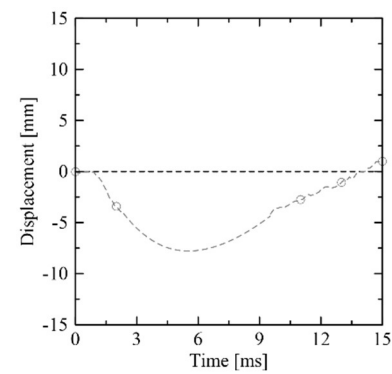
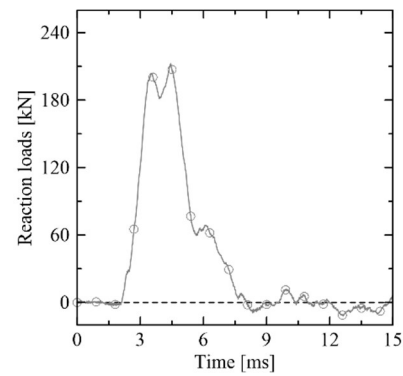
Ce-Ref-1.2 (V18) – data collected before and after the impact



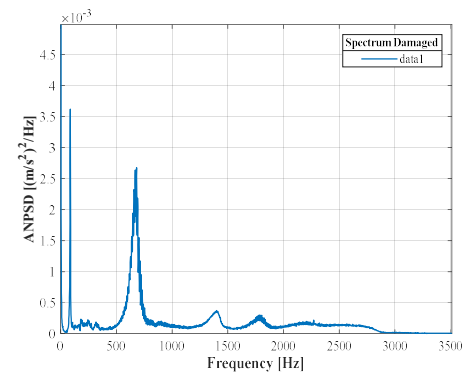
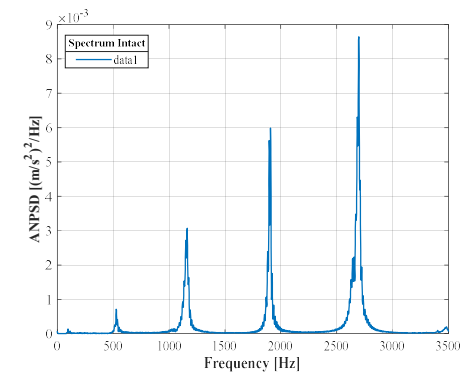
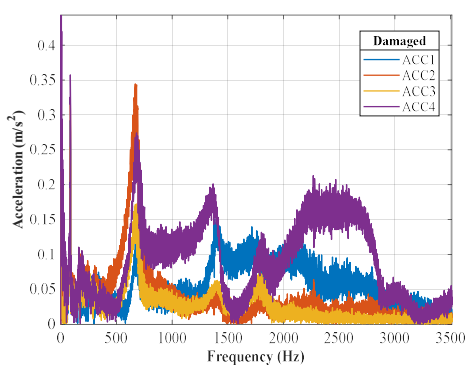
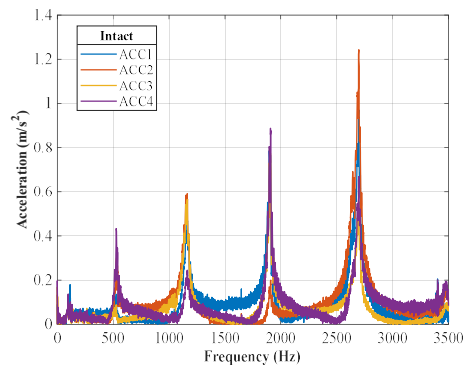
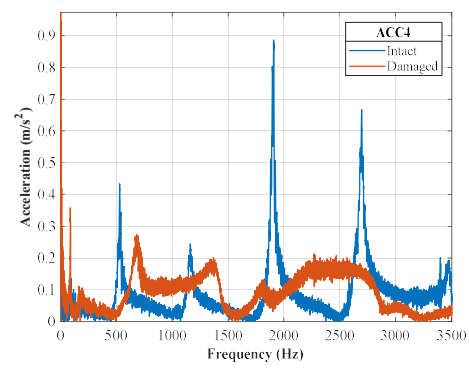
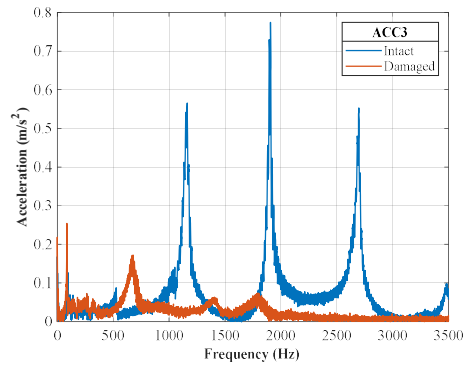
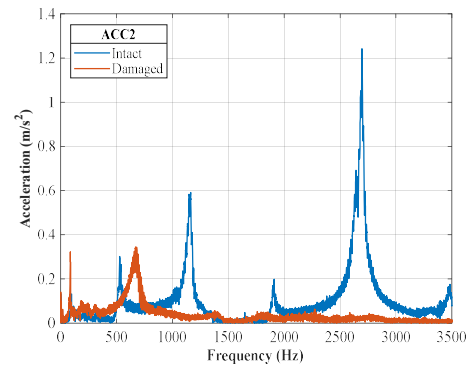
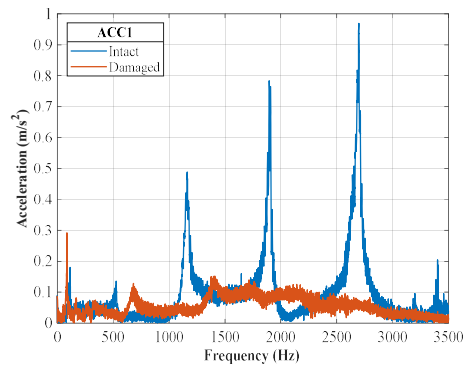
Ce-PVA-1.2 (V21) – single impact test data



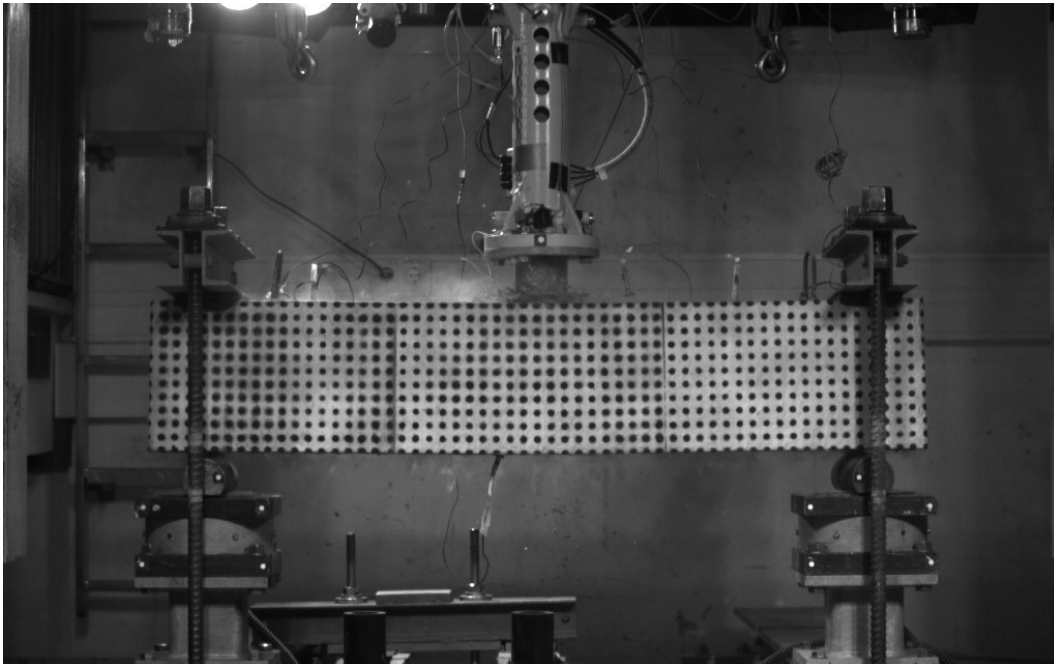
Transversal reinforcement configuration	With stirrups
Strengthening specification	PVA
Acceleration pressure [bar]	1.2
Age substrate [days]	42
Age SHCC [days]	30
Impactor velocity [m/s]	29.5
Kinetic energy [J]	6166.5
Specimen mass before the test [kg]	143.8
Specimen mass after the test [kg]	143.8
Accountable breakout material [kg]	0.0



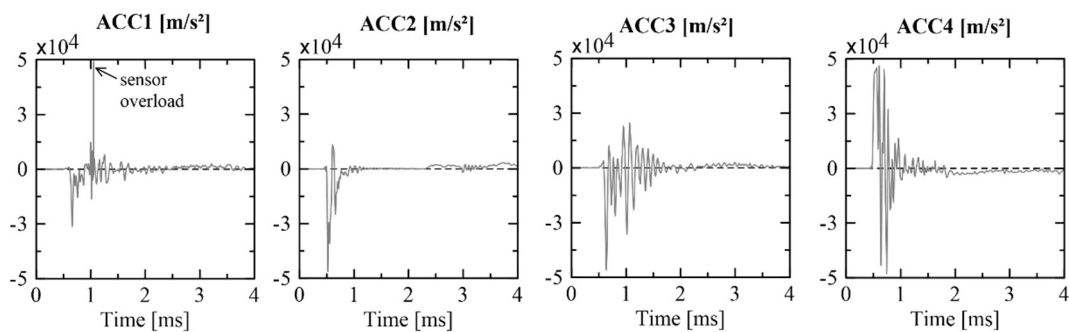
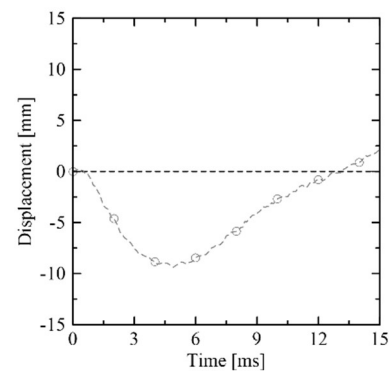
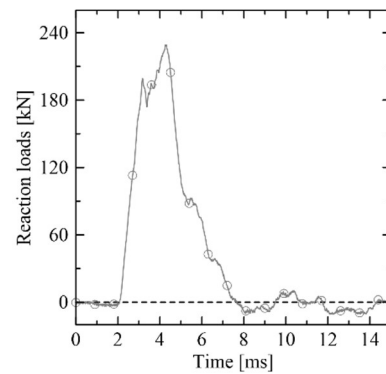
Ce-PVA-1.2 (V21) – data collected before and after the impact



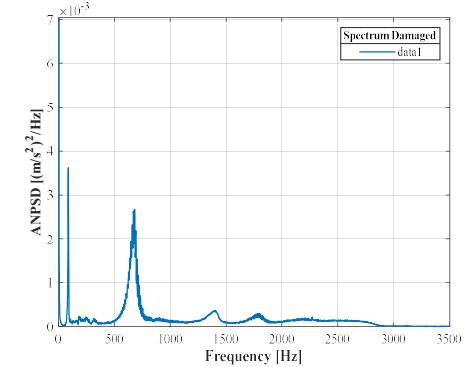
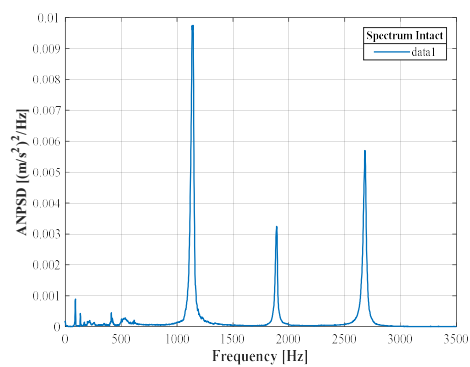
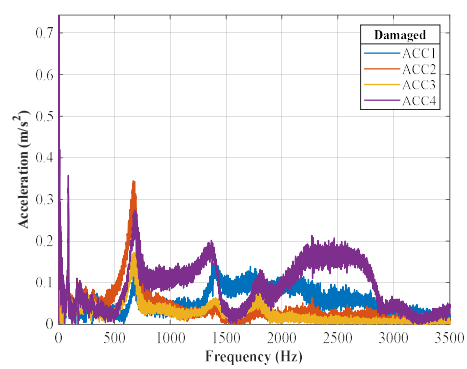
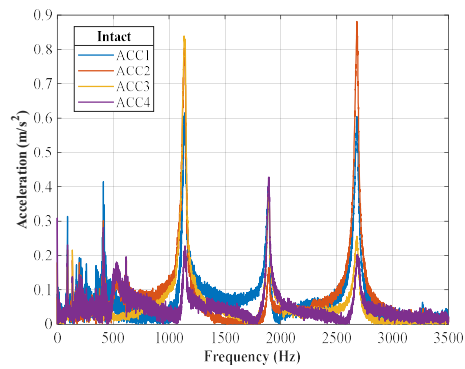
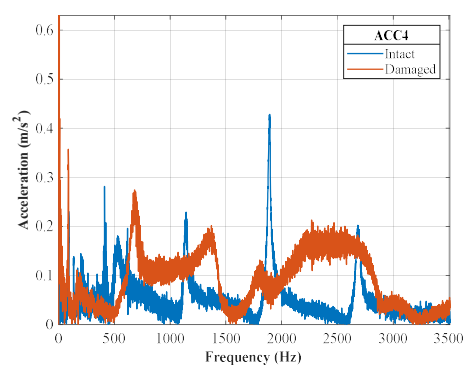
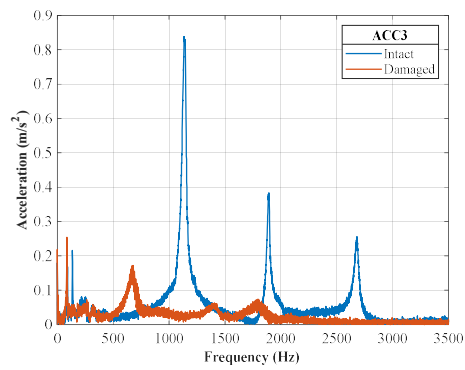
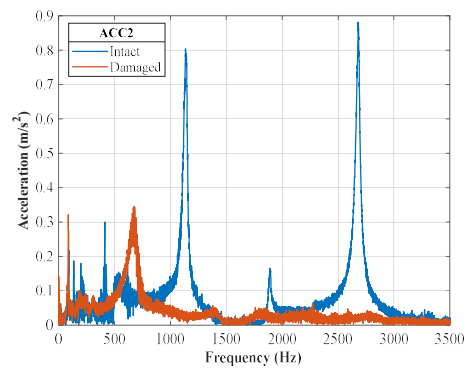
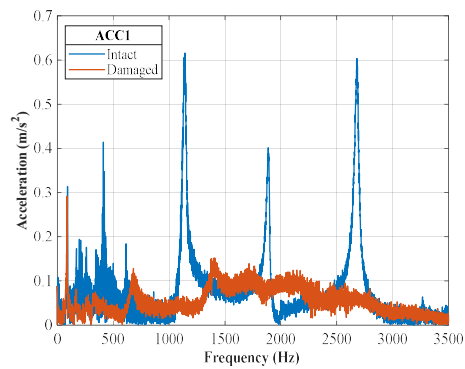
Ce-PE-1.2 (V22) – single impact test data



Transversal reinforcement configuration	With stirrups
Strengthening specification	PE
Acceleration pressure [bar]	1.2
Age substrate [days]	42
Age SHCC [days]	30
Impactor velocity [m/s]	29.9
Kinetic energy [J]	6356.4
Specimen mass before the test [kg]	142.5
Specimen mass after the test [kg]	142.4
Accountable breakout material [kg]	0.1

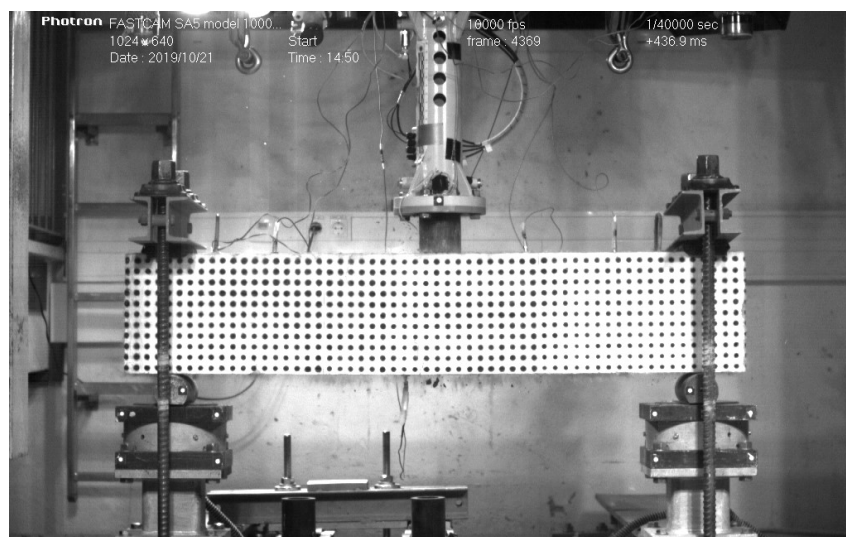


Ce-PE-1.2 (V22) – data collected before and after the impact

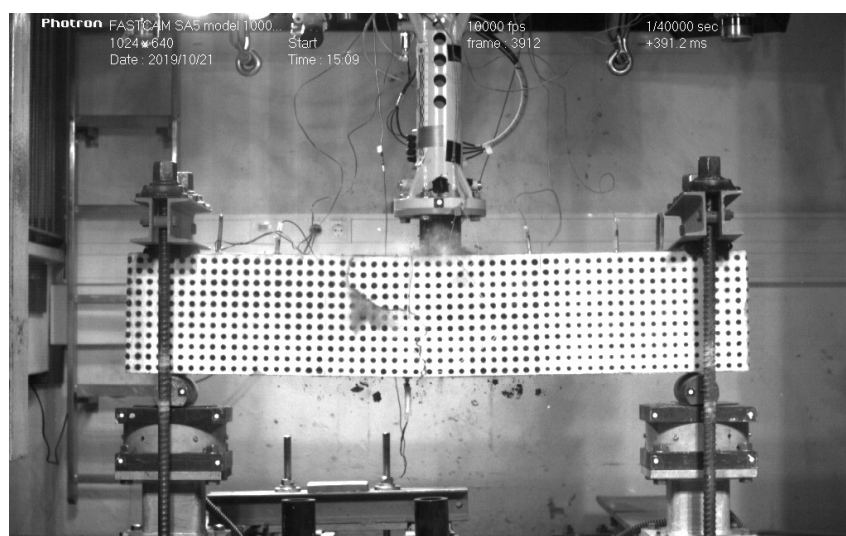


Se-PVA-0.8 (V20) – multiple impacts

1st impact

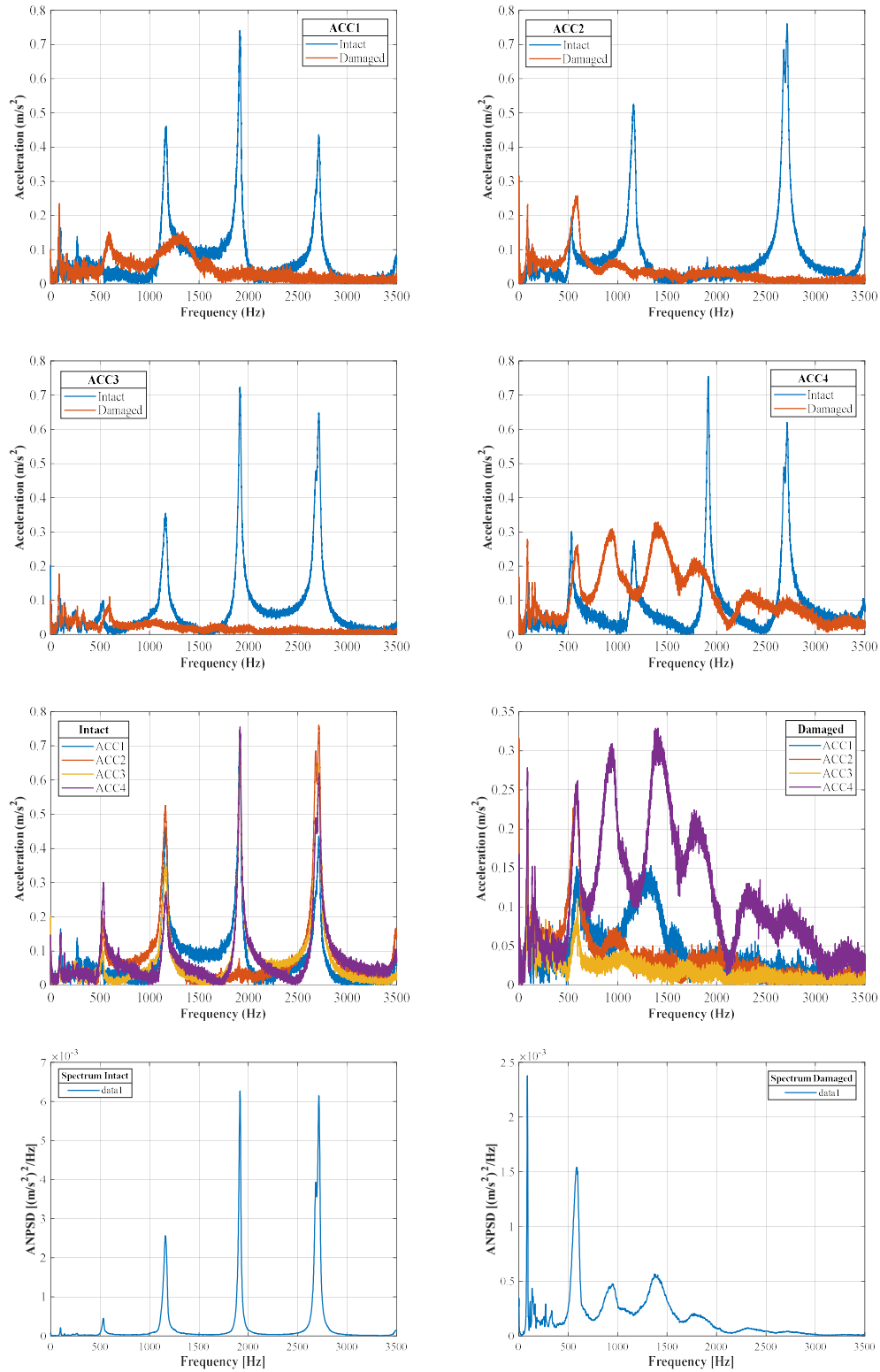


2nd impact

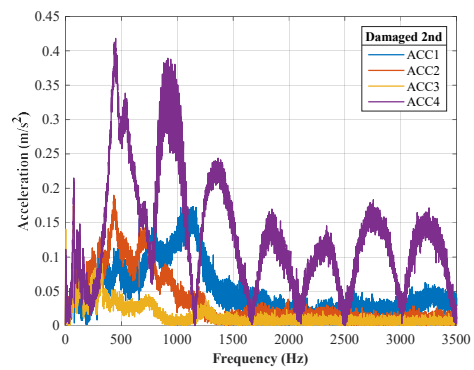
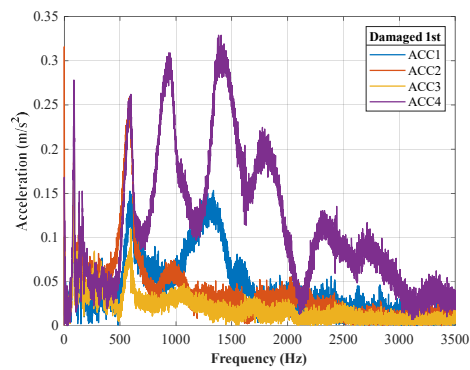
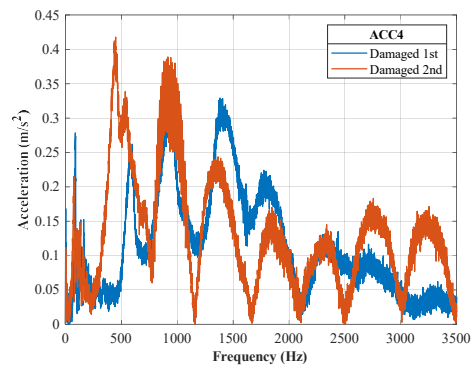
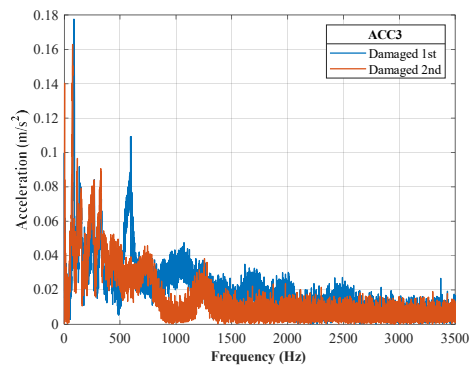
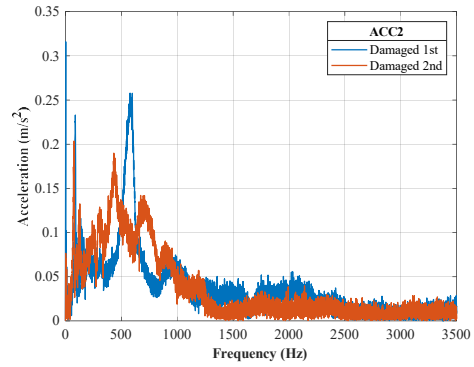
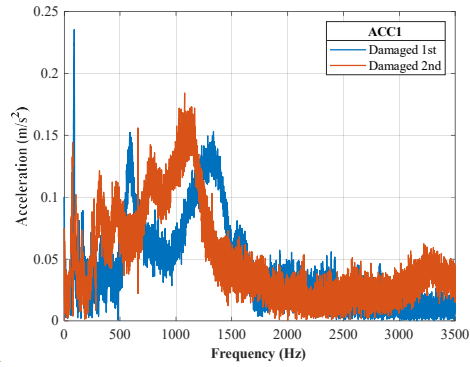


Transversal reinforcement configuration	Without stirrups
Strengthening specification	PVA
Acceleration pressure [bar]	0.8
Age substrate [days]	41
Age SHCC [days]	27
Average impactor velocity [m/s]	26.3
Kinetic energy [J]	4910.5

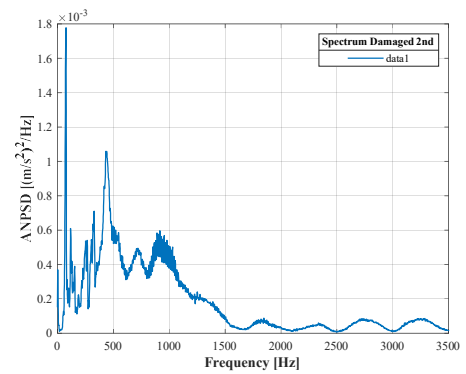
Se-PVA-0.8 (V20) – first impact response



Se-PVA-0.8 (V20) – second impact response

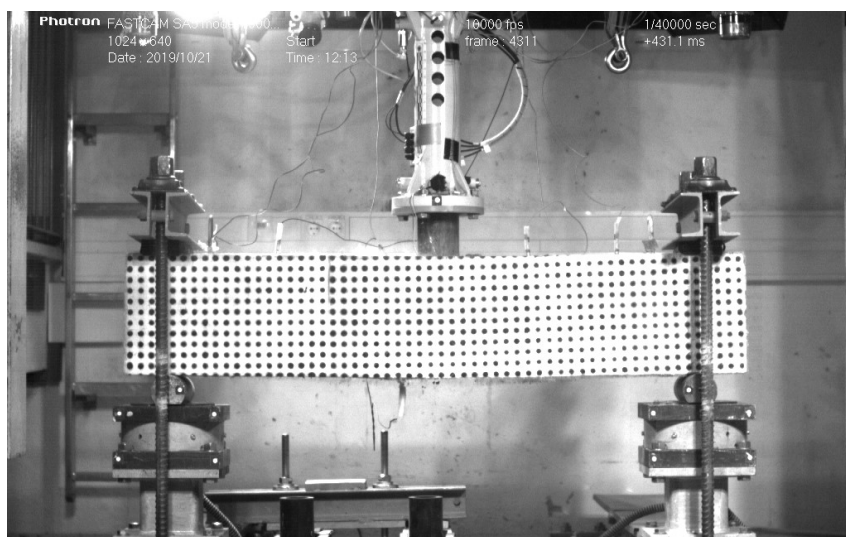


See previous page

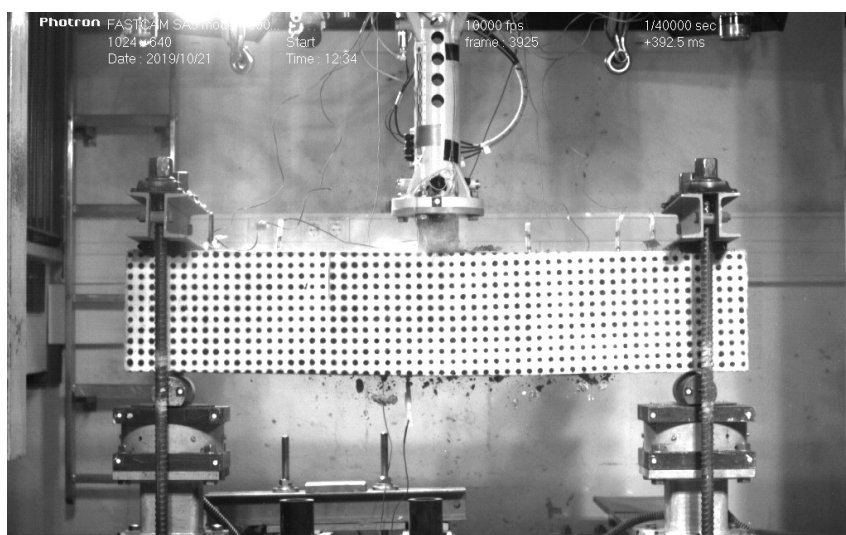


Se-PE-0.8 (V16) – multiple impacts

1st impact

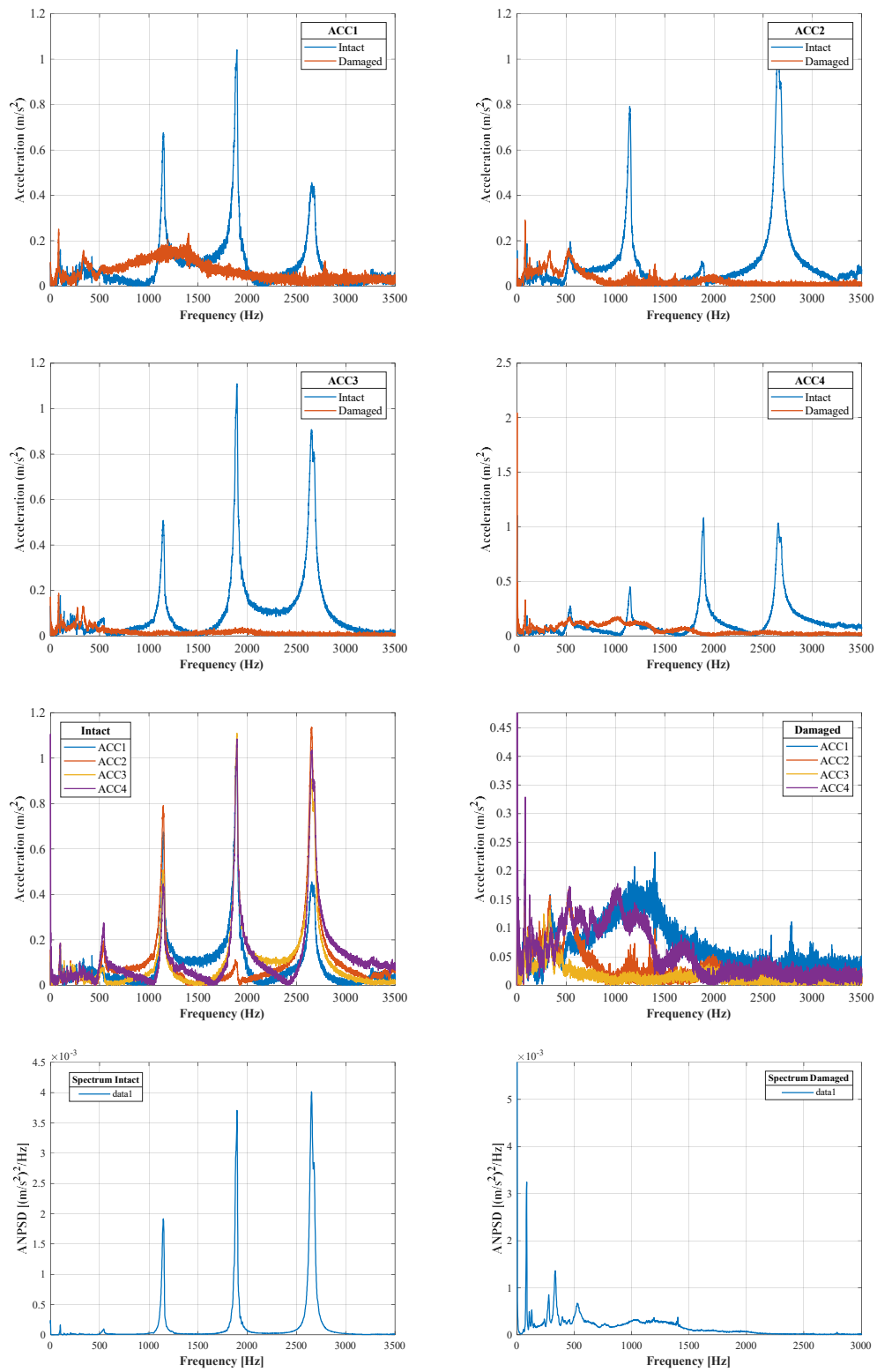


2nd impact

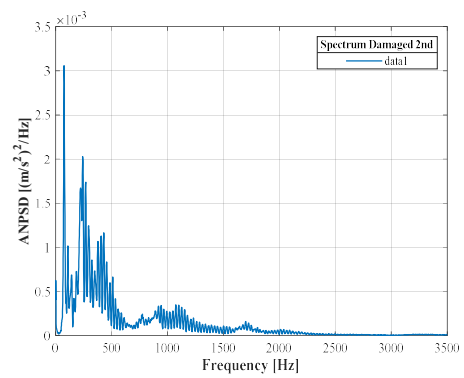
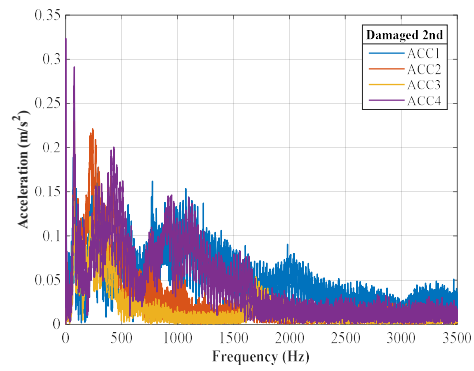
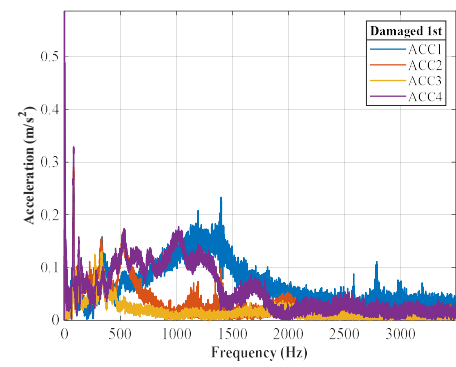
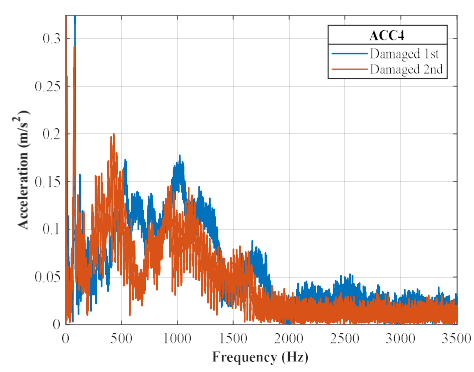
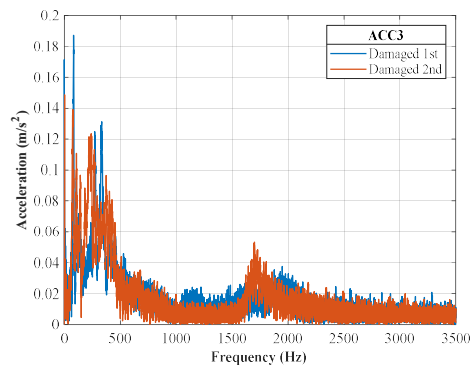
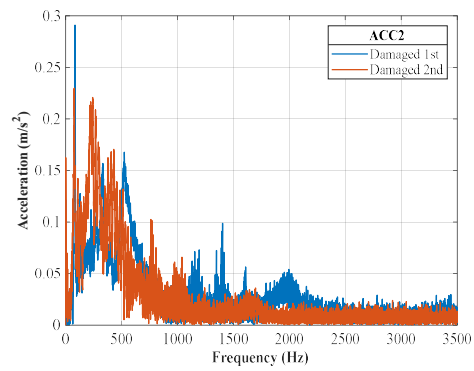
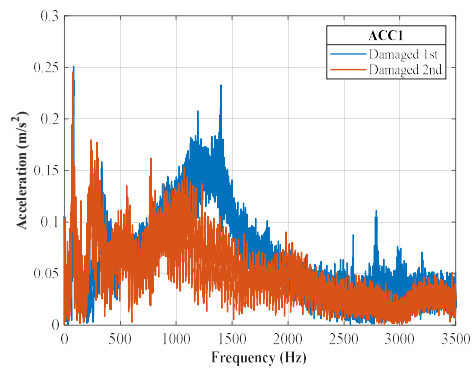


Transversal reinforcement configuration	Without stirrups
Strengthening specification	PE
Acceleration pressure [bar]	0.8
Age substrate [days]	41
Age SHCC [days]	27
Average impactor velocity [m/s]	25.7
Kinetic energy [J]	4700.1

Se-PE-0.8 (V16) – first impact response



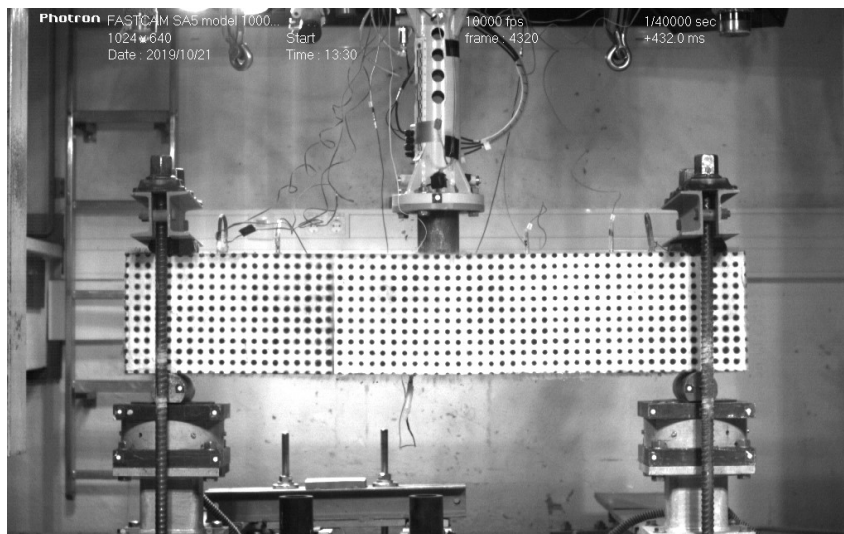
Se-PE-0.8 (V16) – second impact response



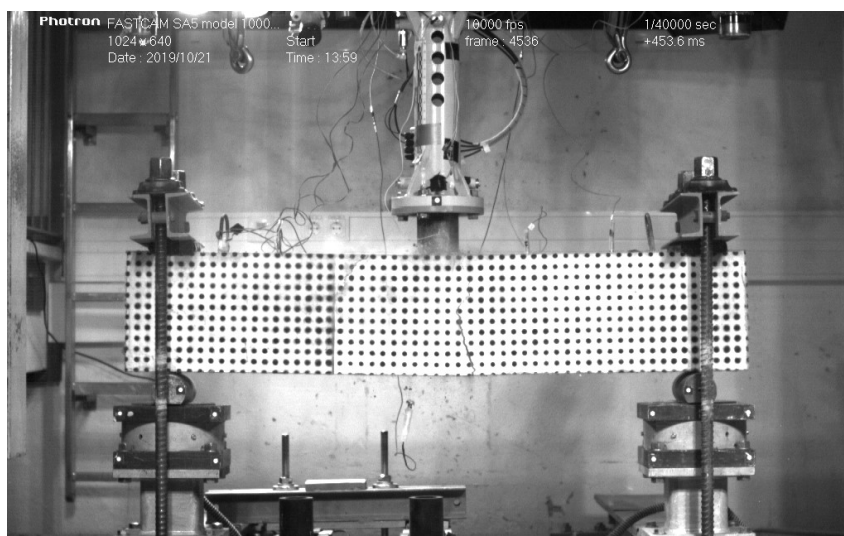
See previous page

Ce-PVA-0.8 (V19) – multiple impacts

1st impact

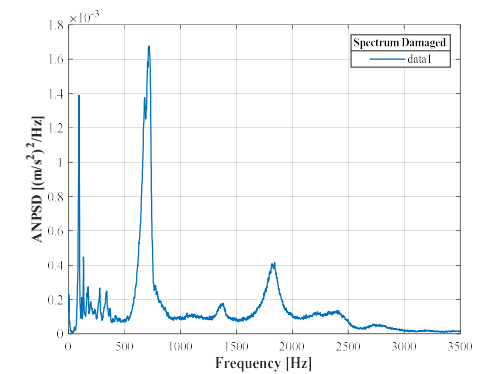
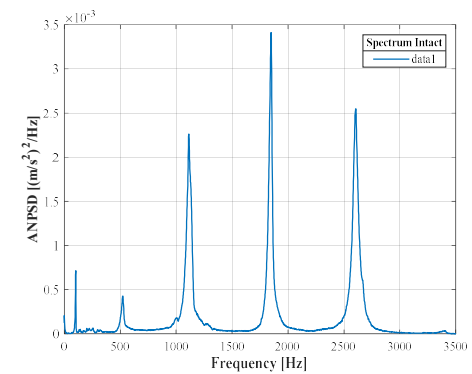
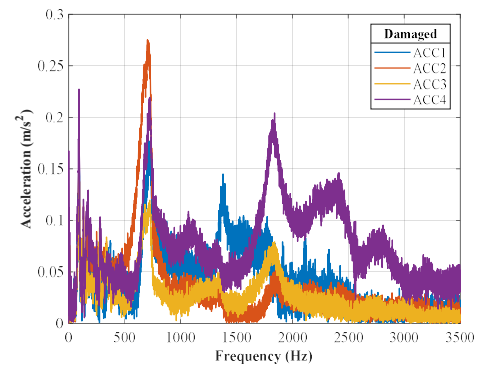
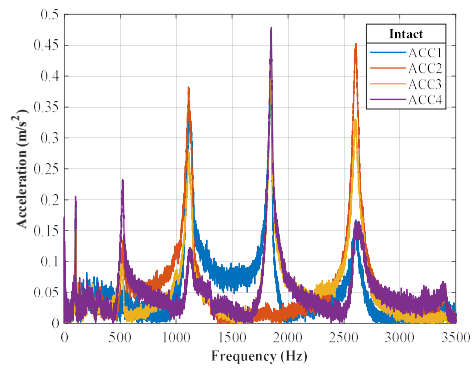
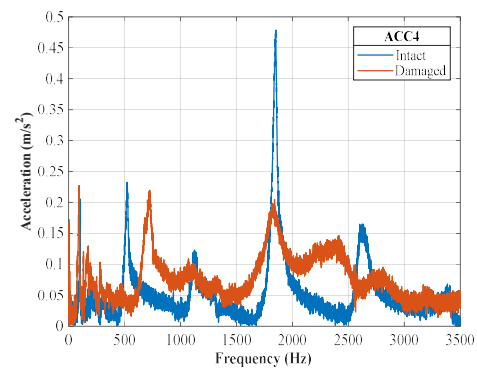
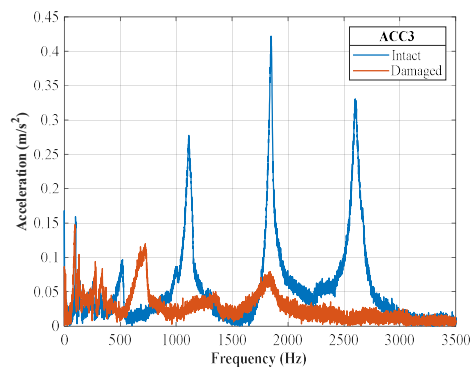
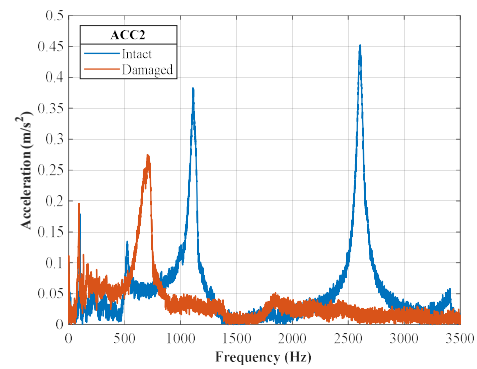
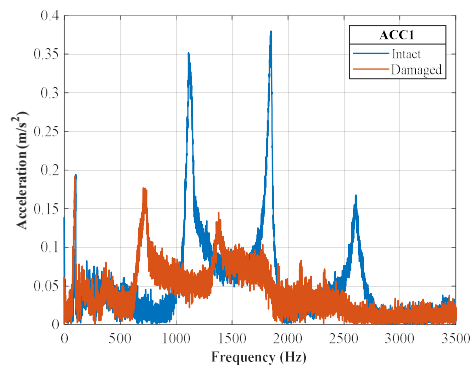


2nd impact

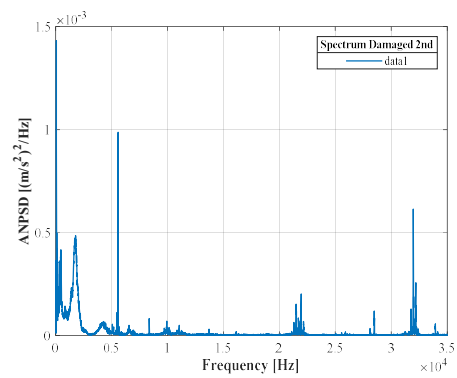
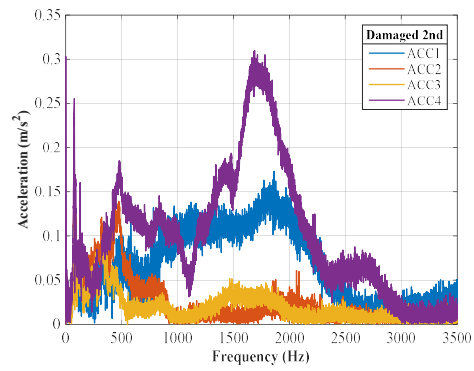
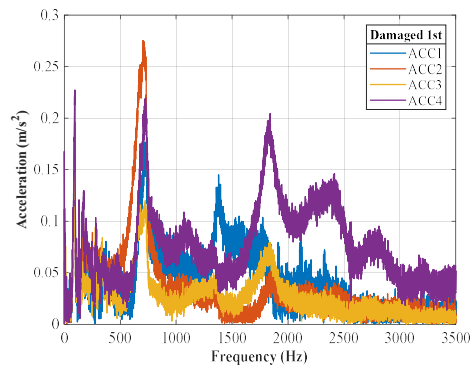
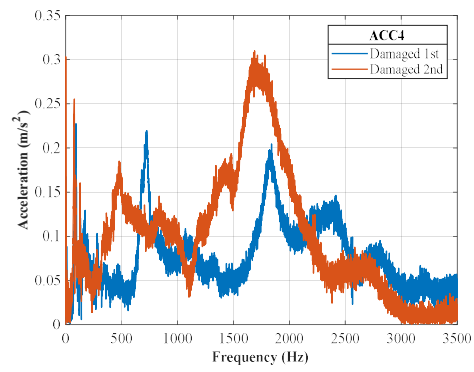
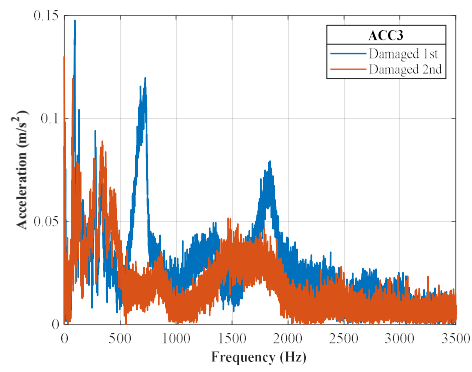
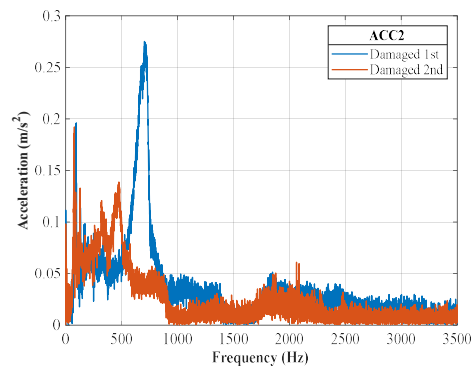
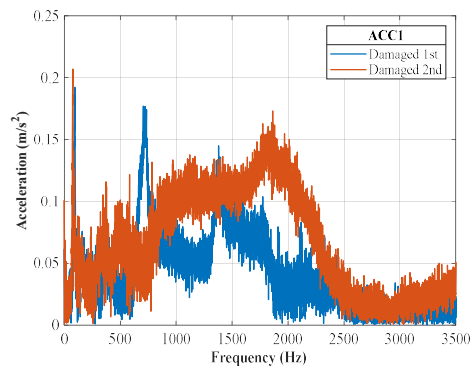


Transversal reinforcement configuration	With stirrups
Strengthening specification	PVA
Acceleration pressure [bar]	0.8
Age substrate [days]	41
Age SHCC [days]	27
Average impactor velocity [m/s]	25.8
Kinetic energy [J]	4718.5

Ce-PVA-0.8 (V19) – first impact response



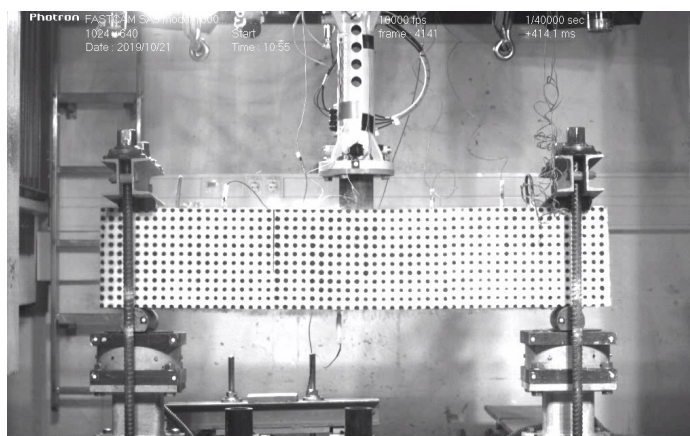
Ce-PVA-0.8 (V19) – second impact response



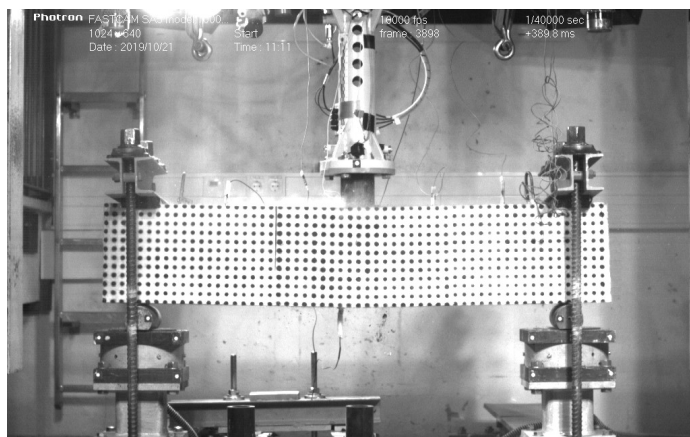
See previous page

Ce-PE-0.8 (V15) – multiple impacts

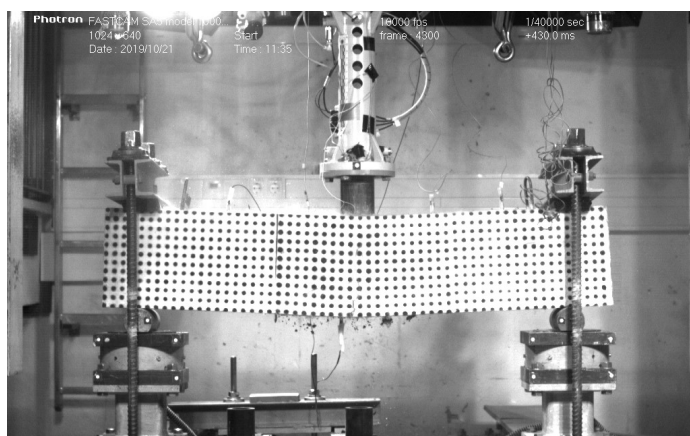
1st impact



2nd impact

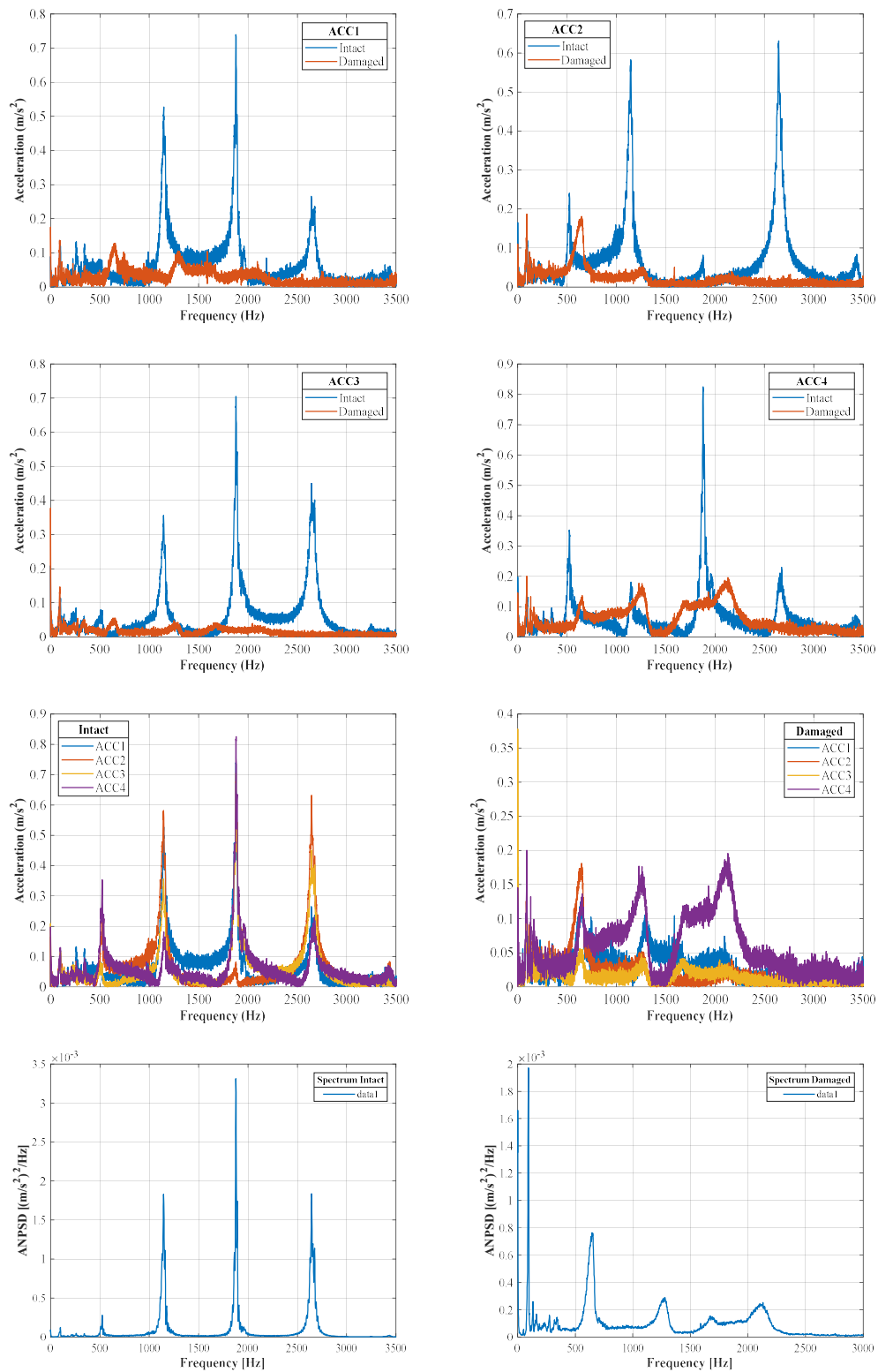


3rd impact

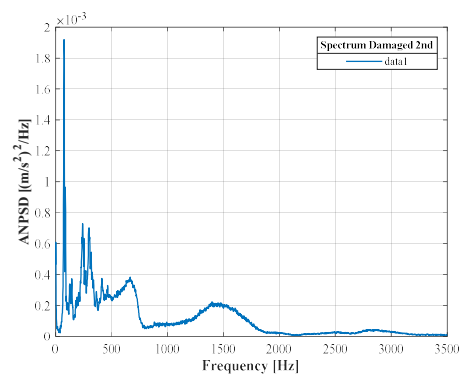
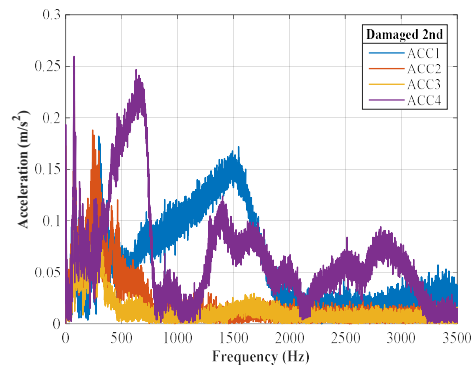
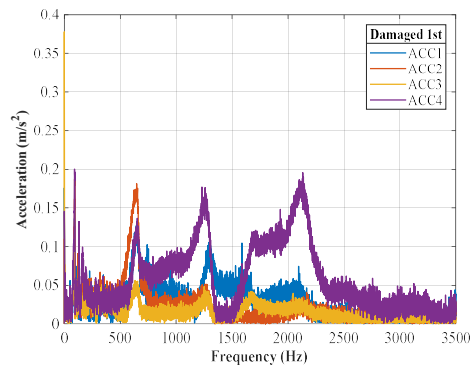
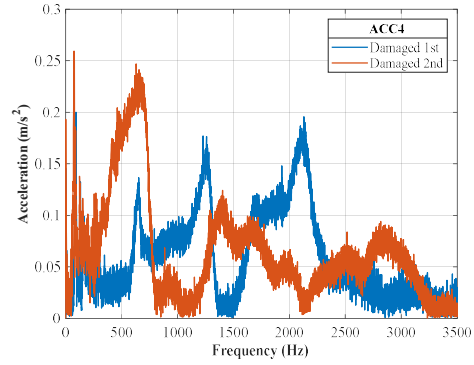
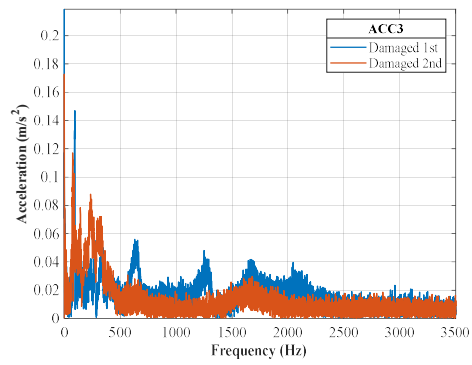
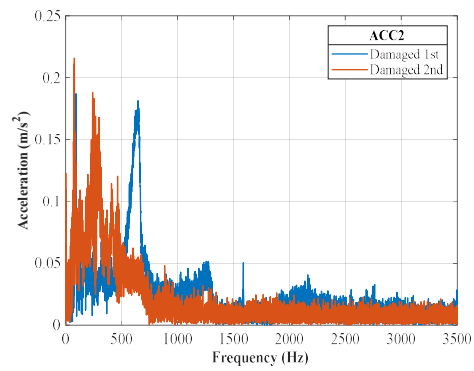
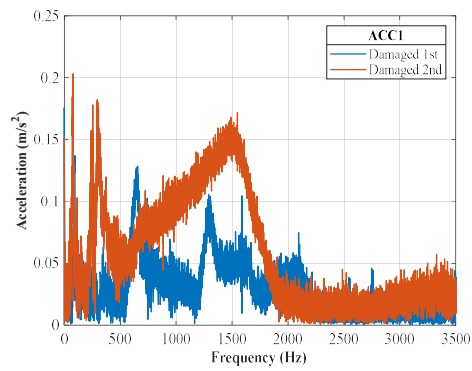


Transversal reinforcement configuration	With stirrups
Strengthening specification	PE
Acceleration pressure [bar]	0.8
Age substrate [days]	41
Age SHCC [days]	27
Average impactor velocity [m/s]	26.3
Kinetic energy [J]	4918.2

Ce-PE-0.8 (V15) – first impact response

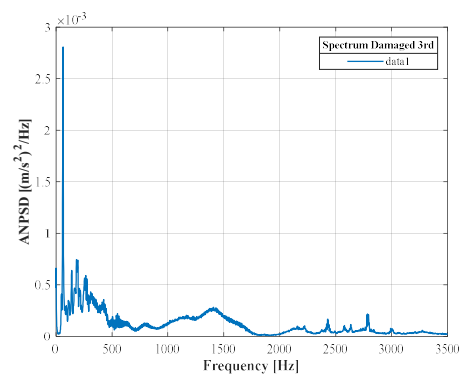
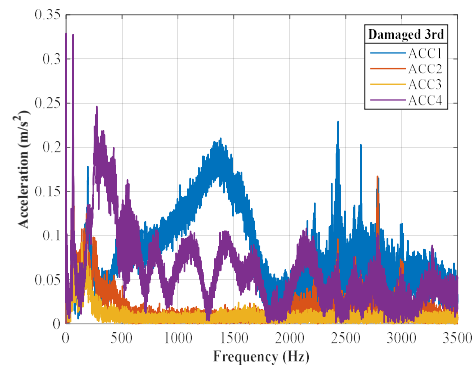
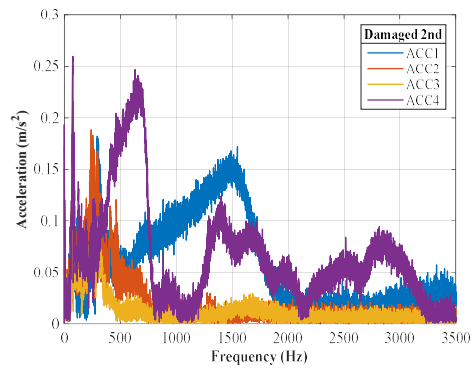
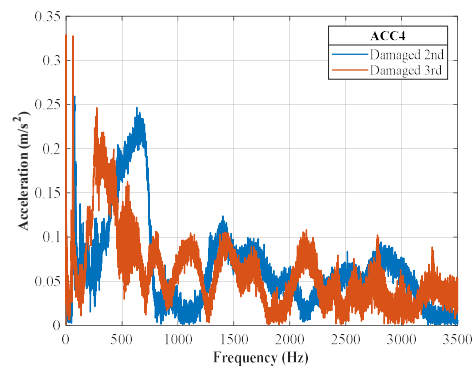
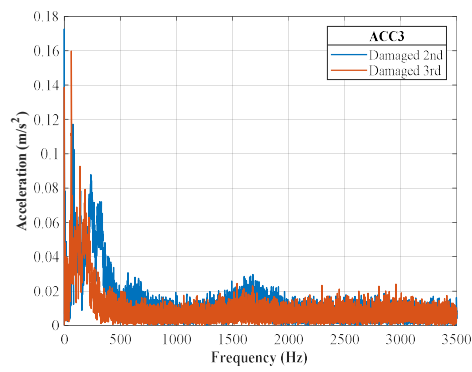
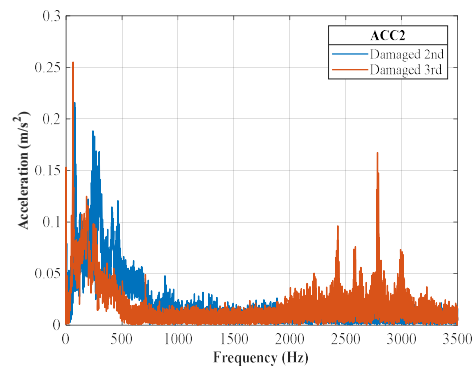
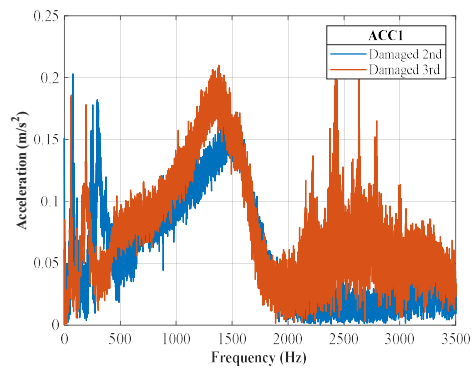


Ce-PE-0.8 (V15) – second impact response



See previous page

Ce-PE-0.8 (V15) – third impact response



See previous page